Experimental and Theoretical Investigation of the Mechanisms of Kānuka Wood Smoke Formation for Food Smoking

A thesis presented in partial fulfilment of the requirements for the degree of

Doctor of Philosophy

in

Chemical and Bioprocess Engineering

at Massey University, Palmerston North,

New Zealand

Nadeem Caco

2026

Abstract

The consistent production of smoked foods with a tunable aroma profile presents an industrial challenge, often relying on the subjective skill of artisan operators rather than precise process control. While temperature is known to be a key factor, the underlying mechanisms governing smoke chemistry and heat dynamics are less understood. This thesis aimed to deconstruct the thermochemical processes of kānuka wood pyrolysis to establish a framework for predictable and controllable smoke generation. The research objectives were to: (1) determine the intrinsic decomposition kinetics of kānuka wood; (2) characterise the temperature-dependent evolution of its volatile aroma profile; (3) quantify the influence of process parameters on its specific enthalpy of reaction; and (4) develop a predictive model to simulate and optimise the process.

Thermogravimetric Analysis (TGA) was used to determine the decomposition kinetics of kānuka's principal components (hemicellulose, cellulose and lignin). The specific volatile organic compounds (VOCs) comprising the smoke's aroma profile were identified and quantified across a temperature range of 200-520 °C using Pyrolysis-Gas Chromatography/Mass Spectrometry (Py-GC/MS). The heats of primary and secondary reactions were measured using TGA-differential Scanning Calorimetry (TGA-DSC). Py-EGA/MS was also used to study the formation kinetics of key aroma compounds. Finally, these experimental insights were integrated into a one-dimensional, transient model that solves coupled equations for heat transfer, mass transfer and reaction kinetics to simulate pyrolysis in a thermally thick bed of wood.

The experimental results revealed that smoke composition is highly temperature-dependent, with carbohydrate-derived compounds (e.g., fufural) dominating at 200-350 °C and lignin-derived phenolics (e.g., guaiacol, syringol) surging above 400 °C. Importantly, TGA-DSC analysis demonstrated that small particle sizes (<90 μm) and high samples masses promote exothermic secondary reactions due to low bed permeability, leading to increased char yield and potential

thermal runaways. This finding identified bed permeability, governed by particle size, as the critical parameter for controlling local temperature and by extension the smoke's aroma. The numerical model confirmed these relationships, showing that slower heating rates, lower final temperature and deeper beds bias the aroma proxy towards compounds formed at 200-300 °C, while faster heating rates and shallower beds shift it towards the 300-400 °C range.

In conclusion, this research provides the first comprehensive thermochemical characterization of kānuka wood for smoking applications. It establishes a novel conceptual framework that moves beyond simple temperature control to identify bed permeability and secondary reaction management as the key to process consistency. By clarifying the fundamental mechanisms and providing a predictive model, this thesis provides the scientific basis to help transform food smoking from an operator dependent art into a predictable, tune-able and repeatable science.

Acknowledgements

I would like to express my deepest and most profound gratitude to Professor Jim R. Jones, who first sparked my interest in engineering as an undergraduate and later guided me as a supervisor. His influence has shaped not only the course of my research but also the course of my life. I consider him one of the most important people in shaping who I am today, both as a researcher and as a person. Professor Jones has gone far beyond what is expected of a supervisor, offering unwavering support, generosity and kindness at every step. Because of his guidance, I have been able to pursue opportunities and a life I once only dreamed of. More than a mentor, he has been a role model, a friend and a source of inspiration. Words cannot truly capture the depth of my gratitude, but I will remain forever thankful for the privilege of learning from him.

I would like to extend my heartfelt and enduring thanks to Associate Professor Jim (Qun) Chen, whose guidance has been invaluable in building my confidence as an engineer. He has always been positive and supportive in my research, while never hesitating to guide me firmly when I was on the wrong path, helping me find my way forward. His willingness to go above and beyond, even making himself available across time zones, on weekends and during holidays, reflects a generosity of spirit for which I will always be deeply grateful. From him I have learned not only about research but also about humility, integrity and the importance of character. His example has left an permanent mark on me, and I will carry those lessons with me for the rest of my life.

I am also sincerely grateful to Associate Professor Graham Eyres for his support and guidance, particularly with my experimental work and analysis. Although we did not work as closely together, his assistance was pivotal to the successful completion of this thesis. I greatly appreciate the kindness and encouragement he has always shown me through this journey.

I would also like to thank Dr. Georg Ripberger for his brief but valuable supervision at the beginning of my thesis. Much of the research presented here is, in many ways, an extension of his

work and hypotheses in pyrolysis. I am grateful for his contributions and for the foundation he provided which helped shape the direction of this thesis.

I would also like to extend my thanks to the many people who have supported me throughout this journey. From lab managers and technical staff, whose assistance made so much of my experimental work possible, to my fellow PhD students and colleagues, who shared their advice, encouragement and friendship. I am also grateful to the many people I met at conferences, workshops and seminars, whose insights broadened my perspective and enriched my research. There are too many to name individually, but each has contributed in their own way to this thesis and to my development as a researcher. Finally, I am thankful to Massey University for providing an environment in which I could learn, grow and hopefully contribute to science.

Finally, I would like to express my deepest gratitude to my family. To my girlfriend, Amanda McTaggart, thank you for your love, patience and understanding throughout this journey. You have been by my side through the hardest moments and your constant support has given me the strength to keep going when I needed it most.

To my son, Archie, you have been my greatest source of joy and perspective. Your curiosity, laughter and presence have reminded me of what truly matters in life and has inspired me to persevere through the challenges of this thesis.

To my parents and family, thank you for instilling in me a love of learning and for always believing in me. Your encouragement and sacrifices have made this journey possible, and I am endlessly grateful.

Table of Contents

List of Figures

List of Tables

List of Symbols

Latin Letters

A = Pre-exponential factor [s^{-1}]

c_p = Specific heat capacity [$J \cdot kg^{-1} \cdot K^{-1}$]

ΔH = Specific enthalpy of reaction [$kJ \cdot kg^{-1}$]

Δx = Spatial step size [m]

Δt = Timestep size [s]

E = Activation energy [$kJ \cdot mol^{-1}$]

h = heat transfer coefficient [$W \cdot m^{-2} \cdot K^{-1}$]

k = Thermal conductivity [$W \cdot m^{-1} \cdot K^{-1}$]

L = Bed depth [m]

m = Mass [kg]

$\dot{m}$ = Mass rate per volume [kg·m^{-3}·s^{-1}]

M = Molar mass [kg·mol^{-1}]

N = Number of grid nodes [–]

P = Pressure [Pa]

Q = Volumetric heat source term [J·m^{-3}·s^{-1}]

R = Universal gas constant (8.314) [J·mol^{-1}·K^{-1}]

S = Source term for mass [kg·m^{-3}·s^{-1}]

t = Time [s]

T = Temperature [K]

u = Superficial gas velocity [m·s^{-1}]

V= Volume [m^3]

Y = Yield coefficient [–]

k = Kinetic rate constant [s^{-1}]

C = concentration [mol m^{-3}]

y = Molar fraction [-]

K = Permeability [m^2]

F = Flux [W· m^{-2}]

q = boundary heat flux [W· m^{-2}]

Pe = Péclet number [-]

Re = Reynolds number [-]

D = Mass diffusion coefficient [m^2 · s^{-1}]

d = Mean diameter of particle [μm]

r = Reaction rate [kg · m^{-3} · s^{-1}]

$D_{[3,2]}$ = Sauter mean diameter [μm]

$\hat{m}$ = mass fraction [-]

k_{bed} = Empirical bed depth constant [mg^{-1}]

n = Reaction order [-]

S^2 = standard deviation [mg · min^{-1}]

SE = Standard error [%]

Greek Letters

ε = Porosity [–]

ρ = Density [kg·m^{-3}]

σ = Stefan–Boltzmann constant (5.67×10^{-8}) [$W\cdot m^{-2}\cdot K^{-4}$]

$\in$ = Surface emissivity [-]

μ = Dynamic viscosity [Pa. s]

δ = Extent of pyrolysis [-]

β = Heating rate ($K\cdot min^{-1}$]

α = Thermal diffusivity [$m^2\cdot s^{-1}$]

Subscripts

$_1$ = Primary pyrolysis products

$_2$ = Secondary pyrolysis products

$cond$ = Condensation

vap = Vaporisation

$perm$ = Permeability

$control$ = Control Volume

i = Wood pseudo-component (H = hemicellulose, C = cellulose, L = lignin)

$char$ = Char fraction

gas = Gas fraction

tar = Tar fraction (condensable vapours + liquid)

$tar, pore$ = Tar vapour in pores

$tar, liquid$ = Liquid tar condensed in solid matrix

sec = Secondary product (from tar cracking)

env = Environment/headspace

$plate$ = Hot plate boundary

Superscript

$n, n+1$ = Current and next timestep

$*$ = Iterative estimate during outer iteration

CHAPTER 1

Thesis Outline

Food smoking is an ancient culinary technique that has been used for millennia to preserve food and impart unique flavours. The process involves exposing food to smoke produced from the controlled burning or smoldering of wood. While smoking was originally developed as a preservation method, in modern times it is primarily valued for the complex and appealing flavours it creates in foods like meat, fish and cheese. Despite its long history and continued popularity, many aspects of the smoke generation process and its effects on food remain poorly understood from a scientific perspective.

This thesis aims to provide a comprehensive theoretical and experimental investigation into the mechanisms of smoke formation during culinary wood smoking. The overarching goal is to develop a deeper understanding of the chemical and physical processes involved in smoke generation to optimize smoking techniques for flavour development while minimizing the formation of potentially harmful compounds such as polycyclic aromatic hydrocarbons (PAHs). This work is motivated by several key factors:

1. The need to reduce levels of polycyclic aromatic hydrocarbons (PAHs) in smoked foods. PAHs are carcinogenic compounds that can form during wood pyrolysis and smoking. Regulatory bodies like the European Union have recently lowered allowable PAH limits in smoked foods (European Union, 2003), creating pressure on producers to better control PAH formation, especially for producers in NZ which relies heavily on the export of food products.
2. Growing consumer demand for "clean label" smoked products with authentic flavours but minimal use of artificial smoke flavourings'. This has renewed interest in optimizing traditional smoking methods.

3. A lack of fundamental scientific understanding of smoke formation mechanisms and how they relate to flavour development and PAH production. Most existing smoke techniques have been developed empirically rather than through systematic study.
4. The potential to leverage new analytical techniques and modelling approaches to gain insight into the complex physiochemical processes involved in smoke generation.

Previous research has made important contributions to our understanding of wood pyrolysis and smoke formation, but significant knowledge gaps remain. Early studies in the mid-20th century provided foundational insight into the basic chemical composition of wood smoke and the major compounds responsible for smoke flavour (Fiddler *et al.*, 1966; Montazeri *et al.*, 2013; Vazquez, Tello and Peterson, 2025; Wasserman, 1966). Researchers identified key flavour compound groups such as phenols, carbonyls, and organic acids produced during wood pyrolysis (Montazeri *et al.*, 2013). The 1960-1980s saw more detailed investigations into wood pyrolysis mechanisms, reaction kinetics, and the effects of process parameters like temperature and heating rate (Shafizadeh, F., 1982). Studies during this period elucidated the basic stages of wood decomposition – initial moisture evaporation followed by hemicellulose, cellulose and lignin breakdown.

In recent decades, advances in analytical instrumentation have enabled increasingly detailed characterisation of smoke composition and the identification of trace compounds contributing to flavour. Gas chromatography-mass spectrometry (GC-MS) and related techniques have been particularly valuable for separating and identifying the hundreds of volatile and semi-volatile organic compounds present in wood smoke. Studies have mapped how smoke composition varies with wood species, smoking conditions, and other factors.

There has also been growing research interest in understanding and mitigating PAH formation during smoking. Studies have examined how PAH levels correlate with factors like wood type, temperature, oxygen availability and smoking method (Das *et al.*, 2023). This has led to

recommendations for reducing PAH content, such as using hardwoods, controlling temperature and modifying smoker designs.

Modelling efforts have also advanced, with researchers developing increasingly sophisticated mathematical models of wood pyrolysis and smoke generation. These range from simplified global kinetics models (Solanki, Baruah & Tiwari, 2022) to complex multiphysics simulations incorporating heat transfer, mass transfer and chemical reactions. Such models have provided valuable insights into the interactions between different physical and chemical processes during smoking.

Despite these important advances, several key knowledge gaps remain that this thesis aims to address:

1. Limited understanding of the relationships between wood decomposition kinetics, volatile compound evolution and flavour development. While the basic stages of wood pyrolysis are known, there is a need for more detailed mapping of how specific flavour and aroma compounds form as a function of temperature, time, wood species and extent of wood decomposition.
2. Insufficient data on the chemical kinetics and thermodynamics of smoke formation reactions under conditions relevant to food smoking. Most existing kinetic studies focus on high temperature, fast pyrolysis rather than lower temperature, slow processes typical in food smoking.
3. Lack of comprehensive models linking fundamental pyrolysis chemistry and physics to practical smoking outcomes like flavour profiles and PAH levels. Existing models often focus narrowly on either wood decomposition or smoke composition without bridging the two.
4. Limited investigation of the effects of wood particle size, bed depth and other physical parameters on smoke generation in real smoking systems.

5. Need for better understanding of how to optimize traditional smoking methods to maximise desirable flavours while minimizing harmful compounds. This requires linking fundamental smoke formation mechanisms to sensory and food safety outcomes.

To address these gaps, this thesis takes the approach of combining experimental analysis, kinetic modelling and investigation of practical smoking parameters. The key objectives are:

1. To comprehensively characterize the thermal decomposition behaviour, reaction kinetics and evolved gas composition during pyrolysis of kānuka wood, a species commonly used for smoking in New Zealand. This will provide foundational data on smoke precursor formation.
2. To develop improved kinetic models for wood pyrolysis and volatile evolution under conditions relevant to food smoking. These will link wood decomposition to the formation of specific flavour/aroma compounds and PAHs.
3. To investigate the effects of key physical parameters like wood particle size, bed depth and heating rate on smoke generation processes and composition. This will bridge between the fundamental pyrolysis behaviour and practical smoking performance.
4. To elucidate the thermodynamics of smoke formation reactions, particularly the interplay between endothermic primary pyrolysis and exothermic secondary reactions. This is critical for understanding and controlling temperature evolution during smoking.
5. To develop integrated model for smoke generation incorporating reaction kinetics, heat transfer and physical effects for a model hot plate smoking system. This will provide a framework for optimizing smoking conditions.

The experimental work utilizes a combination of thermogravimetric analysis (TGA), differential scanning calorimetry (DSC), and evolved gas analysis techniques like pyrolysis-gas chromatography-mass spectrometry (Py-GC/MS). These allow precise measurement of mass loss, heat flow and volatile evolution during controlled pyrolysis experiments.

For kinetic modelling, model-fitting methods are employed to extract kinetic parameters from thermal analysis data. Multiple heating rate experiments enable more robust kinetic analysis. The kinetic models are then integrated with the heat transfer to simulate smoke generation in a wood particle.

The thesis is structured as follows:

Chapter 2 provides a comprehensive literature review covering the history and cultural significance of food smoking, wood composition and pyrolysis chemistry, smoke composition and flavour chemistry, polycyclic aromatic hydrocarbon formation, and modelling approaches for wood pyrolysis and smoke generation.

Chapter 3 focuses on the kinetic analysis and modeling of the pyrolysis process. It compares different kinetic modelling approaches and develops improved multi component kinetic schemes for describing kānuka wood decomposition and volatile formation. The chapter also examines the effects of particle size and heating rate on apparent kinetics.

Chapter 4 presents a detailed characterisation of the thermal decomposition behaviour and evolved gas composition during pyrolysis of kānuka wood. This includes analysis of mass loss behaviour, identification of key volatile compounds and mapping of compound evolution as a function of temperature and conversion extent.

Chapter 5 investigates the thermodynamics of smoke formation reactions, particularly the contribution of endothermic primary pyrolysis and exothermic secondary reactions. It examines how overall thermal behaviour changes with extent of conversion and physical parameters like sample mass (which correlates to bed depth) and particle size.

Chapter 6 develops an integrated model of smoke generation in a hot plate smoking system, incorporating reaction kinetics and heat transfer and key physical effects. The model is used to examine how different parameters influence temperature evolution and volatile release.

Chapter 7 discusses the results of the model, focusing on the effects of tortuous path length on the tar forming reactions and its effect on smoke yield and composition.

Chapter 8 provides overall conclusions and recommendations for optimizing smoking processes based on the fundamental insights gained. It also suggests direction for future research to further advance understanding of smoke formation mechanisms.

By systemically investigating the physiochemical processes involved in culinary smoke generation from a fundamental wood decomposition chemistry to practical smoking parameters, this thesis aims to provide a more complete and quantitative understanding of smoke formation mechanisms. The insights gained will help inform the development of improved smoking techniques that maximise desirable flavour compounds while minimising potentially harmful compounds like PAHs. More broadly, the work demonstrates the value of applying rigorous scientific analysis and modelling approaches to traditional food processing methods. The fundamental knowledge generated may also find applications in related fields like biomass pyrolysis for biofuel production.

CHAPTER 2

Literature Review

Culinary smoking is a traditional food preservation and flavouring method that has evolved significantly over time, from early smoldering practices to modern smoke generation technologies. This literature review explores the processes, technologies and wood types used in food smoking, emphasising both traditional and modern approaches. It details the primary smoking methods: cold smoking, hot smoking and liquid smoke application as well as the significance of pellicle development in improving smoke adhesion to meat surfaces.

The review also examines smoke generation technologies including smoldering, friction and steam smoker, highlighting how these methods impact the composition of smoke and the formation of undesirable compounds such as polycyclic aromatic hydrocarbons (PAHs). The type of wood used, such as hardwoods like oak and fruit woods like apple, plays a critical role in determining the flavour profile and safety of smoked foods. The chemical composition of wood and the complex mixture of compounds in smoke-carbonyls, phenolics, acids and others – are thoroughly analysed to understand their impact on both flavour and toxicity.

The thermochemical decomposition of wood, focusing on components like cellulose, hemicellulose and lignin and their decomposition pathways as discussed, illustrating how various pyrolysis conditions influence smoke characteristics. A key theme thoroughout is the balance between generating desirable smoky flavours and minimizing health risks associated with toxic compounds. The review also addresses the mathematical models used to simulate pyrolysis and drying processes, emphasising their role in optimising smoke production for consistent results.

Finally, analytical techniques such as Py-GC/MS, HPLC and NMR are covered for their contribution to understanding smoke composition and wood thermochemical decomposition. This review aims to provide a comprehensive understanding of the factors influencing smoke

production, quality and safety in culinary applications, guiding the development of better smoke generation and application practices in food industries.

2.1 Introduction

Culinary smoking is an ancient technique used by many cultures to flavour and preserve food, most commonly fish and meat (Lingbeck *et al.*, 2014; Ledesma, Rendueles and Díaz, 2016b). European countries traditionally smoked food using alder wood, but recently oak and beech are becoming more popular. In North America, a larger variety of woods are used, including hickory, mesquite and maple, along with some fruit tree woods such as cherry and apple(Stumpe-Viksna *et al.*, 2008). Although other biomaterials such as herbs and spices can be used, they are less common.

Smoke, which can be generated in several different ways, where the most archaic of these is smoldering and combustion, and by more modern techniques such as hot plate and friction, can be infused in several ways. Early smoking practices were probably discovered in antiquity by early humans who left meat hanging by a fire to dry it and to keep it away from predators, and who then discovered that it tasted different and lasted longer. However, in the modern world, and after the Torry Kiln was invented at the Torry Research Station in Scotland in 1939 (Figure 2-1) (Burgess *et al.*, 1965), food smoking has become more sophisticated, and well controlled.

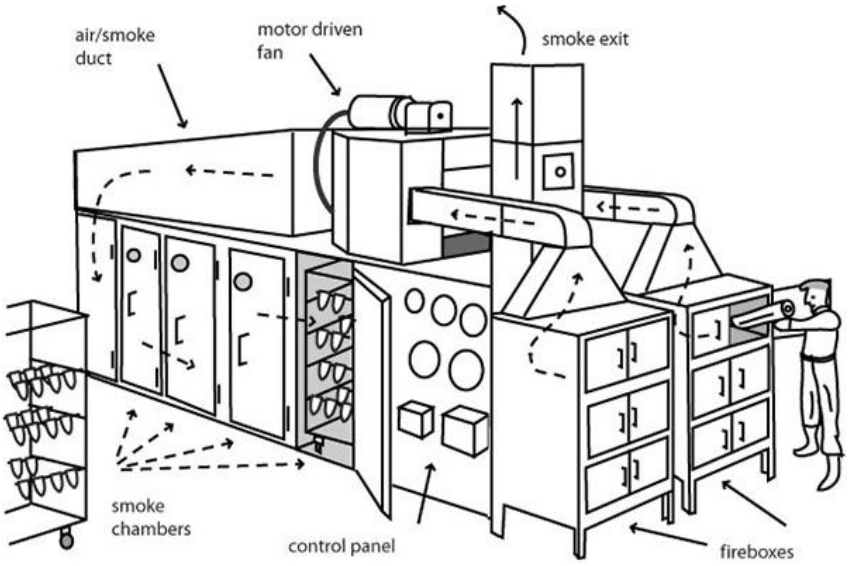

Figure 2-1: Illustration of the Torry Kiln Design (Burgess *et al.*, 1965).

In industrial settings, modern smoking machines are usually large stainless-steel containers (based off the original Torry Kiln) that are temperature and humidity controlled, where food hangs or sits on perforated trays, while smoke is pumped in from an external smoke generator. Although the smokehouses are well designed, there is less sophistication and control when it comes to the way the smoke is generated.

Smoke is a complex mixture of compounds and while applying smoke to food is a method of adding natural flavour and preservatives to the food (Ledesma, Rendueles and Díaz, 2016a), the process of smoke generation does have some drawbacks. Mainly, this is because the process of smoke generation is not well controlled, that is, the conditions of generation are not uniform and therefore smoke is produced across a wide range of temperatures in environments that range from 0-20% oxygen. The consequence is that some undesirable smoke compounds are produced, namely the polycyclic aromatic hydrocarbons (PAHs), which are known carcinogens (Stołyhwo and Sikorski, 2005; Varlet *et al.*, 2007; Pöhlmann *et al.*, 2013; Kpoclou *et al.*, 2014; Abdel-Shafy and Mansour, 2015).

There are three main ways of smoking; cold smoking, hot smoking and liquid smoking(Ledesma, Rendueles and Díaz, 2016a). This section will cover these three methods in more detail. Apart from liquid smoking, there are usually pre-smoking practices that must be completed to get a desirable finished product. The main practice is the development of a pellicle on the surface of meats (The Culinary Institute of America (CIA) 2011). A pellicle is a skin of proteins on the surface of the meat. The proteins help by chemically binding smoke compounds, and thus more smoke is adsorbed onto the surface of the meat. It is developed by letting meat hang or sit in a dry environment, usually a refrigerator. The pellicle development step also dries the meat surface, thus making the surface wrinkled which increases the surface area, further increasing the amount of smoke that can be absorbed.

Cold smoking is usually an indirect method, where the smoke generator (where smoke is produced) and smokehouse (where food is contacted with the smoke), are separated, usually by a large pipe that allows the smoke to naturally cool to 20-30°C, before entering the 'smokehouse', which is also maintained at 20-30°C. Due to the low temperature, the meat is not actually cooked during this process and thus has to be either cooked after smoking or as is more common, heavily cured in a brine solution before smoking. Cold smoking can take between 24 hours or even several days a week.

Hot smoking is much faster than cold smoking, with smoking being no longer than 24 hours. This makes it an inherently safer option, both operationally and regarding food safety. Smoking above the recommended temperature of 80°C will have adverse side effects, as the physical structure of the food will deteriorate. It will also lose more moisture at higher temperatures and thus dries out the food, along with rendering out the fat, which reduces the overall yield of the finished product.

After the pellicle development step, food is usually hung in a 'smokehouse' that is kept at 60-80°C, to simultaneously cook the meat or food item and flavour it with the smoke compounds. This is hot smoking.

Liquid smoke, also referred to in literature as 'smoke flavourings', are products that are produced by condensing the smoke vapours that are produced during pyrolysis, smoldering or combustion of wood. The condensation step is then usually followed by a filtration and a fractionation step that separates the heavy tars which contain the undesirable (PAH) compounds and concentrates the lighter compounds that have the desired olfactory properties. Additional purification and concentration steps can also follow to make the liquid smoke with all the desirable properties. Commercial liquid smoke is mostly water (70%), and organic aromatic compounds making up the rest (30%), with <1% tarry compounds. These products are applied by mixing with water and then spraying, vaporizing or dripping directly on food products.

The main positive aspect of using liquid smoke is that it's cheaper by avoiding the smoking step during processing. Some drawbacks of liquid smoke are that it doesn't impart the same physical characteristics of traditional smoking, which give smoked food their recognizable and possibly desirable texture. From the point of view of the consumer, this technique is viewed as 'unauthentic' and thus is harder to market.

2.1.1 Smoke Generation Technology

While generation of smoke has evolved over time. The objective has always been to produce the most desirable volatile organic compounds via the pyrolysis and/or combustion of wood. Although smoke generators and smoke houses are still primitive in their operation, commercial kits have become quite sophisticated. Recently there has been pressure on commercial smoked food producers to manufacture more consistent products with lower levels of carcinogenic compounds, especially Polycyclic Aromatic Hydrocarbons (PAHs) and to operate them in an environmentally conscious manner by reducing the emissions. The most common methods of smoke generation will be discussed in the following subsections.

2.1.1.1 Smouldering

Smouldering is the most ancient and common method of generating smoke. According to Varlet *et al.* (2007), 65% of all smoked fish in 2002 were smoked by smouldering. Wood in the form of sawdust or wood chips of varying sizes is used. The wood is usually placed in a compartment or fed from a hopper into a heated zone. Heating can occur by various methods, including superheated steam or air injection, a heating coil, a gas burner, a hot plate or by burning of methylated spirits, in a pan that sits underneath the bed of wood, or heating may be simply self-sustaining smouldering combustion. Sometimes the bed of wood is agitated to improve the heat transfer, and enough air (oxygen) is supplied to sustain the reaction. In continuous operations, the wood is often placed on a heated grate, so that once it has charred, it can fall through into a tray of water while fresh wood is continuously supplied from a hopper above. The very simplest method

used by many artisanal smoked food producers, such as butchers and restaurant chefs, is to place wood chips directly onto either a small, prepared fire, hot burning coals, or into a hot pan. The heat source provides the necessary heat to begin the decomposition. Air will be present to some extent in all of these, and so smouldering combustion will occur at the surface of the particle exposed to the air, where temperatures can reach 800°C as discovered by Toth *et al* (1982). If smouldering combustion is the only heat source, it can take some time because the wood chip limits the amount of air able to ingress into the pile. Other heat sources, hot coals or a heated pan, will progress the smoke generation more quickly. However, they all have essentially no control over the quality or quantity of smoke that is produced.

2.1.1.2 Friction

Friction smoking has been developed more recently, in the last 30 years. The technique pushes a log of wood onto a rotating wheel creating friction. This causes the wood temperature to increase high enough for pyrolysis reactions to occur, producing smoke. It is significantly less common than smoldering and hot plate smokers, with less than 5% of all smoked fish being smoked using this technique in 2002 (Varlet *et al.*, 2007).

Temperature control during continuous operation is achieved by contacting the wood with the friction wheel for a small duration, usually 10 seconds, and then removing it for several seconds or minutes. According to a study that evaluated the PAH content of Frankfurter type sausages using different smoke generation methods, friction smoking produced the lowest concentration of PAHs on the sausages with a BaP equivalent of 0.03 ± 0.01 μg/kg (Pöhlmann *et al.*, 2013). The study also found that friction smoking produced the lowest levels of CO in ppm, and thus this method is the most environmentally friendly method with respect to greenhouse gas emissions.

2.1.1.3 Wet Smoker (Steam smoker)

The steam smoke generation method is an endothermic method that produces smoke by passing super-heated steam through a bed of wood sawdust or chips. The smoke produced using this

method is considered moist because of the condensed water from the steam. The steam also flushes out any oxygen that may be present in the smoking chamber, thus making this a flameless method. Pyrolysis temperatures usually reach 400°C with this method(Fessman, 1973; Rusz and Kopslova, 1974; Fessman and Fessman, 1979; Schuldt, 1979; Zwaig and Schossig, 1979).

2.1.2 Types of Smokers

A well-designed smoker should be able to produce a smoke with the desirable flavour and colour components and without carcinogenic compounds, attached to a smokehouse where the flow of smoke is even, and the temperature and humidity are well controlled so that the smoked products are made consistently. To achieve such a delivery, every component of the system should be perfected, from the feedstock (wood) to the smoke generator, to the smokehouse and all the connecting pipework in between. Separating the smoke generator from the smokehouse is also advantageous as it allows for independent control of the components such as the environment and temperature inside the generator and the smokehouse. It also allows for post processing of the smoke such as filtering or electrostatic precipitation of harmful PAHs as they make their way from the generator to the smokehouse.

2.1.3 Consumer grade smokers available in NZ

The most basic and cheapest of the available smokers is the box smoker. Many manufacturers make various configurations of this product (Figure 2-2), however they all function the same. It is essentially a cast iron or stainless-steel container with ventilation. The metal container is filled with smoking wood chips and then placed inside of a gas or charcoal barbeque, where the heat and flame of the barbeque is used to decompose the wood and release the smoky compounds. They cost anywhere from $13 (NZD) for the SAMBA (Warehouse, 2018) stainless steel box to $55 (NZD) (TURFREY, 2018) for the weber Q smoker.

Figure 2-2: Box smokers commonly sold at retail stores in NZ.

The next step up from the above smokers are stand alone smokers. These do not require the heat of a barbeque to function. The simplest of these is a portable fish smoker that uses methylated spirits or Isopropyl alcohol as the heating source. Typically a round stainless steel plate is provided, which is filled with clean burning fuel such as isopropyl alcohol and placed under a perforated stainless steel sheet. Above that are wire racks, where the meat (these are marketed as fish smokers), is placed for smoking. A light stainless steel lid is provided to contain the smoke. Ventilation on the bottom is provided via round holes drilled to the ouside walls (Figure 2-3). This smoker works well and can typicall smoke 1-2 fillets of fish at a time, depending on the size in under 20 minutes.

Figure 2-3: Maxistrike Portable Fish Smoker Small (The Warehouse, 2026).

Non-portable smokers are also sold in various sizes and configurations. They are typically in the shape of a barrel (Figure 2-4), black in colour and use combustion of some type of food as the heating source. Although more modern smokers are starting to use electrical heating elements.

Figure 2-4: Common barrel smokers sold in NZ by manufacturers such as Charmate and Gasmate amongst various others

Control of heat and thus smoke generation using these smokers is not easy. They all use charcoal as the heating source making it difficult to reduce heat without removing combusting charcoal, which is not only dangerous, but the process would require opening the combustion chamber and thus introducing oxygen, which could lead to excess combustion.

2.1.4 Species of Wood

When it comes to choosing the right wood to use for smoking, often it's based on the geographical location where the smoking is taking place. In New Zealand, mānuka wood is popular because it is a native wood that is abundantly available. However, the so-called mānuka smoking wood available in stores is kānuka, which is a distinctly different species although was only recognized as different in 1983. Other popular woods are Pohutukawa and Tawa. Around the world, hardwood species are used most as they are considered to impart a superior smoke aroma and flavour. Some hardwoods that are used are oak, chestnut, hickory, mesquite and beech. Fruit trees are used for their distinct aromatics, most commonly cherry and apple, although it is recommended that only

organically grown wood should be used, as chemical pesticides that are commonly used to increase crop yields can end up in the smoke. Softwoods such as pine or fir have been shown to contain undesirable resins that produce acrid aroma and flavour components such as terpenes. Aromatic herbs and spices have also been used to add flavour and aroma.

2.1.5 Wood Composition

Wood that is harvested and used commercially, such as that for smoke generation falls into two categories, namely hardwoods and softwoods. The terminology does not necessarily relate to the physical hardness of the wood but is related to the mechanism of reproduction of the tree, specifically the seed structure. Softwoods come from gymnosperm trees, with the largest group of these being conifer trees such as pines. Hardwoods come from angiosperms, with most of the species in this category being deciduous. The characteristics which distinguish hardwoods from softwoods are flowers, endosperm within their seed, the production of fruits and the majority have broad leaves rather than needle or scale like leaves(Goldstein, 1977).

To understand the composition of wood smoke and its interaction with food, the composition of the wood itself must first be understood. Wood can be thought of as a porous material that is comprised of three main components; i), cellulose; ii), hemicellulose; and iii), lignin, with all the other organic molecules grouped together and commonly referred to as extractives in addition to the inorganic minerals.

There are three main sections of a stem or trunk of a tree: heartwood, sapwood and bark. The inner part, the heartwood, is mostly composed of dead cells and makes up much of the stem in most tree species. Sapwood is the outer part of the stem and is the layer between the heartwood and bark near the outside part of the stem. This is the living part of the tree, and as the tree grows, new layers of sapwood are added, known as rings. Older sapwood cells die and become part of the heartwood section of the tree. The composition of bark differs considerably from the heart and sapwood.

The primary constituent of most wood species is cellulose, which makes up between 40-50% of the total mass of the cell wall (Zugenmaier, 2008). It is a linear polymer of a hydro-D-glucopyranose units linked by β-(1→4) glyosidic bonds (Figure 2-5). The number of glucose units that make up a cellulose molecule is between 300 to 15,000. The molecular weight of cellulose ranges from 50,000 to 2.5 million, depending on species. Degrees of polymerisation (DP) is usually assigned for cellulose of various species.

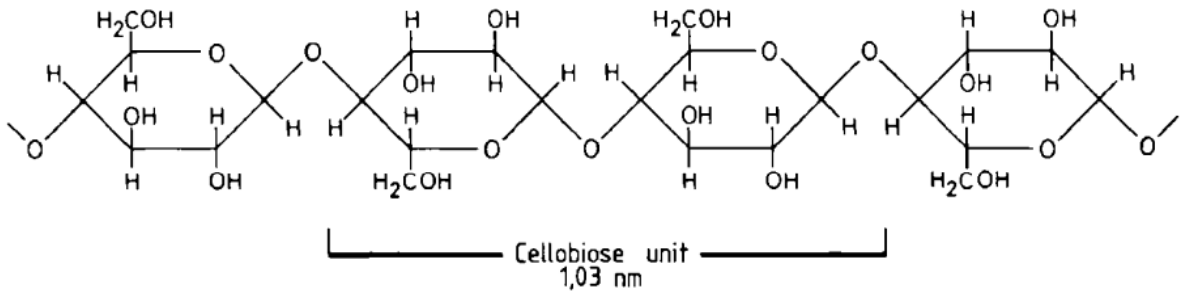

Figure 2-5: Structural formula of cellulose.

DP is the ratio of the molecular weight of the cellulose to the molecular weight of the individual unit of glucose. Plant cellulose usually ranges between 7,000 and 15,000 DP (Pettersen, 1984; Fengel and Wegener, 1989) is known to decrease with the age of the cell as the cellulose structure naturally oxidises in the environment. Within the stem of an individual tree, the heartwood has the lowest DP as this is the oldest part of the tree, and most of the cells have died by the time the tree has been harvested. The sapwood has the highest DP.

Cellulose is very linear and has the desire to form hydrogen bonds within the cellobiose units and with other cellulose molecules. When multiple cellulose molecules form such as occurs in wood, they have the tendency to form very crystalline structures. This combination of crystallinity and strong hydrogen bonds makes cellulose highly recalcitrant to mild solvent extractions, requiring severe, highly alkaline chemical treatment (such as Kraft pulping) to isolate it from the wood matrix.

Apart from cellulose, wood also contains other non-cellulosic polysaccharides and similar molecules, which are collectively referred to as hemicellulose. They have a similar function to cellulose and are supporting material for the cell wall. Hemicellulose (Figure 2-6) includes a mixture of polysaccharides that are composed of the following sugars: glucose, mannose, galactose, xylose, arabinose, rhamnose, fucose, 4-O-methyl-D-glucuronic acid and galacturonic acid residues (Pettersen, 1984; Fengel and Wegener, 1989).

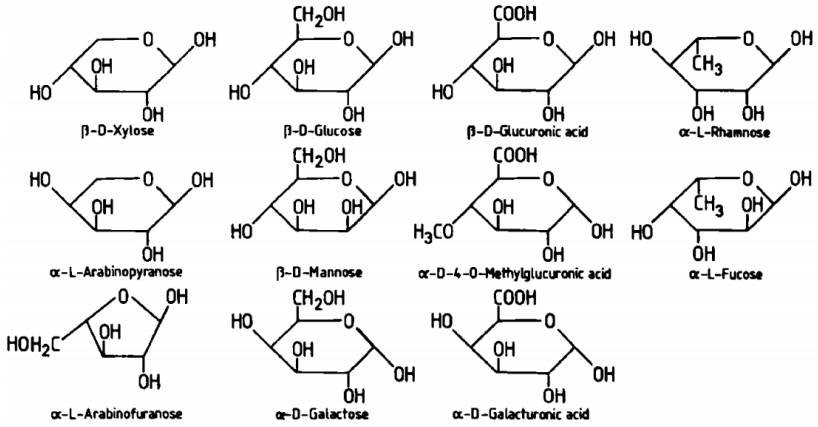

Figure 2-6: Formulas of sugars that make up the polysaccharides known as hemicellulose

In the plant world, lignin is only second to cellulose in abundance and importance, however in wood, they are typically the third most abundant constituent. They range from 20-40% of the total mass of wood cell (Fengel and Wegener, 1989). They are complex 3D polymers composed of phenyl propane units (Figure 2-7). As with cellulose, lignins are also very insoluble in solvents, and thus difficult to isolate chemically. Lignins are usually released in the pulping process as a by-product, where they are then used for their calorific value to produce heat for energy production. The lignins are usually deformed and thus chemically and structurally different to the wood lignin they were extracted from originally, and thus are usually referred to by the name of the process of extractions, e.g. "Kraft lignin", "Klason lignin" etc. The elemental composition of lignin is approximately 64% carbon with 6% hydrogen and 29% oxygen with <1% making up everything else (Murugan *et al.*, 2008).

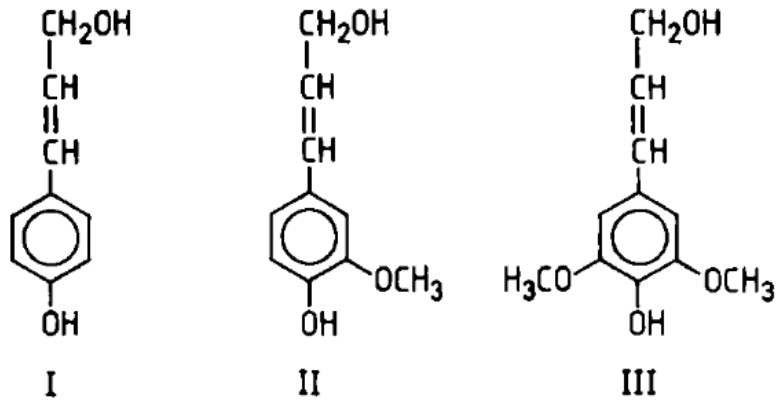

Figure 2-7: The building blocks of Lignin. p-coumaryl alcohol (I), coniferyl alcohol (II) and sinapyl alcohol (III).

Wood contains a class of other organic constituents that include aliphatic, aromatic and alicyclic compounds, hydrocarbons, ketones, alcohols, acids, esters, phenols, resins and terpenes, amongst many more and are collectively referred to as extractives. These can easily be extracted using a water or organic solvent wash, hence the name(Kasparbauer, 2009).

Inorganic constituents or ash also make up part of the wood cells. Wood mostly contains alkali metals, usually in the form of salts. The main constituents of the ash are calcium, potassium, phosphorus and magnesium. Wood can contain up to 2% ash, but rarely exceeds 1% (Kofman, 2016), while wood bark has the highest ash content and can exceed 5% of the total mass.

2.1.6 Thermochemical decomposition of Wood

The thermochemical decomposition mechanisms that are relevant to the smoking process can be divided into three distinct categories:

- Drying
- Pyrolysis
- Combustion

Wood drying is typically carried out at temperatures of about 82°C and up to 132°C(Oltean, Teischinger and Hansmann, 2007). Even at these relatively low temperatures, considerable change

can occur within the structure of the wood. Firstly, free water is evaporated, then bound water. Water can also be separated from hydroxyl groups of adjacent polysaccharide chains, because of which new hydrogen bonds are formed. Cracks can also form with very rapid drying, especially if drying occurs in a dry environment (Hanhijarvi *et al.*, 2003).

Pyrolysis is the thermochemical decomposition of wood in the absence of oxygen and at elevated temperatures of 200 – 500°C. The process results in the formation of a gaseous phase that contains non-condensable gases, condensable (tars) gases, alongside a solid residue that is referred to as char.

When air is introduced, combustion occurs. This could be partial or complete, depending on the concentration and flow rate of oxygen that encounters the pyrolysis products and whether it is combustion of the volatile products or combustion of the char residue, which are each referred to as flaming and glowing combustion, respectively.

Numerous factors can affect the thermochemical decomposition of wood. The main factors are the highest treatment temperature (HTT), available oxygen in the environment, moisture content of the wood, humidity of the environment, the wood species, the particle size, the bulk density, pressure and heating rate. Many authors have demonstrated that HTT is considered to be the most influential (Chan, Kelbon and Krieger, 1985; Boroson *et al.*, 1989; Fantozzi *et al.*, 2007a; Chen, Zhou and Zhang, 2014).

To understand the process of smoking in more detail, the decomposition reactions that are associated with the individual components (cellulose, hemicellulose and lignin) of wood will be discussed in the following sections.

2.1.7 Thermochemical decomposition of cellulose

Although cellulose is not the first component that will undergo thermochemical decomposition, it is discussed here first as it is the main component in the majority of wood species, especially those

used for smoking (Pettersen, 1984). Two alternative pathways have been identified for the decomposition of cellulose (Shafizadeh, 1984). The first pathway, dominates and occurs at temperatures of less than 300°C. At this temperature, cellulose undergoes bond scission, which reduces the DP. Also occurring are the elimination of water (drying), the formation of free radicals of carbonyl, carboxyl, and hydrogen peroxide groups, production of carbon monoxide, and carbon dioxide and the formation of highly reactive char. The second pathway occurs at temperatures above 300°C. In the absence of oxygen (pyrolysis), further bond scissions, fission and disproportionation reactions occur, which produce a mixture of anhydrous sugars and lower molecular weight volatile products. In the presence of oxygen (combustion and/or smouldering) the reactive char and volatile molecules formed will decompose further.

2.1.8 Thermochemical decomposition of hemi-cellulose

Hemi-cellulose is the least stable of the three components of wood and so is the first component to decompose when wood is subjected to heat stress. When modelling the decomposition of hemicellulose, researchers use xylan (Figure 2-5) as the model compound, which does not consider the heterogeneous nature of that group of polysaccharides. In a study conducted by Werner and colleagues (2014) where a variety of seven different hemicelluloses (xylan, arabinoxylan, arabinogalactan, galactomannan, glucomannan, xyloglucan, β-glucan) were studied, they concluded that all hemicelluloses are not the same and that in fact they decompose at different temperatures, with xylan being the least stable. When the composition of gases was analysed, it was found that xylan decomposition formed more carbon dioxide than other hemicelluloses. Decomposition of the other six hemicelluloses also produced a significant amount of carbon monoxide, methane, methanol, furfural, 5-hydroxy-methylfurfural and anhydrous sugars.

Xylan also differed to other polysaccharides in the way it decomposed, as shown in by the mass loss curve (Figure 2-8) below, where its maximum mass loss occurred at 243°C and 292°C. Other studies have also shown a similar result (Varhegyi *et al.*, 1989; Lv, Wu and Lou, 2010). The mass

loss for the other hemicelluloses occurred between 200 – 250°C. This agrees with other literature that have shown hemicellulose to degrade between 200-315°C (Yang *et al.*, 2007; Lv, Wu and Lou, 2010).

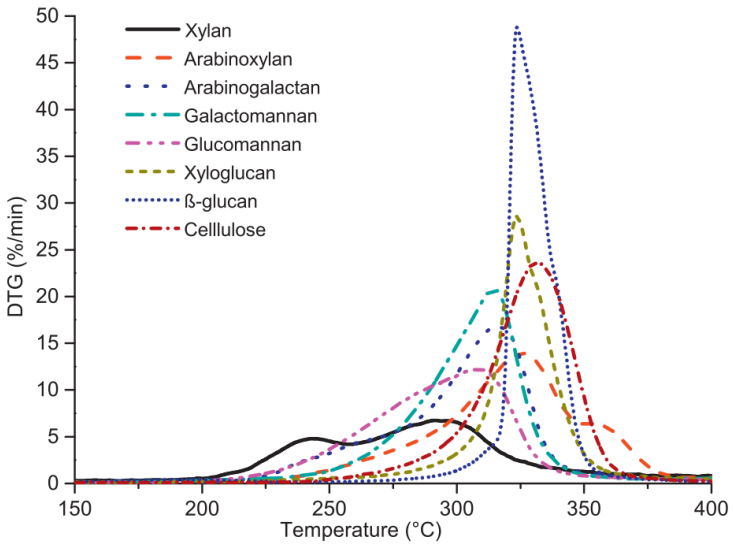

Figure 2-8: Derivative mass loss curve for seven different hemicelluloses and cellulose.

Some authors argue that hemicellulose decomposition is exothermic (Yang *et al.*, 2007), due to the complexity of the nature of hemicelluloses, the exothermicity is dependent on the type of hemicellulose that is present in the wood, and this differs by species. Considering most authors use the molecule xylan as a proxy for hemicellulose, it is easy to see why this conclusion is made. In refuting this, Werner *et al* (2014) tested a variety of different hemicelluloses and found that the majority were in fact endothermic, apart from xylan, which was clearly exothermic. (Figure 2-9).

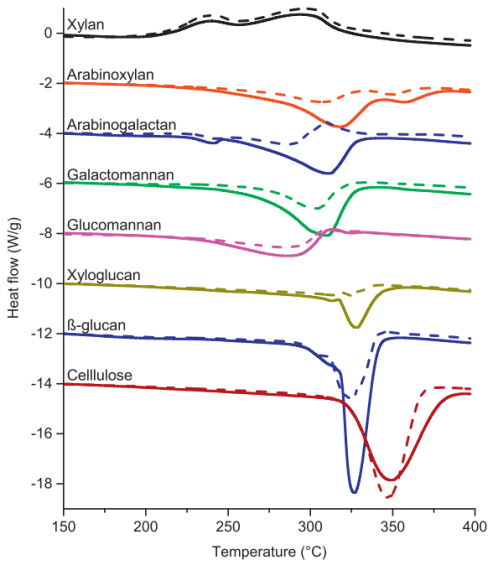

Figure 2-9: Heat flow curve of various hemicelluloses analysed by Werner et al. in open (solid lines) and closed (dashed lines) sample pans. Heat flow is displayed in W/g of initial sample mass.

2.1.9 Thermochemical decomposition of Lignin

Lignin thermochemical decomposition is very important to understand for the purpose of smoke production because it is composed of many aromatic rings with various branches that have a wide range of chemical reactivity, resulting in a wide range of temperature for the thermochemical decomposition, starting at 100°C and continuing up to 900°C (Yang *et al.*, 2007) as shown by Figure 2-10.

Although the thermochemical decomposition occurs across a very wide range of temperatures, it is very slow relative to cellulose and hemicellulose decompositions with less than 0.14 wt. %/°C according to Yang *et al* (2007).

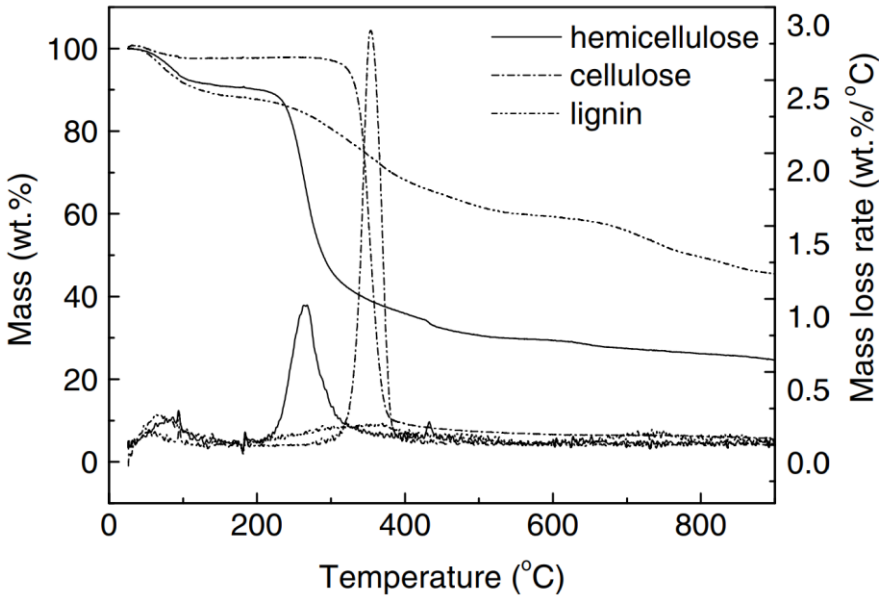

Figure 2-10: Thermochemical decomposition of hemicellulose, cellulose and lignin in an oxygen free environment.

Unlike cellulose and most hemicelluloses decomposition (excluding xylan), the breakdown of lignin is exothermic (Yang *et al.*, 2007a).

2.1.10 Combustion

Combustion is the result of temperature and oxygen acting upon the surface of the char residue and volatile compounds produced during pyrolysis. Both the char residue and volatiles produced are very different, depending on the temperature of pyrolysis and therefore, the reactions of combustion will differ. However, with complete combustion, the final products are the same, namely carbon dioxide and water. Incomplete combustion, also referred to as smouldering (discussed earlier in section 2.1.1.1), results from an insufficient supply of oxygen to oxidize all the carbonaceous compounds.

Lignin pyrolysis produces more (up to 40 wt. %) char residues (Yang *et al.*, 2007), compared to cellulose and hemicellulose (less than 15 wt. %). Therefore, char residue produced from wood of high lignin concentrations will require a higher temperature for glowing combustion(Shafizadeh, 1984). Flaming combustion occurs when wood is converted into volatile gases during pyrolysis,

the gases are then oxidised in the presence of oxygen, producing a flame. Glowing combustion occurs by oxidising the char solid residue that forms during pyrolysis.

2.2 Kinetics of thermal decomposition of wood

Degradation of biomass kinetics is studied either isothermally or non-isothermally. During the isothermal analysis, biomass is placed in a heated chamber which is set at a constant temperature and the sample weight change is recorded as a function of either temperature or time. During non-isothermal analysis, the temperature in the chamber increases with time based on an assigned heating rate. The methods are used to determine Arrhenius kinetic parameters.

Although there have been many experimental studies, there is still no universally accepted model that can predict the pyrolysis rate and provide a priori knowledge about the final decomposition over a wide range of parameters, such as particle size. Most kinetic studies are conducted using TGA because the mass of the sample is the most convenient property in the study of global chemical kinetics (Mamleev, Bourbigot and Yvon, 2007).

Di Blasi C (1993, 2008) suggested various classes of mechanisms for wood pyrolysis. The models are categorized into three distinct classes: (1) one-step global model; (2) one-step multi-reaction models and; (3) two-step semi global model. One step global model considers pyrolysis first proposed by Bramford *et al.* (1946) as a single step first order reaction of the following form:

$$\frac{dC}{dt} = -kC \tag{2.1}$$

where,

k = kinetic constant = $Ae^{\left(\frac{-E}{RT}\right)}$

A = pre-exponential rate constant (s^{-1})

E = Activation energy (kJ mol^{-1})

R = Ideal gas constant = 8.314 (J mol^{-1} K^{-1})

C = concentration of species (mol m^{-3})

The one-step multi reaction model (Class 2) considers those pyrolysis reaction mechanisms which involve simultaneous and competing first order reactions, in which wood decomposes to produce the various primary pyrolysis products, i.e. char, tar and oil (following the mechanism proposed by Shafizadeh and Chin (1977).

$$\text{Wood} \rightarrow (\text{Volatiles} + \text{gas})_1$$

$$\text{Wood} \rightarrow (\text{Char})_1$$

While this reaction mechanism accounts for multiple products of wood pyrolysis, it neglects to include the effects of secondary reactions and the vapour phase residence time. This is accounted for in two-step semi global models (class 3) which are two-step reactions in which the pyrolysis products of the primary reactions further decompose to produce secondary products (also the following mechanism proposed by Shafizadeh and Chin (1977).

$$\left.\begin{array}{l} \text{Wood} \rightarrow (\text{Volatiles} + \text{gas})_1 \\ \text{Wood} \rightarrow (\text{Char})_1 \end{array}\right\} \quad \text{Primary Reactions}$$

$$(\text{Volatiles} + \text{Gases})_1 \rightarrow (\text{Volatiles} + \text{Gases})_2 + (\text{Char})_2 \quad \text{Secondary Reactions}$$

By including the secondary reactions in the kinetic scheme, the product yields become a function of not only temperature but also vapour-phase residence time and heating rate. Secondary tar reactions can occur at sufficiently high temperatures if given enough vapour phase residence time.

They are classified as both homogeneous when occurring in the vapour phase and heterogeneous being catalysed by the char. Cracking, re-polymerization, condensation and partial oxidation are all processes which can occur during secondary reactions (Morf, Hasler and Nussbaumer, 2002).

This scheme may provide accurate results for the modeling of very small, single particles; however, it does not scale, either to larger particles or to multi particle system. In these the size of the particles and the structure of the bed affect the residence time and local concentrations where the volatiles interact with the char as they move along the pressure gradient and escape into the surrounding void volume. Accounting for such effects is extremely difficult. The approach needed is to experimentally determine the kinetic parameters for each system (geometry, particle size, heating rate).

Fantozzi et al. (2007a) used the principles of the class 3 model suggested by Di Blasi (1996) where she divided the models into three classes, to model a rotary kiln pyrolysis reactor. According to Di Blasi, as heat is provided, wood undergoes primary endothermic reactions according to the scheme shown in Figure 2-11 below, resulting in the production of primary gas, tar and char. If the reaction is then allowed to continue to reach higher temperatures and given for enough vapour phase residence time, then the primary tar will decompose further to produce permanent secondary gas and char.

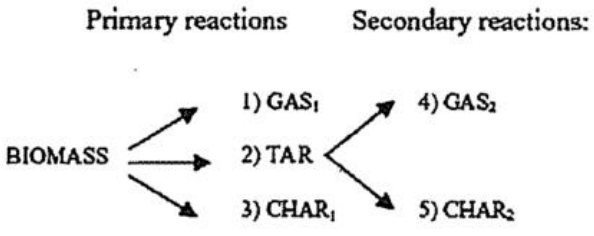

Figure 2-11: Simplified scheme for biomass pyrolysis.

In the work by Fantozzi et al. (2007a), a model was developed using this scheme to simulate the change in product yields with respect to moisture content, rotational speed of the rotary kiln drum

and bed density of the wood chips and the results showed a good fit to the model classes suggested by Di Blasi (1996).

1.11 Drying mathematical Models

Experimentally, it has been shown that when studying heating as a function of time during pyrolysis of large wood particles, a plateau of temperature is observed at about 100°C. The duration of the plateau is proportional to the moisture content. It is termed the drying plateau and is considered to start at about 80°C and end at 120°C. Modeling the drying process is therefore important as it can have a significant impact on temperature prediction, especially in systems containing many particles.

Researchers have developed several ways to numerically model the drying regime of wood when subject to heat, such as during pyrolysis, combustion or even low temperature drying of biomass, <200°C. Chan and Krieger (1983) treated drying as an additional decomposition reaction with an Arrhenius expression. This technique has two advantages; (1), it includes an activation energy, which accounts for both a temperature dependent evaporation rate and the fluctuations in strength of bound water; and (2), it has numerical stability in a mathematical code that handles many Arrhenius expressions. It also has its disadvantages however, mostly due to the experimentally derived nature of the exponents in the Arrhenius expression. To get around this Bruchmu¨ller et al. (2011) treated drying as a boiling process around the temperature of 100°C, by balancing the energy required for water vaporisation and the energy absorbed by the particle from the surroundings. When $T > T_{vaporisation}$ then drying took place, until either $T < T_{vaporisation}$ or the mass of water available was consumed.

2.2.1 Pyrolysis mathematical models

Early pyrolysis models like that developed by Bamford, Crank and Malan (1946) were based on the following assumptions; 1), one-dimensional heat and mass transfer, 2), only conductive heat transfers within the solid particle was accounted for, 3), re-condensation of volatile products (including water) was neglected, 4), char shrinkage was neglected, 5), wood was considered a homogeneous solid, and last wood was considered to be dry with no free-water available.

One of the most comprehensive pyrolysis models was suggested by Shafizadeh and Chin (1977) who focused on the decomposition kinetics when analysing the thermal behavior of cottonwood, concluding that the thermal behavior of wood is the sum of its three main components: cellulose, hemicellulose and lignin. The products of pyrolysis identified were char, tar and gas. They also pyrolysed the components separately to measure their contribution to the final product yields. For example, cellulose was found to be the major contributor towards the volatile products (tar and gas), while lignin contributed more towards the char yield. The products of the individual pyrolysed components also seemed to add-up to the yields from the pyrolysis of wood, suggesting that there is very little to no interaction between the components during pyrolysis. Figure 2-12 shows this proposed kinetic model. Although they did mention that further heating of the volatiles will result in the formation of secondary gas and char, no kinetic model for this reaction pathway was proposed. This model has served as the basis for almost all pyrolysis models and studies since.

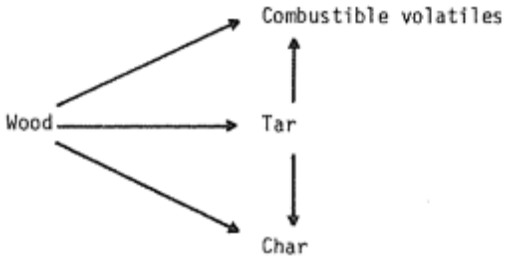

Figure 2-12: Kinetic model proposed by Shafizadeh & Chin.

In the recent past, various pyrolysis models have been presented by a number of authors (Di Blasi, 1996; Grønli, 1996; Bellais, 2007; Park, Atreya and Baum, 2009; Ratte *et al.*, 2009; Lam, Oyedun and Hui, 2012) that have both included the mechanism of Shafizadeh and Chin (1977)and have managed to remove some of the assumptions originally proposed by Bamford, Crank and Malan (1946). All these models consider the diffusion of gaseous products through the particle which is commonly described by Darcy's Law of fluid flow in porous media. Some have also included shrinkage in their models Hagge and Bryden (2002).

2.3 Chemical composition of Smoke

Smoke is a complex mixture of many compounds that contribute to flavour, colour and the preservative properties of foodstuffs. Identification of the individual compounds (Ralph and Hatfield, 1991; Chevance and Farmer, 1999; González-Vila *et al.*, 2001; Pöhlmann *et al.*, 2013; Ledesma, Rendueles and Díaz, 2016a; Kosowska *et al.*, 2018) has proven difficult due to the large number of compounds and their similarities, which makes it hard to isolate them with techniques such as gas chromatography. Researchers have resulted to grouping these compounds into classes. It is also very difficult to establish their organoleptic properties. This is especially hard for wood smoke, as the composition and intensity of the smoke is highly dependent on many factors, including wood species, smoking temperature, oxygen levels, particle size, moisture content and smoker design.

Although smoking was historically a technique used for preservation of meats, today the main objective is to change the organoleptic properties of foodstuffs, most importantly the colour and flavour. Over 1000 compounds have been identified in wood smoke, with almost 40% of them being volatile compounds (VCs) (Chevance and Farmer, 1999; Ahmad, 2003; Kosowska *et al.*, 2018). Most of the VCs are carbonyls, followed by phenolic compounds, acids, furans, esters, alcohols and various other compounds (Woods, 2003). Not all the compounds in wood smoke contribute positively to the organoleptic properties of foodstuffs. Various authors have attempted

to categorise the compounds into two categories: i) Desirables and ii) Undesirables (Ledesma, Rendueles and Díaz, 2016a). The Undesirables include phenol, methyl alcohol, acetone and PAHs. The rest of the compounds (including phenol derivatives) contribute positively or neutrally to the organoleptic properties.

2.4 Smoked Food Toxicology

Some undesirable compounds are produced during the smoking process, which can not only negatively damage the foodstuffs being smoked, but also the consumer. The main toxic compounds that are found in smoked food are discussed in this section.

2.4.1 Polycyclic Aromatic Hydrocarbons (PAHs)

The most widely known toxic compounds that are produced during the smoking process are PAHs. They were first discovered in 1775 by Percivall Pott in London. He noticed that rates of cancer were higher in those who swept the chimneys in St. Bartholomew's Hospital(Brown and Thornton, 1957). Since then, researchers have extensively studied the carcinogenic, mutagenic and bioaccumulative capacities of PAHs. These health risks are strictly monitored and reported by several major international scientific and regulatory authorities. The International Agency for Research on Cancer () evaluates the cancer-causing potential of PAHs, definitively classify benzo[a]pyrene (BaP) as a Group 1 human carcinogen and several others as Group 2B possible carcinogens (Sampaio *et al.*, 2021; Montano *et al.*, 2025). From an environmental and exposure standpoint, the United States Environmental Protection Agency (US EPA) has established a widely recognised list of 16 priority pollutant PAHs based on their severe toxicity, mutagenic properties and environmental persistence (Samburova, Zielinska and Khlystov, 2017; Montano *et al.*, 2025). In the specific context of food safety, the European Food Safety Authority (EFSA) evaluates dietary exposure by utilising a specific group of four PAHs (the PAH4) as primary indicators for assessing genotoxic and carcinogenic risks in food products ((Sampaio *et al.*, 2021). Furthermore, the Joint Food and Agriculture Organisation/World Health Organisation (FAO/WHO) Expert

Committee on Food Additives (JECFA) has formally classified 13 specific PAHs as being both genotoxic and carcinogenic, specifically evaluating the risks posed by food processing methods such as culinary smoking (Sampaio *et al.*, 2021). Table 2-1 below lists the 16 PAHs controlled by the European commission (European Commission, 2003). Their levels are dependent on the food and method of smoking (Stołyhwo and Sikorski, 2005; Essumang, Dodoo and Adjei, 2013). The Food Safety Authority of Australia and New Zealand (FSANZ) maintain a watching brief (FSANZ, 2019).

Table 2-1: Chemical characteristics and structures of the 16 priority polycyclic aromatic hydrocarbons (PAHs) regulated by the European Union.

Compound	Abbreviation	Molecular Weight	Chemical Structure
Benzo(*a*)pyrene	B*a*P	252	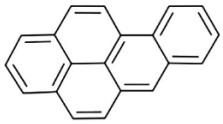
Benz(*a*)anthracene	B*a*A	228	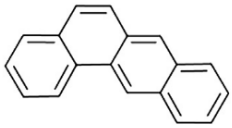
Benzo(*b*)fluoranthene	B*b*F	252	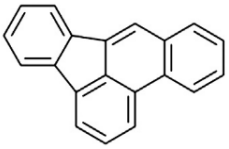
Benzo(*j*)fluoranthene	B*j*F	252	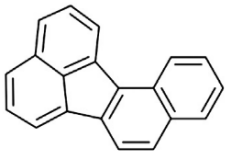
Benzo(*k*)fluoranthene	B*k*F	252	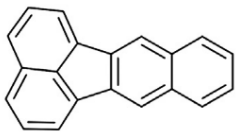
Benzo(*g,h,i*)perylene	B*ghi*P	276	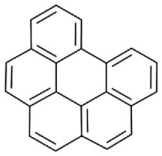

Chrysene	Ch	228	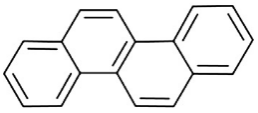
Cyclopenta(*c,d*)pyrene	CPP	226	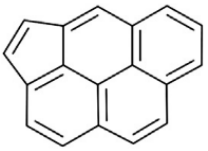
Dibenz(*a,h*)anthracene	DB*ah*A	278	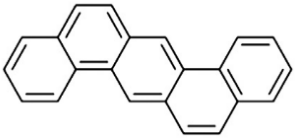
Dibenzo(*a,e*)pyrene	DB*ae*P	302	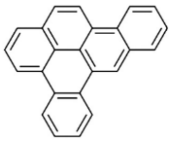
Dibenzo(*a,h*)pyrene	DB*ah*P	302	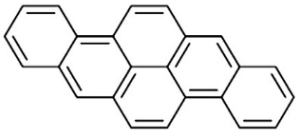
Dibenzo(*a,i*)pyrene	DB*ai*P	302	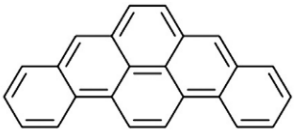
Dibenzo(*a,l*)pyrene	DB*al*P	302	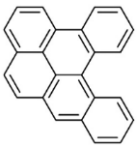
Indeno(*1,2,3,c,d*)pyrene	IP	276	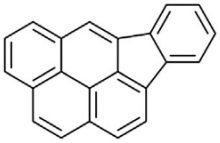
5-Methylchrysene	5MeCh	242	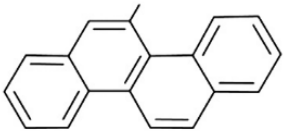
Benzo(*c*)fluorene	B*c*F	216	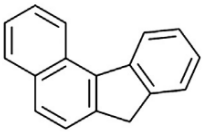

2.5 Analysis techniques for wood thermochemical decomposition

Wood thermochemical decomposition has been studied for many reasons, including to understand the drying times of wood for lumber and fuel, for the pyrolysis and combustion behaviour of wood and for the conversion of wood into biofuels. The techniques used for these studies can be directly applied to the understanding of the thermochemical decomposition of wood to produce smoke for culinary smoking of foodstuffs. In this section, the main techniques will be discussed and how they can be used to further understand the decomposition of wood and the formation of desirable smoke compounds.

2.5.1 Elemental analysis

Elemental analysis is conducted on the raw wood and later the char residue left over from the thermochemical decomposition process (smoking). Carbon, hydrogen, nitrogen and oxygen are usually the elements of interest and are either determined by the more frequently used method of total oxidation (combustion analysis) or by atomic spectroscopy (Oasmaa and Meier, 2005).

2.5.2 Thermo-analytical methods

The thermo-analyser is a simple device that consists of four main components; i), a scale, ii), a furnace, iii), a controller and, iv), a computer (Murugan *et al.*, 2008). Samples of wood are placed in a crucible that is suitable for the temperature in which the wood will be subjected to for the purpose of the particular analysis. Alumina, aluminium or platinum crucibles can be used. An empty reference crucible is also used. Mass loss of the sample is recorded over time as the sample is heated. Heat flow and temperature of the sample relative to the reference crucible are also recorded as functions of time. There are three main thermo-analytical techniques: thermo-gravimetric analysis (TGA), differential thermal analysis (DTA) and differential scanning calorimetry (DSC).

When a TGA analysis is conducted, a sample is heated, usually in a nitrogen or other inert gas environments, and the mass loss is measured with time. Some of the results that can be obtained from a TGA analysis are the evaporation reactions, degradation reactions, oxidation or reduction reactions, sublimation, and any other heat induced changes that can occur in wood. There are two modes of operation, isothermal or dynamic (Reina, Velo and Puigjaner, 1998). The isothermal mode increases the temperature of the sample at a steady rate and measures the heat flow required to achieve this, whereas the dynamic mode supplies a constant heat flux and so measures the change in temperature. Often the dynamic mode is chosen, as this requires less experimental data (Tia, Bhattacharya and Wibulswas, 1991) to determine things such as the reaction rates and heats of activation (Murugan *et al.*, 2008). It is important to remember that when packing a crucible for TGA analysis, it is recommended that it only be loosely packed, with light tapping on the outside of the crucible. Results have shown that forced packing, due to the nature of the different particle sizes and forces used to push down on the wood particles and pack them in a crucible, makes the results unreproducible (Kissinger, 1956). DTA is a simpler technique, only measuring the difference in temperature of the sample and reference as a function of time (Murugan *et al.*, 2008).

DSC does not include mass loss; it measures the difference in the amount of energy required to increase the temperature of the sample and the reference as a function of temperature. It is most commonly used to measure the heat capacities (c_P) of wood and products of pyrolysis such as the char (Grønli, 1996; Radmanović, Đukić and Pervan, 2014).

Although these techniques are vital in understanding the kinetics of the pyrolysis, drying and various other reactions, they do not give any information about the volatile compounds that are formed. For this, other techniques are needed.

2.5.3 Gas Chromatography and Mass Spectroscopy

Gas chromatography (GC) is an excellent technique to separate and identify the many volatile compounds produced in wood smoke. A pyrolysis reactor can be added to a GC (Py-GC) analyser to produce smoke under controlled conditions and the gases (smoke) produced can be subsequently directly separated and analysed with very high resolution (Ralph and Hatfield, 1991; Sjostrom and Alen, 1999; Scholze and Meier, 2001; Shen and Gu, 2009). GC is often combined with mass spectroscopy (MS) to better identify compounds in a mixture. Py-GC/MS is a very attractive technique for its minimal sample preparation but lacks in the ease of applying this technique for quantification of pyrolysis gases. To quantify gases, a standard must be prepared, which eliminates the benefit of the ease of operation and sample preparation (González-Vila *et al.*, 2001).

The pyrolysis gases of wood decomposition are not only large in quantity, but many are very similar in chemical structure, making them difficult to separate and therefore identify. Some researchers have developed multidimensional gas chromatography techniques to better separate and identify the compounds(Bertsch, 1999). In two-dimensional gas chromatography (2D-GC) for example, a secondary column, usually nonpolar is used, where a portion of the gas stream is injected to better separate the mixture.

The Py-GC/MS is considered an important technique because the organoleptic compounds in smoke are expected to be those that are volatile. Massey University has a Py-GC/MS and our collaborations, University of Otago have a GC-O (Olfactory), and both groups have considerable experience using it for pyrolysis studies.

However, pyrolysis smoke contains many compounds that are too large to be identified via GC techniques alone, even with very robust columns and high temperature programs. These are generally described as the tarry compounds and constitute a significant portion of the condensable fraction in wood smoke (Commandre *et al.*, 2018). Thus, other techniques, such as high-

performance liquid chromatography (HPLC) (Gerdes *et al.*, 2002; Mohan, Pittman and Steele, 2006) are often used to identify the larger compounds. These compounds are usually polar or non-volatile. HPLC is usually paired with a spectroscopy technique such as electrospray mass spectroscopy (HPLC/ES-MS), which can identify most of the oligo-metric compounds that cannot be detected using GC/MS (Gerdes *et al.*, 2002). Sample preparation is also difficult with HPLC, as volatiles must be first condensed in a separate pyrolysis reactor thus the compounds are not directly analysed as is the case with Py-GC/MS. Compounds are usually detected using a refractive index detector (RID) when using HPLC, compared to the flame ionization detector (FID) commonly employed by GC analysis. The RID has a wider range of sensitivity and the signal highly depends on the compound structure (Sjostrom and Alen, 1999).

2.5.4 Nuclear Magnetic resonance (NMR) analysis

Nuclear magnetic resonance is likely the best technique for the quantitative analysis of functional groups as well as the analysis of the structural elements such as the aromatic nuclei and side chains of compounds. It's most useful for the quantification of various fatty acids and triglycerides found in the volatile components of smoke. However, there are some drawbacks to using NMR. Firstly, large sample quantities are required to conduct analysis, and that analyses are usually very costly, especially for modern Fourier transform (FT), NMR instruments (Sjostrom and Alen, 1999).

Three methods of NMR can be used for the determination of various functional groups in the biomass or the products of pyrolysis (smoke), these are ^{1}H, ^{13}C and ^{31}P NMR. ^{1}H can be used for the analysis of acetate derivatives, which will determine aliphatic hydroxyl, phenolic hydroxyl groups, and benzyl alcohol groups. ^{13}C NMR can similarly be used to determine total hydroxyl, primary hydroxyl, benzyl alcohol, and phenolic groups. Quantitative ^{31}P NMR is particularly valuable for this application as it utilises phosphorylating reagents to tag specific hydroxyl groups, allowing for the precise quantification of the phenolic compounds responsible for smoke flavour. Considering the scope of this thesis, HPLC and NMR were not used in this work.

CHAPTER 3

Decomposition Kinetics of Kānuka Wood Chips

3.1 Introduction

While this work is focused on the generation of culinary smoke from kānuka wood, the subject of wood pyrolysis is not new. Indeed the kinetics of decomposition reactions of wood and its main components – extractives, hemicellulose, cellulose and lignin – across the temperature range from 85°C to 550°C, at atmospheric pressure and under an inert atmosphere have been analysed by many researchers over many decades(Thurner and Mann, 1981; Di Blasi and Russo, 1994; Reina, Velo and Puigjaner, 1998; Svenson, Pettersson and Davidsson, 2004; Lv, Wu and Lou, 2010; Chen, Zheng and Zhu, 2013; Cui, Zhang and Shang, 2013; Di Blasi and Branca, 2013; Reschmeier *et al.*, 2014). Pyrolysis of wood is a complex process that results in several products grouped into three main types: char, tar and gas. Generally, the interest in this process has been in the char product as a metallurgical reactant, or for agricultural applications, or for the sequestration of CO_2 in the battle to mitigate climate change. However, here the interest is in the tar and gas species, as these are the products that have the potential to end up on food in the smokehouse. It has been found that a variety of factors affect the decomposition of wood, such as: temperature, heating rate, particle size, particle shape, particle density and bed density of wood, moisture content and chemical composition (Fengel and Wegener, 1989; Bridgwater, Meier and Radlein, 1999; Mohan, Pittman and Steele, 2006; Aboulkas and El Harfi, 2008; Shen and Gu, 2009; Di Blasi, Branca and Galgano, 2010; Glass and Zelinka, 2010; Bennadji *et al.*, 2013; Di Blasi *et al.*, 2013; Chen, Zhou and Zhang, 2014; Mate and Babler, 2016). Chemical composition can be treated as effectively controlled in this study: all experiments used a single species, kānuka, sourced from one batch of wood chips and

therefore likely from one or a small number of trees. Some intrinsic heterogeneity is unavoidable, such as differences between heartwood and sapwood, tree age and site conditions. However, these effects are minor relative to the uniformity of the feedstock and are not expected to bias the inferred decomposition kinetics. This kinetic analysis isolates temperature and thermal history rather than composition differences and therefore any departure from the broader literature are interpreted cautiously as potential attributes of kānuka.

In this chapter, the kinetic rates and mechanisms are determined for the decomposition of kānuka particles under regimes that remove or minimize the effect of heat and mass transfer limitations and are purely driven by chemical kinetics. This is achieved by using very small particle sizes (<90 μm to 600 μm in diameter). Here, kinetic models will be compared to experimental results and to literature values. In this chapter, the results of kānuka decomposition experiments using a thermogravimetric analyser (TGA), will be first discussed. Then, the mathematical non-linear regression models will be described and the results will be presented and discussed.

3.2 Experimental Section

3.2.1 Sample preparation

Kānuka wood chips (Figure 3-1 (a)) were acquired from Opōtiki, who supply most culinary smoking facilities in New Zealand. The wood chips arrived in 10 kg bags, and the wood chips in any one bag came from one or a small number of trees. One bag was isolated, and all consequent samples were acquired from this one bag. It was stored at room temperature throughout the duration of this work. For the thermogravimetric analysis, approximately 100 g of wood chips were collected from the bag.

Figure 3-1: (a) Unprocessed kanuka wood chips, (b) kanuka wood chips after being ground and before sieving

These were then dried in a 105°C drying oven overnight to make them easier to grind. After they were dry, they were ground using a stone grinder. To minimise heat generation during the grinding process and prevent altering the decomposition characteristics of the wood chips, the mill grinder was operated in a pulsating manner. The grinder was turned on for 5 seconds, followed by a cooling period where it was turned off for duration ranging from 10 seconds to 5 minutes, allowing the chamber to cool adequately before the next grinding cycle began. At this point, the ground wood chips were of varying sizes from <15 μm to 2-3 mm in diameter (Figure 3-1 (b)). Therefore, they were sieved to meet pre-determined particles sizes of 90 to 600 μm and <90μm. This specific 90 μm cutoff was chosen because it corresponds to a standard analytical sieve size and marks a critical physical threshold for the packed bed. As demonstrated later in this study, below 90 μm, the interstitial bed permeability decreases so significantly that it severely restricts the escape of volatiles, allowing for the direct observation of pore blocking, self-pressurisation and the resulting promotion of secondary char forming reactions. The two batches of desired particle sizes were then dried in a drying oven at 105°C for 24 hours and then placed in a desiccator to keep them from adsorbing moisture from air.

3.2.2 Experimental apparatus

The experimental apparatus used here was the simultaneous thermal analyser NETZSCH STA 449 F1 Jupiter®, supported by a laptop computer running windows® 10 software, with the NETZSCH

Proteus thermal analysis software used to control the apparatus, acquire data and analyse the results. A schematic of the STA 449 F1 Jupiter® is shown below (Figure 3-2).

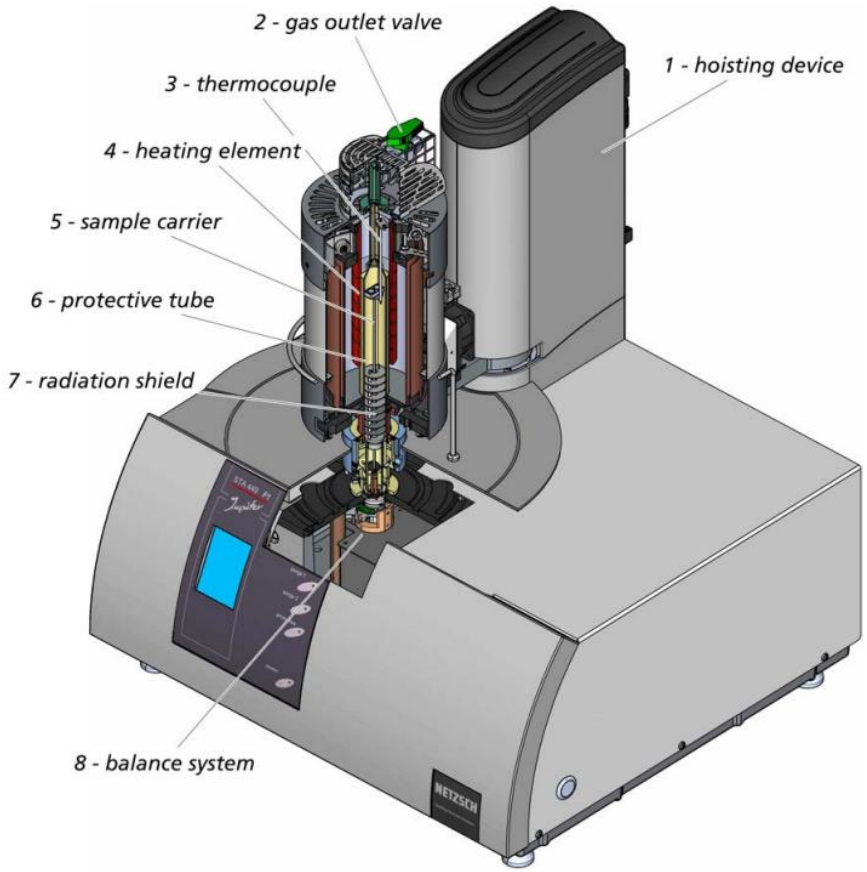

Figure 3-2: Schematic of the STA449 F1

The system is top loading, using a balance design that has been tested and proven over several decades (top loading). This makes it more robust and easier to handle compared to other systems that have, for example, balance arms. Figure 3-3 shows how the sample and reference crucibles sit on the ceramic sample carrier. The reference crucible is used to obtain the DSC (differential scanning calorimetry) signal which will be discussed in subsequent chapters.

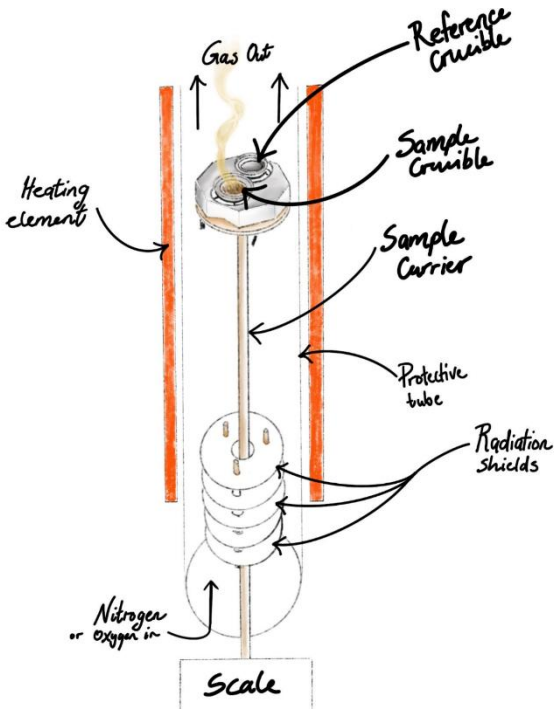

Figure 3-3: Schematic of the sample carrier, showing the placement of sample and reference crucibles.

3.2.3 Experimental Procedure

There are several considerations when conducting thermogravimetric analysis experiments for the kinetic study of a reactant:

1) deciding on an appropriate heating rate for a particular sample mass (mass);
2) the effect of the laboratory environment on the analyser; and
3) understanding that every crucible is slightly different and its geometry will have variable heat and mass transfer effects on the sample its carrying.

To dwell on these considerations here is important in order to understand the reason for the way the experiments were conducted. It is worth noting that these experiments were conducted to acquire the mass loss *vs* time plots (TG), as well as the differential heat plots (differential scanning calorimetry (DSC)). Therefore, although some considerations may not be important specifically for

TG analysis, they are important to consider in the DSC analysis which will be discussed in later chapters.

Selecting sample mass and particle size appropriate to the heating program is critical to minimise heat and mass transfer artefacts. Intrinsic decomposition kinetics are governed by temperature and conversion; the programmed heating rate shapes the temperature history and apparent response but does not make the reaction rate proportional to $\frac{dT}{dt}$. To limit internal thermal gradients, a practical criterion is to restrict the characteristic sample thickness such that

$$L \leq \sqrt{\frac{\alpha_{eff}\Delta T_{allow}}{\beta}} \tag{3.1}$$

where $\alpha_{eff} = \frac{k_{eff}}{\rho c_p}$ is the effective thermal diffusivity of the particle bed, $\beta = \frac{dT}{dt}$ is the heating rate and ΔT_{allow} is an acceptable temperature lag. Very low heating rates and very small masses can lengthen experiments and degrade signal-to-noise, so a balanced design was adopted: forty-five runs spanning particle diameter 90 μm < D_P < 600 μm at β = 1, 2.5, 5, 10 and 20 K/min with sample mass of 3, 6, 12, 18 and 24 mag; for D_p < 90 μm, the same heating rates were used with masses of 5, 10, 15 and 20 mg. The rationale for mass adjustments is detailed in the subsequent chapter on specific enthalpy of reaction.

Aluminium crucibles with a diameter (ø) of 6 mm were chosen for these experiments because they could handle the desired temperature range (T_{max} = 580 °C), and they were relatively inexpensive, so they could be discarded after each run. This removes the recycling step from analysis and thus reduces time and variability.

A typical experimental run consisted of first running an empty crucible under identical conditions (discussed here) to the sample crucible first to establish a baseline which is then later subtracted from the sample run to remove noise from the result. Once the baseline was established, the baseline crucible was first weighed by the system, this new weight was taken as the crucible weight

for the sample run. The sample was then loaded into the crucible and approximated on a scale to ±0.5 mg of the desired mass. It was then evenly distributed within the crucible, and a rod of a specific weight was placed on the sample to pack it. The force on the particle bed was proportional to the weight of the rod, and since the same rod was used for all samples, it ensured that they were all packed with the same force. The sample was then loaded on top of the sample carrier (Figure 3-3), where first the sample weight was measured by the analyser, and then the run began. Heating of the sample within the STA furnace was achieved via a precision electrical resistance heating element. Heat is transferred to the packed wood chips primarily through conduction from the heated ceramic sample carrier and the base of the aluminium crucible, alongside radiation from the furnace walls. This mechanism, combined with the high thermal conductivity of the crucible and the small sample sizes, was designed to ensure uniform heating and minimise thermal gradients across the particle bed. The first step in the heating profile consisted of heating the sample to 105 °C to remove any moisture in the wood. It was held at this temperature for 45 minutes, after which it was cooled down to 50 °C and held for 40 minutes. Next, the sample was heated to 580 °C (T_{max}) and held isothermal for 40 minutes, then cooled to 50 °C and held isothermal for 40 minutes. It was then heated again to 580 °C and immediately cooled to 50 °C, then held isothermal for 40 minutes. Lastly the sample was again heated to 580 °C. At the end of this step, the run was terminated. All cooling was done at a rate of 20 K/min. All runs were under inert atmospheric conditions. Nitrogen gas flows both through the furnace at 50 mL/min and around the outside of the furnace at 20 mL/min. The latter nitrogen is a protective measure to reduce the oxidative stress on the furnace. The 50 mL flow is to ensure an inert reacting environment for the sample. To maintain inert (pyrolysis) conditions, high purity (99.99%, instrument grade) nitrogen was used.

3.2.4 Kinetic analysis methods

Fundamental rate laws

For a one reactant type, the rate law is as follows:

$$Rate = -\frac{d[A]}{dt} = k[A]^n \tag{3.2}$$

where $[A]$ is the concentration of reactant A, k is the rate constant and n is the reaction order. For example, for a zero order (n=0) reaction, equation (3.2) can be modified and integrated as follows

$$-\frac{d[A]}{dt} = k[A]^0 = k \; as \; [A]^0 = 1 \tag{3.3}$$

Integrating equation (3.2) gives:

$$\int_{[A]_0}^{[A]_t} d[A] = \int_0^t k dt \tag{3.4}$$

$$[A]_t = -kt + [A]_0 \tag{3.5}$$

If the reaction is truly zero order, the plot of $[A]_t$ *vs* time should produce a linear slope in the negative direction, whose slope is equal to the reaction rate and the intercept equal to the initial concentration, $[A]_0$.

This procedure can be repeated for higher order reactions (n=1 and n=2), which will yield the following equations:

$$for \; n = 1 \quad \ln[A]_t = \ln[A]_0 - kt \tag{3.6}$$

$$for \; n = 2 \qquad \frac{1}{[A]_t} = kt + \frac{1}{[A]_0} \tag{3.7}$$

These rate laws can be modified for reactions which are temperature dependent using the Arrhenius equation. Where for a single reaction, the following equation (3.8) describes the decay rate:

$$\frac{d\alpha}{dt} = A \exp\left(-\frac{E}{RT}\right)(1-\alpha)^n \tag{3.8}$$

where A, E and n are the pre-exponential factor, activation energy and reaction order, respectively. Here α is used to denote the dimensionless amount of reactant consumed as this will be helpful in describing the reaction model that follows. The Arrhenius equation is an exponential decay model; thus equation (3.6) is the best fit to this model, hence a first order reaction can be assumed here. In pyrolysis, the rate equation has three or more terms with the form of equation (3.8) where n=1. By plotting the integral of this equation as a log vs 1/T plot, a few regions appear with approximately linear slopes. These can be used as first guesses for the terms A and E of the rate terms (Figure 3-4). Iteration is then needed.

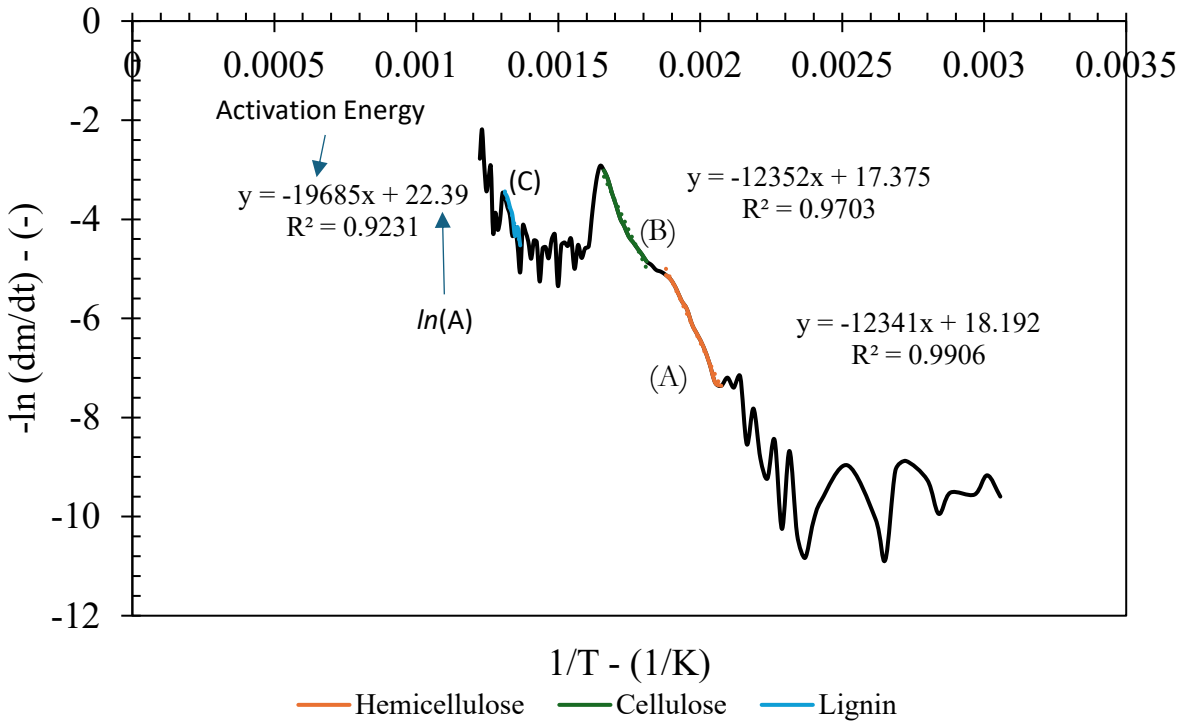

Figure 3-4: natural log of the differential mass loss (dm/dt) vs. 1/T of a 3 mg sample of wood chips with particle size between 60 and 600 µm pyrolysed at 1 K/min to a treatment temperature of 580°C to demonstrate the initial guess of Activation Energy, E and pre-exponential factor, A for the three components – (A) Hemicellulose, (B) Cellulose and (C) Lignin.

Assuming constant heating rates, equation (3.9) can be integrated over the temperature range of the reaction as follows:

$$I = \frac{A}{\beta_T} \int_{T_0}^{T} \exp\left(-\frac{E}{RT}\right) dT \tag{3.10}$$

where *I* is the integral term, which represents the cumulative effect of the reaction rate over a specified temperature range and β_T is the constant heating rate.

It is possible to consider wood decomposition as the sum of three component (i.e. hemicellulose, cellulose and lignin) decaying independently. The model for wood decay can therefore be modelled using the following equation:

$$m_{kānuka} = 1 - [c_{hemicellulose}\alpha_{hemicellulose} + c_{cellulose}\alpha_{cellulose} + c_{lignin}\alpha_{lignin}] \tag{3.11}$$

The coefficient *c* expresses the contribution of the individual components to the overall reaction of kānuka. For each component, the reacted fraction, α is given by

$$\alpha_i = \frac{m_{0,i} - m_{t,i}}{m_{0,i} - m_{tf,i}} \tag{3.12}$$

where $m_{0,i}$, $m_{t,i}$ and $m_{tf,i}$ are the initial sample mass, the current sample mass and the final sample mass of the reacting component, *i*.

The least squared error (LSE) of equation (3.11) is then calculated for the model and experimental mass loss (TG). It is iterated for the most optimal parameters (A, E and c) of each component using the GRG nonlinear solver on Excel to minimise the LSE. However, due to the non-linearity of the Arrhenius rate law, the local minimum is not unique, thus, a satisfactory initial guess for the parameters is crucial to acquire a good fit.

3.3 Results and Discussion

It is common to present thermogravimetric results of wood decomposition and other biological materials as the mass loss vs. temperature plots. From the integral (TG) plot (mass (mg) vs. Temperature (°C)), one can easily determine the moisture content, volatiles produced and char

yield. However, it is the differential plots (-dm/dt vs. temperature) that show the characteristics of the decomposition mechanism of the sample, and it is possible to distinguish between different substances. Both plots provide useful information in the interrogation of the reaction kinetics of kānuka.

3.3.1 Repeatability

Due to the extended duration of the experimental runs, it was not practical to perform duplicates or triplicates for every sample. Therefore, to address this limitation, samples at the lower extremes - specifically those with a mass of 3 mg, where the noise-to-signal ratio is highest- were randomly selected and run in duplicates, with a significant interval of time separating each run. The mass loss versus temperature (TG) and differential mass loss versus temperature (DTG) plots from these duplicates were compared to ascertain whether the repeatability of the experiments was satisfactory. The raw results of these duplicates are presented below (Figures 3-5 to 3-8).

The TG and DTG plots for the smallest sample mass, which should exhibit the highest noise-to-signal ratio and thus the greatest variability, clearly demonstrates that for all the heating rates employed in this research, the repeatability is satisfactory. The squared errors between each run for the TG results ranged from 0.008 to 0.017, and from 0.014 to 0.98 for the DTG results. These low squared error values indicate minimal variance between the duplicate runs, confirming the reliability of the experimental method even under conditions where variability is expected to be the highest.

As an added measure to ensure that each sample was representative and thoroughly mixed, a specific mixing procedure was implemented before extracting a sample. The parent batch of wood chips was mixed with a spatula twenty-three times by rotating the spatula in a circular clockwise motion halfway between the perimeter and the centre of the cylindrical container used for the samples. This meticulous mixing process was intended to minimise any discrepancies arising from uneven distribution of particle sizes, moisture content, or composition within the batch. A

standardised mixing method reduces potential human error and enhances the reproducibility of the results.

In summary, although it was not feasible to run duplicates or triplicates for every sample due to the length of the experimental runs, the approach of running duplicates for randomly selected samples for the low mass samples provided sufficient evidence of satisfactory repeatability.

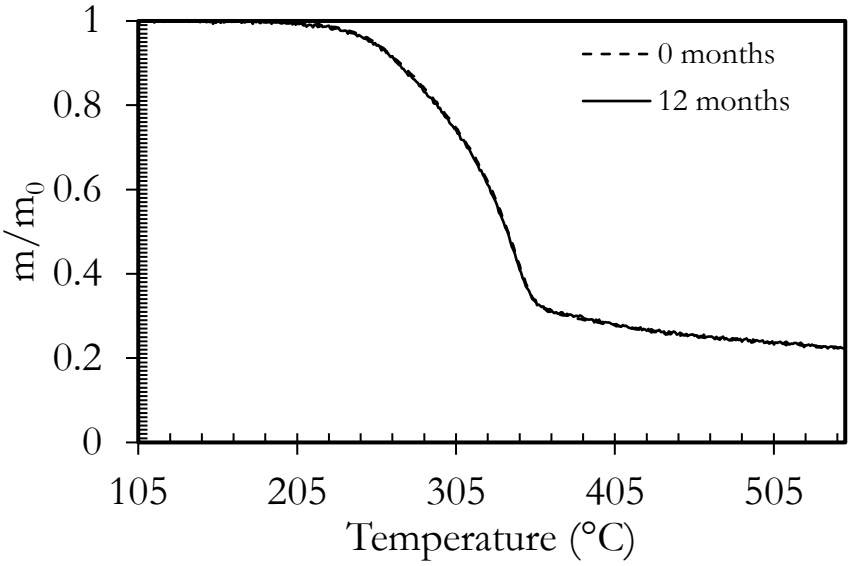

Figure 3-5: The repeatability of the TG signal of a 3 mg sample of kānuka heated at a rate of 2.5 K/min after 12 months between sample runs.

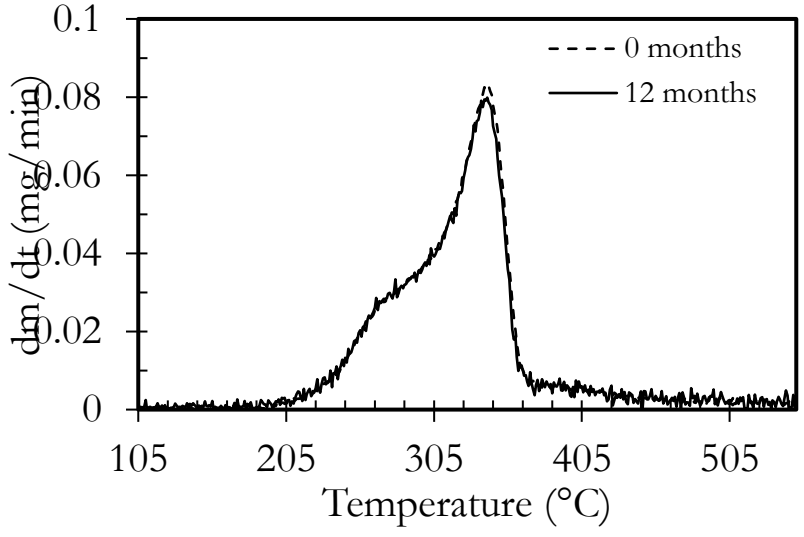

Figure 3-6: The repeatability of the DTG signal of a 3 mg sample of kānuka heated at a rate of 2.5 K/min after 12 months between sample runs.

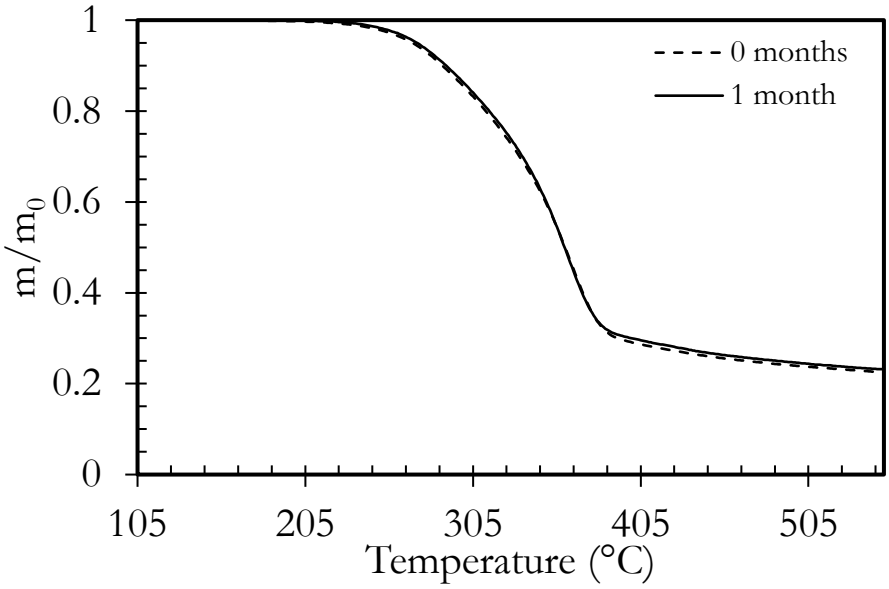

Figure 3-7: The repeatability of the TG signal of a 3 mg sample of kānuka heated at a rate of 10 K/min after 1 month between sample runs.

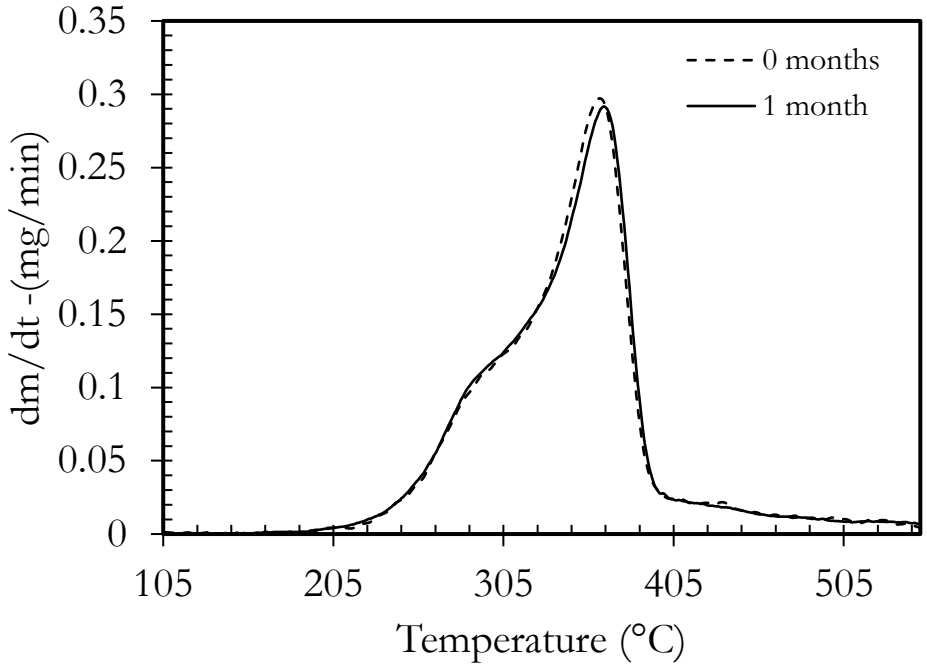

Figure 3-8: The repeatability of the DTG signal of a 3 mg sample of kānuka heated at a rate of 10 K/min after 1 month between sample runs.

3.3.2 Product yields

The relationship between char yield (and the volatile yields) and sample mass in kānuka wood pyrolysis provides important insights into the factors influencing solid product formation during

thermal decomposition. Notably, the data (Figure 3-9 to 3-11) shows that smaller particle sizes, specifically those under 90 microns, produce higher char yields than larger particles, such as those between 90 and 600 microns. An exponential saturation function, $y = a + b(1-e^{(-cx)})$, was fitted to the dataset to capture the non-linear, concave-down relationship between char yield (%) and sample mass (mg). The form reflects the diminishing returns: as mass increases from very small values, bed depth (and thus volatile path length and residence time) grows, enhancing secondary charring and raising yield; beyond a characteristic mass scale (1/c), additional mass contributes progressively less and the response approaches the asymptote a + b. Physically, a represents the near-transport-free baseline yield and b the mass induced increment attributable to secondary reactions, and c sets the mass scale of the approach to plateau. Within the 3-24 mg range, the behaviour trends towards but does not reach saturation, consistent with incomplete development of transport limited secondary reactions. This function is also used later (chapter 5) to fit the specific enthalpy of reactions (J/g) vs. char yield (%) following the methodology by Jones *et al.*, (2020).

It is hypothesised here that this variance is largely driven by differences in bulk density and resultant permeability in each sample. According to the well-known Kozeny-Carmen equation, permeability, κ in a packed bed of particles depends on the bed porosity and particle diameter. So even with equivalent particle porosity, smaller particles packed into a bed with significantly reduced permeability – for this example of particles with a diameter of <90 μm, the permeability is ~28 times lower than the larger particles between 90 and 600 μm. This reduced permeability hinders the escape of volatile decomposition products, both increasing the concentration of volatiles because the pressure increases and permitting greater occupancy of adsorption sites where secondary reactions occur, increasing the residence time of gases in the reaction zone. Consequently, the more intimate interaction between volatiles and the solid char layers promotes secondary reactions that enhance char formation. Jones, Chen and Ripberger (2020) explained this increase in secondary reactions to be related to both the number of adsorption sites that can be occupied (a function of pressure) and the opportunity for interaction (a function of the flow

channel). They observed that increasing sample mass resulted in more char yield. Here, this research instead changes the pore size to achieve a similar increase in yield. Nevertheless, it is the same mechanism in Jones *et al*.., (2020) , the smaller pores were inside the wood particles, but here the smaller pores are in the interstitial space. The outcome is that smaller pores have greater internal surface area and so have more adsorption sites and because they are more restrictive generate higher internal driving pressures of volatiles. Both factors result in more secondary reactions.

Extrapolating the fitted mass-yield curves in Figures 3-9 and 3-10 to a theoretical sample mass of zero estimates the cahr yield in the limit where secondary reactions are negligible. The y-intercept for the coarser particles (90 - 600 μm) is ≈16.48% (dry basis), whereas the intercept for the finer particles (< 90 μm) is ≈25.64%. These intercepts represent the minimum char yields expected for each size class under the present heating program.

The impact of pressure within the reaction environment also plays a pivotal role in shaping char yield (this will be discussed in further detail in chapter 5). Elevated pressures drive the escape of volatile compounds but also increases interactions with the char layer and promotes additional reactions that enhance secondary char formation. This effect of pressure is a function of particle size, internal pore size distribution and interstitial pore volume, because both these restrict gas escape, which increases local pressure and creates an environment where reactive intermediates are retained long enough to undergo further transformation. Supporting studies (Basile *et al*., 2014) on pyrolysis under varying pressures demonstrated that higher pressure settings intensify char formation by trapping volatile compounds and promoting reactions with solid carbon, leading to similar outcomes to those observed in very small particles (D_P < 90 μm). This high-pressure effect aligns with broader findings in biomass pyrolysis, where gas flow restrictions and secondary reactions are critical to char yield (Miller, Richard Steven; Bellan, 1997). The narrowing and temperature shift in the differential thermogravimetric (DTG) peak in smaller particles provides

further insight into the mechanisms of pyrolysis (discussed further in the following sections of this chapter).

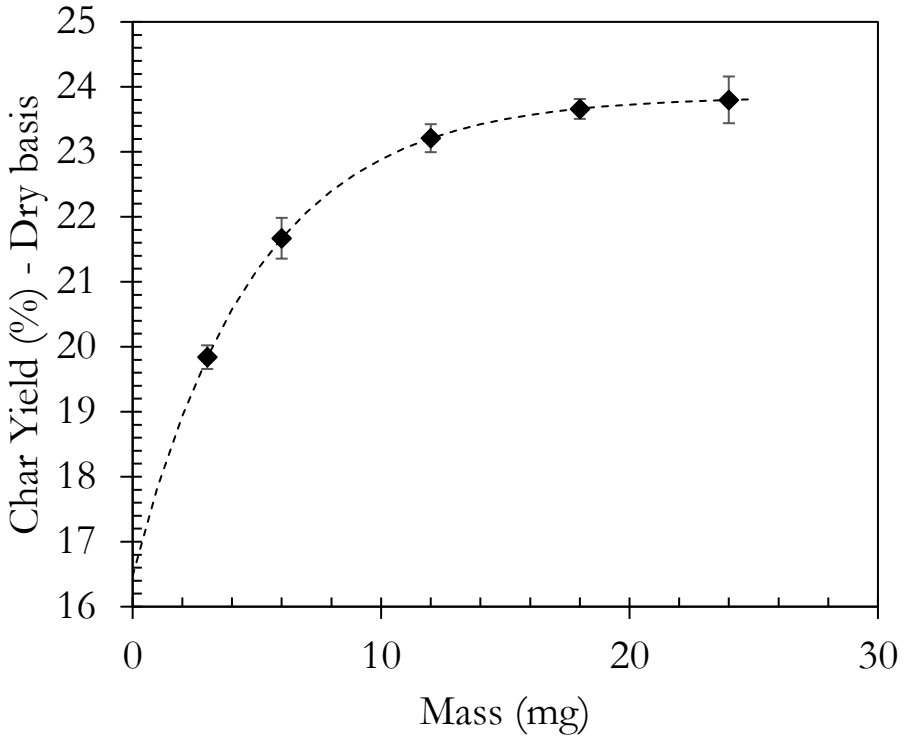

Figure 3-9: relationship of mass size to char yield (%) on a dry basis for kānuka samples with an average particle size range of 90 < DP < 600μm heated at 1, 2.5, 5, 10 and 20 K/min. The char yield at various heating rates were used to calculate the standard error as the heating rates were used to calculate the standard error as the heating rates are all assumed to be in the slow pyrolysis regime and do no effect char yield. Model (dashed line) was fitted using single exponential saturation model; $y = 16.47 + 7.4(1-e^{(0.2x)})$, $R^2 = 0.99$.

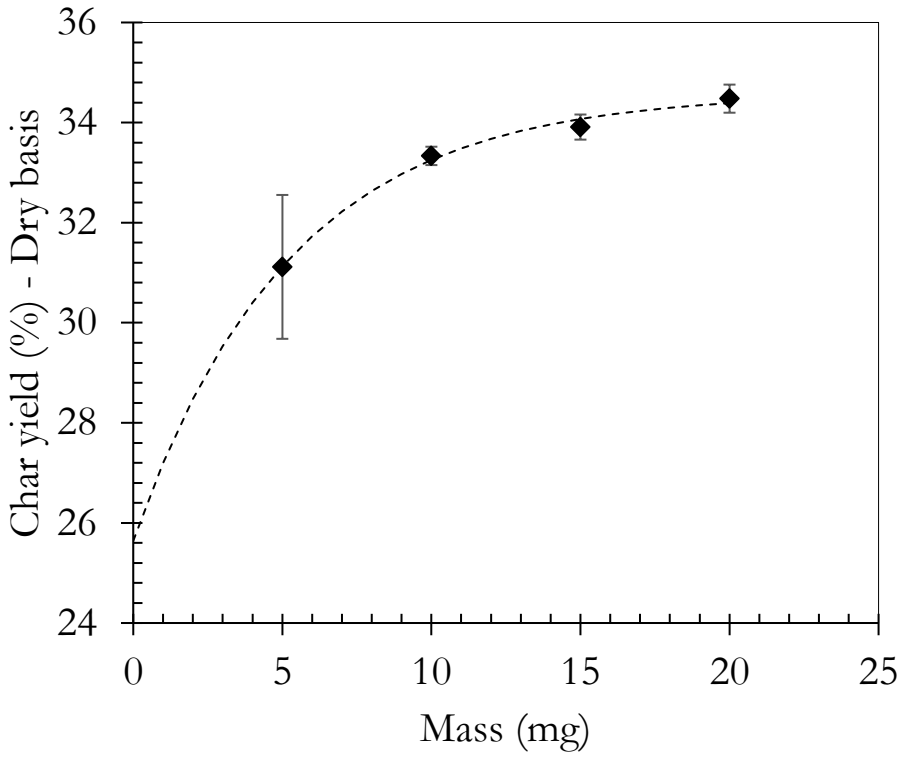

Figure 3-10: Relationship of sample mass to char yield (%) on a dry basis for kānuka samples with an average particle size range of < 90 µm heated at 1, 2.5, 5, 10 and 20 K/min The char yield at various heating rates were used to calculate the standard error as the heating rates are all assumed to be in the slow pyrolysis regime and do not affect char yield. Model (dashed line) was fitted using single exponential saturation model; $y = 25.64 + 8.94 (1 - e^{(0.19x)})$, $R^2 = 0.99$.

These findings have significant implications for optimising smoke generators. If high volatiles are desired – such as for applications focused on food smoking but also in gasification systems where syngas is the desired product – using larger particles to increase bed permeability can facilitate this outcome, however, not so large that diffusion through the interstitial voids dominates. To test this, single particles of 6 and 12 mg each were cut from the same kānuka wood used for this study.

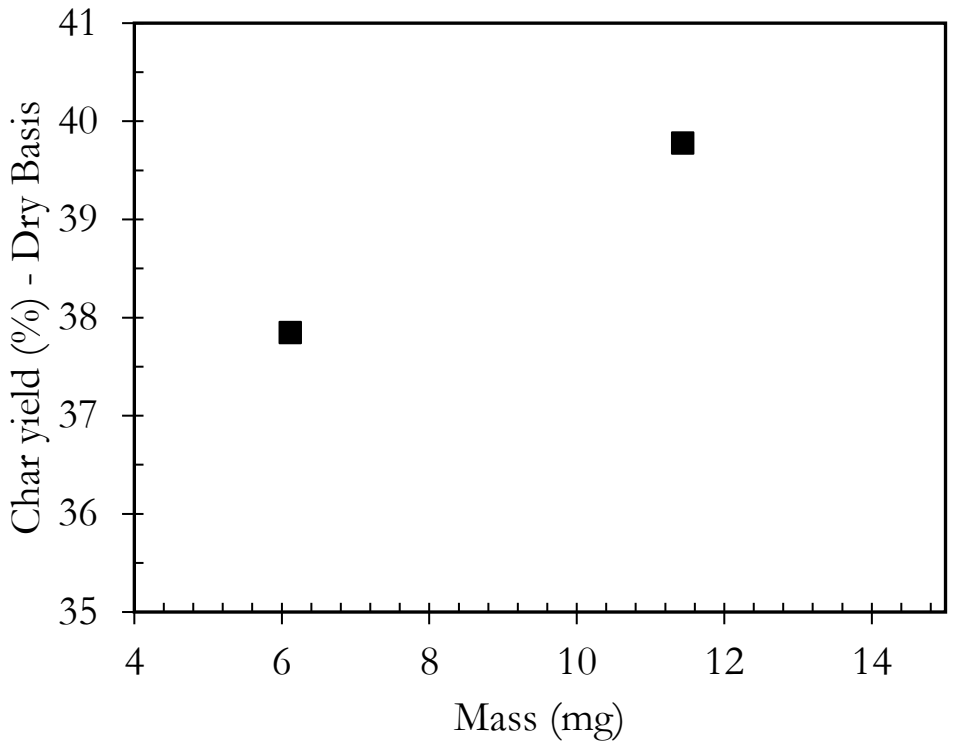

Figure 3-11: Char yield of single particles with mass of 6 and 12 mg showing diffusion in the interstitial voids of the wood dominating. These samples were pyrolysed at a heating rate of 10 K/min.

When pyrolysed, they had elevated char yields of above 35% (Figure 3-11), which is more like the small particle size (D_P < 90 μm) wood chips. This suggests that the elevated char yield observed in single wood particles is comparable to very fine particles which suggests similar reduced porosity and the localised conditions within the particle. These conditions will restrict the escape of volatiles, increase the pressure and promote secondary reactions that favour char formation over volatile release.

3.3.3 Thermal decomposition characteristics of Kānuka

The thermal decomposition characteristics of kānuka are explored by examining the differential mass loss (DTG) and mass loss (TG) curves when pyrolysed under inert conditions. Later, non-linear regression models are used to extract the kinetic parameters of activation energy and pre-exponential factor for the cellulose, hemicellulose, or hollo-cellulose if they cannot be distinguished, and lignin components of wood.

3.3.4 Effect of heating rates

The differential mass loss (DTG) thermos-grams of untreated kānuka wood chips pyrolysed at five heating rates, 1, 2.5, 5, 10 and 20 K/min, under inert atmospheric conditions are shown below in Figure 3-12. The pyrolysis reactions generally start at 200 °C for all sample masses and heating rates for particle sizes of 90 - 600 μm. This result is similar to many thermogravimetric analysis of wood found in literature (Kissinger, 1956; Di Blasi and Russo, 1994; Reina, Velo and Puigjaner, 1998; Bellais, 2007; Slopiecka, Bartocci and Fantozzi, 2012; Corbetta *et al.*, 2014; Reschmeier *et al.*, 2014). However, the DTG plots of samples with the lower particle diameters (< 90 μm), show that pyrolysis reactions start lower at between 150 and 180 °C (Figure 3-13). Another difference between the two particle sizes is the number and location of the DTG peaks. Samples of the larger particle diameter (90 – 600 μm) exhibit a complex, overlapping decomposition profile characteristic of lignocellulosic biomass. Rather than presenting as discrete peaks, the degradation of the three main structural components manifests as distinct regions on the mass loss rate curve: a prominent leading shoulder between 270 °C – 325 °C (associated with hemicellulose), a sharp primary maximum between 325 °C – 380 °C (associated with cellulose) and a broad, extended high-temperature tail between 400 °C – 425 °C (associated with the slower degradation of lignin). The quantitative separation of these overlapping thermal regimes into individual constituent peaks is addressed via mathematical deconvolution in section 3.3.5. However, the smaller particle samples do not show all three peaks and those that are seen have shifted peak temperature, especially for the middle peak, which has reduced to 300°C.

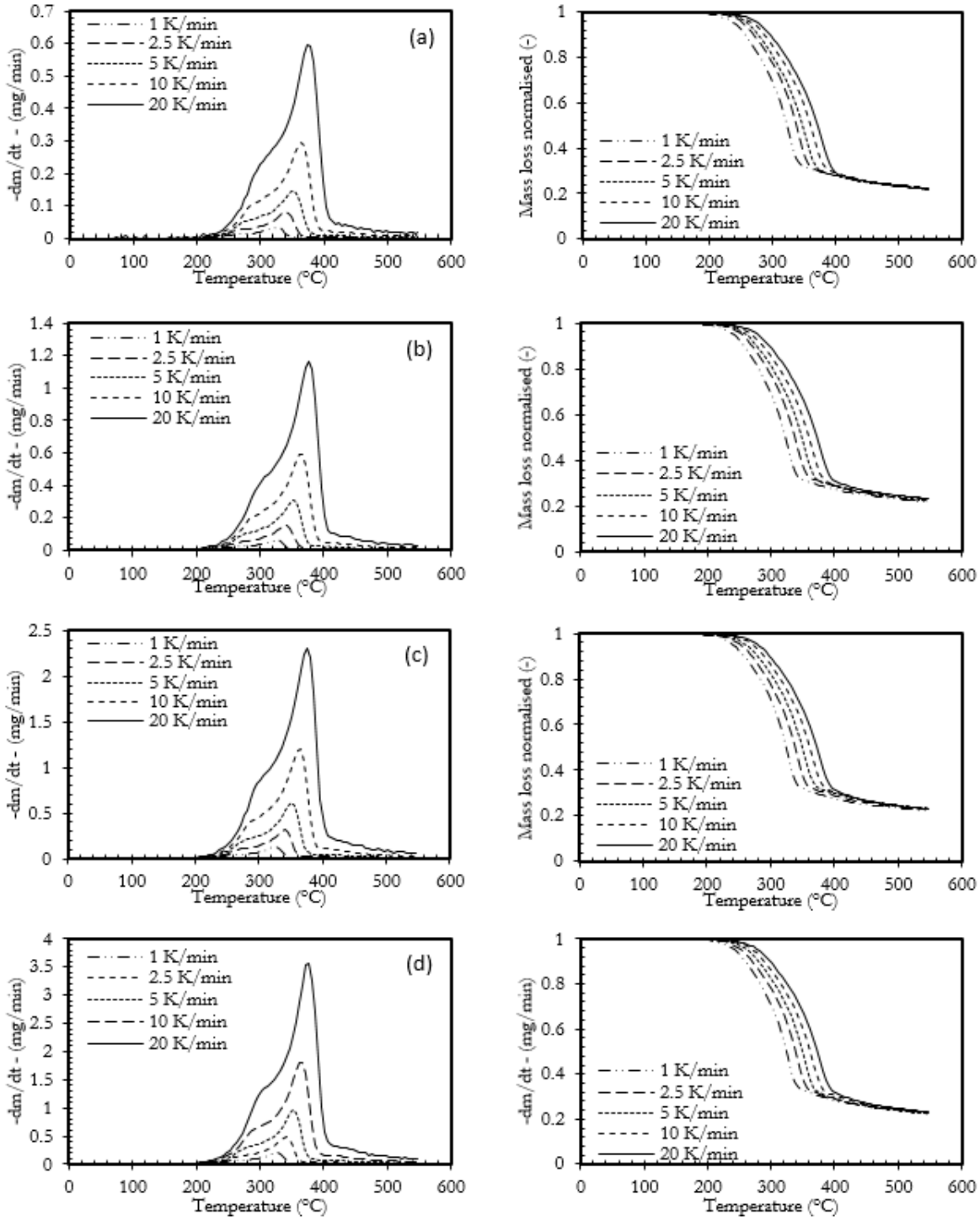

Figure 3-12: DTG and TG thermographs of the decomposition of kānuka wood chips of diameter between 90 and 600 microns. (a) 3 mg, (b) 6 mg, (c) 12 mg, (d) 18 mg

These peaks have been suggested to correspond to the decomposition of the main components of wood, i.e. hemicellulose, cellulose and lignin (Koufopanos, Lucchesi and Maschio, 1989). The following section (Section 3.3) presents a kinetic analysis to investigate whether it is possible to model the decomposition of kānuka wood as the sum of the decomposition rates of its main components.

As heating rates increase, both the onset of mass loss and the peaks shift to higher temperatures. This shift is a consequence of the limitations of heat and mass transfer, where larger samples exhibit more thermal lag and where higher heating rates accentuate it. These results agree with the literature (e.g., Aboulkas and El Harfi, 2008; Slopiecka, Bartocci and Fantozzi, 2012; Chen, Zhou and Zhang, 2014). However, the final char yields remain constant (Figures 3-9 & 3-10) for the same sample mass irrespective of heating rates, except in the smaller sample masses, which are less but have more scatter because the noise to signal ratio is higher this highlights that variability is an issue with a biological samples, where wood itself varies between heartwood, sapwood, the age of the wood and its position in the tree. Smaller samples tend to accentuate this variability.

The effects of heat and mass transfer on the peak temperature of decomposition for the three main components of wood (hemicellulose, cellulose and lignin) can be mitigated by plotting the peak temperature *vs* heating rate (Figure 3-13) and assuming an exponential saturation relationship as described by equation (3.13) – (3.15). The experimental peak temperatures plotted for each component were distinguished by identifying the local maxima or distinct inflection points in the case of overlapping shoulders, directly from the derivative thermogravimetric (DTG) curves at each heating rate.

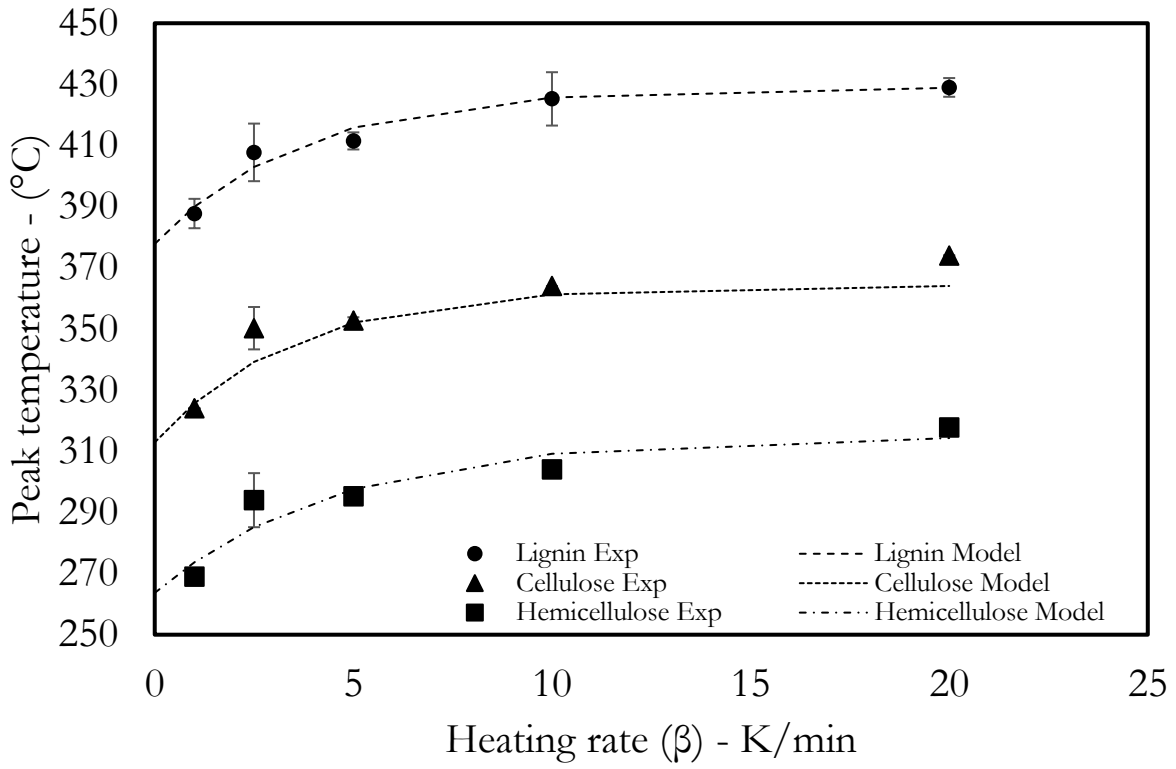

Figure 3-13: The relationship of peak temperature of decomposition of the main components of wood vs. the heating rate of kānuka wood chips of particle diameter of 90 – 600 microns. Experimental (symbols) data points ('Exp') denote the peak temperatures extracted from the DTG profiles, while the 'Model' (dashed) lines represent the non-linear regression fits described by Equations 3.13, 3.14 and 3.15.

$$T_{peak}^{Hemicellulose} = 263.68 + 51.33\left(1 - e(-0.217\beta)\right), \qquad R^2 = 88.7\% \tag{3.13}$$

$$T_{peak}^{Cellulose} = 312.92 + 57.8\left(1 - e(-0.288\beta)\right), \qquad R^2 = 92.0\% \tag{3.14}$$

$$T_{peak}^{Lignin} = 377.82 + 50.67\left(1 - e(-0.270\beta)\right), \qquad R^2 = 95.8\% \tag{3.15}$$

As $\beta \rightarrow 0$, the effect of thermal lag is removed and the peak temperature for the components can be deduced. For hemicellulose, cellulose and lignin, the temperature at which the peak decomposition occurs is 263 °C, 312 °C and 377 °C, respectively.

The thermal decomposition behaviour of cellulose is notably influenced by the heating rate during thermal analysis. Extrapolating to a theoretical heating rate of 0 K/min, the peak decomposition temperature of cellulose is approximately 312 °C. At practical heating rates (1 – 20 K/min), this peak temperature shifts higher, ranging from 312°C to 364 °C. This shift is consistent with findings in the literature, where higher heating rates result in delayed decomposition due to kinetic constraints and thermal lag. For instance, Yang *et al.* (2007) reported that the peak decomposition temperature of cellulose increases from around 315 °C at lower heating rates to about 360 °C at higher heating rates, attributing this to the reduced time available for thermal decomposition at each temperature. Similarly, Kawamoto (2017) observed that the peak decomposition temperature shifts to higher values with increasing heating rates because of decreased time for heat transfer and reaction completion.

The observed decomposition temperatures of cellulose are consistent with those reported for pure cellulose in the literature. Broido and Nelson (1975)found that pure cellulose decomposes with a peak temperature around 320 °C at a heating rate of 10 K/min. Antal, Varhegyi and Jakab (1998) noted that the peak decomposition temperature of pure cellulose could reach up to 355 °C.

Similarly, the thermal decomposition of lignin is influenced by the heating rate, exhibiting distinct characteristics compared to cellulose. At heating rates of 1 – 20 K/min, the peak decomposition temperature of lignin is between 377°C to 429 °C. This behaviour is in line with findings from literature, which highlight lignin's sensitivity to heating rate changes due to its complex and heterogeneous structure. Yang *et al.* (2007) noted that lignin decomposes over a broad temperature range, typically from 250 °C to 500 °C, owing to its intricate network of phenolic units. Kawamoto

(2017) further explains that lignin undergoes complex pyrolytic reactions involving multiple pathways, contributing to its wide decomposition temperature span.

At heating rates from 1-20 K/min, the peak decomposition temperature of hemicellulose was found here to be 260 °C to 320 °C. However, it is difficult to compare the decomposition kinetics of hemicellulose with values in literature, as hemicellulose is a mixture of many polysaccharides, whose composition depends on many factors, including the species of the tree (Scheller and Ulvskov, 2010). However, some values for Xylan and other polysaccharides said to be typical of wood hemicellulose have been evaluated by several authors. The values for peak decomposition temperature found by Z. Lei *et al.,* (2019) for hemicellulose extracted from *Camellia oleifera* shell was between 291.3 °C and 318.3 °C, for heating rates of 5 K/min to 20 K/min respectively. Wei-Hsin Chen *et al* (Chen *et al.*, 2020) found peak decomposition temperature for xylan was found to be between 207 and 252 °C. Another study (Yeo *et al.*, 2019) has published results for decomposition of xylan, with peak temperature decomposition occurring between 232 to 332 °C. So, while there is a range of results, these are not dissimilar to the 263 °C to 314 °C found here for hemicellulose.

3.3.5 Kinetic analysis

The decomposition of wood is a complex process and deriving the kinetic rates is not trivial, because there are multiple parallel and competing reactions taking place. In this section, the kinetic rates are analysed using the model-based method. Firstly, the DTG curves are modelled as a composite of separate Arrhenius relationships for the hemicellulose, cellulose and lignin components of wood, using the approach by Varhegyi *et al.,* (2002b).

Model-based method

The model-based method is described in section 3.2.4. A non-linear regression model was used to obtain the best fit Arrhenius parameters. The results of this model compared to experiments is presented in Figures 3-14 to 3-16 for the larger size fraction of particles, 60 – 600 μm, and in

Figures 3-17 to 3-20 for the smaller size fraction, < 90 μm. As discussed in section 3.4, the first peak is intended to represent hemicellulose decomposition, the second peak represents cellulose and the third, very wide peak is intended to represent lignin. The derived kinetic parameters (activation energy, E and pre-exponential factor, A) for all fits are presented in Tables 3-1 (for 90-600 μm particles) and 3-2 (for ≤90 μm particles). Rather than acting as fixed constants, the key finding revealed in Table 3-1 is that these apparent kinetic parameters are dynamic and sensitive to both sample mass and heating rate. Specifically, the data demonstrates that both increasing sample mass and increasing heating rates generally lead to elevated apparent activation energies, a direct consequence of internal heat and mass transfer limitations delaying thermal degradation. In the following subsections, the results of the model-based method will be compared as a function of sample mass and heating rate for the larger particles, after which the smaller particles are discussed. Mechanisms responsible for the differences will be discussed. The weighted average activation energy across the five heating rates for hemicellulose decomposition obtained was 120.7 kJ/mol with a standard error of ±1.7 kJ/mol. For cellulose it was 189.9±2.9 kJ/mol and for lignin it was 53.6±2.3 kJ/mol. These values agree with those presented in the literature (Grønli, 1996; Reina, Velo and Puigjaner, 1998; Svenson, Pettersson and Davidsson, 2004; Slopiecka, Bartocci and Fantozzi, 2012; Reschmeier *et al.*, 2014).

3.3.5.1 Mass variation in kinetic parameters (90-600 μm particles)

The results (Table 3-1) indicate that mass variations in kānuka wood samples directly influence the kinetic behaviour of decomposition. For instance, the activation energies (E) and pre-exponential factors (A) for hemicellulose, cellulose and lignin show noticeable changes across different masses. Generally, larger samples (e.g., 18 mg) show slightly elevated activation energies, suggesting that as the sample mass increases, the reaction will be initiated at higher temperature. This trend aligns with findings from Grønli (1996) where larger samples were noted to exhibit delayed thermal degradation due to heat transfer limitations within the bulk.

3.3.5.2 Impact of Heating Rates on Decomposition (90-600 μm particles)

Heating rate is a crucial parameter affecting the thermal degradation profile of kānuka wood. Higher heating rates generally lead to an increase in the activation energy for each component (hemicellulose, cellulose and lignin) in all sample masses. For example, in the 3 mg samples, the activation energy for cellulose at 20 K/min is significantly higher (198 kJ/mol) than that at 1 K/min (186 kJ/mol). This observation is consistent with findings in the pyrolysis literature (Varhegyi *et al.*, 1989; Grønli, 1996; Grønli, Várhegyi and Di Blasi, 2002a) where increased heating rates typically result in thermal lag, requiring higher temperature for decomposition to occur. This is due to the reduced time available for thermal equilibrium across the wood chips, which escalates the apparent energy barrier.

Comparing these results with established literature (Kissinger, 1956; Vyazovkin, 2003; Mamleev, Bourbigot and Yvon, 2007; G. Lv, Wu and Lou, 2010; Grieco and Baldi, 2011) values highlights both consistencies and deviations. The activation energy for cellulose decomposition in kānuka wood, for instance, ranges between 159.8 and 204.1 kJ/mol, depending on the heating rate and sample mass. This range aligns closely with literature values for similar biomass types, where activation energies for cellulose typically span 150-200 kJ/mol (Reina, Velo and Puigjaner, 1998; Svenson, Pettersson and Davidsson, 2004; G. J. Lv, Wu and Lou, 2010; Park, Atreya and Baum, 2010).

Table 3-1: Kinetic parameters for kanuka wood with particle diameter from 90 to 600 microns, fitted to a three independent reaction model.

		Hemicellulose			Cellulose			Lignin					
Heating Rate K/min	Sample mass mg	E kJ/mol	Ln A	c	E kJ/mol	Ln A	c	E kJ/mol	Ln A	c	S^2 DTG	S^2 Yield	SE TG
1	3	119	22.2	19.7	186.1	33.4	43.5	38.8	2.6	15.8	3.6	1.8	0.0003
1	6	135	26	16	166	29.4	47.7	40.4	3	15	4.6	1.9	0.0100
1	12	137.4	26.5	15.5	178	31.8	46.8	42	3.4	15.8	4.2	1.4	0.0005
1	18	130.3	24.9	16.3	180	32.2	45.5	44.9	3.9	15.2	4.3	1.7	0.0005
2.5	3	123.4	23.6	19.3	184.9	33.2	46.4	52.1	5.8	11.8	4	1.6	0.0004
2.5	6	120.6	23	18.9	180.4	32.3	45.2	51.5	5.8	12.3	3.7	1.4	0.0003
2.5	12	127.4	26.5	18.8	206.8	31.8	43.8	49.2	3.4	14.9	3.4	1.8	0.0003
2.5	18	134.4	26.1	16.1	180.4	32.3	46	47.1	5.1	15.1	4.2	1.4	0.0005
5	3	113.3	21.6	22	182.2	32.8	45.4	60.7	7.9	10.4	3.6	1.6	0.0003
5	6	109.6	20.7	23.5	200.9	36.2	42.1	67.6	9.3	10.8	2.5	0.7	0.0001
5	12	115.9	22.1	20.6	194.7	35.1	48	55.4	7.1	13.2	3.3	1.4	0.0002
5	18	118.6	22.7	19.8	203.9	36.8	43.2	52.8	6.7	14.7	3.2	1.5	0.0003
10	3	113.8	21.9	22.5	200.5	36.1	42.4	50.7	6.9	12.8	3	0.5	0.0002
10	6	115.1	22.6	17.8	159.8	28.5	51.7	86.2	12.4	8.1	5.3	1.5	0.0006
10	12	115.7	22.3	20.9	196.2	35.3	43.3	58.5	8.2	11.6	3.1	1.2	0.0001
10	18	118.1	22.9	20	197.5	35.6	43.5	57.1	7.9	13.7	2.9	1.1	0.0002
20	3	116.7	22.8	22.3	198.6	35.7	43.5	49.5	7.3	12.9	3.5	0.6	0.0002
20	6	113.9	20.1	22.1	204.1	34.6	42	53.9	5.9	13	3	0.7	0.0002
20	12	116.4	22.7	21.3	197.3	35.5	42.7	56.7	8.4	13.3	3	0.5	0.0002
20	18	118.7	23.2	20.3	198.9	35.8	42.9	57.6	8.6	13.9	2.5	0.8	0.0001

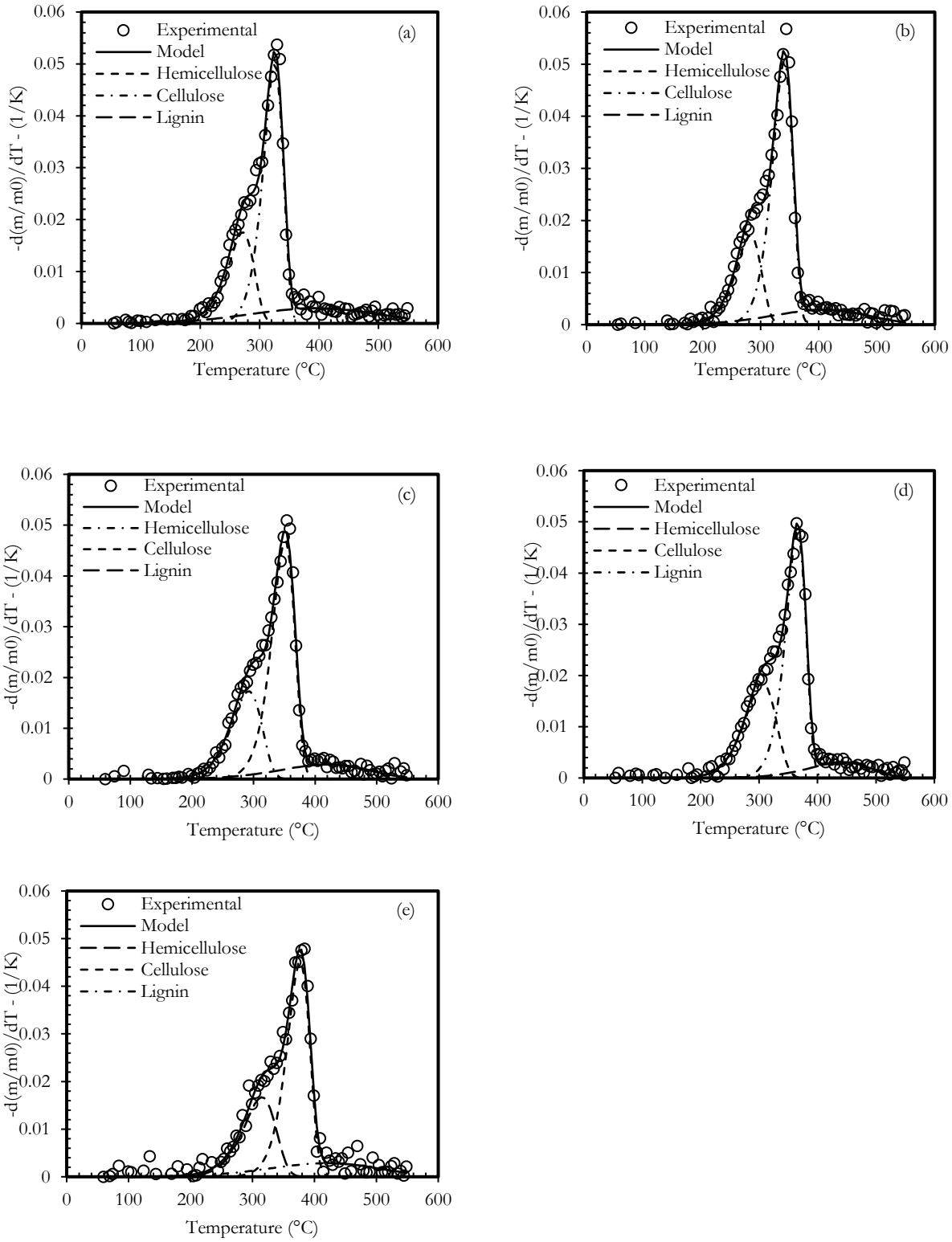

Figure 3-14: Kinetic evaluation of 3 mg of kanuka wood chips of particle size between 90 and 600 microns at five heating rates of (a) 1, (b) 2.5, (c) 5, (d) 10 and (e) 20 K/min, assuming three parallel independent first order reactions

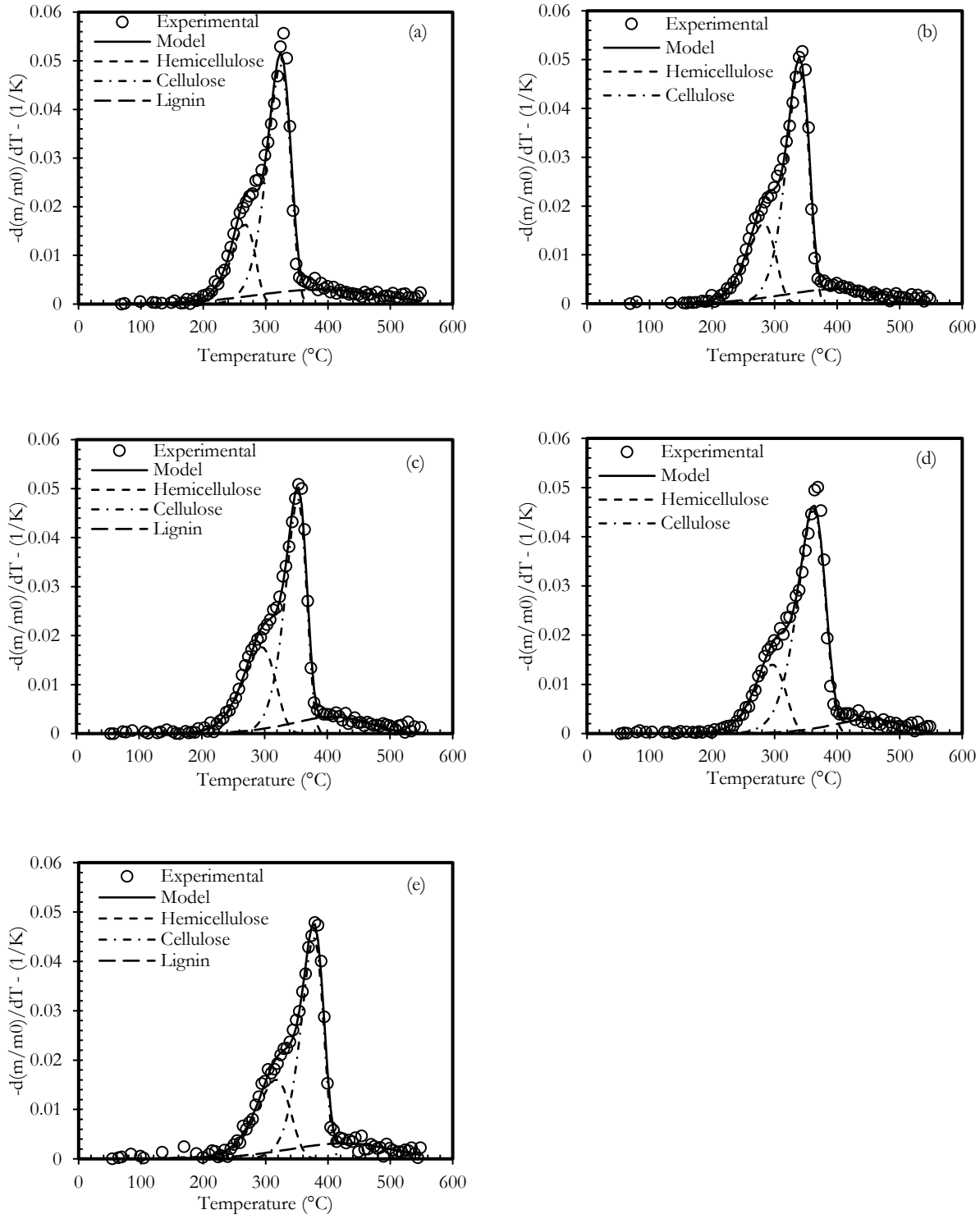

Figure 3-15: Kinetic evaluation of 6 mg of kanuka wood chips of particle size between 90 and 600 microns at five heating rates of (a) 1, (b) 2.5, (c) 5, (d) 10 and (e) 20 K/min, assuming three parallel independent first order reactions

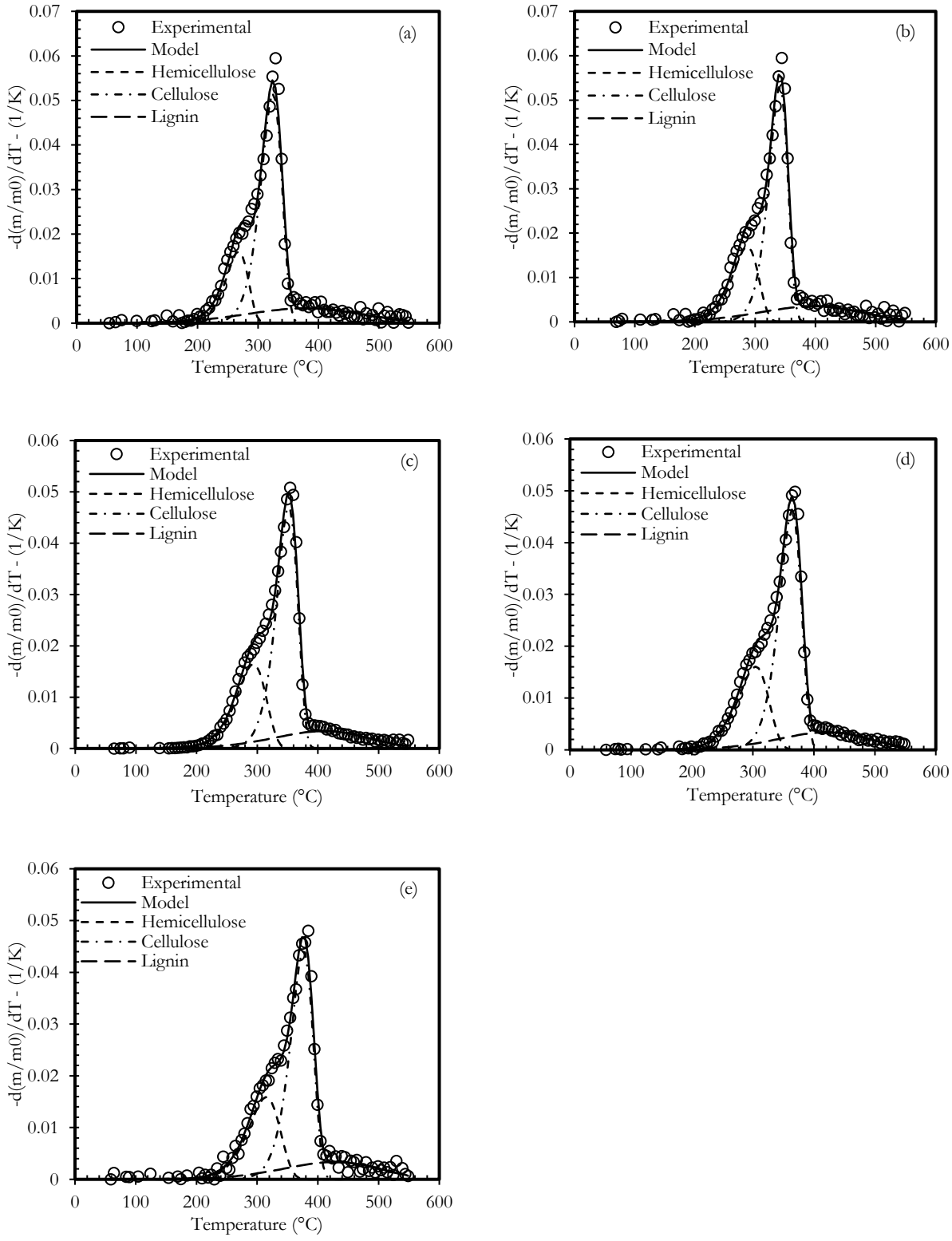

Figure 3-16: Kinetic evaluation of 12 mg of kanuka wood chips of particle size between 90 and 600 microns at five heating rates of (a) 1, (b) 2.5, (c) 5, (d) 10 and (e) 20 K/min, assuming three parallel independent first order reactions

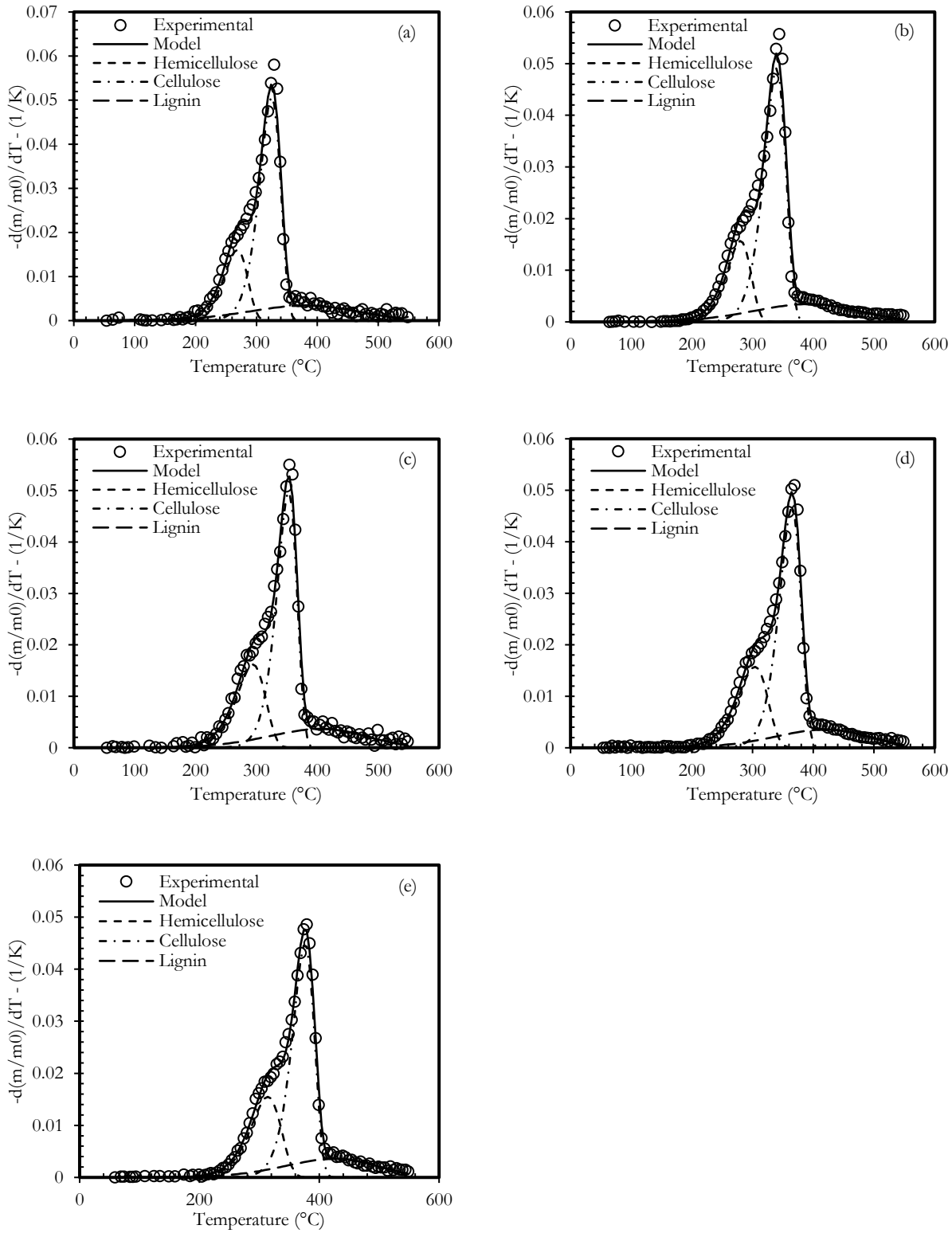

Figure 3-17: Kinetic evaluation of 18 mg of kanuka wood chips of particle size between 90 and 600 microns at five heating rates of (a) 1, (b) 2.5, (c) 5, (d) 10 and (e) 20 K/min, assuming three parallel independent first order reactions

The kinetic parameters for kānuka wood with particle sizes less than 90 microns reveal notable differences when compared to those for larger particle sizes (90-600 microns), reflecting the influence of particle size on decomposition characteristics. Most notable in the ≤ 90 μm results is the lack of a third peak at the start of the differential mass curve (DTG), and therefore a three-component model can't be applied. Instead, a two-component model is used here, and the first peak is considered a combination of hemicellulose and cellulose decomposition which together are called holocellulose – this will be discussed, later in this section. The analysis includes activation energies (E) and pre-exponential factors (A) across various heating rates (1, 2.5, 5, 10 and 20 K/min), which all show distinct patterns influenced by particle size.

3.3.5.3 Activation Energy and Pre-exponential Factor (≤ 90 μm particles)

In samples with particle sizes below 90 microns, the activation energy for both holocellulose and lignin generally fall within a narrower range compared to the larger particles (90-600 microns). For example, at a heating rate of 10 K/min, the activation energy for holocellulose in smaller particles is around 109.1 to 110.0 kJ/mol. This is lower than both hemicellulose and cellulose decomposition of the larger particles, which range from 113 to 137 kJ/mol and 165 to 206 kJ/mol, respectively.

3.3.5.4 Tar Flooding and Pressure Effects

Smaller particles with their increased surface area-to-volume ratio, can release a larger quantity of volatiles quickly, leading to an accumulation within the interstitial space of the bed. This accumulation results in a localised pressure build-up as volatiles maybe generated faster than they can diffuse out of the low-permeability interstitial structure formed by the fine particles.

Furthermore, there is some evidence that the initial decomposition may be liquid (Ripberger, 2016), which then volatilises. A build-up of liquid can cause flooding of the interstitial space, which further exacerbates the pressure. However, caused, this increase in pressure has several consequences. Firstly, the elevated pressure can alter the kinetics of the decomposition reactions. While the activation energy for Holocellulose observed in smaller particles is lower than that for both

hemicellulose and cellulose decomposition, this value does not completely account for the localised exothermicity resulting from rapid volatile release and retention, leading to increased secondary reactions. When volatiles are unable to escape freely, they may undergo secondary homogeneous and/or heterogeneous reactions within the confined space, generating additional heat and potentially modifying the chemical pathway of decomposition. This 'self-heating' effect can lead to accelerated degradation rates for holocellulose, while cellulose and hemicellulose peaks are masked due to the intense thermal overlap and rapid volatilisation. The build-up of volatiles and pressure essentially compresses the reaction pathways, leading to a singular, narrower peak.

3.3.5.5 Comparison with Larger Particles: Lower Pressure and Defined Peaks

In contrast, larger particles with sizes between 90-600 microns show distinct peaks for hemicellulose and cellulose. The lower surface-area-to-volume ratio of these particles results in a slower release of volatiles, which diffuses more effectively within the bed. The larger interstitial spaces between particles in these samples have higher permeability, allowing volatiles to escape more readily and liquid flooding to be less likely. As a result, pressure build-up is reduced, which means the reactions progress more independently, without significant thermal interference from rapid volatile accumulation. Consequently, the decomposition pathways for hemicellulose and cellulose remain separate, with two distinct peaks observed, along with a broader peak for lignin.

This lower pressure environment for larger particles is essentially due to differences in the overall pore network. As noted earlier single blocks of wood of 6 and 12 mg have similar char yield to the ≤ 90-micron particles and so have a similar pore network. The larger particles, 90 – 600 μm, on the other hand, have a larger interstitial network of larger pores, which facilitates the easy escape of volatiles which means bed pressure is lower, results in lower char yield. It also results in more stable kinetic parameters. Activation energies and pre-exponential factors for hemicellulose and cellulose in larger particles are typically higher than those observed for holocellulose in smaller particles, reflecting the fact that these reactions proceed without the added thermal 'boost' from secondary

reactions. For example, activation energies for holocellulose in smaller particles might be around 109-114 kJ/mol at a heating rate of 10 K/min, while the average hemicellulose and cellulose decomposition in larger particles can show activation energies upwards of 115-127 kJ/mol. This difference further emphasises the role of particle size and pressure in modifying reaction kinetics.

Table 3-2: Kinetic parameters for kānuka wood with particle size less than 90 microns, fitted to a three independent reaction model.

		Holocellulose			Lignin					
Heating Rate K/min	**Sample mass mg**	**E kJ/mol**	**Ln A**	**c**	**E kJ/mol**	**Ln A**	**c**	**S^2 DTG**	**S^2 Yield**	**SE TG**
1	5	109.4	19.1	48.5	40.8	2.9	31.3	0.7	4.1	0.0003
1	10	118	23.2	47.5	43.5	6.3	21.2	9.5	3.2	-
1	15	106.3	18.3	51.8	43.9	3.8	17.4	5.7	1.53	0.0006
1	20	107.1	18.5	50.5	46.8	4.5	17.6	4.6	3.8	0.0004
2.5	5	107.9	19.1	54.1	44.3	4.7	17.1	5.3	1.5	0.0005
2.5	10	107.2	18.9	52.7	46.7	5.1	16.7	5.5	1.3	0.0005
2.5	15	108.1	19.1	52	46.2	5.1	17.4	5.6	1.2	0.0005
2.5	20	107.6	19	51.5	46.1	5	17.7	5.6	1.2	0.0005
5	5	110.3	19.9	54.3	45.9	5.6	17	5.7	1	0.0006
5	10	110.6	19.9	52.2	45.3	5.5	17.4	5.9	0.9	0.0006
5	15	108.8	19.5	52.5	46.6	5.7	17.7	5.8	1.2	0.0006
5	20	109.3	19.7	51.9	46.5	5.7	18.2	5.8	1	0.0006
10	5	109.1	19.8	54.2	45.7	5.5	17.1	5.6	1	0.0006
10	10	110	20.1	52.4	46	6.3	18	5.2	1.3	0.0004
10	15	110.3	20.1	50.5	48.1	6.6	16.7	6	0.7	0.0005
10	20	110.7	20.2	50.1	47.4	6.5	17.6	5.8	0.7	0.0005
20	5	114.9	21.3	52.2	43.3	6.4	18.3	7.3	0.7	0.0008
20	10	114	21.2	51.7	45.3	6.8	18.2	6.4	0.5	0.0006
20	15	114.6	21.2	51.6	46.9	7	18.1	6.8	0.7	0.0007
20	20	114.9	21.3	50.8	47	7	18.5	6.3	0.7	0.0006

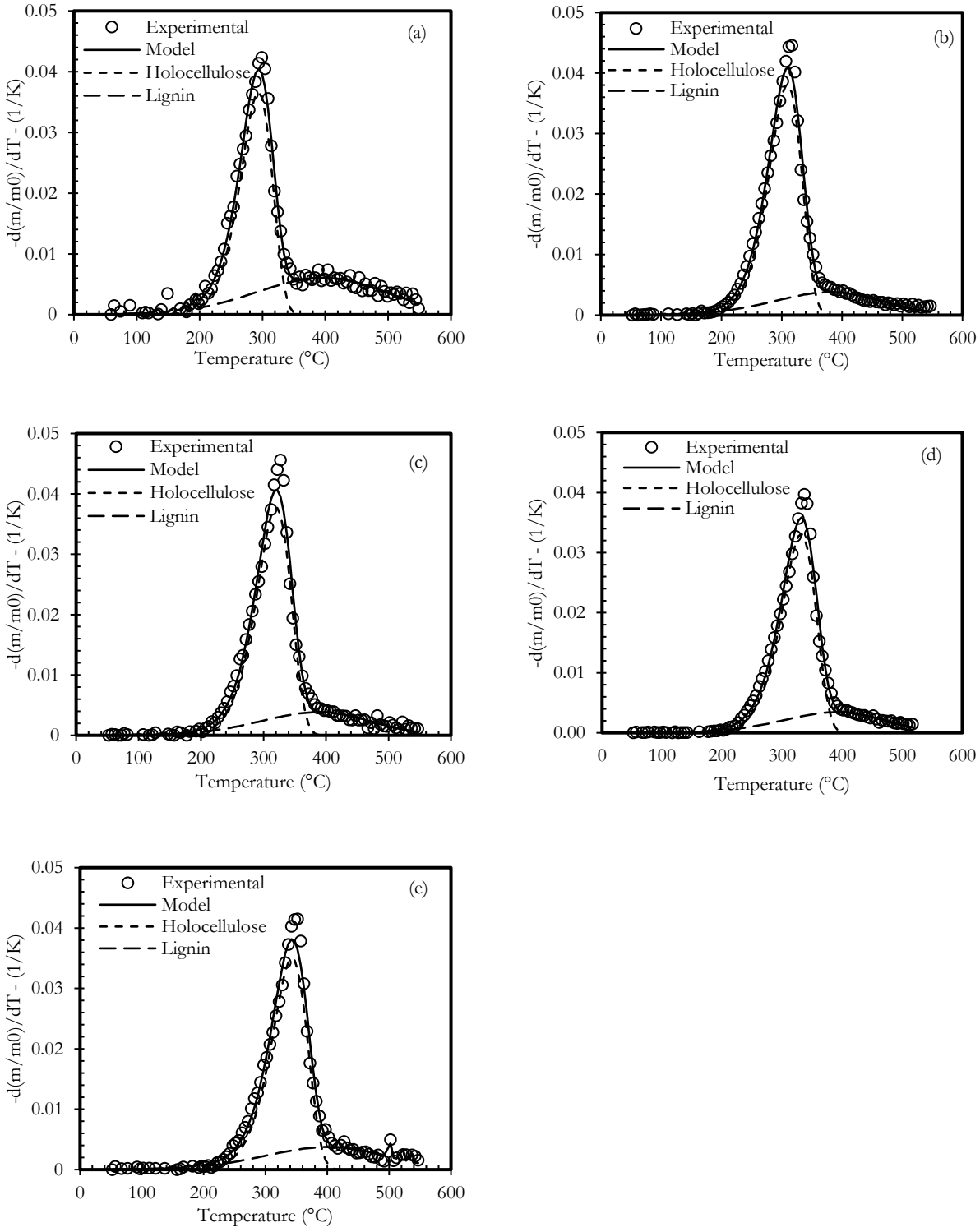

Figure 3-18: Kinetic evaluation of 5 mg of kanuka wood chips of particle size ≤ 90 microns at five heating rates of (a) 1, (b) 2.5, (c) 5, (d) 10 and (e) 20 K/min, assuming three parallel independent first order reactions

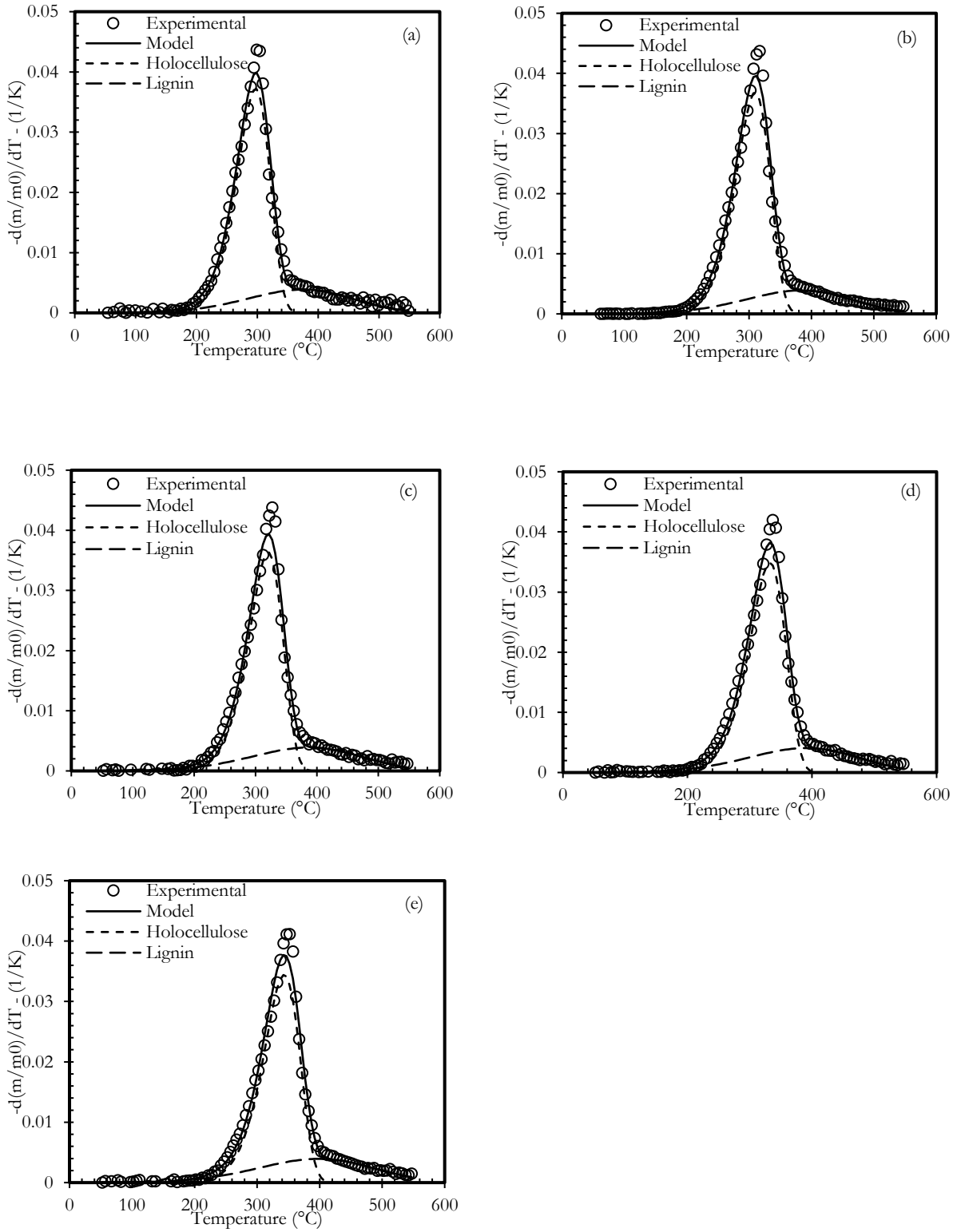

Figure 3-19: Kinetic evaluation of 10 mg of kanuka wood chips of particle size ≤ 90 microns at five heating rates of (a) 1, (b) 2.5, (c) 5, (d) 10 and (e) 20 K/min, assuming three parallel independent first order reactions

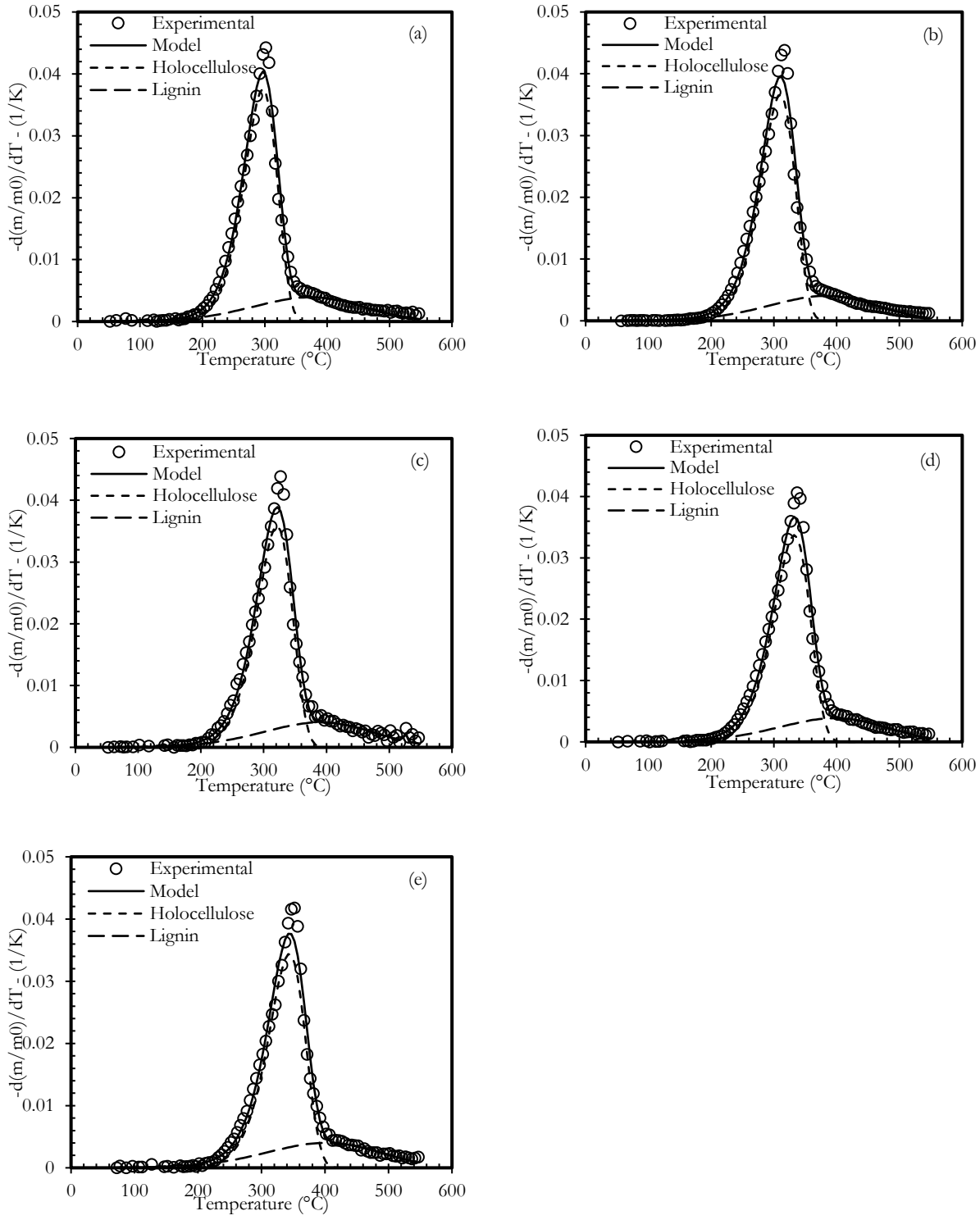

Figure 3-20: Kinetic evaluation of 15 mg of kanuka wood chips of particle size ≤ 90 microns at five heating rates of (a) 1, (b) 2.5, (c) 5, (d) 10 and (e) 20 K/min, assuming three parallel independent first order reactions

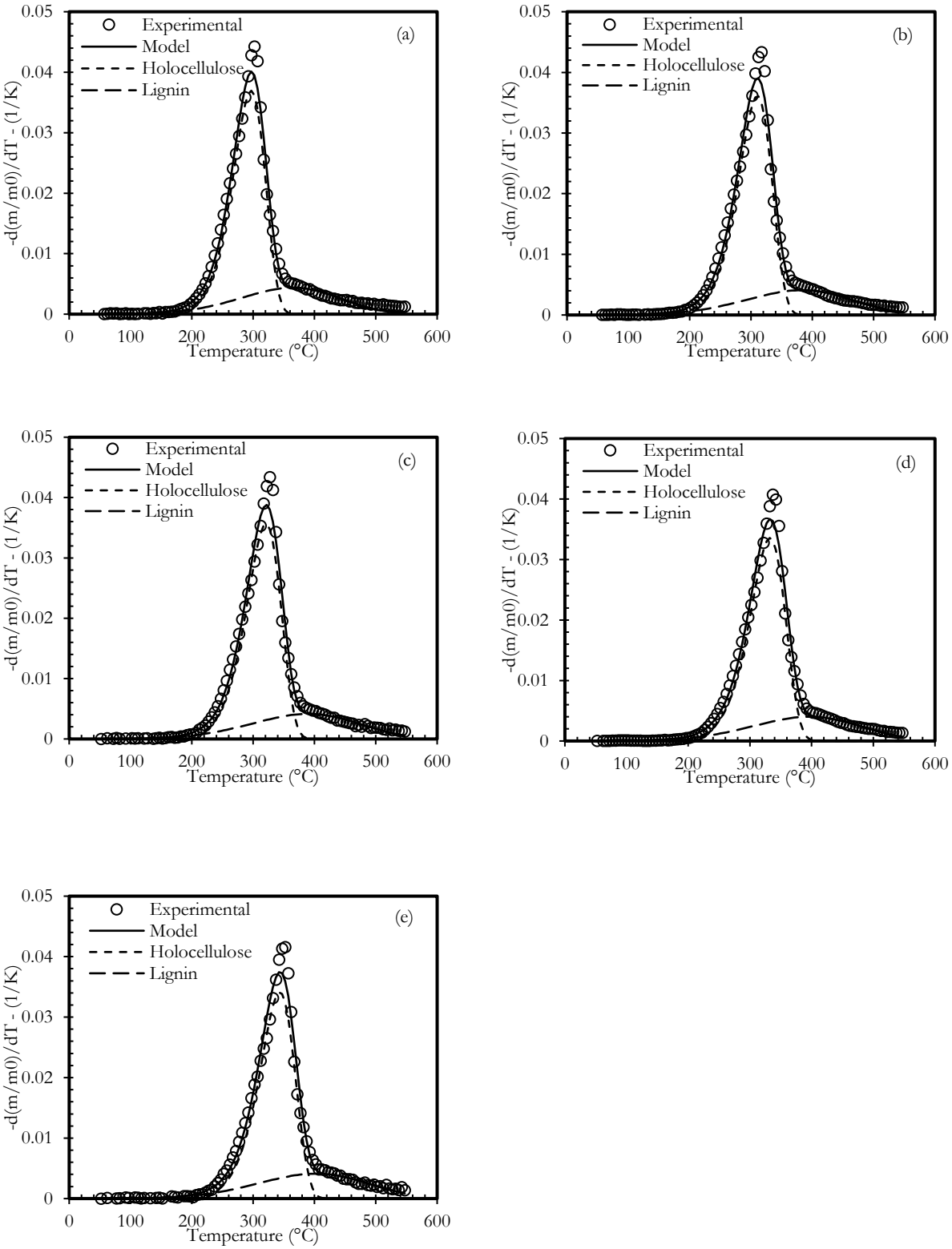

Figure 3-21: Kinetic evaluation of 20 mg of kanuka wood chips of particle size ≤ 90 microns at five heating rates of (a) 1, (b) 2.5, (c) 5, (d) 10 and (e) 20 K/min, assuming three parallel independent first order reactions

3.4 Implications for smoke Generator Design and Operation

These insights have critical implications for designing and operating smoke generators, where controlled pyrolysis is essential to achieve a desirable aroma profile. Within a production environment this means controlling the temperature of pyrolysis and the extent of secondary reactions by influencing the factors that affect local pressure within particles and the bed and the residence time of the volatiles before they leave the bed.

Smoke generators have a few levers that can be used to control temperature, pressure and residence time. These are the method of heating, the proximity of the heat source to the particles, the size of the particles, the interstitial porosity between particles, the transit distance between the volatile generation points and escape from the bed and the relative direction of mass and heat transfer, nothing that the method of heating may be direct e.g., hot gas (superheated steam) or indirect from a radiant surface. Of these levers, the operating parameters are the rate of heat input and highest treatment temperature and the particle size which determines the interstitial porosity. The rest are design parameters of the smoke generator, noting also that particle residence time in the smoker can also be controlled, because once volatiles have been generated, the particles are not making a productive contribution to smoke generation. It is also possible that bed height, i.e., the transit distance between the volatile generation points and escape from the bed can also be manipulated using an adjustable weir or like.

When designing a smoke generator that uses fine particles, attention must be given to the potential for volatile flooding and pressure build-up. Elevated pressures in a packed bed can lead to uneven heating, excessive char formation and potentially uncontrolled release of volatiles, which may not only compromise the quality of the smoke but also pose safety risks.

To mitigate these effects, smoke generator designs may need to incorporate mechanisms for pressure regulation, such as adding a vacuum or optimising particle bed thickness to enhance permeability. Alternatively, the use of larger particles may be preferred to avoid excessive pressure build-up. However, larger particles might require a higher initial energy input to reach the decomposition temperature uniformly, which could impact the energy efficiency of the smoker.

Moreover, the self-heating effect observed in smaller particles under high-pressure conditions could lead to an unpredictable aroma profile. In smoke generation, the quality of the smoke is closely tied to the stable decomposition of wood components, particularly hemicellulose, cellulose and lignin, which release specific compounds responsible for aroma. If pressure fluctuations cause irregular pyrolysis, the resulting smoke may lack consistency and may even produce unwanted by-products, impacting the flavour and toxicology profile of smoked food.

3.5 Conclusion

This chapter delved into the pyrolysis kinetics of kānuka wood chips under inert atmospheric conditions. The findings underscore the significant influence of particle size on both char yield and decomposition behaviour. Notably, smaller particles (≤ 90 μm) had higher char yields compared to larger particles (90-600 μm). This result is attributed to the reduced bed permeability inherent with finer particles, which impedes the escape of volatile decomposition products. The restricted volatile release increases the pressure and hence the residence time of gases within the reaction zone, promoting secondary reactions that enhance secondary char formation. This observation is explained by the Kozeny-Carmen equation (Section 5.4.5), which relates permeability to particle diameter and bed porosity, and is supported by previous work by other researchers.

The thermal decomposition characteristics, as revealed by the differential thermogravimetric (DTG) curves, exhibited distinct patterns based on particle size. Larger particles displayed three separate peaks corresponding to the decomposition of hemicellulose, cellulose and lignin. In contrast, smaller particles showed only two peaks, with the hemicellulose and cellulose peaks overlapping. This difference is likely due to elevated local pressures and enhanced secondary reactions in beds of fine particles, which alter the decomposition pathways and thermal profiles (to be discussed in detail in chapter 5).

Kinetic parameters were determined using model-based methods. In the model-based approach, mutli-component reaction model was employed, fitting the TGA data to three independent reactions for larger partciles and two for smaller particles. The activation energies obtained for hemicellulose (~120 kJ/mol), cellulose (~190 kJ/mol) and lignin (~54 kJ/mol) were consistent with literature values.

This study also explored the impact of heating rate and sample mass on the kinetic parameters. Higher heating rates generally resulted in increased activation energies due to thermal lag and

reduced time for thermal equilibrium within the samples. Larger sample masses exhibited slightly higher activation energies, possibly due to heat transfer limitations with the bulk material. These observations are in agreement with established pyrolysis literature (Vyazovkin, 2000), confirming the accuracy of the experimental design and analytical methods.

From a practical standpoint, these findings have significant implications for the design and operation of smoke generators and pyrolysis systems. Controlling particle size and hence bed permeability emerge as critical factor in influencing char yield and therefore volatile release during smoke generation. For applications aiming to maximise volatile production – such as culinary food smoking or syngas generation in a gasification system – optimising particle size to enhance bed permeability is crucial. Conversely, for applications where higher char yield is desired, utilising smaller particles may be advantageous due to their propensity to promote secondary char forming reactions.

CHAPTER 4

Effects of Operating Parameters on the Aroma Profile of Kānuka Wood Chips

4.1 Introduction

The unique aroma profile of wood smoke has attracted increasing interest from researchers and industries, including those in the food and beverage sectors. Despite this interest, the relationship between pyrolysis conditions and the composition of the aroma-active volatiles from kānuka wood remains poorly understood and a systematic investigation of this relationship is yet to be conducted.

This chapter aims to address this gap by providing a detailed, temperature-resolved analysis of the compounds responsible for the distinctive aroma of kānuka wood smoke. The thermal decomposition and volatile aroma profile of kānuka wood smoke were investigated across a wide range of pyrolysis temperatures using pyrolysis-gas chromatography/mass spectrometry (Py-GC/MS) and pyrolysis-evolved gas analysis/mass spectrometry (Py-EGA/MS). Py-GC/Ms was employed to characterise the volatile organic compounds (VOCs) produced during pyrolysis and to evaluate how the chemical composition of the smoke evolves with increasing temperature. The high-resolution data obtained from this technique allowed for the identification of key aroma-active compounds and their relative contributions to the overall profile. To complement these findings, Py-EGA/MS was utilised to study the thermal release pattern of selected compounds of interest. This method provided critical insights into the chemical kinetics and mechanistic pathways associated with the formation and degradation of these compounds under varying thermal conditions.

The integration of these two analytical approaches enables a comprehensive understanding of the thermochemical processes driving the generation of kānuka smoke's aroma-active constituents.

These findings not only improve our understanding of the thermal decomposition of kānuka wood but also offers a scientific basis for optimising smoke generation processes for industrial applications.

4.2 Experimental

To analyse the smoke flavour and aroma markers of kānuka wood smoke, pyrolysis-gas chromatography-mass spectrometry (Py-GC/MS) and evolved gas analysis-mass spectrometry (EGA-MS) were employed using Frontier Laboratories Multi-shot Pyrolyser (EGA/PY-3030D) coupled with a Shimadzu gas chromatograph-mass spectrometer (GCMS-QP2010 Ultra).

4.2.1 Py-GC/MS analysis

For Py-GC/MS analysis, 2.5-3 mg of kānuka wood samples were introduced into the pyrolyser at specified temperatures ranging from 200°C to 500°C (in increments of 10°C). Each sample was pyrolysed for 4 minutes, with helium as the carrier gas. The pyrolyser interface and GC injection port temperatures were maintained at 325 °C. The GC analysis was conducted in split mode with a split ratio of 1:150 and a column flow rate of 1.0 mL/min, operating under linear velocity control mode at 26.1 cm/s.

A Shimadzu SH-Rxi-5ms capillary column (30 m length, 0.25 mm ID, 0.25 μm film thickness) with a stationary phase of 5% diphenyl, 95% dimethylpolysiloxane was utilised to separate the pyrolysates. GC oven temperature increases from 40 to 320 °C at a heating rate of 10 K/min. The MS interface temperature was set to 250°C, and the ion source was maintained at 230°C. The electron energy was adjusted to 70 eV, with a mass scan range of m/z 50-550. Compound identification was performed using Shimadzu MS Solution software and AMDIS (Automated Mass Spectral Deconvolution and Identification System, NIST) with retention indices compared to the NIST11 Library. Relative peak areas were calculated as a proportion of the total detected peak area to enable comparison of volatile compounds across temperatures.

4.2.2 EGA-MS Analysis

For EGA-MS analysis, 1.0-1.5 mg of kānuka wood samples were gradually heated from 70°C to 500°C at a constant rate of 10°C/min. The same Frontier Laboratories Multi-shot Pyrolyser and Shimadzu GC-MS system were used, but with an EGA tube (UADTM-2.5N) serving as the GC column (2.5 m length, 0.15 mm ID, no stationary phase). The interface, GC injection port and oven temperatures were maintained at 300°C. To minimize fragmentation, the electron energy was reduced to 20 eV. Selected ion chromatograms (EICs) were extracted from the total ion chromatograms (TICs), focusing on ions identified as significant contributors to the total signal and linked to sensory properties of smoke flavour.

In the Evolved Gas Evolution analysis (EGA).

- The total ion chromatogram (TIC) represents the summed intensity of all the detected ions at each scan event corresponding to sample temperature.
- The extracted ion chromatogram (EIC) highlights specific ions contributing to the TIC.

4.2.3 Proximate analysis using TG-DSC

A proximate analysis of kānuka wood was conducted using a Netzsch STA 449 F1 Jupiter® Simultaneous Thermal Analyser (TG-DSC) following ASTM E113-08 standards (International, ASTM, 2014). Oven-dried, finely milled sawdust samples (~5.5 – 6 mg) were loaded into Pt-Rh crucibles lined with thin-walled alumina liners (6.8 mm outer diameter, 85 μL volume). The sawdust was compacted using a metal rod slightly smaller in diameter than the liner.

The analysis was carried out under a nitrogen atmosphere with:

- Purge gas flow: 50 mL/min
- Protected gas flow for balance: 20 mL/min

The heating protocol included:

1. Heating to 105°C and holding for 1 hour to eliminate residual moisture.
2. Gradual heating to 900°C at 5°C/min.
3. Post-900°C, the purge gas was switched to air to burn off remaining combustible matter in the crucible, leaving behind the ash.

This analysis provided insight into the moisture content, volatile matter, the fixed carbon and the ash content of the wood.

4.2.4 Quantification and kinetic modelling of volatile formation

In the EGA-MS analysis, the total ion chromatogram (TIC) represents the summed intensity of all detected ions at each scan events, corresponding to the sample temperature. To investigate the formation of specific compounds, extracted ion chromatograms (EICs) are used to highlight the evolution of ion fragments. The analysis of this EIC data was performed by de-convolving overlapping peaks and subsequently deriving quantitative and kinetic parameters from the temperature-dependent intensity data, which is proportional to the rate of volatile evolution.

For all calculations, the temperature data, initially recorded in °C, was converted to Kelvin (K). The experimental heating rate (β), set at 10 °C/min, was converted to K/s for kinetic modelling. To address potential numerical issues arising from varying signal magnitudes and to standardise the data for modelling, the raw EIC intensity was normalised by its maximum value (Appendix 1.1), yielding a dimensionless signal ranging from 0 to 1.

4.2.4.1. Peak deconvolution

Peak deconvolution is essential for resolving overlapping evolution profiles, which appear in biomass pyrolysis from the concurrent degradation of its primary components (hemicellulose, cellulose and lignin) and potentially secondary reactions. The normalised intensity is modelled as a sum of N Gaussian functions, where each function corresponds to an individual decomposition event:

$$I_{norm}(T) = \sum_{i=1}^{N} \alpha_i \exp\left(-\frac{(T-\mu_i)^2}{2\sigma_i^2}\right) \quad (4.2)$$

Here, for each peak I, (α_i) is the amplitude, (μ_i) is the mean temperature (peak centre in °C), and (σ_i) is the standard deviation (controlling peak width). The number of peaks, N, was determined based on initial estimates of peak positions. Gaussian functions are employed as they effectively approximate the symmetric shapes observed in EGA curves, providing a good basis for separating multi-stage thermal decomposition processes.

The model parameters (α_i,μ_i, σ_i) were optimised using a non-linear least squared fitting. To ensure a physically plausible solution, initial parameter estimates and bounds were established. Initial amplitudes were derived from the normalised intensity near the anticipated peak centres, means were set to the estimated positions and an initial width of 20 °C was used. Constrains were applied to bound amplitudes between 0 and 2 (2x the maximum), means to within ±30 °C of their initial estimates and standard deviations between 5 °C and 100 °C. This optimisation yields the refined parameters for each de-convoluted peak and the composite fitted curve.

Polycyclic aromatic hydrocarbons (PAHs) were among the most important compound classes of interest due to their well-documented carcinogenicity. However, the methodology and instrumentation employed in this study were not sufficiently sensitive to detect PAHs, as their concentrations fell below detection limits.

4.2.4.2. Kinetic modelling of volatile formation

Kinetic parameters for each de-convolved peak were determined using the Coats-Redfern integral model-fitting method (Coats and Redfern, 1964), which is well-suited for non-isothermal data. This

approach assumes first-order reaction kinetics (n=1), a common and effective approximation for the thermal decomposition of biomass pseudo-components.

For each individual peak i, the conversion fraction, (α_i), is determined as the normalised cumulative integral of its de-convolved intensity profile:

$$\alpha(T) = \frac{\int_{T_0}^{T} I_i(T')dT'}{\int_{T_0}^{T_e} I_i(T')dT'} \tag{4.3}$$

This calculation, performed numerically, yields an (α) value that progresses from 0 to 1, quantifying the fraction completion of volatile release for that specific sub-process.

The Coats-Redfern method linearises the integrated form of the Arrhenius rate equation. For a first-order reaction, this is expressed as:

$$\ln\left(\frac{-ln(1-\alpha)}{T^2}\right) = \ln\left(\frac{AR}{\beta E_a}\right) - \frac{E_a}{RT} \tag{4.4}$$

where (E_a) is the activation energy (J/mol), (A) is the pre-exponential factor (s^{-1}) and (R) is the universal gas constant (8.314 J/mol K). To ensure the validity of the approximation, the linear regression was performed on data points within the conversion ranged of $0.05 < \alpha < 0.95$. By fitting ($y = \ln\left(-\frac{ln(1-\alpha)}{T^2}\right)$) against ($x = 1/T$), the activation energy is derived from the slope ($m = -E_a/R$) and the pre-exponential factor is derived from the intercept ($c = \ln\left(\frac{AR}{\beta E_a}\right)$). The quality of the linear fit for each kinetic determination was assessed by the coefficient of determination (R^2). This methodology provides key kinetic parameters (E_a and A) for each distinct volatile formation step identified during deconvlution.

4.3 Results & Discussion

This section details the influence of temperature on the aroma profile of kānuka wood smoke and formation pathways of key aroma compounds.

4.3.1 Characterisation of kānuka wood

Proximate and ultimate analyses provide essential information on the composition and properties of the kānuka wood chips, which influence its thermal behaviour. In this study, the proximate and ultimate analysis results for kānuka wood chips are presented in table 4-1.

4.3.1.1 Proximate analysis

The volatile matter content of kānuka wood was found to be 80%, which is at the higher of the range reported for various wood species. For instance, (Reina, et al., 1998) reported values of volatile matter ranging from 70% to 80% for different types of wood. Similarly (Mallick, Barbhuiya and Banik, 2019) and (Surahmanto *et al.*, 2017) observed volatile matter contents of around 63% to 70% in their study of biomass pyrolysis kinetics. A high volatile matter content is indicative of a biomass that releases a significant amount of volatiles upon heating, which is beneficial for smoke generation.

The fixed carbon content of kānuka wood was measured at 17.29%, which is also on the higher side compared to other woody biomasses. Some authors (Chen, Zhou and Zhang, 2014; Daouk *et al.*, 2018) reported fixed carbon contents ranging from 15% to 20% for various hardwood species. A higher fixed carbon content suggests that kānuka wood has a substantial amount of carbon remaining after volatile substances are released, contributing to production of bio-char during pyrolysis (Grønli, 1996).

Table 4-1 compares the proximate and ultimate analysis of kānuka wood chips used in this study with literature values reported by Wright (2021) for the same species. Overall, the elemental composition and thermochemical properties of the experimental feedstock align closely with the

literature, confirming the general consistency of the kānuka species used in this work. The carbon (50.12% vs. 50.56%), nitrogen (0.20% vs. 0.21%) and overall volatile matter (81.94% vs. 80.84%) show good agreement.

Minor deviation are observed in the hydrogen content (7.61% vs. 6.37%) and ash content (0.40% vs.0.77%). These slight variations are well within the expected natural heterogeneity of biomass which is heavily influenced by environmental factors such as the age of the tree, location, soil composition and the proportion of heartwood to sapwood and bar in the specific batch.

Table 4-1: Proximate and ultimate analysis of kānuka wood on a dry weight basis (wt. %), comparing the experimental feedstock with literature values from Wright (2021). Oxygen values are calculated by difference (100 - C - H - N - S - Ash).

	Component	*Kānuka (%)*	*Wright (2021)*
Proximate Analysis	**Volatile Matter**	81.94 ± 1.76	80.84±0.09
	Fixed Carbon	17.71 ± 0.88	18.4±0.38
	Ash	0.40 ± 0.07	0.77±0.38
Ultimate Analysis	**Carbon**	50.12 ± 0.03	50.56±0.40
	Hydrogen	7.61 ± 0.53	6.73±0.43
	Nitrogen	0.20 ± 0.02	0.21±0.02
	Sulphur	Not detected	0.02±0.04
	Oxygen*	41.67 ± 0.53	42.85±0.49

The ash content of 0.40%, which is at the lower end of the typical range reported for woody biomass (Kasparbauer, 2009). Ash contents in wood generally range from 0.2% to 2% (Vassilev, et al., 2010). The low ash content is advantageous for a continuous smoke generator as it minimises issues related to slagging, fouling and other problems with smoke generators and even gasifiers (Parthasarathy and Narayanan, 2019).

4.3.1.2 Ultimate analysis

The carbon content of kānuka wood was determined to be ~49%, which is consistent with values reported for other hardwood species, typically ranging from 45% to 50% (Demirbas, 2004). The hydrogen content was measured at ~7.7%, which is slightly higher than the typical range of 6% to 7% for woody biomass (Daouk *et al.*, 2018). Higher hydrogen content can contribute to a higher heating value, enhancing the energy potential of the biomass but also potentially making it more difficult to control temperature (Parikh, et al., 2005).

The nitrogen content was found to be 0.2%, which is within values reported in literature (Antal and Grønli, 2003). Low nitrogen content is desired in a smoke generator, as it leads to lower potential emissions of nitrogen oxides (NO_x) in the event of high temperature combustion (Koppejan, 2016). The sulphur levels were below the detection levels (<0.01%), which is typical for wood biomass and advantageous for preventing sulphur dioxide (SO_2) formation (Antal and Grønli, 2003).

The oxygen content, calculated by difference was ~43.2%. High oxygen content is characteristic of biomass and influences the combustion and gasification processes by affecting the energy content and combustion efficiency (Koppejan, 2016).

4.3.2 Effect of residence time

The effect of residence time of wood in the pyrolyser was investigated to determine the optimal residence time that would give the most informative results while minimising experimentation time. Initially, the residence time was incrementally increased from 1 to 16 minutes (Figure 4-1). It was observed that this change led to a marked narrowing and better differentiation (Refer to Figure 4-1, points A, B, C, and D, where there appears to be a merging or lack of differentiation at 1-minute residence time) of the chromatographic peaks. Such behaviour can be attributed to the completion of primary pyrolysis reactions and the commencement of secondary reactions, which generally involve further cracking of complex molecules into smaller, more volatile components (Bridgwater,

Meier and Radlein, 1999). As these primary and secondary products have different volatilities and thermal stabilities, their separation and resolution become evident under optimised residence times. Extending the residence time beyond 4 minutes did not result in any significant alterations to the chromatogram. This plateau effect can be interpreted as the stabilisation of pyrolysis dynamics where most of the reactive biomass constituents have undergone substantial thermal decomposition and the system possibly reaches a quasi-equilibrium state (Mohan, Pittman and Steele, 2006).

Similar observations have been reported in the literature. Faix *et al.* (1991) conducted Py-GC/MS studies on the pyrolysis of various wood species, including beech and spruce. They found that increasing the residence time improved the resolution of chromatographic peaks due to more complete volatilisation and decomposition of biomass constituents. Their research aimed to enhance analytical methods for lignocellulose materials by optimising pyrolysis conditions to achieve better separation and identification of pyrolysis products.

In another study, Pastorova *et al.* (1994) investigated the pyrolysis of cellulose using Py-GC/MS and observed that longer residence times allowed for the formation and detection of additional low-molecular-weight compounds such as furans and cyclopentenones. This was attributed to secondary cracking reactions of primary pyrolysis products. Their work highlighted the importance of residence time in influencing the product distribution and improving the analytical resolution of complex mixtures derived from biomass.

Meir and Faix (1992) reviewed the analytical pyrolysis of lignin and lignocellulosic materials, emphasizing that residence time is a critical parameter in Py-GC/MS analysis. They noted that too short a residence time may result in incomplete pyrolysis and broader peaks due to overlapping compounds.

These findings show that getting the residence time right is key in pyrolysis studies. Choosing the best residence time helps get clearer analytical results and makes the data reflects real-world

pyrolysis conditions. It also helps avoid wasting energy and time in experiments, making the research more efficient overall. The residence time of 4 minutes was chosen for subsequent samples because it represents a practical balance, providing sufficient time for significant pyrolysis reactions to occur and for the development of a differentiated chromatographic profile, yet avoiding unnecessary prolongation that does not yield additional insights. This duration is also more aligned with real-world smoking applications, where longer residence times are common due to the nature of traditional smoking processes. By selecting a residence time that mirrors more closely practical conditions, our findings become more applicable to industrial and artisanal smoking processes, enhancing the relevance and applicability of this study.

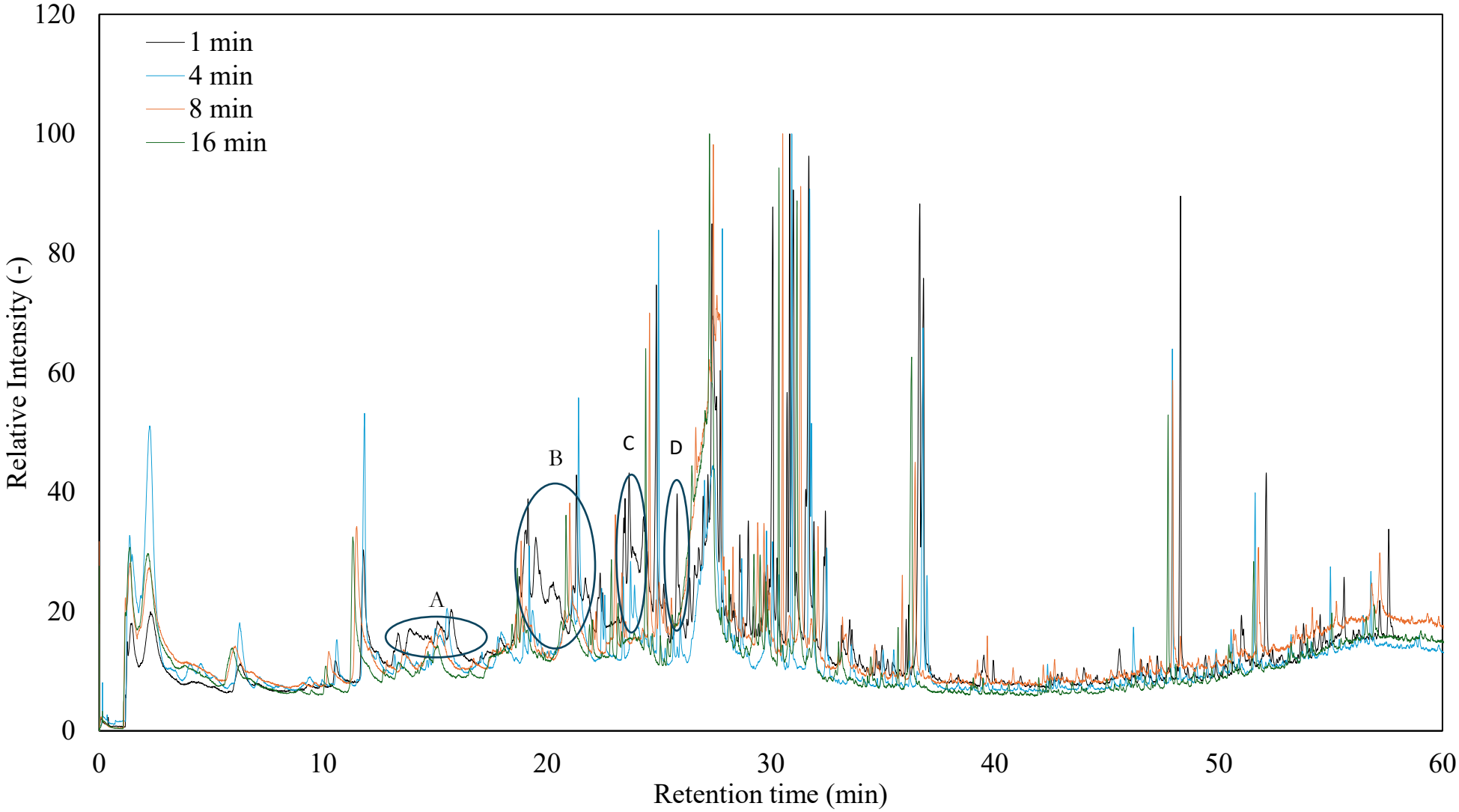

Figure 4-1: Effects of residence time on the chromatogram of kānuka wood pyrolysis at 10 K/min heating rate from a temperature of 40-320°C

4.3.3 Effect of temperature on aroma profile

Py-GC/MS analysis of kānuka wood identified 186 volatile organic compounds (VOCs) across a temperature range of 200-520 °C. This covers a detailed profile of the thermal decomposition products. Table 4-2 classifies these compounds by chemical group showing the compositional range of kānuka wood smoke.

Key VOCs include phenolics such as guaiacol derivatives (e.g., 4-vinylguaiacol) creosol and syringol which dominate the profile due to lignin decomposition. Furfural an aldehyde formed from hemicellulose break-down (dehydration of pentose sugars in hemicellulose) (Pavlath and Gregorski, 1988; Meng *et al.*, 2017; Ye *et al.*, 2021; Ndao *et al.*, 2025) and acetic acid (formed from the cleavage of acetyl groups in hemicellulose) are also significant. Their abundance highlights their role in defining the sensory aroma attributes of kānuka smoke, with phenolics contributing substantially to the identified volatiles.

The phenolic class comprising of 47 compounds, consists mainly of methoxyphenols such as syringol and creosol, derived from the thermal fragmentation of lignin's syringyl and guaiacyl units. The most significant aldehyde in terms of contribution to aroma include the compounds furfural and 5-hydroxymethylfurfural (5-HMF). Ketones are also an abundant class of compounds identified which include the compound furylhydroxymethyl ketone. In total, 14 aldehydes and 8 ketones were identified. Both arise from carbohydrate depolymerisation in hemicellulose and cellulose (Di Blasi, Branca and Galgano, 2010; Werner, Pommer and Broström, 2014; Chen *et al.*, 2017). Acetic acid is the most abundant acid identified and at lower temperatures it is known to form from the de-acetylation of hemicellulose. Alcohols and lactones were also identified, such as furfurly alcohol and 5-methyl-2(3H)-furanone. These indicate cellulose decomposition (Pavlath and Gregorski, 1988). Nitrogen-containing compounds of which a total of 44 were identified. These include amines, amides and heterocycles – likely originating from minor proteinaceous material or Maillard reactions induced by pyrolysis conditions.

Other abundant VOCs that were identified include non-condensable hydrocarbons (10 compounds), sulphur-containing compounds (7) and miscellaneous compounds grouped this way for simplicity as they range in functional groups from esters to fused heterocycles (27 compounds).

Table 4-2: The total number of unique compounds that were identified from the chromotographs of kānuka wood chips pyrolysed from 200-520°C at 4 mins residence time and 3 mg sample mass

No.	*Chemical Class*	*Compound Name*
1	Acids	Acetic acid
2		Decanoic acid
3		Formic acid hydrazide
4		Homovanillic acid
5		3-Hydroxy-4-methoxybenzoic acid
6		Propanoic acid, anhydride
7		Tetradecanoic acid
8	Aldehydes	3-Furaldehyde
9		Benzaldehyde, 3-hydroxy-, oxime
10		Benzaldehyde, 3-hydroxy-4-methoxy-
11		Benzaldehyde, 3-methoxy-, oxime
12		Benzaldehyde, 4-hydroxy-3,5-dimethoxy-
13		Furfural
14		4-Hydroxy-2-methoxycinnamaldehyde
15		1H-Imidazole-2-carboxaldehyde
16		1H-Imidazole-4-carboxaldehyde
17		1H-Pyrrole-2-carboxaldehyde
18		1H-1,2,3-Triazole-4-carboxaldehyde
19		5-methyl-2-furaldehyde
20		2,5-Furandicarboxaldehyde
21		2,5-Dihydroxybenzaldehyde
22		5-Hydroxymethylfurfural
23		5-Acetoxymethyl-2-furaldehyde
24	Ketones	2-Butanone, 3-methoxy-3-methyl-
25		2-Acetyl-2-methyltetrahydrofuran
26		Furyl hydroxymethyl ketone
27		Ethanone, 1-(2,5-dihydroxyphenyl)-
28		Ethanone, 1-(2-furanyl)-
29		Ethanone, 1-(3-hydroxy-4-methoxyphenyl)-
30		Ethanone, 1-(4-hydroxy-3,5-dimethoxyphenyl)-
31	Alcohols	Ethanol
32		furfuryl alcohol
33		1H-Imidazole-1-ethanol, .alpha.,2-diphenyl-
34		Propargyl alcohol
35		5-((5R,8aR)-8-Butyloctahydroindolizin-5-yl)pentan-2-ol
36		dihydrosinapyl alcohol
37		(E)-3-(4-hydroxy-3-methoxyphenyl)prop-2-en-1-ol
38		DL-2,3-Butanediol
39		1,3-Dioxolane-2-methanol
40		3-Furanmethanol

41	Aromatic	Furan
42	heterocycle	Furan, 2-methyl-
43	Lactone	5-methyl-2(3H)-furanone
44		2(3H)-Furanone
45		2H-Pyran-2-one, 5,6-dihydro-6-pentyl-
46	Enone	Levoglucosenone
47	Pyrone	Maltol
48		4H-Pyran-4-one, 3,5-dihydroxy-2-methyl-
49		3,6-Dimethyl-4H-furo[3,2-c]pyran-4-one
50	Anhydride	2H-Pyran-2,6(3H)-dione
51	Aromatic hetercycle	Naphtho[2,1-b]furan
52	Non-condensable	Carbonyl sulfide
53	hydrocarbon	Chloromethane
54		Cyclopropane, 1-chloro-1-methyl-
55		Methane, nitroso-
56		Methanethiol
57		Neopentane
58		Nitrogen dioxide
59		3-Penten-1-yne, (Z)-
60		Propane, 2-methyl-1-nitro-
61		Propane, 2-methyl-2-nitro-
62	Phenols	Phenol, 2-methyl-
63		m-cresol (3-methylphenol)
64		Phenol, 2,4-dimethyl-
65		Phenol, 2,5-dimethyl-
66		Phenol, 2,6-dimethyl-
67		Phenol, 3,4-dimethoxy-
68		Phenol, 2-methoxy-4-vinyl- (4-vinylguaiacol)
69		2-Methoxy-5-methylphenol (creosol)
70		Phenol, 2,6-dimethoxy- (syringol)
71		Phenol, 2,6-dimethoxy-4-(2-propenyl)- (4-allylsyringol)
72		4-methylsyringol (2,6-dimethoxy-4-methylphenol)
73		3-Allyl-6-methoxyphenol
74		Eugenol
75		trans-Isoeugenol
76		Apocynin (acetovanillone)
77		Mequinol (4-methoxyphenol)
78		Catechol
79		1,2-Benzenediol, 4-methyl- (4-methylcatechol)
80		1,2,3-Benzenetriol (pyrogallol)
81		Benzaldehyde, 2,4-dihydroxy- (2,4-dihydroxybenzaldehyde)
82		3,5-Dimethoxy-4-hydroxycinnamaldehyde (sinapaldehyde)
83		2-Propenal, 3-(4-hydroxy-3-methoxyphenyl)- (coniferaldehyde)
84		Phenol, 4-(ethoxymethyl)-2-methoxy-
85		2-Naphthalenol, 3-methoxy-
86		7-Methoxy-1-naphthol
87		(-)-Nortrachelogenin
88		4,4'-Dihydroxy-3,3'-dimethoxystilbene
89		Desaspidinol
90		2,4-Dihydroxy-6-propylbenzoic acid

91		1-(2,4-Dihydroxyphenyl)-2-(4-methoxy-3-nitrophenyl)ethanone
92		Phenanthrene, 3-methoxy-
93		3-Hydroxy-2-(3-hydroxy-4-methoxyphenyl)-7-methoxy-4H-chromen-4-one
94		4H-1-Benzopyran-4-one, 2-(3,4-dimethoxyphenyl)-7-hydroxy-
95		4H-1-Benzopyran-4-one, 3-(3,4-dimethoxyphenyl)-6,7-dimethoxy-
96		4H-1-Benzopyran-4-one, 5-hydroxy-6,7-dimethoxy-2-phenyl-
97		4H-1-Benzopyran-4-one, 6,7-dimethoxy-3-phenyl-
98		Pectolinaringenin
99		2-(4-Hydroxyphenyl)-3,6,8-trimethoxy-5-hydroxy-4H-1-benzopyran-4-one
100		2',5,8-Trimethoxyisoflavone
101		5,6,8,3',4'-Pentahydroxy-7-methoxyflavone
102		5,6,8,4'-Tetrahydroxy-7-methoxyflavone
103		6H-Dibenzo[b,d]pyran-6-one, 7,9-dihydroxy-3-methoxy-1-methyl-
104		Xanthen-9-one, 1,3,5,8-tetrahydroxy-
105		Anthraquinone, 1,4,5,7-tetrahydroxy-2-methyl-
106		7-Acetyl-3-(diacetylmethyl)-6-hydroxy-2,5-dimethylbenzofuran
107		2-Pentanone, 1-(2,4,6-trihydroxyphenyl)
108		1-Butanone, 1-(2,4,6-trihydroxy-3-methylphenyl)-
109	Sulfur-Containing	Methanethiol
110		Carbonyl sulfide
111		S-Methyl pentanethioate
112		S-Methyl 3-methylbutanethioate
113		2,3-dimethyl-5-[(methylthio)propyl]pyrazine
114		Disulfide, methyl (methylthio)phenylmethyl
115		Bis(2-methyl-4,5-dihydro-3-furyl) Disulfide
116	Other	1,3,5-Trioxepane
117		1,3-Dioxolane
118		1,2,5-Oxadiazole
119		2,2-Diethyl-2-sila-1,3-dioxacyclohexane
120		2,2,3,3,4,4-Hexamethyltetrahydrofuran
121		Propane-1,1-diol dipropanoate
122		Oxalic acid, allyl butyl ester
123		Oxalic acid, dicyclobutyl ester
124		Oxalic acid, cyclobutyl hexyl ester
125		2-Butenoic acid, 2-methoxy-, methyl ester, (Z)-
126		Fumaric acid, dipropargyl ester
127		2-Propenoic acid, ethenyl ester
128		2-Propenoic acid, 3-phenyl-, phenyl ester, (E)-
129		2-Propenoic acid, 3-phenyl-, 4-methylphenyl ester
130		1,2,4,5-Tetrazine
131		1,2,4-Triazolo[4,3-b]pyridazin-6(5H)-one
132		Phthalic anhydride
133		Diethyl Phthalate
134		3,7-Dimethyl-2,3,3a,4,5,6-hexahydro-1-benzofuran #
135		6-Methoxy-3-methylbenzofuran

136		Naphtho[2,1-b]furan
137		Benzo[b]thiophene, 2-ethyl-
138		3(4H)-Dibenzofuranone, 4a,9b-dihydro-6-(6-hydroxy-m-tolyl)-8,9b-dimethyl-
139		2,3,4-Trimethoxydibenzofuran
140		4-Methylene-3,4-dihydroisocoumarin
141		6H-Dibenzo[b,d]pyran-6-one, 7,9-dihydroxy-3-methoxy-1-methyl-
142		3,6-Dimethyl-4H-furo[3,2-c]pyran-4-one

Temperature-dependent trends mirror those found in hardwood pyrolysis (González-Vila *et al.*, 2001; Kasparbauer, 2009; Lingbeck *et al.*, 2014; Vazquez, 2022) with lignin breakdown starting early (≤200 °C) and continuing throughout, this breakdown typically forms phenolic compounds. Hemicellulose and cellulose typically produce acids, aldehydes, ketones and furans and starts around ≥220 °C. Kānuka wood smoke appears to be rich in phenolic compounds such as guaiacol and creosol, which contribute spicy-woody aromas and syringol contributes some sweet smokiness; vanillin-like aldehydes (e.g., 3-hydroxy-4-methoxybenzaldehyde) add vanilla notes to the profile. Subsequent sections will examine temperature-dependent yields, sensory impacts as well as the formation mechanisms in more detail.

4.3.3.1 Temperature-dependent yields of key VOCs

The relative yields of VOCs from kānuka wood pyrolysis exhibited clear temperature-dependent patterns. This reflects the sequential thermal degradation of its biopolymeric components. hemicellulose at lower temperatures of 200 to 300 °C, cellulose at intermediate ranges of 300 to 400 °C and lignin persisting across the entire span analysed of 200 to 520 °C. This aligns with established pyrolysis kinetic studies (Murugan, Mahinpey, Keith E. Johnson, *et al.*, 2008; G. J. Lv, Wu and Lou, 2010; Park, Atreya and Baum, 2010; Branca and Di Blasi, 2016).

Total VOC peak areas increased substantially from ~0.28 × 10^6 at 200 °C to a maximum of ~55.3 × 10^6 at 500 °C, indicating enhanced volatilisation and potential secondary cracking at peak temperatures (Mohan, Pittman and Steele, 2006; Shen and Gu, 2009). This trend of rapidly

increasing yield of smoke with temperature is consistent with observations made by several researchers studying slow pyrolysis of various wood species. Higher temperature favours gas and liquid product formation over char as more energy is available for bond breaking(Scott, Piskorz and Radlein, 1985).

Table 4-3: Relative contribution (%) of major compound classes across temperature ranges 200-520°C. The data used to produce this table is found in Appendix 1.2.

Compound Class	200–300°C (%)	300–400°C (%)	400–520°C (%)
Phenol	23.7	48	57.6
Furan	6	10	12.9
Aldehyde	40.6	13.3	6.6
Ketone	0.8	6.8	7.6
Acid	16.1	13.7	10.8
Others	12.8	8.3	4.6

Phenolic compounds, the dominant class showed <25% presence below 300 °C but surged to comprise nearly 60% of total peak areas above 400 °C (Table 4-3). For example, 2-methoxy-4-vinylphenol (a guaiacol derivative) was undetectable at low temperatures but reached peak areas exceeding 3.3×10^6 at 500 °C. Similarly, eugenol and 4-methylsyringol (2,6-dimethoxy-4-methylphenol) peaked at 450-520 °C, with areas of around $2.5\text{-}2.6 \times 10^6$. This delayed phenolic release is indicative of lignin decomposition (Grønli, Várhegyi and Di Blasi, 2002b; Lu, Y. C. Lu, *et al.*, 2017). In comparison, studies on eucalypt wood (belonging to the same family as kānuka; Myrtaceae) report analogous temperature driven increases in methoxyphenols but with potentially higher eugenol content due to species specific lignin composition. Kānuka on the other hand produced elevated syringol analogs (e.g., 2,6-dimethoxyphenol at ~2.3×10^6 at 500 °C) suggesting a sweeter smoky profile distinct from eucalypt's more resinous notes (Maleknia, Bell and Adams, 2009).

Furans and aldehydes primarily from hemicellulose and cellulose predominated at 200-350 °C accounting for 30-40% of peak areas. Past around 400 °C (Table 4-3), these compounds started to

diminish, dropping to below 15%. Furfural is typically a hemicellulose decomposition marker, emerged at 210 °C (~0.26 × 10^6) and maximised at 310-350 °C (~1.58 × 10^6), likely via pentose dehydration and possibly started to decline at higher temperature due to thermal instability (Sun *et al.*, 2023). 5-HMF followed a similar trajectory, peaking at around 300-400°C. These trends are like those in pine wood pyrolysis where furan yields peak at moderate temperatures before secondary cracking reduces them. However, kānuka showed lower 5-HMF relative to furfural as compared to softwood smoke, possibly due to its hardwood like hemicellulose structure with fewer hexoses (Gade, 2010). Aldehydes like vanillin and coniferyl aldehyde also increased progressively up to 400-450 °C (~1.1 × 10^6), consistent with lignin side-chain oxidation reaction in biomass pyrolysis (Kawamoto, 2017).

Ketones (e.g., 2-cyclopenten-1-one derivatives) and acids (e.g., acetic acid) showed intermediate peaks at 350-450 °C, making up 15-25% of areas, while alcohols like coniferyl alcohol increases gradually, remaining minor (<10%). Research on the difference of wood species for smoke generation such as hardwoods or fruitwoods shows similar volatile shifts (Yin *et al.*, 2021).

Overall, kānuka's VOC profile resembles that of other hardwoods in temperature dependence, with phenolic compounds dominating at higher temperatures.

4.3.4 Kinetics of key compound formation

The thermochemical breakdown of kānuka wood generates many volatile organic compounds, including odorants, as previously discussed. This section presents the proposed mechanistic formation pathway for the key odorants identified in the smoke of kānuka wood. A kinetic deconvolution approach is employed to dissect the complexity of the evolution profiles, resolving them into constituent kinetic events. This analysis provides a quantitative framework for probing the underlying reaction mechanisms and understanding how processing conditions can shape the final aroma critical to food smoking. They were evaluated by first normalising the raw intensity by the maximum intensity of the same compound.

4.3.4.1 Carbohydrate-Derived (Furfural, 5-Hydroxymethylfurfural, Furfuryl Alcohol)

These compounds are formed from the pyrolysis of the polysaccharide fractions of kānuka wood (hemicellulose and cellulose). They are known to contribute sweet, caramel-like and baked notes which are important for balancing the sharper phenolic character of wood smoke.

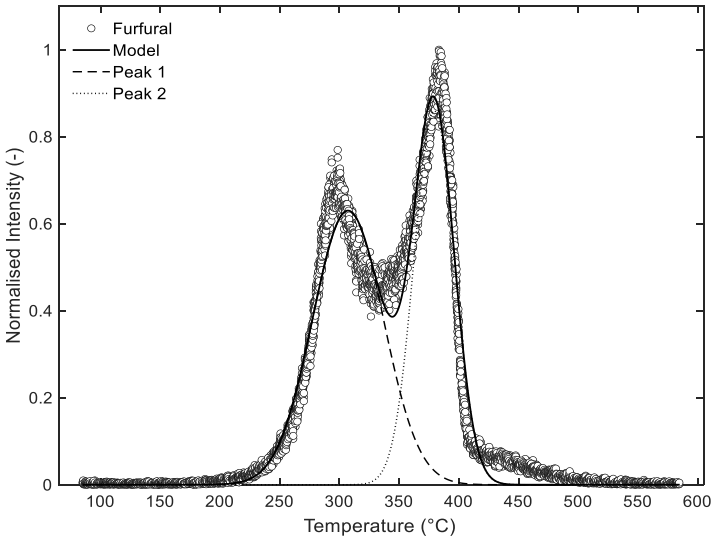

Figure 4-2: Kinetic deconvolution of the Py-EGA-MS evolution profile for furfural (m/z =96) from kānuka wood pyrolysis. Experimental data (circles) are fitted by an overall two-peak (line).

The bi-modal evolution profiles for Furfural (m/z = 96; Figure 4-2) and 5-Hydroxymethylfurfural (5-HMF; m/z = 126; Figure 4-3) during kānuka wood pyrolysis. These profiles, each broken down into two distinct kinetic peaks point to different formation pathways tied to the thermal breakdown of hemicellulose and cellulose in the wood. This type of two-peak pattern is typical of wood (Grønli, Várhegyi and Di Blasi, 2002b). Hemicellulose decomposes at lower temperatures (usually 220-315 °C) (G. Lv, Wu and Lou, 2010) because of its less ordered, branched structure full of five-carbon (C5) sugars like xylose and six-carbon (C6) sugars like mannose. Cellulose, on the other hand, has a more structured chain of β-1,4-linked glucose units (Fengel and Wegener, 1989) and needs higher temperatures, typically above 315 °C to decompose (Antal, Varhegyi and Jakab, 1998). The slow heating rate of 10 °C/min used in these experiments helps separate these overlapping processes, which might blend at faster rates.

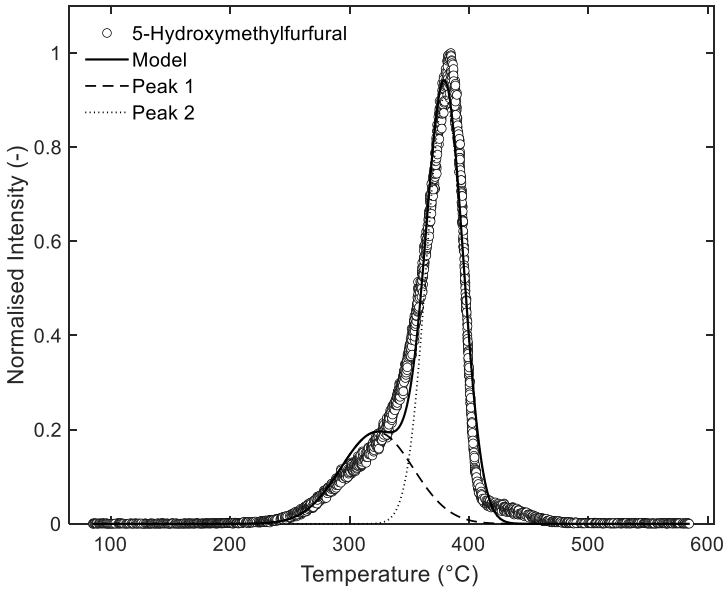

Figure 4-3: Kinetic deconvolution of the Py-EGA-MS evolution profile for 5-Hydroxymethylfurfural (m/z =126) from kānuka wood pyrolysis. Experimental data (circles) are fitted by an overall two-peak (line).

The first peak at lower temperatures (Peak 1), with activation energy of 111.24 kJ/mol for furfural and 107.22 kJ/mol for 5-HMF, comes from the initial breakdown of hemicellulose. These energy values match what has been reported in studies for hemicellulose pyrolysis, ranging from 80-120 kJ/mol (Varhegyi *et al.*, 1989a; Svenson, Pettersson and Davidsson, 2004; Lei *et al.*, 2019), which covers the steps needed to break sugar linkages and remove water (Soukup-carne, Fan and Esteban, 2022). For 5-HMF, it

forms from C6 sugars in hemicellulose by changing to a fructose-like form and then losing three water molecules. Acidic groups like uronic acids and acetyl units in hemicellulose can speed up these reactions by acting as catalysts, leading to higher yields at milder temperatures (Ye *et al.*, 2021; Yuan *et al.*, 2021). In kānuka wood, which is about 20-30% hemicellulose, this peak likely drives the early release of furan odorants, with the highest intensity around 280-320 °C (Derba-maceluch *et al.*, 2023).

The second peak at higher temperatures (Peak 2), around 350-420°C, relates to later reactions from cellulose breakdown. Cellulose pyrolysis mainly produces sugar derivaties like levoglucosan

through bond shifts between sugars, but with continued heating, these turn into 5-HMF as a central compound (Wang *et al.*, 2020). The activation energy for this stage, based on the model fit, fits with known values of cellulose pyrolysis (150-250 kJ/mol), including the higher barriers for opening up the structured chains and re-arranging molcules (Liang, Ries and Hine, 2023). For furfural, this second peak comes from the further breakdown of 5-HMF from cellulose, where formaldehyde (CH_2O) is removed from the hydroxymethyl group. This step has an activation energy of about 322-375 kJ/mol, as shown in computational models (Meng *et al.*, 2017).

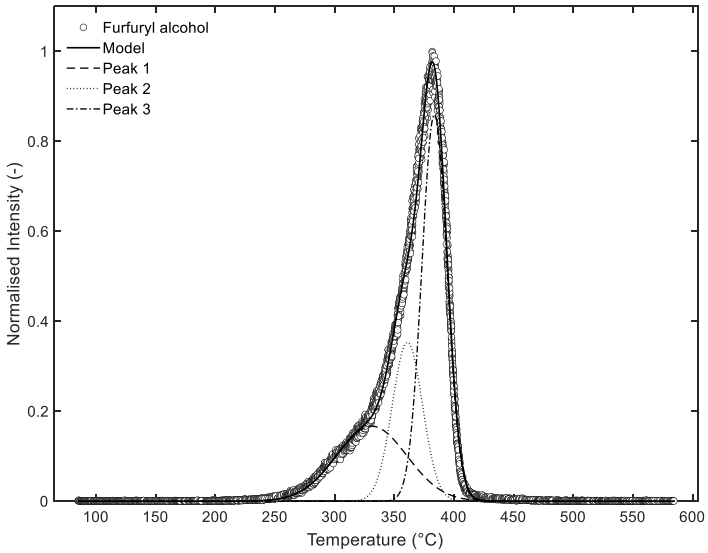

Figure 4-4: Kinetic deconvolution of the Py-EGA-MS evolution profile for Furfuryl alcohol (m/z =98) from kānuka wood pyrolysis. Experimental data (circles) are fitted by an overall two-peak (line).

For 5-HMF, the second peak may come from slower release from tough cellulose parts or ties with lignin in kānuka wood, affecting the breakdown rates (Duan and Ji, 2024). These results line up with earlier research on biomass pyrolysis, where hemicellulose and cellulose interact and can change peak temperatures, sometimes boosting 5-HMF amounts through cross-effects (Wang *et al.*, 2020).

Unlike furfural and 5-HMF, the Py-EGA-MS data show that Furfuryl alcohol (m/z = 98; Figure 4-4) has a tri-modal evolution profile during kānuka wood pyrolysis, broken down into three kinetic

peaks that reflect multi-stage formation from carbohydrate fractions (Pavlath and Gregorski, 1988). The first peak (Peak 1), with an activation energy of 113.31 kJ/mol, aligns with hemicellulose decomposition, matching reported values (100-120 kJ/mol) for initial dehydration and reduction steps in sugar pyrolysis (Yeo *et al.*, 2019). Furfuryl alcohol forms primary from C5 sugars like xylose through partial hydrogenation of furfural intermediates or direct cyclization with hydroxyl-methyl addition, catalysed by acidic moieties in hemicellulose. The second peak (Peak 2; 307.04 kJ/mol) corresponds to cellulose-derived pathways, involving higher energy barriers for levoglucosan fragmentation and subsequent furan ring assembly (Chen *et al.*, 2017). The third peak (Peak 3; 398.47 kJ/mol) likely arises from late-stage reactions in refractory char or lignin-carbohydrate complexes, were thermal cracking yields minor amounts via radical mechanisms.

In addition to their chemical origins, furfural 5-HMF and Furfuryl alcohol help shape the smell and taste of wood smoke by adding sweet, caramel-like and baked flavours that soften the strong phenolic tones from lignin compounds. Furfural gives a sweet, bready and slight almond scent, with an odour threshold of 3-15 ppb, making it noticeable even in small amounts in smoke (Sung, 2013). 5-HMF adds caramel and burnt sugar notes, with thresholds of 10-50 ppb, and links to flavours like those in heated foods and smokes. Furfuryl alcohol contributes burnt, caramel and cooked aromas, with an odour threshold around 1-8 ppm, enhancing sweetness in smoke matrices. Studies on sensory effects show how they work together: furfural boosts nutty and sweet impressions when mixed with other furans or phenols, while 5-HMF and Furfuryl alcohol deepen caramel flavours alongside maltol or vanillin, as seen in smoke products (Vazquez, 2022). In kānuka wood smoke, these compounds probably help even out harsher notes from guaiacol and syringol, creating a more balanced taste for food uses. Still, too high pyrolysis temperatures could break down these furans into unwanted compounds, highlighting the value of controlled smoking to get the best sensory results.

4.3.4.2 Guaiacyl-Derived Compounds

As discussed previously, phenols make up most of the smoke aroma profile, especially at higher temperatures. These compounds are pre-dominantly derived from the decomposition of lignin. Lignin pyrolysis is a complex process involving de-polymerisation, side-chain cleavage and re-arrangement reactions yielding a wide range of phenolic compounds, many of which are odorants (Yeo *et al.*, 2019).

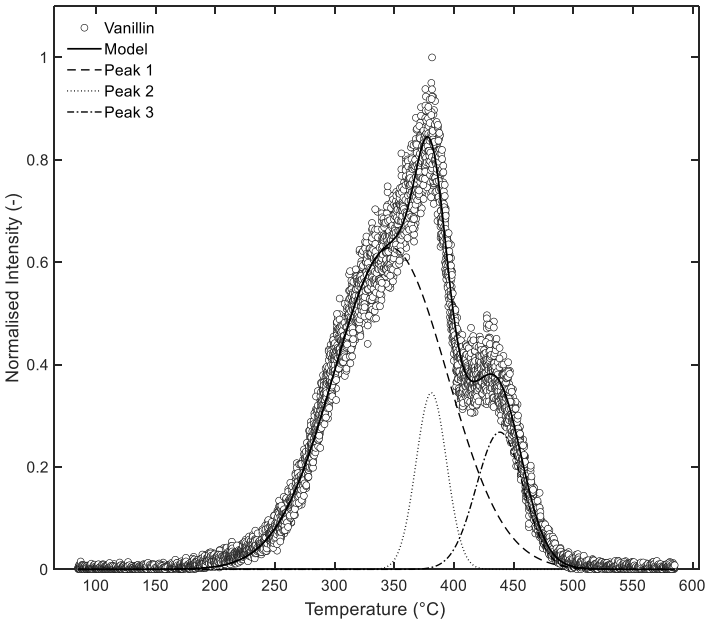

Figure 4-5: Kinetic deconvolution of the Py-EGA-MS evolution profile for vanillin (m/z = 152) from kānuka wood pyrolysis. Experimental data (circles) are fitted by an overall three-peak model (line)

The formation of these phenolic compounds stems from the thermal decomposition of lignin's three primary monolignol building blocks: p-hydroxyphenyl (H), guaiacyl (G) and syringl (S) units. These building blocks are linked primary via the β-O-4 ether links as well as β-5, β-β and 5-5 linkages (Kawamoto, 2017). In hardwoods such as kānuka, a higher S/G ratio (1.5-2.5) favours dimethoxylated phenolics from S-units, while G-units produce monomethoxylated derivates, and H-units or secondary demethoxylation yield simpler phenols (Yuan *et al.*, 2022).

Guaiacyl (G) units prevalent in kānuka lignin undergo depolymerisation to yield monomethoxylated phenolics via homolytic cleavage and radical. The tri-modal evolution profile for vanillin (m/z = 152; Figure 4-5) illustrates multistage kinetics with peak 1 centred around 325 °C with an activation energy of 70.06 kJ/mol ($A = 9.11 \times 10^2$ 1/s), possibly stemming from primary depolymerisation of G-units, involving β-O-4 scission and oxidation of coniferyl alcohol precursors to form the aldehyde group. This relatively low activation energy value aligns with values reported values of acid-catalysed homolytic scissions (50-80 kJ/mol; Li, 2015) where hemicellulose-derived acids such as acetic acid significantly lower the barriers by promoting protonation and dehydration steps. In kānuka wood, this early peak likely reflects enhanced catalytic effects from polysaccharide interactions, therefore promoting vanillin release at lower-than-expected temperatures compared for example with pure lignin (Nguyen *et al.*, 2016). The low to modest pre-exponential factor suggests a controlled, diffusion limited process in the solid state (Jayarama Krishna, Korobeinichev and Vinu, 2019). The second peak, peaking around 375 °C with an activation energy of 322.71 kJ/mol ($A = 2.61 \times 10^{23}$ 1/s) corresponds to a more radical-mediated re-arrangements within more crystalline lignin. It likely involves the conversion of cinnamyl intermediates to vanillin through side-chain oxidations and ring-preserving fragmentations. This elevated energy barrier is consistent with experimental studies on guaiacyl model compounds (250-350 kJ/mol) (Pe III *et al.*, 2023). The exceptionally high pre-exponential factor points to a rapid, entropy-favoured chaotic process once initiated (Li *et al.*, 2025). In the context of kānuka wood, this dominant peak shows the significant role of G-unit abundance in promoting the high vanillin yields at intermediate temperatures.

The third peak is centred around 430 °C with an activation energy of 246.19 kJ/mol ($A = 3.42 \times 10^{15}$ 1/s). This peak is likely due to the late-stage secondary reactions in refractory char residue. This energy value fits reported ranges for char-derived volatiles (200-300 kJ/mol) where thermal cracking overcomes aromatic cross-linking formed during earlier charring.

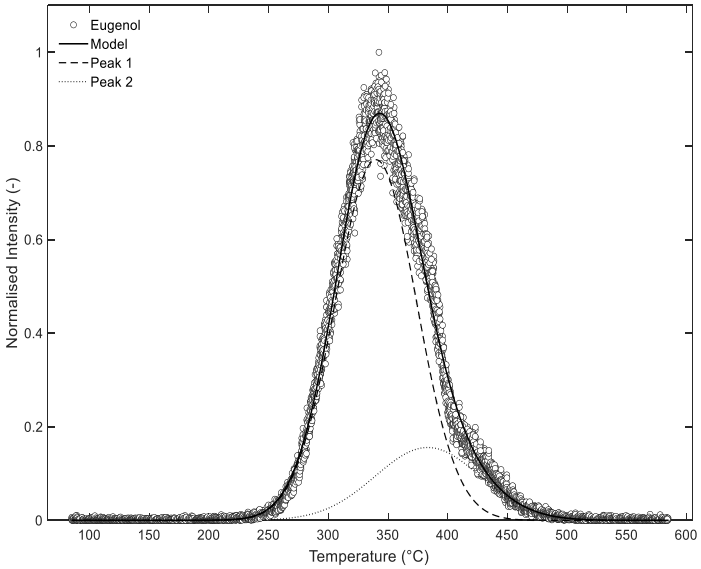

Figure 4-6: Kinetic deconvolution of the Py-EGA-MS evolution profile for eugenol (m/z = 164) from kānuka wood pyrolysis. Experimental data (circles) are fitted by an overall two-peak model (line)

Eugenol (m/z = 164; Figure 4-6) presents a bi-modal profile with peak 1 centred at around 350 °C with an activation energy of 100.15 kJ/mol ($A = 5.57 \times 10^5$ 1/s). This is most likely the result of allylic bond scission in G-unit propenyl side chains, a radical initiated process matching values reported in literature of 90-110 kJ/mol (Shen *et al.*, 2024). Peak 2 is centred around 380 °C and has an activation energy of 86.89 kJ/mol ($A = 1.02 \times 10^4$ 1/s). This peak likely captures the process of isomerisation of coniferyl alcohol or hydrogenation in the pyrolytic phase with lowered barriers – possibly catalysed by acid (Pan *et al.*, 2024).

Coniferyl aldehyde (m/z = 178, Figure 4-7) shows bi-modal kinetics like Eugenol. Peak 1 appears to centre low at around 280 °C with an activation energy of 112.67 kJ/mol ($A = 5.25 \times 10^7$ 1/s) and is likely the result of coniferyl alcohol dehydration. Peak 2 is quite a bit higher at 390 °C with an activation energy of 110.57 kJ/mol ($A = 1.15 \times 10^6$ 1/s) and could be due to oxidation reactions at higher temperatures (Kawamoto, 2017).

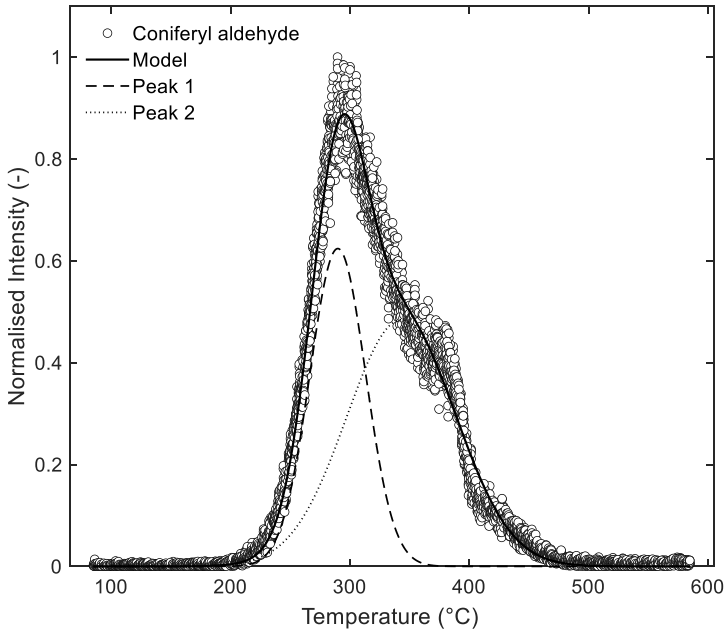

Figure 4-7: Kinetic deconvolution of the Py-EGA-MS evolution profile for coniferyl aldehyde (2-Propenal, 3-(4-hydroxy-3-methoxyphenyl)-; m/z = 178) from kānuka wood pyrolysis. Experimental data (circles) are fitted by an overall three-peak model (line)

2-Methoxy-4-vinylphenol (m/z = 150; Figure 4-8) also shows three distinct peaks (tri-modal). Peak 1 appears to be centred on 325°C with an activation energy of 100.15 kJ/mol (A = 7.16×10^5 1/s). This compound is most likely formed due to the β-O-4 cleavage to form vinyl groups (Yang *et al.*, 2021). Peak 2 and 3 which peak at 390 °C (E =175.75 kJ/mol, A = 5.93×10^{11} 1/s) and 430 °C (E =196.07 kJ/mol, A = 8.33×10^{11} 1/s), respectively are likely due to de-carboxylation and dehydration with rising energies for C-C bonds.

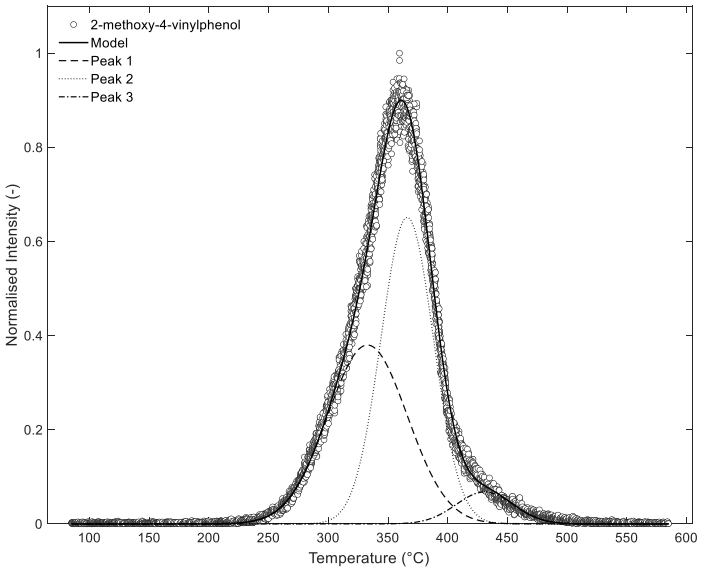

Figure 4-8: Kinetic deconvolution of the Py-EGA-MS evolution profile for 2-methoxy-4-vinylphenol (m/z = 150) from kānuka wood pyrolysis. Experimental data (circles) are fitted by an overall three-peak model (line).

4.3.4.3 Syringyl-Derived compounds

Syringyl (S) units in hardwoods such as kānuka produce dimethoxylated phenols under pyrolysis conditions through similar pathways but with higher methoxy retention (Yuan *et al.*, 2022). Phenol, 2,6-dimethoxy- also known as syringol (m/z = 154; Figure 4-9) appears to show tri-modal kinetics. Peak 1 maxima appears at around 350 °C with a relatively low activation energy of 88.22 kJ/mol ($A = 2.73 \times 10^4$ 1/s) is likely due to ether cleavage (Asmadi, Kawamoto and Saka, 2011a). Peak 2 ($E = 255.61$ kJ/mol, $A = 8.57 \times 10^{17}$ 1/s) has a maximum around 380 °C and likely involves β-O-4 scission in (S)-polymers and peak 3 ($E = 325.28$ kJ/mol, $A = 7.10 \times 10^{21}$ 1/s) is likely due to char cracking as it appears to occur at higher temperatures, peaking at 440 °C (Pe III *et al.*, 2023).

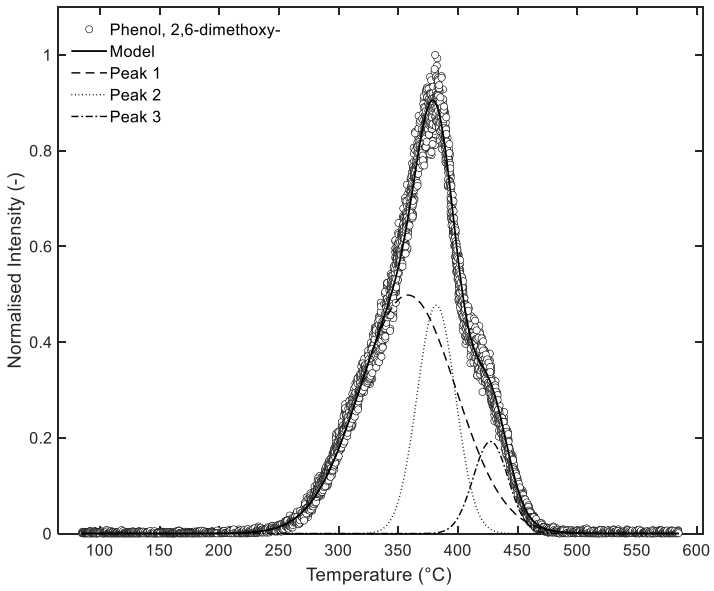

Figure 4-9: Kinetic deconvolution of the Py-EGA-MS evolution profile for syringol (Phenol, 2,6-dimethoxy-; m/z = 154) from kānuka wood pyrolysis. Experimental data (circles) are fitted by an overall three-peak model (line).

4-Methylsyringol (m/z = 168; Figure 4-10) parallels this with peak 1 also around 350 °C with an activation energy of 85.15 kJ/mol (A = 1.97×10^4 1/s) likely also to be the result of methylated cleavage. Peak 2, also around 380 °C (E = 200.73 kJ/mol, A = 4.11×10^{13} 1/s) from core S-breakdown and peak 3 around 440 °C (E = 400.86 kJ/mol, A = 4.37×10^{27} 1/s) from alkylations (Holmberg *et al.*, 2016)

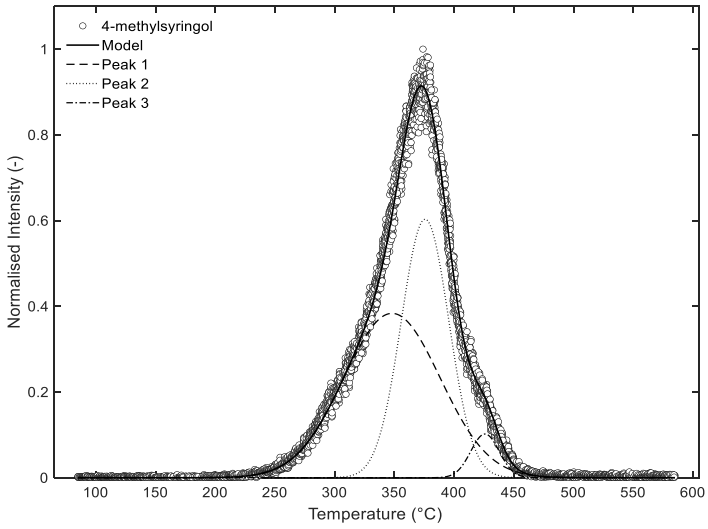

Figure 4-10: Kinetic deconvolution of the Py-EGA-MS evolution profile for 4-methylsyringol (m/z = 168) from kānuka wood pyrolysis. Experimental data (circles) are fitted by an overall three-peak model (line).

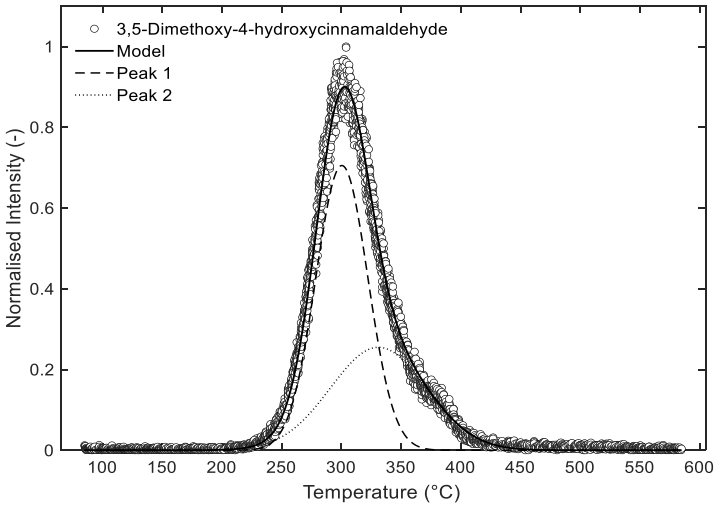

Figure 4-11: Kinetic deconvolution of the Py-EGA-MS evolution profile for sinapaldehyde (3,5-Dimethoxy-4-hydroxycinnamaldehyde; m/z = 208) from kānuka wood pyrolysis. Experimental data (circles) are fitted by an overall two-peak model (line).

3,5-Dimethoxy-4-hydroxycinnamaldehyde also known as sinapaldehyde (m/z 208; Figure 4-11) is bi-modal with peak 1 maximum reached at 310 °C with an activation energy of 141.6 kJ/mol (A =

2.03 × 10^{10} 1/s) and are likely formed because of S-cinnamyl dehydration of sinapyl alcohol precursors. These values of activation energy align well with literature values of 120-150 kJ/mol (Obst and Landucci, 1986). The second peak, centred around 350 °C with an activation energy of 80.87 kJ/mol (A = 1.34 × 10^{4} 1/s) possibly involves a secondary reaction pathway to form aldehydes. The lower activation energy indicates catalytic assistance.

4.3.4.4 Simple Phenols

Phenol (m/z = 94; Figure 4-12) shows tri-modal evolution with the third distinct peak around 500 °C. The first peak maximum is around 320 °C and has an activation energy of 88.97 kJ/mol (A = 6.26 × 10^{4} 1/s) which could be formed via H-unit or demethoxylation (Asmadi, Kawamoto and Saka, 2011b).

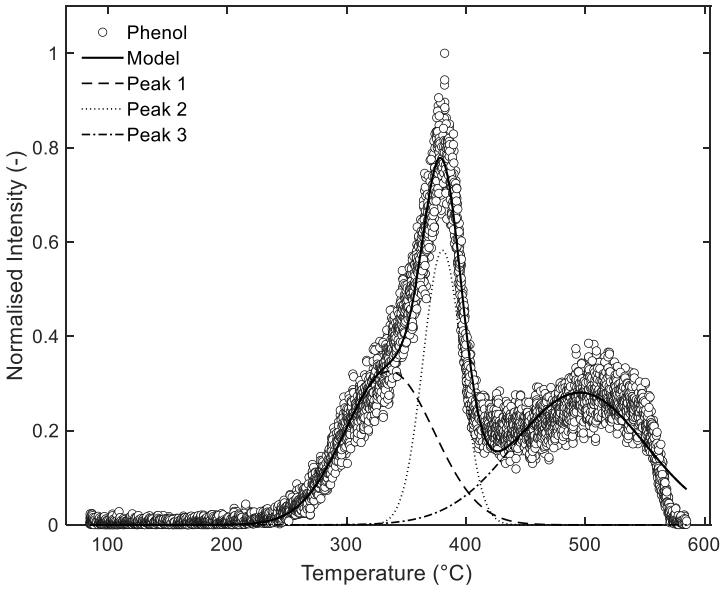

Figure 4-12: Kinetic deconvolution of the Py-EGA-MS evolution profile for phenol (m/z = 94) from kānuka wood pyrolysis. Experimental data (circles) are fitted by an overall three-peak model (line).

Peak 2 is likely due to cracking reactions due to its modest activation energy of 252.95 kJ/mol (A = 5.76 × 10^{17} 1/s) which occur at higher temperatures due to the higher energy requirements to break bonds. Peak 3 is likely due to secondary cracking reactions influenced by primary

carbohydrate secondaries. It has an activation energy of 101.92 kJ/mol (A = 1.03×10^4 1/s)(Dou, Henrikki and Richards, 2020).

m-Cresol (m/z = 108; Figure 4-13) exhibits a tri-modal evolution profile like that of phenol. In fact, the peaks all appear to have a maximum at relatively the same temperature, and their activation energies are very similar with slightly higher activation energies for peak 2 and 3 of 320.22 kJ/mol (A = 1.58×10^{23} 1/s) and 135.12 kJ/mol (A = 2.42×10^6 1/s), respectively. This likely means they both share similar formation pathways.

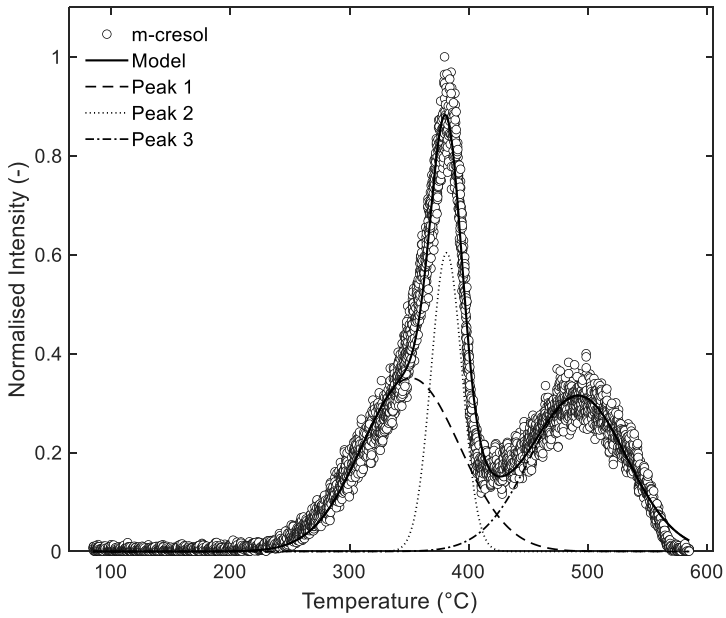

Figure 4-13: Kinetic deconvolution of the Py-EGA-MS evolution profile for m-cresol (m/z = 108) from kānuka wood pyrolysis. Experimental data (circles) are fitted by an overall three-peak model (line).

Similarly, Catechol (m/z = 110; Figure 4-14) displays tri-modal profile. Peak 1 has slightly lower activation energy than both Phenol and m-Cresol of 66.42 kJ/mol (A = 2.58×10^2 1/s). The lower activation energy suggests that acids from primary reactions of hemicellulose facilitate this pathway (Yerrayya, Natarajan and Vinu, 2019).

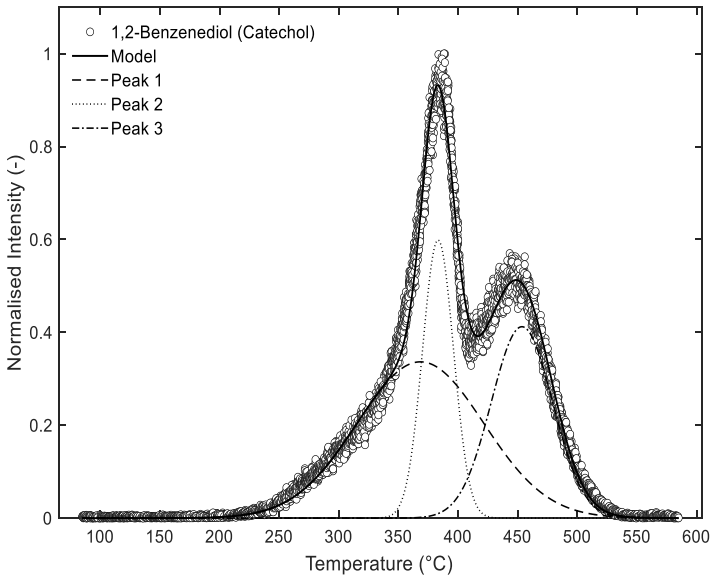

Figure 4-14: Kinetic deconvolution of the Py-EGA-MS evolution profile for catechol (1,2-Benzenediol; m/z = 110) from kānuka wood pyrolysis. Experimental data (circles) are fitted by an overall three-peak model (line).

Peak 2 has a similar activation energy to that of m-Cresol of 321.38 kJ/mol ($A = 1.65 \times 10^{23}$ 1/s). Peak 3 also is indicative of late-stage oxidation or cracking in char, where residual hydroxylated fragments undergo radical recombination or decarbonylation. The intermediate activation energy of 193.73 kJ/mol ($A = 1.85 \times 10^{11}$ 1/s) is indicative of a transition from barrier limited to diffusion controlled processes in the char (Cavallotti *et al.*, 2018).

Simple phenolics such as phenol, m-cresol and catechol display broader activation energy ranges (60-320 kJ/mol) compared to methoxylated derivatives. This is due to their predominatntly secondary origins from demethoxylation, alkylation and char reactions (Lu, Y. Lu, *et al.*, 2017). These compounds often form via cascading pathways: for instance, guaiacol demethoxylates to catechol and then potentially to phenol. This diversity results in irregular formation pathways and because these compounds are known to impart bitter and / or medicinal notes, it further highlights the need to control smoke formation process.

4.4 Conclusion

This comprehensive investigation into the smoke aroma profile of kānuka wood chips shows the intricate relationship between operating parameters and the resulting aroma profile. This provides foundational insight for industrial smoke generation.

The identification of 186 VOCs highlights kānuka diverse aroma profile. Phenols from lignin decomposition dominate at higher temperatures (>400 °C)/ In contrast, carbohydrate-derived compounds like furfural, 5-HMF and Furfuryl alcohol peak at lower temperatures (200-350 °C). Temperature dependent yields align with biopolymer degradation kinetics – hemicellulose and cellulose volatilise early, while lignin persists over a longer temperature range.

Kinetic modelling via peak deconvolution reveals mutli-stage mechanisms with activation energies of 60 – 400 kJ/mol, indicating primary depolymerisation, secondary cracking and char reactions. Bi- or tri- modal evolution profiles show the influence of catalytic effects from acids and interactions between biopolymers, offering a semi-quantitative basis for predicting aroma profiles. These results not only advance understanding of kānuka's thermochemical behaviour but also can guide process optimisation.

This page is intentionally left blank.

CHAPTER 5

Thermodynamic Behaviour of Kānuka Wood Chips

5.1 Introduction

The pyrolysis of wood is a critical process in the art of food smoking. Wood chips are used as a source of fuel and smoke flavour in a variety of traditional and modern smoking methods. The specific enthalpy of reactions that occur during the pyrolysis of wood chips is of particular importance in smoker design as it determines the amount of heat that is produced by the wood chips and the efficiency of the smoking process. Additionally, temperature control is crucial in food smoking as it affects the formation of smoke yield and potential formation of harmful compounds.

During the pyrolysis process, reactions can be both endothermic and exothermic. Primary reactions are generally accepted as endothermic. Exothermic reactions are the result of secondary heterogeneous reactions. This exothermicity makes temperature control difficult in smoke generation. It also promotes the formation of char, and the depletion of primary decomposition products. While the outcome on smoke aroma is unknown, increased yield means that the smoke yield will be lowered and therefore it would be beneficial to minimise these reactions.

Therefore, because of the great range between endo-exothermicity, the specific enthalpy of reactions during the pyrolysis process is an important parameter in the design of smoking equipment, yet there is little consensus in literature (Jones, Chen and Ripberger, 2020) on what the right value for the specific enthalpy of reactions is. Primary specific enthalpy of reaction can range between 200 J/g and 500 J/g and secondary reactions can range from -2500 J/g and -4000 J/g (Roberts, 1971; Chen *et al.*, 2014; Jones, Chen and Ripberger, 2020).

Understanding the specific enthalpy of reactions and the kinetics of the pyrolysis process is crucial to control the temperature during the smoking process and minimise the formation of harmful compounds. This chapter will discuss the specific enthalpy of reactions that occur during the pyrolysis of kānuka wood chips, as determined by Thermogravimetric Analysis-Differential Scanning Calorimetry (TGA-DSC). The TGA-DSC technique allows for the simultaneous measurement of the weight and heat changes that occur during the pyrolysis process, providing valuable information on the thermal behaviour of the wood, the exothermic secondary reactions and the chemical reactions that occur during decomposition. This chapter will focus on the specific enthalpy of reaction and its importance on temperature control during the smoking process, and how it can affect the smoke yield and the formation of harmful compounds, specifically PAHs, char and ways to minimise them. Additionally, this chapter will address the challenges determining the specific enthalpy of reactions.

5.2 Experimental

The experiments conducted in this study aimed to study the specific enthalpy of reactions of kānuka wood chips during pyrolysis. Two batches of kānuka wood chips that varied in particle size were used. The first batch had a particle size range of 90 microns to 600 microns, while the second batch contained particles of less than 90 microns. In total, eight different samples were used: 3, 6, 12, 18 and 24 mg of wood chips from the first batch and 5, 10, 15 and 20 mg samples from the second batch.

The experiments were carried out in a NETZSCH STA 449 F1 Jupiter thermogravimetric analyser (TGA) using a laptop installed with windows 10 running NETZSCH Proteus thermal analysis software to control the apparatus, record data and analyse the results. The details of the instrument have been introduced in Chapter 3.

The samples were heated at varying heating rates of 1, 2.5, 5, 10 and 20 K/min using aluminium crucibles with a diameter of 6 mm. These crucibles were chosen because they could withstand temperatures up to 600°C, the specified maximum safe temperature, and were relatively inexpensive. Prior to the experiments, a baseline was conducted using an empty crucible to ensure accurate results.

The heating profile used for these experiments first heated the sample to 105°C and held there for 45 minutes to remove all moisture, then cooled down to 50°C where it was held for 40 minutes. Next, it was heated to 580°C and held there for 40 minutes and then cooled to 50°C for 40 minutes. This last heating step was repeated two more times, after which the run was terminated. All cooling was done at a rate of 20 K/min. Instrument grade (99.99%) nitrogen gas was chosen to provide an inert environment. Two streams of nitrogen gas were flowing during the experiments, a flow of 50 mL/min inside the furnace to provide the inert atmosphere, and 20 mL/min on the outside jacket to provide resistance against oxidation.

5.3 Data analysis: Calculation of Heat of Pyrolysis

The specific enthalpy of reaction was determined from the TGA-DSC data. The overall heat of pyrolysis was calculated using the method developed by (Jones, Chen and Ripberger, 2020), which removes the effects of emissivity, absorptivity and surface heat transfer. The resulting heat flow represents the specific enthalpy of reaction and the sensible heat. The heat of pyrolysis (ΔH_{py}) was calculated as follows:

$$\Delta H_{py} = \frac{1}{m_{wood,0}}\left(\int_{t_0}^{t_\infty}(Q_{biomass} - Q_{char})_t dt - \int_{t_0}^{t_\infty}\Delta Q_{sensible,t}\, dt - \int_{t_0}^{t_\infty}\Delta Q_{loss,t} dt\right) \quad (5.1)$$

The first integral term, representing the difference between the heat flow of the biomass and the resulting char, was calculated by integrating the respective DSC curve between the first & third thermal sweep to 550 °C. The second integral term, the sensible heat, was calculated as the difference between the arithmetic average sensible heat of the first and third thermal sweep to 550 °C:

$$\int_{t_0}^{t_\infty}\Delta Q_{sensible,dt}\, dt = \int_{T_0}^{T_\infty}\overline{C_{P,wood,T}}\, m_{wood,T}\, dT - \int_{T_0}^{T_\infty} C_{P,char,T}\, y_\infty m_{wood,0}\, dT \quad (5.2)$$

where,

$$\int_{T_0}^{T_\infty} \overline{C_{P,wood,T}}\, m_{wood,T}\, dT = \frac{(1-\delta)C_{P_{wood},T} + y_\infty \delta C_{p,char,T}}{1-\delta(1-y_\infty)} \tag{5.3}$$

Eq. (5.2) represents an approximate expression for the difference in the integrated sensible heat between the wood sample and the char during the pyrolysis process. And δ (5.4) is a dimensionless parameter that quantifies the extend or progress of pyrolysis reactions. It measures the fraction of the total possible mass loss that has occurred up to a given temperature, T, relative to the complete mass loss at the end of the thermal heating cycle.

$$\delta = \frac{y}{y_\infty} = \frac{1-\left(\frac{m_{wood,T}}{m_{wood,0}}\right)}{1-\left(\frac{m_{wood,\infty}}{m_{wood,0}}\right)} \tag{5.4}$$

The heat capacities for kānuka wood ($c_{P,wood,T}$) and char ($c_{P,char,T}$) were determined experimentally (See Appendix 3) and are described by the following relationship:

$$c_{P_{wood},T} = 0.0041T + 1.0562 \left[\frac{J}{gK}\right] \tag{5.5}$$

$$c_{P_{char},T} = 2\times10^{-8}T^3 - 2\times10^{-5}T^2 + 6.4\times10^{-3}T + 0.89 \left[\frac{J}{gK}\right] \tag{5.6}$$

The third integral term is the environmental heat loss term which accounts for heat dissipated to the surroundings during the heating process. It was calculated by plotting the net heat flow (which accounts for the specific enthalpy of reaction of wood subtracting any sensible heat due to change in heat capacity) against the inverse of the heating rate (60/R). A sample calculation can be found in Appendix B.

5.4 Results & Discussion

The investigation is structured to first present and interpret the results from two distinct sample batches, separated by particle size: a larger fraction (90 - 600 μm) and a smaller fraction (< 90 μm).

For each batch, the effects of mass and heating rate on the measured outcomes are systematically examined. Following this, a comparative discussion is presented to combine the findings from both batches.

5.4.1 Analysis of batch 1 (Particle size: 90 – 600 μm)

The char yield from the pyrolysis of the 90-600 μm particles showed a clear dependence on the initial sample mass, as illustrated in Figure 5-1. The equation used to fit the data has the form:

$$Y_\infty = Y_p + Y_{s,max}(1 - \exp(-k_{bed}m)) \quad (5.7)$$

Where Y_∞ is the final char yield (%), Y_p is the primary char yield, $Y_{s,max}$ is the maximum possible secondary char yield (limited by the fraction of primary reactive volatiles available for secondary heterogeneous reactions), k_{bed} is a rate constant (proportional to the probability of secondary reactions per unit path length, influenced by factors such as the tortuous path length and catalytic sites) and m is the initial sample mass – and is a proxy for tortuous path length in the crucible.

As the mass of the wood chips increases, so did the percentage of char produce. The yield rose from 19.4% from a 3 mg sample to 24.4% for a 24 mg sample. This trend agrees with literature, which attributes higher char yields in larger samples to enhanced secondary reactions due to physical transport phenomena within the sample bed. A larger sample mass has a longer tortuous path through which volatile products must travel to escape, increasing the number of interactions of the volatiles with the hot char, which acts as a catalyst for secondary reactions (Di Blasi, 1996; Grønli, 1996). Further analysis of these results provides deeper insight, indicating that the initial primary char yield ($y_{1^\circ,0}$), when extrapolating to zero sample mass is 16.48%. This is very close to the primary char yield for Pinus *radiata* of 16.28% observed by Jones *et al.*, (2020) As mass increases and promotes secondary reactions, an additional 7.38% of the mass is converted into secondary char, leading to a theoretical maximum yield ($y_{inf,lim,max}$) of 23.86%. This is a little lower than the

8.42% secondary char or 24.80% maximum yield found for Pinus *radiata* observed by Jones *et al.*, (2020).

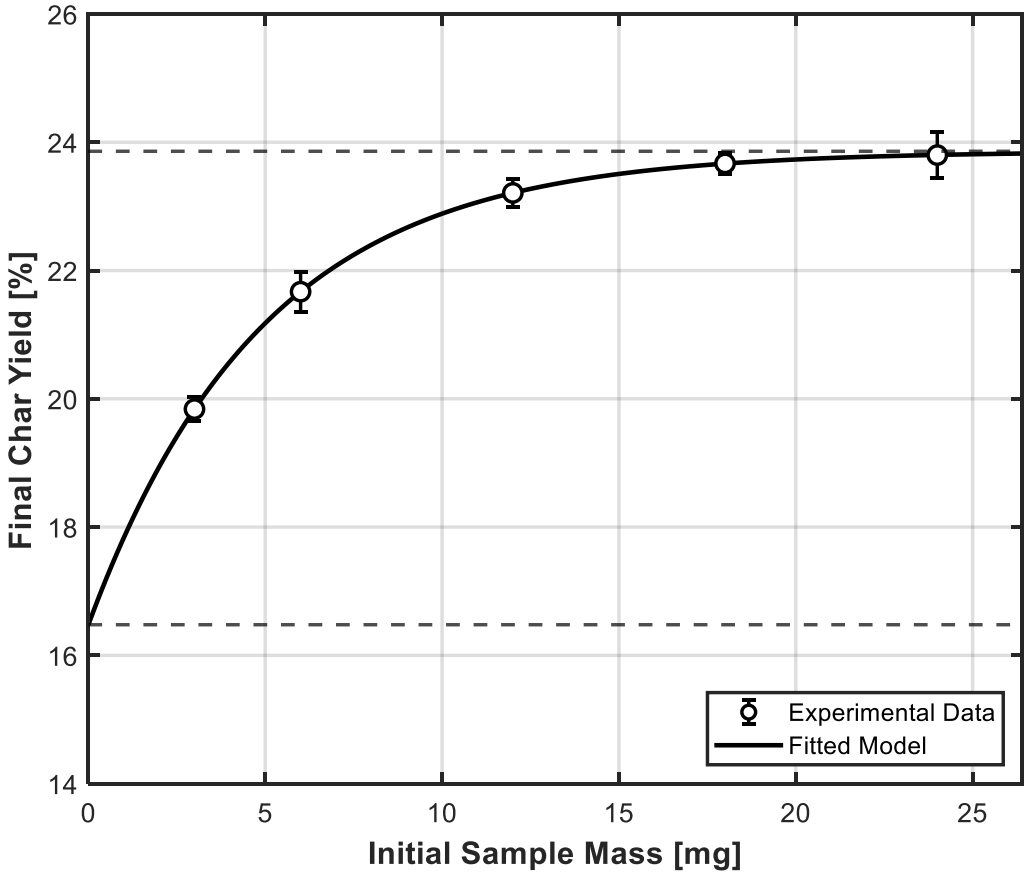

Figure 5-1: Char Yield (%) vs. mass (mg) of the samples from batch 1 with particle size range of 90 to 600 microns with a R2 of 0.96.

A notable aspect of the results is the trend in data variability. The smallest samples (3 mg) exhibit high variability, which is expected for a heterogenous organic material where such a small mass may not be fully representative of the bulk composition. As the sample mass increases towards 18 mg, the variability in the results decreases, indicating that the sample is becoming more representative.

However, at 24 mg, the variability increases again. This is attributed to a procedural artefact: at this mass, the sample volume sometimes exceeded the crucible's capacity. Consequently, even for a

constant mass of 24 mg, variations in bed density and bed height likely occurred, altering the heat and mass transfer characteristics and leading to the observed increase in result inconsistency.

5.4.2 Effect of mass on specific enthalpy of reactions

The specific enthalpy of reaction, indicating the net energy release or absorption also varied significantly with sample mass, as shown in Figure 5-2. For smaller masses, the reaction was less exothermic, becoming progressively more so as mass increased.

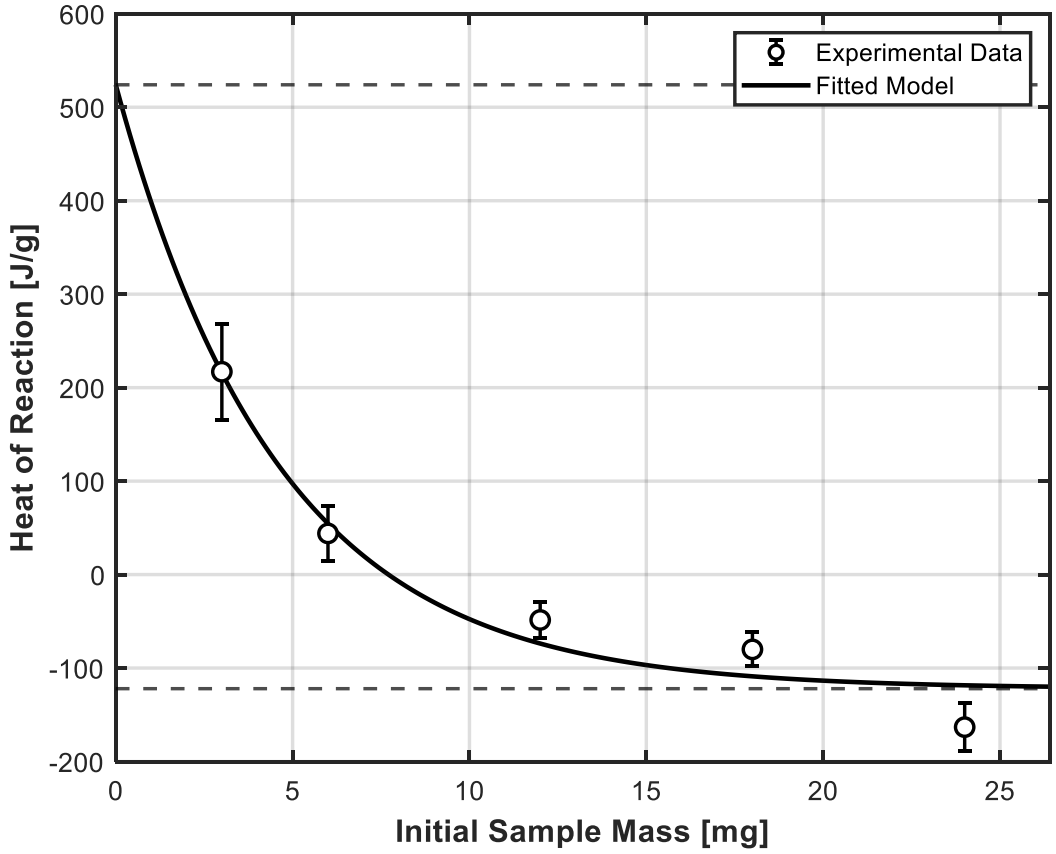

Figure 5-2: Heat of pyrolysis vs mass (mg) of batch 1 experiments with particle size range of 90 to 600 microns for varying heating rates.

This trend is a direct consequence of the interplay between heat and mass transfer limitations within the packed sample bed inside the crucible.

Physically, increasing the sample mass within the crucible directly increases the depth of the sample bed. While the particle density of the wood remains relatively constant, a deeper bed has two

profound effects. Firstly, it creates significant mass transfer resistance; the primary volatiles formed must navigate a longer, tortuous path to escape. This extended residence time within the hot, reactive zone increases the interactions between the volatiles and char, resulting in more secondary reactions and formation of secondary char (Mehrabian *et al.*, 2012). Secondly, due to the characteristically low thermal conductivity of biomass, a thicker sample bed develops significant temperature gradients. While the crucible walls are heated, the core of the sample heats more slowly (Cai & Liu, 2008).

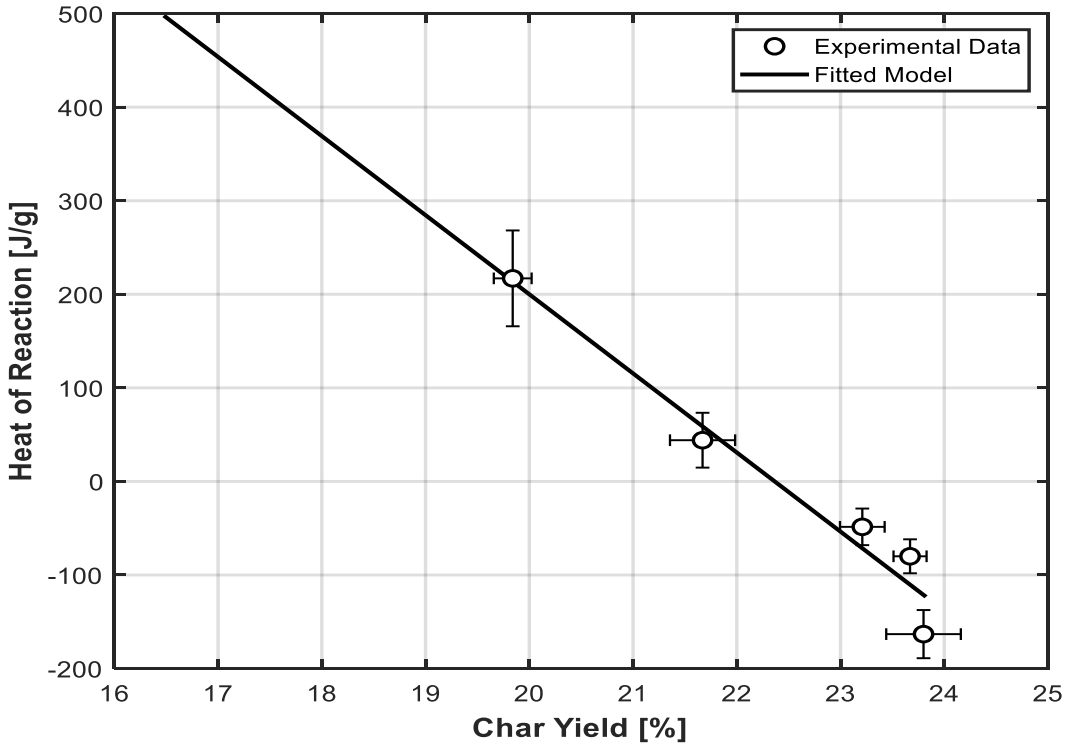

Figure 5-3: Specific enthalpy of reaction vs char yield (%) of batch 1 experiments with particle size range of 90 to 600 microns for varying heating rates.

The crucial link to the specific enthalpy of reaction lies in these secondary reactions. While primary pyrolysis reactions are endothermic (requiring energy), the secondary reactions – including the cracking, repolymerisation and condensation of volatiles on the surface of existing char – are known to be strongly exothermic (Babu, 2008). Figure 5-2 shows the 90 – 600 μm particles that the primary pyrolysis reactions to be endothermic with a specific enthalpy of reaction ($\Delta H_{py,1^\circ}$) of

+497.86 J/g, while secondary heterogeneous reactions are strongly exothermic, releasing -624.19 J/g ($\Delta H_{py,2°,HET}$). In larger samples, the heat generated by these exothermic reactions within the bed's core can lead to a "self-heating" effect, raising the local temperature above that of the crucible walls. This localised temperature rise further accelerates the rate of these same exothermic secondary reactions, creating a positive feedback loop.

Therefore, the observed shift from a less to a more exothermic process as sample mass increases is a clear indicator of the transition from a process dominated by endothermic primary pyrolysis to one significantly influenced by exothermic secondary reactions (in larger samples with high mass transfer resistance). The tighter clustering of results for larger samples (pre-24 mg) also reflects this, as the process becomes governed more by bulk properties of the packed bed and less by the stochastic variation in small samples of anisotropic materials. This finding aligns with studies demonstrating that conditions promoting secondary reactions, such as increased sample mass or pressure, cause the overall specific enthalpy of reaction to shift from endothermic to exothermic (Jones, Chen and Ripberger, 2020).

5.4.3 Analysis of Batch 2 (Particle size: ≤ 90 μm)

For the finely ground samples, all <90 μm, the char yield again demonstrated a strong positive correlation with the initial sample mass, as shown in Figure 5-4. The char yield increased substantially from 25.64% to 34.59% as the mass increased. Crucially, the overall magnitude of char yield is notably higher across the entire mass range compared to Batch 1. This is a direct result of the physical differences in the packed bed created by the smaller particles. This shows that even at very low mass (theoretical mass of zero), the char yield is much higher for the < 90-micron particles due to their physical nature. The ≤ 90 μm particles form a bed with significantly lower permeability and a more tortuous escape path for volatiles compared to the larger particles of Batch 1.

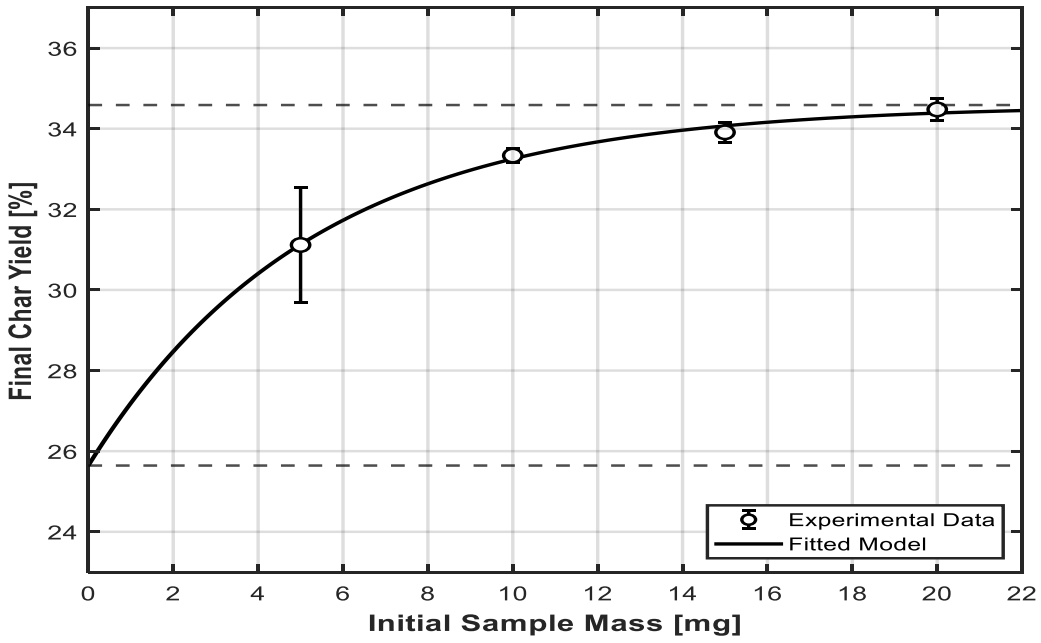

Figure 5-4: Char yield (%) vs. mass (mg) of the samples from batch 2 with particle size ≤90 microns for varying heating rates with an R2 of 0.97.

This effect of mass transfer limitations is particularly evident when examining the outlier at low mass: the 5 mg sample pyrolysed at the slowest heating rate of 1 K/min yielded only 25.6% char. This is substantially lower than the >31% yield from the other 5 mg samples heated at 2.5-20 K/min. At a constant mass and particle size, the initial bed height and tortuosity are identical. Therefore, the difference must be attributed to the kinetics of volatile evolution versus the rate of their escape. At the slow rate of 1 K/min, volatile generation is sufficiently slow that the volatiles can diffuse through the low-permeability bed and escape before their local concentration becomes high enough to initiate significant secondary reactions.

However, a modest increase in the heating rate to 2.5 K/min appears to push the rate of volatile generation beyond a critical threshold, where it surpasses the rate at which volatiles can escape through the packed bed. This leads to a rapid increase in the local concentration of volatiles, promoting both heterogeneous (volatile-char) reactions on the char surface and homogenous (volatile-gas or volatile-volatile) reactions within the voids of the bed.

This suggests a critical phenomenon may be occurring within the low-permeability bed, analogous to the onset of flooding in a packed bed reactor. As hot primary volatiles rise from the lower sections, they encounter cooler zones in the upper layers of the bed, causing heavier tar components to condense. This initiates a two-stage pore-blocking process. First, the condensed liquid tars physically obstruct the fine pores of the bed of wood, increasing the local pressure and slowing the escape of other volatiles. This in turn promotes secondary reactions. Second, as these reactions proceed, the trapped tars repolymerise into solid secondary char, which builds up within the pore spaces, further reducing the permeability and increasing the tortuosity of the escape path. This build-up of solid material impedes the flow of newly generated volatiles, increasing the local backpressure. Such an increase in local pressure is well documented to suppress the formation of liquid products and strongly promote secondary reactions that lead to char (Brown *et al.*, 2000). This pore-blocking and self-pressurisation mechanism would explain the sharp-non-linear jump in char yield observed. It also explains why, once this low-permeability state is established, the effect of increasing sample mass has a less pronounced impact on char yield than seen in Batch 1, the 90 – 600 μm particles, because the system has already reached a state where bed permeability, rather than just bed depth, becomes the dominant rate-limiting factor.

5.4.4 Effect of mass on specific enthalpy of reactions and char yield

The specific enthalpy of reaction for Batch 2, the fine particles ≤ 90 microns, presented in Figure 5-5, shows a similar trend to Batch 1, the 90 – 600 μm particles, where the reaction becomes more exothermic as the sample mass increases. This reflects the increasing dominance of exothermic secondary reactions as the bed depth increases.

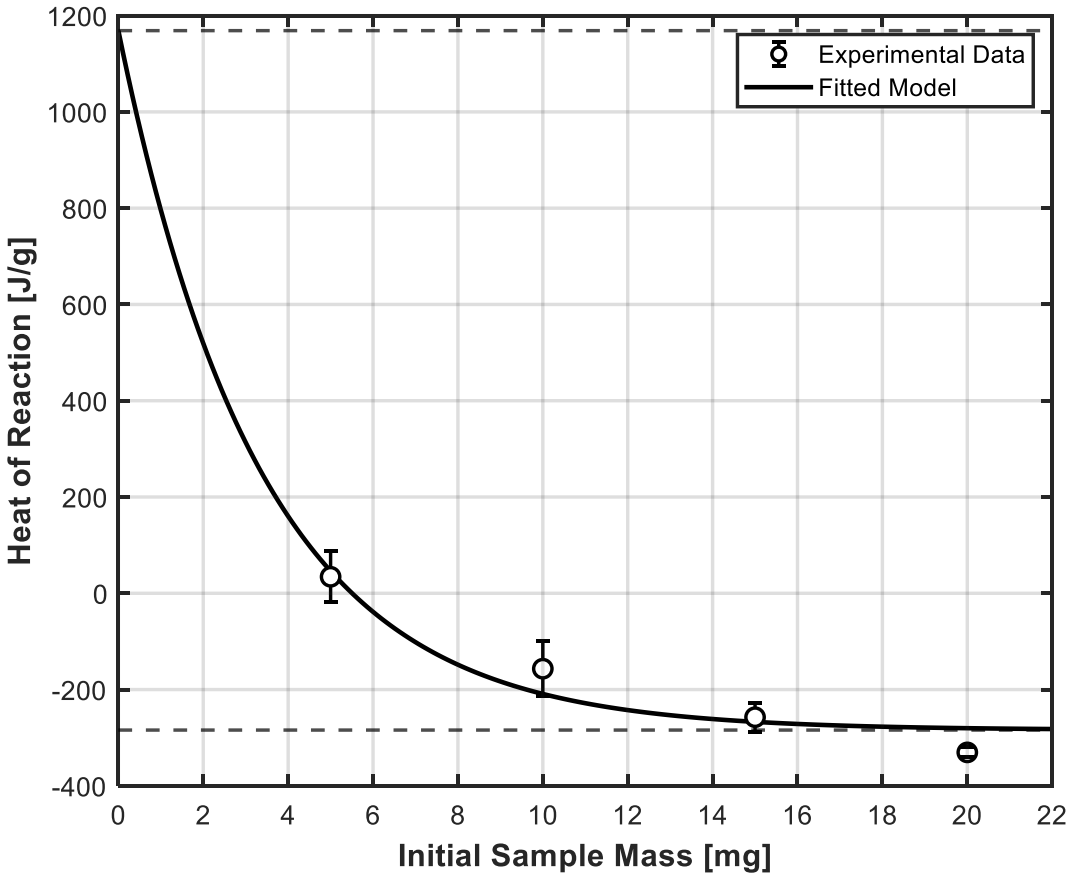

Figure 5-5: Specific enthalpy of reaction (J/g) vs. mass (mg) of the samples from batch 2 with particle size range of ≤ 90 microns.

However, a critical distinction is observed when comparing the overall specific enthalpy of reaction between the two batches. The results of Batch 2, the fine particles ≤ 90 microns, are consistently more exothermic than those for Batch 1, the 90 – 600 μm particles, at equivalent sample masses. This is a direct consequence of the severe inter-particle (between particles) mass transfer limitations discussed in the previous section.

This observation is strongly supported by the derived thermodynamic parameters. The primary heat of pyrolysis for Batch 2, the fine particles ≤ 90 microns was determined to be +629.46 J/g, significantly more endothermic than for Batch 1, the 90 – 600 μm particles. However, this is overshadowed by an even more pronounced increase in the exothermicity of the secondary reactions, with the secondary heterogeneous reaction heat being -954 J/g. The secondary specific

enthalpy of reaction is almost 50% greater than that of Batch 1, highlighting the profound impact of the low-permeability bed on promoting these heat-releasing pathways. A comparison is made later in this discussion for when the primary specific enthalpy of reaction of Batch 2 is fixed to that from Batch 1.

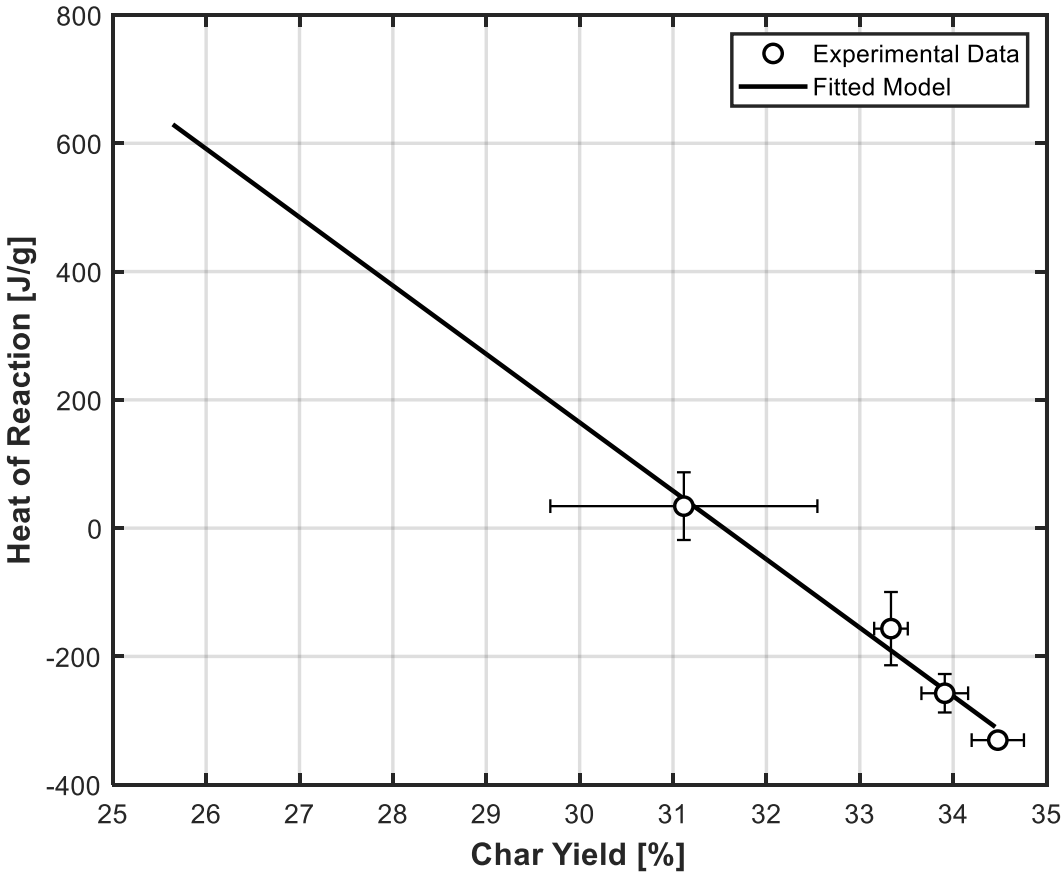

Figure 5-6: Specific enthalpy of reaction vs Char yield (%) of batch 2 experiments with particle size ≤ 90 microns for varying heating rates.

The low-permeability bed formed by the fine particles is so effective at trapping volatiles that it overwhelmingly promotes the exothermic secondary reactions that generate char. While the excellent heat transfer into each small particle efficiently drives the initial endothermic primary pyrolysis, the subsequent trapping of these volatiles within the packed bed is the dominant effect. The intense promotion of exothermic secondary reactions driven by the pore blocking and self-pressurisation phenomena leads to a much greater net release of heat compared to the more

permeable bed of Batch 1. This explains why the overall process for the smaller particles is significantly more exothermic.

5.4.5 Quantitative Analysis of Bed Permeability and Consequent Pressure Generation

To move beyond a qualitative description, the dramatic difference in mass transfer resistance between the two batches can be estimated quantitatively. The permeability (K), a measure of a porous medium's ability to allow fluids to pass through it, can be estimated using the Kozeny-Carmen equation. This equation is widely used to evaluate fluid dynamics in packed bed and is given by:

$$K = \frac{\varepsilon^3 D_P^2}{180 * (1-\varepsilon)^2} \tag{5.8}$$

Where ε is the bed porosity (void fraction) and D_P is the mean particle diameter. To perform this calculation with greater accuracy, we use the Sauter Mean Diameter ($D_{[3,2]}$), which is the most appropriate average for calculations involving flow through porous media as it correctly weights the influence of finer particles. It is calculated from the full particle size distribution via the formula:

$$D_{[3,2]} = \frac{1}{\sum\left(\frac{\widehat{m_i}}{d_i}\right)} \tag{5.9}$$

Where $\widehat{m_i}$ is the mass fraction and d_i is the mean diameter of particles in each size interval. (Full calculations are presented in the Appendix 4)

For Batch 1 (90 – 600 μm), using the experimental sieve analysis data, the Sauter Mean Diameter was calculated to be $D_{P1} \approx 367.2\,\mu m$. For batch 2, particles ≤ 90 microns, the Sauter Mean Diameter was calculated to be $D_{P2} \approx 68.8\,\mu m$.

With these diameters and an assumed porosity (ε) of 0.4, the permeabilities are; batch 1, particles 90 – 600 μm: 1.33×10^{-11} m^2 and batch 2, fine particles of ≤ 90 μm: 4.69×10^{-13} m^2.

The ratio of K_1/K_2 is ~28. This means the permeability of the larger particle bed (Batch 1) is approximately 28 times larger than that of Batch 2. According to Darcy's Law, the pressure drop required to force a fluid through a porous medium is inversely proportional to its permeability. Therefore, for the same rate of volatile gas production, the internal pressure generated within the fine powder bed will be more than an order of magnitude higher than in the course chip bed.

5.4.6 Comparative analysis (Batch 1 & 2)

The profound effect of particle size is now visually and quantitatively clear. To isolate the effect of mass transfer on the thermodynamics, we can normalise the Batch 2 data by assuming the intrinsic energy of the primary chemical reaction is constant. By fixing the primary heat for Batch 2 to the value from Batch 1 ($\Delta H_{py,1^\circ} = 497.86 \frac{J}{g}$), the model calculates a new secondary heat of -802.69 J/g. This normalised comparison gives some insight into the effect of mass transfer limitations: even when the primary specific enthalpy of reaction is assumed to be identical, the secondary reactions in the powder bed are still more exothermic than in the course chip bed. This confirms that the dominant physical change is the severe restriction of mass transfer caused by the higher bed density of the smaller particles which results in a lower bed permeability.

5.4.7 Implications for the design and operation of a food smoke generator

The primary goal of a food smoke generator is to efficiently produce a high yield of desirable aromatic volatiles while minimising solid char and harmful by-products. This comparative analysis provides clear design principles.

The use of small kānuka particles, ≤ 90 μm in a conventional packed bed smoke generator such as a hot plate smoker is shown to be both inefficient and potentially uncontrollable. The data reveals that secondary reactions dominate, converting a significant fraction (> 15%) of potential smoke compounds directly into solid char. This represents a significant loss of feedstock efficiency. Furthermore, the exothermicity of these secondary reactions creates a high risk of thermal runaway and localised hot spots. Research into smoke composition, such as the work by (Vazquez, 2022) as well as smoke analysis from this work (Chapter 4) has shown that pyrolysis temperatures exceeding 400-450°C favour the formation of undesirable and potentially carcinogenic PAHs. The conditions observed in Batch 2, with a highly exothermic secondary reaction pathway, are therefore highly conducive to producing a lower quality, potentially more hazardous smoke. Moreover, the high-temperature secondary reactions are known to crack desirable phenolic compounds – responsible for characteristic smoky flavours and antioxidant properties into lighter, less flavourful gases like CO and CH_4 while also producing acrid compounds such as acetic acid.

Conversely, the larger particle size of Batch 1 provides a much more favourable operational regime. The secondary reactions are present but not dominant, leading to a lower total char yield and more moderate heat release. This implies a more controllable, lower-temperature process which avoids thermal runaway, is essential for generating a desirable smoke profile. An ideal smoke generator must therefore be engineered to favour the mechanisms of Batch 1 and suppress those of Batch 2. This can be achieved by using larger feedstock like chips or shavings, avoiding compaction of the fuel bed and ensuring adequate ventilation to remove volatile products before they can undergo

secondary reactions. The quantitative permeability analysis underscores this point: a design that maximises bed permeability is key to maximising smoke quality.

5.5 Conclusion

In conclusion, this chapter has presented the results of a study on the specific enthalpy of reactions during the pyrolysis of kānuka wood chips and its relationship to smoker design. The results of the study have shown that the specific enthalpy of reactions and char yield are affected by the mass, particle size and heating rate of wood chips, and that these factors need to be taken into consideration when designing and optimising the smoking process. The kinetics and aroma profile analysis from the previous chapters indicate the faster heating rates do not affect aroma profile or the kinetics of the reactions and so in all cases it is generally recommended to optimise the wood chips to minimise limitations of heat and mass transfer by reducing the particle size and mass (or in the case of a smoker, the depth of wood chips) to maximise smoke (volatiles) yield.

CHAPTER 6

One-Dimensional Mechanistic Model of a Hot Plate Smoker – Conceptual, Numerical Formulation and Model Validation

6.1 Introduction

As discussed in earlier chapters, the process of wood smoking, a traditional method for food preservation and flavour enhancement, is a complex interplay of drying, pyrolysis and under certain conditions, combustion. The generation of smoke, rich in desirable aromatic compounds as well as potentially less desirable constituents like Polycyclic Aromatic Hydrocarbons (PAHs), is primarily a result of the thermal decomposition of wood. Understanding the fundamental mechanisms governing this decomposition is crucial for optimising smoke generation processes, for instance to achieve a high yield of smoke with a specific aroma profile while minimising harmful by-products.

Laboratory-scale experiments provide invaluable fundamental data on wood decomposition pathways and the chemical characteristics of smoke. However, translating these findings directly to the design and optimisation of larger-scale smoke generators is often challenging. This is because such experiments may not fully capture the significant influence of coupled heat and mass transfer phenomena that become dominant as the scale of the system increases. At larger scales, temperature gradients, internal pressure build-up and the flow of volatiles through the porous wood structure can profoundly affect reaction rates, product distribution and overall process efficiency.

To bridge this gap, this chapter details the development and formulation of a theoretical one-dimensional (1D) mathematical model designed to simulate the heat and mass transfer effects during the pyrolysis of wood, specifically conceptualised for a hot surface smoker scenario. In such a system, wood (e.g., chips or shavings) is heated by direct contact with, or proximity to, a hot surface, leading to smoke generation. The model presented herein aims to serve as a predictive tool to investigate these coupled transport and reaction phenomena.

The model solves a system of coupled, non-linear PDEs governing energy conservation, mass conservation for various gaseous species and momentum transfer for fluid flow within the porous wood matrix. Concurrently, ODEs describe the chemical kinetics of wood decomposition. Specifically, the model accounts for:

Heat transfer

This includes conduction through the multiphase porous matrix (comprising solid wood, char and interstitial gases), convective heat transport by the flowing mixture of inert gas and pyrolysis derived volatiles and the endothermic/exothermic heat effects associated with the pyrolysis reactions. The thermal boundary conditions are formulated to represent a specified prescribed temperature linearly ramped of the domain (simulating the hot surface) and combined convective and radiative heat exchange with the environment inside the smoker at the other end.

Mass transfer

The model tracks the generation of pyrolysis gas and tar vapour resulting from the thermal decomposition of wood. It then simulates the transport of these volatiles, along with an initial inert gas (Nitrogen, N_2), through the dynamically evolving porous structure. This flow is driven by pressure gradients, which are established due to gas generation and thermal expansion, and is modelled using Darcy's Law. Mass outflow from the system at one of the boundaries is also accounted for.

Pyrolysis Kinetics

A simplified, yet commonly employed, three-reaction parallel scheme is used to represent the primary decomposition of wood into gas, tar and solid char. The temperature dependence of these reaction rates is described by the Arrhenius law, capturing the strong influence of temperature on the pyrolysis process.

The numerical solution of this coupled system of equations is achieved using the Finite Volume Method (FVM) for spatial discretisation combined with an implicit Backward Euler scheme for time integration to ensure stability. A segregated, iterative solution algorithm, featuring nested loops, is employed to handle the inherent non-linearities and the strong coupling between the different physical processes. The model is implemented with the MATLAB (The MathWorks, Inc.) programming environment.

This chapter will provide a comprehensive description of the model's formulation. This includes a detailed presentation of the governing PDEs that represent the underlying physics, the constitutive relations and critical assumptions underpinning the model, the numerical discretisation techniques employed, the specifics of the iterative solution algorithm designed to manage the non-linear couplings, the insights into the practical implementation details derived from the underlying code. Additionally, a critical evaluation of the model's assumptions and their potential limitations will be discussed. The overarching objective is to furnish a thorough and transparent understanding of the model's theoretical basis, its operational capabilities and its inherent constraints, thus establishing the methodological foundation for its subsequent application in simulating and analysing wood pyrolysis processes.

6.2 Conceptual model and Underlying Assumptions

The physical system being modelled is a one-dimensional representation of a bed of wood material (e.g., chips or shavings) of Length L. Initially, this bed consists of solid wood and interstitial

nitrogen gas (N_2) filling its pores. When subjected to heating from an external source (e.g., a hot plate at x=0), the wood undergoes a series of transformations: drying (if moisture is present, though the current model focuses on dry wood pyrolysis), decomposition into char, pyrolysis gas and tar vapour. These generated volatiles mix with the initial nitrogen and migrate through the porous structure, driven by developing pressure gradients (Figure 6-1).

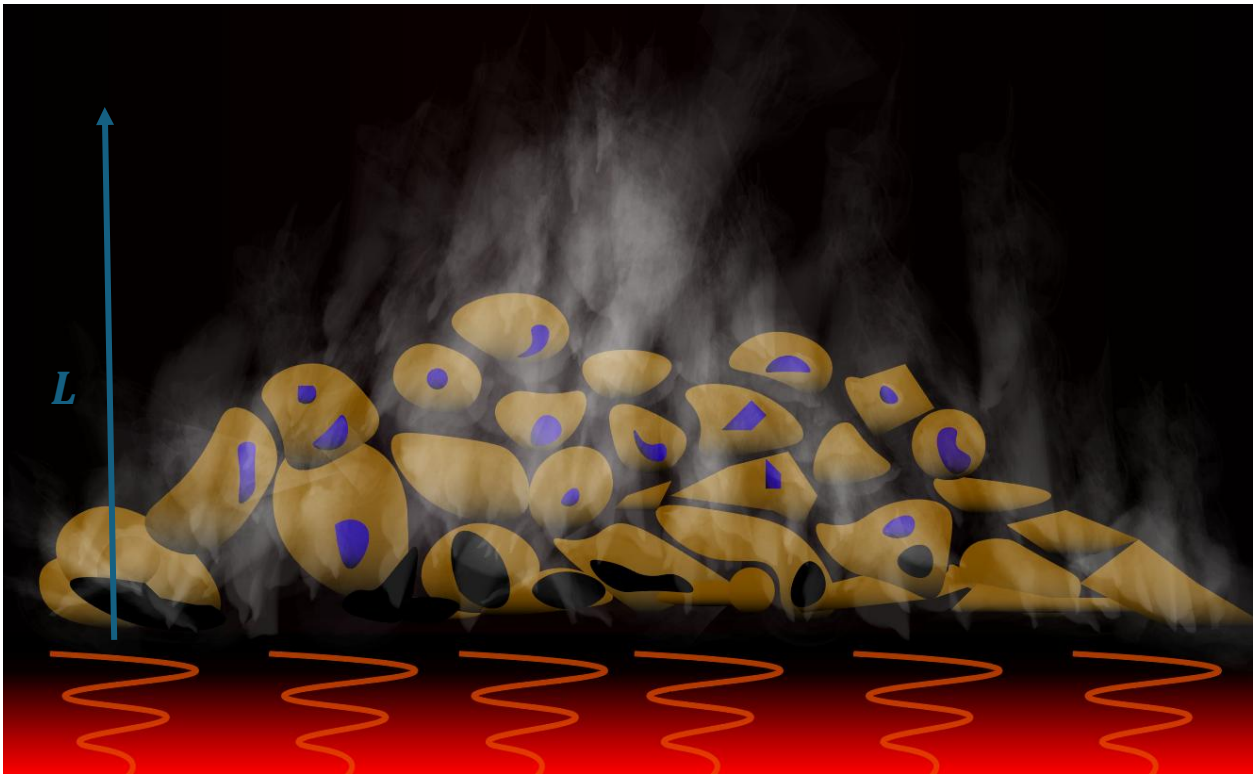

Figure 6-1: Schematic representation of the one-dimensional heat and mass transfer model for the hot plate smoker. A thermally thick, porous bed of wood chips (length L) is heated from the impermeable bottom boundary (x = 0) by a hot plate. Conductive heat transfer drives the primary pyrolysis of the wood matrix, generating solid char and volatile gases. The resulting internal pressure gradient forces the volatile mixture (Pyrolysis gas and tar) upward through the bed via Darcy flow. As these volatiles migrate toward the open top boundary (x = L), they transport heat convectively and undergo temperature-dependent secondary reactions before exiting as culinary smoke.

Numerous mathematical models for drying and pyrolysis of biomass have been represented in the literature over several decades, each varying in complexity and the specific phenomena addressed, often constrained by the prevailing assumptions and available computational resources (Di Blasi, 1996; Gronli *et al.*, 2000; Park, Atreya and Baum, 2010; Lam, Oyedun and Hui, 2012; Bennadji *et al.*, 2013; Werner, Pommer and Broström, 2014). Many earlier models treated wood as a one-dimensional continuous solid heated by an external source, focusing on heat conduction within the solid and heat generation/consumption by reactions. Drying models have often approximated the

drying rate using either an Arrhenius-type expression (Hagge and Bryden, 2002) or a more detailed thermal model considering phase change (Gronli *et al.*, 2000). Pyrolysis reactions have typically been described using global kinetic schemes, ranging from simple one-step models with fixed product yields to more comprehensive multi-step schemes that attempt to capture primary and secondary reactions and variable product yields (Thurner and Mann, 1981; Miller, Richard Steven; Bellan, 1997).

The model developed in this work builds upon these foundations, focusing on the coupled transport phenomena within a porous medium framework. The detailed differential equations and constitutive relations are based on the following key assumptions:

1. **<u>One-Dimensional Porous Medium</u>**

The wood bed is treated as a one-dimensional (1D) continuum, where all dependent variables change only along the x-axis and time. This implies uniformity in the transverse directions. The material is considered a porous medium, with distinct solid and fluid (gas) phases.

- *Justification & Implication:* This is a common simplification for fundamental studies and is computationally less expensive than 2D or 3D models. It is most applicable to scenarios where heat and mass transfer are predominantly in one direction, such as in a thin, wide slab heated on one face or for understanding core behaviour before extending to higher dimensions. For a packed bed of wood chips, as might be found in commonly used hot plate smokers, the 'porosity' in this 1D model refers to the inter-particle void space and the 'solid' phase properties are those of the wood chips themselves. This assumption means that phenomena like cracking of individual large wood pieces are neglected. It's also acknowledged that thermal and transport properties of wood (like permeability) are inherently anisotropic due to its grain structure; for instance, permeability can be orders of magnitude greater along the grain than across it (Siau, 1984). However, in this 1D packed

bed context, an effective isotropic permeability representing the bulk flow resistance of the bed is considered.

2. **Local Thermal Equilibrium (LTE)**

The gas phase species and the solid phase species within any given infinitesimal control volume are assumed to be at the same temperature.

- *Justification & Implication:* This assumption simplifies the energy conservation formulation by requiring only a single temperature field to be solved, rather than separate energy equations for the solid and gas phases coupled by an interfacial heat transfer term. LTE is generally considered valid when the rate of heat exchange between the phases is much faster than the rate of heat transport by conduction or advection through the bulk medium, or the rates of heat generation/consumption by reactions (Sinha *et al.*, 2000).

3. **Negligible Diffusive Mass Transport in Pores (Advection dominated)**

The transport of gaseous species within the pore space due to molecular diffusion (Fickian diffusion) is considered negligible compared to transport by bulk flow (advection) driven by pressure gradients.

- *Justification & Implication:* This assumption is often justified by considering the Péclet number for mass transfer ($Pe_m = \frac{uL}{D_{AB}}$), where u is the characteristic gas velocity (m/s), L is the characteristic length (m) (e.g., particle diameter or bed height), and D_{AB} is the mass diffusion coefficient (m^2/s). If $Pe_m \gg 1$, advection dominates. In many pyrolysis systems, significant gas generation leads to appreciable convective velocities, potentially making diffusive fluxes secondary (Chan, Kelbon and Krieger, 1985). This simplifies the species conservation equations by omitting the diffusive flux terms. However, in regions of very

low gas velocity or near impermeable boundaries, diffusion could play a more important role.

4. **Darcy's Law for Fluid Flow**

The flow of the gas mixture through the porous wood bed is assumed to be governed by Darcy's Law.

- *Justification & Implication:* Darcy's Law describes slow, viscous-dominated flow in porous media and is valid when the Reynolds number based on pore dimensions ($Re_p = \frac{\rho f u d_p}{\mu}$, where d_p is a characteristic pore or particle diameter) is small (typically $Re_p < 1 \; to \; 10$) (Nield and Bejan, 2013). This implies that inertial effects are negligible compared to viscous effects. For packed beds of very small particles (e.g., <90 μm), the resulting pore diameters and interstitial velocities might indeed keep Re_p low. If particle sizes were larger, or flow rates significantly higher (e.g., due to very rapid gas generation), inertial effects might become important, necessitating the use of extended Darcy models like the Darcy-Forchheimer equation. The current model assumes the Darcy regime holds.

5. **Ideal Gas Behaviour**

All gaseous species (N_2, pyrolysis gas and tar vapour) are assumed to behave as ideal gases.

- *Justification & Implication:* This allows the use of the ideal gas law to relate pressure, temperature, solid density and molar mass of the gas mixture. This is generally a reasonable assumption at the high temperatures and moderate (near-atmospheric) pressures encountered in smoke generation applications. Deviations might occur for tar vapours near their condensation temperatures or at very high pressures. Molecular weight of gas is set to 0.044 kg/mol (CO_2), tar to 0.078 kg/mol (Benzene) and nitrogen to 0.028 kg/mol.

6. **Constant Solid Density**

The density of the solid material itself (solid density) (i.e., wood or char substance, excluding pores) is assumed to be constant throughout the process. Mass loss from the solid phase is thus directly reflected as an increase in porosity.

- *Justification & Implication:* This simplifies the calculation of porosity evolution. While some minor changes in bulk density can occur, the dominant effect on bulk density and porosity comes from the conversion of solid mass into volatiles.

7. **No Macroscopic Shrinkage or Swelling**

The overall external dimensions of the 1D domain are assumed to remain fixed. Changes in solid volume are manifested solely as changes in internal porosity.

- *Justification & Implication:* Real wood often undergoes significant shrinkage (or sometimes swelling) during pyrolysis. Neglecting this simplifies the grid and the formulation, but it means the model does not capture changes in bulk sample dimensions, which can affect heat transfer (e.g., contact with heat source) and internal stresses. This assumption is more valid for loosely packed beds of small particles where individual particle shrinkage might not drastically alter the bulk bed dimensions.

8. **Simplified Gas Mixture properties**

While the model tracks individual gas species densities and calculates an average mixture molar mass, the transport properties of the gas mixture viscosity μ, (Pa.s), thermal conductivity k_{gas} (W/(m K)) and its specific heat capacity, $c_{p,gas}$, (J/(kg K)) are assumed to be constant or represented by a single value (e.g., that for nitrogen or an average pyrolysis gas).

- *Justification & Implication:* The actual properties of the gas mixture change with its composition and temperature. Using constant values is a simplification for tractability. More complex mixing rules could be implemented but would add computation overhead.

The impact of this assumption depends on how much the actual mixture properties deviate from the assumed constant values over the range of conditions encountered.

9. <u>Tar Phase Change</u>

Tar is modelled in both vapor (mobile in pores) and liquid (immobile in solid matrix so technically a solid) forms, with phase transitions occurring via first-order kinetics at a temperature threshold ($T_{condensation}$). Condensation ($T < T_{condensation}$) and vaporization ($T \geq T_{condensation}$) include latent heat effects, assuming rapid transitions (large rate constants $k_{cond}, k_{vap} \approx 10^3$ s^{-1}), no effect on porosity or permeability from liquid tar, and exact mass conservation via volume-fraction scaling ($\delta m_{vapour} = -\delta m_{condensate}$ per bulk volume).

- *Justification & Implication:* This extends the model to capture realistic tar behaviour in temperature gradients where vapours condense in cooler zones (especially important in thermally thick beds of wood). The kinetic approach (first order relaxation) simplifies complex thermodynamics (e.g., no equilibrium vapour pressure) and assumes near instantaneous phase changes. Volume scaling ensures precise mass balance despite different storage fractions (pores vs. solid matrix) which minimises overall mass error.

The physical problem being modelled, therefore, is that of a one-dimensional bed of wood (initially dry or containing bound moisture, though the current formulation focuses on dry wood decomposition reactions primarily) of known length, L. This bed is situated in what is assumed to be a stagnant, inert gaseous environment. At one boundary (x = 0), the wood bed is subjected to a heat flux, simulating contact with or proximity to a hot surface. This heat flux can be modelled in various ways, such as a fixed temperature, a temperature ramp or a constant radiative/conductive heat flux. The current model implements a fixed incident heat flux. As the wood bed is heated, energy is initially transferred primarily by conduction through the bed. This energy input leads to an increase in temperature, which then initiates and drives the pyrolysis reactions. These reactions consume wood and produce char, pyrolysis gas and tar vapour, altering the local bulk density and

porosity of the material. The generation of gases leads to an increase in local pressure, inducing a flow of these gases through the porous structure towards regions of lower pressure, typically out of the system. The ongoing reactions also have thermal effects (endothermic or exothermic), contributing to the overall energy balance. Consequently, complex, transient gradients of temperature, pressure, species concentrations and material properties are established and evolve throughout the domain. The model seeks to capture this dynamic evolution.

6.2.1 Governing partial differential equations

Based on the conceptual model and assumptions outlined above, the following set of partial differential equations describes the conservation of mass, momentum and energy within the 1D porous medium (bed of wood).

6.2.1.1 Mass Conservation of Solid Species

The change in bulk density of wood (ρ_{wood}) over time is solely due to its consumption by pyrolysis reactions:

$$\frac{\partial \rho_{wood}}{\partial t} = -r_{wood} \left[\frac{kg}{m^3 s}\right] \tag{6.1}$$

Where r_{wood} represents the total reate of wood consumption [kg/m^3 s] due to all pyrolysis reactions leading to gas, tar and char.

Similarly, char (ρ_{char}) is formed as a solid product of wood pyrolysis and is assumed to be non-reactive under the inert pyrolysis conditions considered (i.e., no secondary gasification of char):

$$\frac{\partial \rho_{char}}{\partial t} = r_{char} \left[\frac{kg}{m^3 s}\right] \tag{6.2}$$

Where r_{char} is the rate of char formation from wood [kg/m^3 s]. The densities ρ_{wood} and ρ_{char}, [kg/m^3] are 'bulk' densities, meaning mass per unit total volume of the porous medium.

6.2.1.2 Mass Conservation of Gaseous Species

For each gaseous species i (where i can be N_2, pyrolysis gas or tar vapour) present in the pore volume of the medium, the general conservation equation in one dimension, accounting for accumulation within the pores, advective transport and generation/consumption, is given by:

$$\frac{\partial(\varepsilon\rho_{i,pore})}{\partial t} + \frac{\partial(\rho_{i,pore}\, u)}{\partial x} = S_i \left[\frac{kg}{m^3 s}\right] \tag{6.3}$$

Here:

- ε is the porosity (dimensionless), representing the fraction of the total volume occupied by gas.
- $\rho_{i,pore}$ is the intrinsic density of gaseous species i within the pores (mass of species i per unit volume of pore space) [kg/m^3].
- u is the superficial gas velocity (Darcy velocity) in the x-direction [m/s]. This is the volumetric flow rate per unit cross-sectional area of the porous medium.
- S_i is the volumetric source rate of species i [$\frac{kg}{m^3 s}$].
    - For Nitrogen (N_2), assumed to be inert: $S_{N_2} = 0$.
    - For pyrolysis gas: $S_{gas} = R_{gas}$, where R_{gas} is the rate of pyrolysis gas formation from wood.
    - For tar vapour: $S_{tar} = R_{tar}$, where R_{tar} is the rate of tar vapour formation from wood.

For tar vapour, the right-hand side (the source term S_i) additionally includes a phase change contribution $\pm S_{phase}$ from condensation (negative, vapour loss) or vaporisation (positive, vapour gain) as detailed in section 6.2.1.5.

It is important to note the distinction between $\rho_{i,pore}$ (intrinsic density in pores) and the term $\varepsilon\rho_{i,pore}$which represents the mass of species i per unit *total volume* of the porous medium.

6.2.1.3 Momentum Conservation for Fluid Flow (Darcy's Law)

As discussed above, the flow of the gas mixture through the porous medium is described by Darcy's law. This law relates the superficial velocity u to the gradient of pressure P, the dynamic viscosity of the gas mixture μ, and the permeability of the porous medium K_{perm}:

$$u = -\frac{K_{perm}}{\mu}\frac{\partial P}{\partial x}\left[\frac{m}{s}\right] \tag{6.4}$$

The dynamic viscosity μ [Pa.s] is assumed constant in this model, which is a simplification as it typically depends on gas composition and temperature. The permeability K_{perm} [m^2] is a property of the porous structure and as will be detailed later, evolves as pyrolysis progresses. Darcy's law essentially replaces a full momentum balance (like Navier-Stokes equations) under conditions of slow, viscous-dominated flow.

6.2.1.4 Energy Conservation

Consistent with the assumption of Local Thermal Equilibrium (LTE), a single energy conservation equation is formulated for the entire porous medium (solid and gas phases combined). This equation accounts for transient energy storage, advection of energy by the flowing gas mixture, conduction of heat through the effective medium and the heat generated or consumed by the pyrolysis reactions:

$$\frac{\partial\left(\rho c_p\right)_{eff}T}{\partial t} + \frac{\partial\left(\rho c_p\right)fuT}{\partial x} = \frac{\partial}{\partial x}\left(\kappa_{eff}\frac{\partial T}{\partial x}\right) + Q_{source} + Q_{phase} \tag{6.5}$$

Where:

- T is the local temperature [K]

- $(\rho c_P)_{eff}$ is the effective volumetric heat capacity of the porous medium [J/m^3 K]. This term represents the energy stored per unit volume per unit temperature change. It is typically calculated as a weighted average of the solid and fluid phase contributions:

$$\rho_s c_{P,s} + \varepsilon(\rho_g c_{p,g}) \tag{6.6}$$

- where, $\rho_s c_{P,s} = \rho_{wood} c_{P,wood} + \rho_{char} c_{P,char}$ is the volumetric heat capacity of the combined solid phases (wood and char), and the $\varepsilon(\rho_g c_{p,g}) = \sum_j (\varepsilon \rho_{j,pore} c_{P,j})$ is the volumetric heat capacity of the gas mixture in the pores. However, the provided code simplifies the accumulation term in the energy equation to primarily consider the solid phase heat capacity:

$$(\rho c_P)_{eff} T \approx (\rho_{wood} c_{P,wood} + \rho_{char} c_{P,char}) T \tag{6.7}$$

This approximation assumes that the thermal mass of the gas within the pores is negligible compared to that of the solid matrix, i.e., $(1-\varepsilon)(\rho_s c_{P,s}) \gg \varepsilon(\rho_g c_{P,g})$, which is generally valid due to the much lower density of gases compared to solids.

$(\rho c_p)_g$ is the volumetric heat capacity of the fluid (gas) mixture being convected [J/m^3 ·K], calculated as: $\sum_j (\rho_{j,pore} c_{P,j})$. The model uses a single $c_{P,gas}$ value for all gaseous species in this term.

κ_{eff} is the effective thermal conductivity of the porous medium [W/m K]. This accounts for heat conduction through both the solid matrix and the gas within the pores. The following volume averaging model is used:

$$\kappa_{eff} = (1-\varepsilon)\kappa_{solid,eff} + \varepsilon \kappa_{gas} \tag{6.8}$$

Where $\kappa_{solid,eff}$ is the effective thermal conductivity of the solid matrix e.g., a mass fraction weighted average of κ_{wood} and κ_{char} as used in the model:

$$\kappa_{solid,eff} = \frac{\rho_{wood}\kappa_{wood} + \rho_{char}\kappa_{char}}{\rho_{wood} + \rho_{char}} \qquad for\ \rho_{wood} + \rho_{char} > 0 \tag{6.9}$$

And κ_{gas} is the thermal conductivity of the gas phase (constant in this model). More sophisticated models for κ_{eff} considering pore structure and tortuousity exist but add unnecessary computational complexity for this 1D application. Q_{surce} is the volumetric heat source or sink term due to the pyrolysis reactions [W/m^3]. It accounts for both the endothermic primary decomposition of wood and the highly exothermic secondary reactions of tar vapour. It is calculated directly from the reaction rates of the reactants (r_{wood} and $r_{tar,secondary}$) and their respective specific enthalpies:

$$Q_{source} = \left(-\Delta H_{primary} r_{wood}\right) + \left(-\Delta H_{secondary} \cdot r_{tar,secondary}\right) \tag{6.10}$$

Where $\Delta H_{primary}$ is the specific enthalpy of primary pyrolysis, per unit mass of wood consumed [J/kg], and $\Delta H_{secondary}$ is the specific heat of the secondary tar reactions [J/kg]. The term Q_{phase} represents the latent heat released or absorbed during tar phase changes as described in section 6.2.1.5.

6.2.1.5 Tar Phase Change (Condensation and Vaporisation)

Primary pyrolysis reactions produce tar initially as a vapour within the pores. As vapour migrates into cooler regions, it can condense into liquid tar, which is assumed to remain immobile in the solid matrix. Conversely, liquid tar can re-vaporise in hotter regions. This phase change is represented as a local, temperature dependent first order process that redistributes tar mass between vapour and liquid phases, while also introducing a latent heat effect in the energy balance.

The vapour mass conservation equation (Equation 6.3) is augmented with a phase-change source term S_{phase}. Where $S_{phase}$is ≤ 0 for condensation and > 0 for vaporisation.

Liquid tar density, $\rho_{tar,liquid}$, evolves according to:

$$\frac{\partial \rho_{tar,liquid}}{\partial t} = -S_{phase}$$

with no transport, since the liquid is assumed immobile and stored in the solid fraction.

6.2.2 Pyrolysis Kinetics – Primary reactions

This work adopts a widely recognised approach where wood is treated as a composite material consisted of its three primary (Chapter 3) pseudo-components: hemicellulose (H), cellulose (C) and lignin (L). Each of these components is assumed to decompose independently yet concurrently, with distinct first-order Arrhenius kinetics. To capture the inherent variability in their decomposition behaviour, the kinetics of each pseudo-component were described using an empirical distribution activation energy model (DAEM).

For hemicellulose, cellulose and lignin alike, 25 sets of Arrhenius parameters (A and E) were determined experimentally from TGA experiments (Chapter 3, table 3-1). Each set of parameters was treated as a discrete sub-reaction within the DAEM, with the initial partial bulk density of each pseudo-component distributed equally across the 25 sets. This empirical DAEM approach reflects the experimentally observed heterogeneity of bond environments in the wood polymers better than a single global rate constant.

The primary decomposition of each pseudo-component into char and volatiles is represented as:

$$\text{Hemicellulose } (\rho_H) \xrightarrow{k_H} \text{char}_H + \text{Volatiles}_H$$

$$\text{Cellulose } (\rho_C) \xrightarrow{k_C} \text{char}_C + \text{Volatiles}_C$$

$$\text{Lignin } (\rho_L) \xrightarrow{k_L} \text{char}_L + \text{Volatiles}_L$$

The rate of consumption for each solid pseudo-component, ρ_i, is assumed to be first order with respect to its remaining bulk density. The rate of change of the partial bulk density of each component i is therefore expressed as:

$$\frac{\partial \rho_{i,s}}{\partial t} = -k_{i,s} \cdot \rho_{i,s} \tag{6.11}$$

where $\rho_{i,s}$ is the partial bulk density of the wood pseudo-component i in set s (kg m^{-3}), and $k_{i,s}$ is the Arrhenius rate constant:

$$k_{i,s} = A_{i,s} \exp\left(-\frac{E_{i,s}}{RT}\right) \tag{6.12}$$

where $A_{i,s}$ is the pre-exponential factor (s^{-1}), $E_{i,s}$ is the activation energy for the decomposition reaction (J/mol), R is the universal gas constant (8.314 J mol^{-1} K^{-1}).

The total partial bulk density of each pseudo-component is obtained by summing over its 25 sets. This independent parallel reaction scheme across hemicellulose, cellulose and lignin captures their decomposition behaviour over different temperature regimes, while also accounting for the experimental variability observed in chapter 3.

6.2.3 Pyrolysis Kinetics – secondary reactions

Following the initial primary decomposition of the main biomass pseudo-components (H, C, L), a complex mixture of volatiles compounds is released. A significant fraction of these primary volatiles consists of "tar", which, in the context of this model is a lumped representation of various condensable organic compounds. These primary tar species are not thermodynamically stable and can undergo further chemical transformations, commonly referred to as secondary reactions, particularly at high temperatures. The tar fraction is fixed at 0.6 of primary volatiles and therefore 0.4 for primary gas. These values were in the ranges reported in literature (Bridgwater, 2006; Ringer *et al.*, 2006; Brownsort, 2009; Brown *et al.*, 2011).

These secondary reactions are important as they influence the final distribution and composition of pyrolysis products. They can lead to the formation of lighter, non-condensable gases (secondary gas) through cracking reactions or conversely to the formation of carbonaceous solids (secondary char) through polymerisation and condensation reactions. Understanding and reasonably modelling these transformations are essential for predicting overall process yields and the quality of the smoke.

In this numerical model, the complex network of secondary tar reactions is simplified into two dominant, parallel pathways. These reactions are assumed to be kinetically controlled and are modelled as first-order processes with respect to the local volumetric concentration of tar within the porous wood matrix. The temperature dependence of these reactions is described by the Arrhenius law.

The two modelled secondary reaction pathways are:

$$\text{Tar } (\rho_T) \xrightarrow{k_{T_G}} \text{Secondary Gas}$$

$$\text{Tar } (\rho_T) \xrightarrow{k_{T_C}} \text{Secondary Char}$$

Secondary gas is a lumped species representing non-condensable gases such as H_2, CO, CO_2, CH_4 and other light hydrocarbons formed from tar decomposition. Secondary char represents the solid carbonaceous material deposited within the pores or on the surface of the existing char matrix due to tar conversion. Table 6-1 below shows the values of the Arrhenius parameters used in this model.

Table 6-1: Arrhenius parameters for tar secondary reactions

Reaction	*A (1/s)*	*E (kJ/mol)*	*Source*
Tar -> Secondary gas	1.48E+06	144	(Chan *et al.*, 1985)
Tar -> Secondary char	1.00E+05	108	(Di Blasi, 1993)

6.2.4 Tar phase change Kinetics

Tar is represented as a vapour (mobile in pores) and solid (immobile in solid matrix) forms, with phase transitions modelled as first-order processes triggered by local temperature relative to a condensation threshold. Large rate constants ($\approx 10^3$ 1/s) enforce near-instantaneous switching. This approach is supported by several researchers who have implemented similar schemes to handle this phenomenon (Dufour *et al.*, 2011; Ding *et al.*, 2025). The formulation preserves tar mass by applying equal and opposite source terms to vapour and liquid bulk densities per unit volume. Latent heat is added consistently to the energy balance. Liquid tar is assumed to not affect porosity or permeability – in reality, tar would block pores and affect permeability.

6.2.5 Porosity Evolution

The porosity (ε) of the wood bed changes as the solid wood decomposes into char and volatile products, therefore altering the volume fraction occupied by the solid material. Assuming that the solid density of the material itself, $\rho_{solid,max}$ (i.e., the density of the wood/char substance excluding any internal pores within the particles, if one were to consider them), remains constant, the porosity can be related to the bulk densities of wood and char:

$$\varepsilon = 1 - \frac{\rho_{wood} + \rho_{char}}{\rho_{solid,max}} \tag{6.15}$$

In this formulation, ρ_{wood} and ρ_{char} are the mass of wood and char per unit *total volume* of the porous medium. The model calculates $\rho_{solid,max}$ based on the initial wood bulk density $\left(\rho_{wood,initial}\right)$ and initial porosity $(\varepsilon_{initial})$:

$$\rho_{solid,max} = \frac{\rho_{wood,initial}}{1 - \varepsilon_{initial}} \tag{6.16}$$

This $\rho_{solid,max}$ is then used as a constant throughout the simulation. This approach effectively assumes that the volume initially occupied by solid wood, upon decomposition, either remains as solid char or becomes void space (pore). The model also implements clamping of porosity within certain bounds:

$$0.3 \leq \varepsilon < 0.7$$

To prevent numerically unrealistic values for example if the char is denser than wood:

$$\varepsilon < \varepsilon_{initial}$$

or

$$\varepsilon > 1$$

This clamping, however, is an artificial constraint and ideally, the physical model should prevent such occurrences. As noted in the above assumptions, this model neglects macroscopic shrinkage or swelling of the bed.

6.2.6 Permeability Model

The permeability (K_{perm}) of the porous bed is a critical parameter that governs the ease with which gases can flow through it. Permeability is highly dependent on the pore structure (size, connectivity, tortuousity) and thus changes significantly as porosity evolves during pyrolysis. The model employs an empirical correlation, similar in form to the Kozeny-Carmen equation, to relate permeability to the current porosity ε and its initial value $\varepsilon_{initial}$:

$$K_{perm} = K_{perm,initial} \left(\frac{\varepsilon}{\varepsilon_{initial}}\right)^3 \left(\frac{1-\varepsilon_{initial}}{1-\varepsilon}\right)^2 [m^2] \quad (6.17)$$

Where $K_{perm,initial}$ is the initial permeability of the unreacted wood bed. This equation qualitatively captures the expected strong increase in permeability as porosity increases (due to

wood consumption). The $(1-\varepsilon)$ term in the denominator reflects the hydraulic radius concept. The model includes checks to ensure $(1-\varepsilon)$ is not zero and also enforces a minimum value for K_{perm} to maintain numerical stability, especially at very low porosities or if ε approaches 1.

6.2.7 Equation of State for Gas Mixture (Ideal Gas Law)

The mixture of gaseous species (N_2, pyrolysis gas and tar vapour) within the pores is assumed to obey the ideal gas law. The total pressure P [Pa] is related to the total molar density of the gas mixture, or equivalently, to its total mass density $\rho_{mix,pore}$ [kg/m^3 of pore volume], local temperature T [K], and the average molar mass of the gas mixture M_{mix} [kg/mol]:

$$P = \frac{\rho_{mix,pore} RT}{M_{mix}} \; [Pa] \tag{6.18}$$

Where R is the universal gas constant. The total density of the gas mixture in the pores is simply the sum of the intrinsic densities of its components:

$$\rho_{mix,pore} = \rho_{N_2,pore} + \rho_{gas,pore} + \rho_{tar,pore} \tag{6.19}$$

The average molar mass M_{mix} is calculated based on the molar fraction $y_i = (\frac{\rho_{j,pore}}{M_j})/(\sum_k \rho_{k,pore}/M_k)$ and the Molar masses (M_j) of the individual gaseous components (k denotes the gas species):

$$M_{mix} = \sum_j y_j M_j = y_{N_2} M_{N_2} + y_{gas} M_{gas} + y_{tar} M_{tar} \tag{6.20}$$

The molar masses of methane is used as a proxy for the molar mass for the pyrolysis gas, and the molar mass of benzene is used as a proxy for the molar mass of tar vapours.

6.2.8 Thermo-physical Properties

A key simplification in the current model is the assumption that several thermophysical properties remain constant throughout the simulation, independent of temperature or composition. Specifically, the intrinsic specific heat capacities of wood ($c_{P,wood}$), char ($c_{P,char}$) and a generic gas phase ($c_{P,gas}$), the intrinsic thermal conductivities of wood (k_{wood}) and char (k_{char}), and the gas phase (k_{gas}) and the dynamic viscosity of the gas mixture (μ) are all treated as constant parameters. However, an apparent heat capacity, thermal conductivity are calculated and updated after each time step which are dependent on temperature and extent of reaction. This is adopted for computational convenience, as implementing temperature and composition-dependent properties would add significant complexity. However, it is acknowledged that in reality, these properties exhibit variation, particularly with temperature (Incropera *et al.*, 2006; Di Blasi, 2008).

6.3 Numerical Solution Method

The system of coupled non-linear governing partial differential equations along with their auxiliary relationships are solved numerically. The chosen method involves spatial discretisation using the Finite Volume Method (FVM) (refer to appendix 5 for the method description) and temporal discretisation using an implicit scheme.

The finite Volume Method is particularly well-suited for conservation problems of this nature because it ensures that physical quantities like mass and energy are conserved both locally (within each discrete control volume) and globally over the entire computational domain. This is achieved by formulating the discretised equations based on flux balances across the boundaries of these control volumes (Suhas V. Patankar, 1980).

Adaptive time-stepping is used to dynamically adjust the size of the time increment (Δt) during the simulation. The time step is refined or coarsened based on criteria such as the rate of change of key variables (e.g., species consumption, temperature changes due to reactions etc.), Courant-

Friedrichs-Lewy (CFL)-like conditions for advective transport, and the convergence behaviour of the iterative solver. This approach enhances computational efficiency by using small time steps only when rapid changes occur, while employing larger steps during periods of slower evolution, without compromising accuracy or stability.

A segregated iterative approach was employed to handle the strong coupling between the various physical processes (e.g., heat transfer, mass transfer, chemical reactions, fluid flow etc.). The governing equations for temperature, pressure, gas velocities and individual species densities are solved sequentially within a nested iterative structure. This involves outer loops to converge temperature with reaction kinetics and material properties and inner loops to converge the coupled gas phase dynamics (pressure, velocity, species concentrations and mixture properties). This iterative segregation allows for the linearization of non-linear terms and the manageable solution of individual equation sets, which are then iterated until overall convergence is achieved for each time step.

These chosen numerical strategies provide a comprehensive and robust framework for simulating the complex, transient and coupled multi-physics phenomena inherent in the pyrolysis of wood.

6.3.1 Space and time discretisation

The transformation of the governing partial differential equations (PDEs) into a system of algebraic equations for numerical solution was done by using specific space and time discretisation techniques. For space discretisation, the finite volume method was used and for time discretisation a first order implicit Euler scheme was utilised. This section outlines these fundamental numerical procedures as applied in this model.

6.3.2 Discretisation of the solid phase equations

The decomposition of each wood pseudo component (H, C, L) is modelled as a set of first order Arrhenius reaction, one for each of the 25 empirical (Chapter 3, table 3-1; A and E) pairs determined in:

$$\frac{\partial \rho_{j,i}}{\partial t} = -k_{j,i}(T_i)\rho_{j,i} \quad where\ i \in \{H, C, L\} \tag{6.21}$$

Where k_i is the temperature dependent reaction rate constant based in equation (6.21) above. The mass fractions of H, C and L used were 0.2, .45 and 0.35, respectively. These were approximated from experimentally determined values for kānuka wood (Appendix 3).

These Ordinary differential equations (ODEs) are solved for each control volume using an implicit Euler method for stability, especially with stiff reaction rates at high temperatures. For a component j at node i, $\rho_{j,i}$:

$$\frac{\rho_i^{n+1} - \rho_i^n}{\Delta t} = -k_i(T^{n+1})\rho_i^{n+1} \tag{6.22}$$

Where the superscript n and n+1 denote the current and the future time step, respectively and $T_i^{n+1,*}$ represents the temperature at node i used for evaluating the rate constant, typically the latest available estimate from the iterative solution scheme for the energy balance.

Re-arranging for ρ_i^{n+1}:

$$\rho_{j,i}^{n+1} = \frac{\rho_{j,i}^n}{1 + k_{j,i}(T^{n+1,*})\Delta t} \tag{6.23}$$

This update is performed independently at each spatial node for each decomposing component j. Importantly, the update for the $\rho_{j,i}^{n+1}$ depends only on local conditions at node I (i.e.,

$\rho_{j,i}^{n}$ and $T_i^{n+1,*}$) and not directly on the densities of component j at neighbouring nodes ($\rho_{j,i+1}^{n+1}$ and $\rho_{j,i-1}^{n+1}$) during specific time steps.

The bulk density of char $\rho_{char,i}$ (kg m^{-3}), at each node I is updated based on the principle of accumulation from two sources: primary decomposition of wood components and secondary reactions of tar.

The governing principle is that the change in char bulk density is due to these formation pathways. The numerical update is performed directly by summing the increments of char formed at node I during the time step Δt:

$$\rho_{char,i}^{n+1} = \rho_{char,i}^{n} + (Primary\ char\ formation)_{i,\Delta t} + (Secondary\ char\ formed)_{i,\Delta t} \quad (6.24)$$

The primary char formed at node i during Δt, is calculated from the mass of each wood pseudo component j that decomposed at node I during Δt and their respective dimensionless char yields ($Y_{char,j}$), determined experimentally (Chapter 3):

$$(Primary\ char\ formed)_{i,\Delta t} = \sum_{j=H,C,L} Y_{char,j}\left(\rho_{j,i}^{n} - \rho_{j,i}^{n+1}\right) \quad (6.25)$$

This term represents the sum of char yield from the actual amount of each wood component that has just decomposed in the current Δt.

The secondary char bulk density formed at node i during Δt, is calculated from the rate at which tar vapour is converted into solid char. This reaction is governed by its own Arrhenius kinetics and depends on the locally availability of tar vapour and the local temperature.

The secondary char formed can therefore be expressed as:

$$(Secondary\ char\ formed)_{i,\Delta t} = R_{tar \rightarrow char,i} \cdot \Delta t \tag{6.26}$$

Where $R_{tar \rightarrow char,i}$ is:

$$R_{tar \rightarrow char,i} = k_{tar \rightarrow char}(T_i) \cdot \left(\varepsilon_i \rho_{tar,pore,i}\right) \tag{6.27}$$

Where ε is the local porosity (-), and $\rho_{tar,pore,i}$ is the solid density of tar vapour in the pores at node i.

It's important to note that the amount of tar available for this reaction, $\rho_{tar,pore,i}$ is determined by the solution of the gaseous species transport which will follow.

6.3.3 Pressure and Velocity Field

The movement of the gaseous mixture (comprising N_2, pyrolysis gas and tar vapour) through the porous structure of the pyrolysing bed of wood is driven by pressure gradients. This section outlines the formulation and numerical solution for the gas pressure and velocity fields.

DARCY'S LAW FOR GAS VELOCITY

The superficial gas velocity, u_g (m s^{-1}), through the porous medium is described by Darcy's Law. For one-dimensional system, this is expressed as:

$$u_g = -\frac{K_{perm}}{\mu}\frac{\partial P}{\partial x} \tag{6.28}$$

Where P is the local gas pressure (Pa), K_{perm} is the local permeability of the porous medium (m^2). Permeability is a function of the evolving porosity of the material, μ is the dynamic viscosity of the

gas mixture (Pa. s), assumed constant in this model and $\frac{\partial P}{\partial x}$ is the pressure gradient in the x-direction (bottom of bed to the top of the bed).

THE PRESSURE EQUATION

The pressure equation is derived to solve for the pressure field. This equation originates from the principle of overall gas mass conservation, combined with Darcy's Law and an equation of state for the gas mixture. The general form of the gas mass continuity equation is:

$$\frac{\partial(\varepsilon \cdot \rho_{mix,pore})}{\partial t} + \frac{\partial(\rho_{mix,pore} u_g)}{\partial x} = S_{volatiles,total} \tag{6.29}$$

Here the $\rho_{mix,pore}$ is the intrinsic density of the gas mixture in the pores, (kg m^{-3} of pore volume) and $S_{volatiles,total}$ is the total volumetric source rate of all gaseous species from pyrolysis reactions (kg m^{-3} total volume s^{-1}).

Assuming the gas mixture behaves as an ideal gas, its density is related to pressure (P), temperature (T) and average molar mass (M_{mix}) by

$$\rho_{mix,pore} = \frac{PM_{mix}}{RT} \tag{6.30}$$

Substituting this and Darcy's Law for u_g into the continuity equation yields a non-linear partial differential equation for pressure P expressed as follows:

$$\frac{\partial}{\partial t}\left(\varepsilon \frac{PM_{mix}}{RT}\right) + \frac{\partial}{\partial x}\left(\left(\frac{PM_{mix}}{RT}\right)\left(-\frac{K_{perm}}{\mu}\frac{\partial P}{\partial x}\right)\right) = S_{volatiles,total} \tag{6.31}$$

This can be written more compactly as:

$$\frac{\partial}{\partial t}\left(\varepsilon\frac{PM_{mix}}{RT}\right)-\frac{\partial}{\partial x}\left(\frac{PM_{mix}K_{perm}}{RT\mu}\frac{\partial P}{\partial x}\right)=S_{volatiles,total} \tag{6.32}$$

This equation is highly non-linear due to the following reasons:

1. The second term on the left-hand side contains the product $P\frac{\partial P}{\partial x}$ (which can be expressed as $\frac{1}{2}\frac{\partial P^2}{\partial x}$ if other coefficients are constant).
2. The term M_{mix} (average molar mass of the gas mixture), T (temperature), ε (porosity) and K_{perm} (permeability) can themselves be functions of the solution variables (e.g., M_{mix} depends on gas composition, T is solved by the energy equation, ε and K_{perm}change with solid decomposition which is temperature-dependent).

Therefore, this was discretised using the FVM for the space terms and the Implicit Euler Scheme for the time derivative. This process is applied to each control volume CV_i (centred at node i) of length Δx.

The general FVM procedure involves integrating this PDE over $CV_i$and over the time interval from $t^n$to t^{n+1}.

$$\int_{t^n}^{t^{n+1}}\int_{CV_i}\frac{\partial}{\partial t}\left(\varepsilon\frac{PM_{mix}}{RT}\right)dVdt-\int_{t^n}^{t^{n+1}}\int_{CV_i}\frac{\partial}{\partial x}\left(\frac{PM_{mix}K_{perm}}{RT\mu}\frac{\partial P}{\partial x}\right)dVdt = \int_{t^n}^{t^{n+1}}\int_{CV_i}S_{volatiles,total}\,dVdt \tag{6.33}$$

Applying the implicit Euler scheme (evaluating space terms at time t^{n+1}) and dividing by the control volume $A_{cross}\Delta x$ (assuming A_{cross}= 1 for one-dimensional flux density) and by Δt

for the first term, we obtain a balance equation for node i. We will evaluate each term individually here.

The Continuous transient term is:

$$\frac{\partial}{\partial t}\left(\varepsilon \frac{PM_{mix}}{RT}\right) \tag{6.34}$$

When integrating over $\Delta t = t^{n+1} - t^{n}$ and dividing by Δt, this becomes:

$$\frac{\left(\varepsilon \frac{PM_{mix}}{RT}\right)_i^{n+1} - \left(\varepsilon \frac{PM_{mix}}{RT}\right)_i^{n}}{\Delta t} \tag{6.35}$$

In this model, the term representing the gas mass at the previous time step n is expressed using the total mixture density at that time, $\left(\varepsilon \rho_{mix,pore}\right)_i^n$. The term for the new time step, n+1, explicitly involves the pressure at the next time step P_i^{n+1} .Therefore, the discretised accumulation term is formulated as:

$$\frac{1}{\Delta t}\left[\left(\varepsilon \frac{M_{mix}}{RT}\right)_i^{n+1,*} P_i^{n+1} - \left(\varepsilon \rho_{mix,pore}\right)_i^{n}\right] \tag{6.36}$$

The first term in the equation above $\left(\varepsilon \frac{PM_{mix}}{RT}\right)_i^{n+1,*}$ is evaluated using the most current estimate of porosity, ε_i^{n+1}, average molar mass $M_{mix,i}^{n+1}$ and temperature T_i^{n+1} available at the current stage of the iterative solution within the time step.

The total gas mass in the pores at node i from the previous time step, n is used and is represented by the second term $\left(\varepsilon \rho_{mix,pore}\right)_i^n$.

The term $\left(\varepsilon \frac{M_{mix}}{RT\Delta t}\right)_i^{n+1,*} P_i^{n+1}$ contributes to the diagonal element D_i of the coefficient matrix $[\boldsymbol{A}_P]$.

The term $\frac{-(\varepsilon \rho_{mix,pore})_i^n}{\Delta t}$ is known and becomes part of the right-hand side vector element $(b_P)_i$.

The continuous space divergence term, representing Darcy flux, is:

$$-\frac{\partial}{\partial x}\left(\frac{PM_{mix}K_{perm}}{RT\mu}\frac{\partial P}{\partial x}\right) \tag{6.37}$$

Recognising that,

$$\rho_{mix,pore} = \frac{PM_{mix}}{RT} \tag{6.38}$$

This term can be written as:

$$-\frac{\partial}{\partial x}\left(\rho_{mix,pore}\frac{K_{perm}}{\mu}\frac{\partial P}{\partial x}\right) \tag{6.39}$$

This term is also non-linear because $\rho_{mix,pore}$ itself depends on pressure, P. To obtain a linear algebraic system for P^{n+1}, the $\rho_{mix,pore}$ within the flux coefficient is evaluated using values from previous state, denoted here as $\rho_{mix,pore,old}$. The model uses gas densities from the previous time step for this purpose. Therefore, the term effectively discretised is:

$$-\frac{\partial}{\partial x}\left(\rho_{mix,pore,old}\frac{K_{perm}}{\mu}\frac{\partial P}{\partial x}\right) \tag{6.40}$$

Integrating this linearised term over control volume I (from bottom face to top face) gives:

$$-\frac{1}{\Delta x}\left[\left(\rho_{mix,pore,old}\frac{K_{perm}}{\mu}\frac{\partial P}{\partial x}\right)_b-\left(\rho_{mix,pore,old}\frac{K_{perm}}{\mu}\frac{\partial P}{\partial x}\right)_t\right]^{n+1} \tag{6.41}$$

The pressure gradients $\frac{\partial P}{\partial x}$ at the faces are approximated using central differences:

Bottom face (b) flux out of CV_i:

$$(F_P)_b=\left(\rho_{mix,pore,old}\frac{K_{perm}}{\mu}\right)_b\frac{P_{i+1}^{n+1}-P_i^{n+1}}{\Delta x} \tag{6.42}$$

Top face (t) flux out of CV_i

$$(F_P)_t=\left(\rho_{mix,pore,old}\frac{K_{perm}}{\mu}\right)_t\frac{P_i^{n+1}-P_{i-1}^{n+1}}{\Delta x} \tag{6.43}$$

The net flux contribution to the balance for CV_i is $((F_P)_t-(F_P)_b)/\Delta x$.

The permeability K_{perm} and viscosity μ at a face are derived from harmonic mean of the values of the adjacent nodes:

$$K_{perm,face}=\frac{2K_{perm,i}\cdot K_{perm,i+1}}{K_{perm,i}+K_{perm,i+1}} \tag{6.44}$$

The same idea for the other mobility variables. The density of the gas mixture $\rho_{mix,pore,old}$ at the faces is calculated as the arithmetic mean of the two nodes on either side of the face (i-1 and i or 1+1 and i).

MATRIX FORMULATION FOR THE PRESSURE FIELD

The set of N_x discretised equations for pressure forms a linear algebraic system:

$$[\boldsymbol{A}_P][\boldsymbol{P}^{n+1}] = [\boldsymbol{b}_P] \tag{6.45}$$

where,

- $[\boldsymbol{P}^{n+1}]$ is the $N_x \times 1$ column vector of unknown pressures $\left[P_1^{n+1}, P_2^{n+2}, \dots, P_{N_x}^{n+1}\right]^T$.
- $[\boldsymbol{A}_P]$ is the $N_x \times N_x$ coefficient matrix, which is tri-diagonal.
- $[\boldsymbol{b}_P]$ is the $N_x \times 1$ known right-hand side column vector.

The general structure of $[\boldsymbol{A}_P]$ is:

$$[\boldsymbol{A}_P] = \begin{pmatrix} D_1 & B_1 & 0 & \cdots & 0 & 0 \\ T_2 & D_2 & B_2 & \cdots & 0 & 0 \\ 0 & T_3 & D_3 & \cdots & 0 & 0 \\ \vdots & \vdots & \ddots & \ddots & \vdots & \vdots \\ 0 & 0 & \cdots & T_{N_x-1} & D_{N_x-1} & B_{N_x-1} \\ 0 & 0 & \cdots & 0 & T_{N_x} & D_{N_x} \end{pmatrix} \tag{6.46}$$

$$D_i = \left(\varepsilon \frac{M_{mix}}{RT\Delta t}\right)_i^{n+1,*} + \frac{1}{\Delta x}\left(\rho_{mix,pore,old} \frac{K_{perm,face}}{\mu}\right)_b^{(i)} + \frac{1}{\Delta x}\left(\rho_{mix,pore,old} \frac{K_{perm,face}}{\mu}\right)_t^{(i)} \tag{6.47}$$

Top off diagonal $T_i = (A_P)_{i,i-1}$ (for i > 1):

$$T_i = \frac{1}{\Delta x}\left(\rho_{mix,pore,old} \frac{K_{perm}}{\mu}\right)_t^{(i)} \tag{6.48}$$

Bottom off diagonal $T_i = (A_P)_{i,i-1}$ (for i > N_x):

$$B_i = \frac{1}{\Delta x}\left(\rho_{mix,pore,old}\frac{K_{perm}}{\mu}\right)_b^{(i)} \tag{6.49}$$

Right-hand side vector elements$(b_P)_i$:

$$(b_P)_i = \frac{1}{\Delta t}\left(\varepsilon\rho_{mix,pore}\right)_i^n + \left(S_{volatiles,total}\right)_i^{n+1} \tag{6.50}$$

This includes the gas mass from the previous time step and the current estimate of the total gas generation rate.

BOUNDARY CONDITIONS

Node 1 (Bottom boundary, x = 0, Hot Plate): Impermeable wall.

The gas velocity is zero, $u_g(x=0)=0$. From Darcy's Law, this implies that $\left.\frac{\partial P}{\partial x}\right|_{x=0} = 0$ (zero Neumann condition). This condition is implemented by modifying the first row of the matrix $[\boldsymbol{A}_P]$ and the first element of $[\boldsymbol{b}_P]$ to reflect zero flux.

This means:

$$D_1 = \frac{1}{\Delta t}\left(\frac{\varepsilon M_{mix}}{RT}\right)_1^{n+1,*} \tag{6.51}$$

Node N_x (Top boundary, x=L, Outlet): Outlet to smoker headspace

The gas is assumed to exit to a region of constant atmospheric pressure, P_{atm}. The flux at the outlet face (top face of node N_x) is driven by the pressure difference $(P_{N_x}^{n+1} - P_{atm})$ over a length half of Δx. This is implemented as a mixed (Robin-type) boundary condition by modifying the equation for node N_x. Therefore, for $i = N_x$:

$$T_{N_x} = -\frac{1}{\Delta x^2}\left(\rho_{mix,pore,old}\frac{K_{perm,face}}{\mu}\right)_T^{N_x} \tag{6.52}$$

$$D_{N_x} = \frac{1}{\Delta t}\left(\frac{\varepsilon M_{mix}}{RT}\right)_1^{n+1,*} - \frac{1}{\Delta x^2}\left(\rho_{mix,pore,old}\frac{K_{perm,face}}{\mu}\right)_T^{N_x} + \frac{1}{\Delta x}\left(\frac{\rho_{mix,pore,old,N_x}K_{perm,N_x}}{\mu\left(\frac{\Delta x}{2}\right)}\right) \tag{6.53}$$

For the right-hand side vector, for $1 \leq i < N_x$:

$$(b_P)_i = \left(\frac{\varepsilon\rho_{mix,pore}}{\Delta t}\right)_i^n + \left(S_{volatiles,total}\right)_i^{n+1} \tag{6.54}$$

For $i = N_x$ (Outlet node):

$$(b_P)_{N_x} = \frac{1}{\Delta t}\left(\varepsilon\rho_{mix,pore}\right)_{N_x}^n + \left(S_{volatiles,total}\right)_{N_x}^{n+1} + \frac{1}{\Delta x}\left(\frac{\rho_{mix,pore,old,N_x}K_{perm,N_x}}{\mu\left(\frac{\Delta x}{2}\right)}\right)P_{atm} \tag{6.55}$$

6.3.4 Gaseous Phase Species Transport and Reactions

The transport equation for the intrinsic pore density $\rho_{j,pore}$ (kg of species j per m^3 of pore volume) of any given species j is given as:

$$\frac{\partial\left(\varepsilon\rho_{j,pore}\right)}{\partial t} + \frac{\partial\left(u_g\rho_{j,pore}\right)}{\partial x} = S_j^{vol} \tag{6.56}$$

FVM DISCRETISATION

This PDE is discretised using the FVM for space terms and the implicit Euler Scheme for the time derivative. For a control volume CV_i centred at node i of length Δx, the discretised equation is:

$$\frac{\left(\varepsilon\rho_{j,pore}\right)_i^{n+1}\left(\varepsilon\rho_{j,pore,i}\right)_i^n}{\Delta t} + \frac{\left(u_g\rho_{j,pore}{}_{j,b}\right)_i - \left(u_g\rho_{j,pore}{}_{j,t}\right)_i}{\Delta x} = \left(S_j^{vol}\right)^{n+1} \qquad (6.57)$$

The first term represents the rate of change of mass of species j stored within the pore volume CV_i (Accumulation term). The component $\frac{1}{\Delta t}\left(\varepsilon\rho_j\right)_i^{n+1}$ contributes to the diagonal coefficient (interior nodes) of the linear system for $\rho_{j,i}^{n+1}$. The porosity, ε_i^{n+1} is the updated value for the current iteration.

The component $\frac{1}{\Delta t}\left(\varepsilon\rho_j\right)_i^n$ is known from the previous time step and is moved to the right-hand side of the algebraic equation.

The face densities $\left(\rho_{j,pore}\right)_b^{(i)}$ and $\left(\rho_{j,pore}\right)_t^{(i)}$ are determined using a first-order upwind scheme based on the direction of the face velocities $u_{g,b}^{(i)}$ and $u_{g,t}^{(i)}$ obtained from the solution to the pressure equation.

For the bottom face (b) of CV_i:

If $u_{g,b}^{(i)} \geq 0$ (outflow), then $\left(\rho_{j,pore}\right)_b^{(i)} = \rho_{j,i}^{n+1}$.

If $u_{g,b}^{(i)} < 0$ (inflow), then $\left(\rho_{j,pore}\right)_b^{(i)} = \rho_{j,i+1}^{n+1}$.

For the top face (t) of CV_i

If $u_{g,t}^{(i)} \geq 0$ (inflow), then $\left(\rho_{j,pore}\right)_b^{(i)} = \rho_{j,i-1}^{n+1}$

If $u_{g,t}^{(i)} < 0$ (outflow), then $\left(\rho_{j,pore}\right)_b^{(i)} = \rho_{j,i}^{n+1}$.

These flux contributions are incorporated into the diagonal and off-diagonal coefficients of the matrix $[\boldsymbol{A}_g]$ (Similar to the pressure field matrix above). The use of upwinding is chosen for its numerical stability in advection-dominated transport.

The reaction term $\left(S_j^{vol}\right)_i^{n+1}$ is the net volumetric rate of production or consumption (secondary tar cracking) of gaseous species j at node i. For Nitrogen (N_2) this is zero. For the other pyrolysis products, it is calculated based on the Arrhenius law for each gas species. These terms are evaluated using the latest available temperature and densities and are included in the right-hand side vector $[\boldsymbol{b}_g]$.

The set of N_x discretised equations for each species j forms a linear algebraic system:

$$[\boldsymbol{A}_g][\rho_g^{n+1}] = [\boldsymbol{b}_g] \tag{6.58}$$

Where $[\rho_g^{n+1}]$ is the $N_x \times 1$ column vector of unknown intrinsic pore densities $[\rho_{g,1}^{n+1}, \rho_{g,2}^{n+1}, \dots, \rho_{g,N_x}^{n+1}]^T$. $[\boldsymbol{A}_g]$ is the $N_x \times N_x$ coefficient matrix, which is tri-diagonal. And $[\boldsymbol{b}_g]$ is the $N_x \times 1$ known right-hand side column vector.

The structure of $[\boldsymbol{A}_g]$ is like that above for the pressure field.

The diagonal elements (D):

$$D_i = \frac{1}{\Delta t}\varepsilon_i^{n+1} + \frac{1}{\Delta x}\max\left(u_{g,b}^{(i)}, 0\right) + \frac{1}{\Delta x}\max\left(-u_{g,t}^{(i)}, 0\right) \tag{6.595}$$

This term combines the contributions from accumulation and the advective fluxes leaving CV_i. This forces the flow out by fixing the velocity to 0 if the flow out of the bottom is negative and if the flow from the top is negative.

The bottom off diagonals

$$B_i = -\frac{\max\left(u_{g,b}^{(i)}, 0\right)}{\Delta x} \tag{6.60}$$

Again, these forces flow out of the domain from the bottom to the top.

The top off diagonals

$$Top_i = -\frac{\max\left(-u_{g,t}^{(i)}, 0\right)}{\Delta x} \tag{6.61}$$

The right-hand side vector, $[\boldsymbol{b}_g]$

$$\left[\boldsymbol{b}_g\right]_i = \frac{1}{\Delta t}\left(\varepsilon\rho_g\right)_i^n + S_{g,i}^{vol} \tag{6.62}$$

This term includes the species densities from the previous time step and the net volumetric reaction source (or sink in terms of tar because of secondary reactions) term. Boundary inflow terms also contribute to $\left[\boldsymbol{b}_g\right]_i$ for boundary nodes.

6.3.4.1 Tar Phase Change

After secondary tar reactions, phase change is applied locally at each node *i* using the current node temperature. This updates $\rho_{tar,tar}$ and $\rho_{tar,liquid}$ and the associated latent heat is added to the energy solver.

For **condensation** ($T_i < T_{condensation}, \rho_{tar,pore}(i) > 0$):

$$\dot{m}_{cond} = \min\left[\frac{\varepsilon\rho_{tar,pore}}{\Delta t}, k_{cond}\varepsilon\rho_{tar,pore}\right],$$

$$S_{phase} = -\dot{m}_{cond},$$

$$Q_{phase} = +\Delta h_{latent}\dot{m}_{cond}.$$

For **<u>vaporisation</u>** ($T_i \geq T_{condensation}, \rho_{tar,pore}(i) > 0$):

$$\dot{m}_{vap} = \min\left[\frac{(1-\varepsilon)\rho_{tar,liquid}}{\Delta t}, k_{vap}(1-\varepsilon)\rho_{tar,liquid}\right],$$

$$S_{phase} = +\dot{m}_{vap},$$

$$Q_{phase} = -\Delta h_{latent}\dot{m}_{vap}.$$

Here S_{phase} is the volumetric source term added to the vapour transport equation. The liquid tar density is updated explicitly after each time step as

$$\rho^{n+1}_{tar,liquid,i} = \rho^{n}_{tar,liquid,i} - S_{phase,i}\Delta t$$

This Euler update ensures δm_{vapour}=δm_{liquid} per bulk volume, preserving tar mass.

6.3.4.2 Boundary conditions

Node 1 (bottom boundary, x=0) same as pressure field, Impermeable wall. The superficial gas velocity therefore is zero. Consequently, there is no advective flux into CV_1 from the bottom face. The coefficient $B_1 = \left[\boldsymbol{A}_g\right]_{1,0}$ is effectively zero. Therefore, the equation for node 1 only involves D_1 and T_1.

Node N_x (top boundary, x=L), gas flow out. The conditions at the top face of the CV_{N_x} depends on the flow direction $u^{(N_x)}_{g,top}$.

A similar upwind scheme used in the pressure field is used here to evaluate the gas outlet (gas leaving the domain).

This tri-diagonal matrix system is solved for each gaseous species using MATLAB™'s built in backslash operator within the inner iterative loop of the simulation.

6.3.5 Discretisation of the energy equations

The energy conservation equation is also discretised using the FVM in space and the implicit Euler scheme in time. This process is applied to each control volume (CV_i) centred at node i and lengthΔx. The resulting discretised algebraic equation for node i can be expressed as a balance of energy change and fluxes:

$$\left(\left(\rho c_p\right)_{eff,i}\frac{T_i^{n+1}-T_i^n}{\Delta t}\right)\Delta x+\left[\left(F_{adv,top}^{n+1}\right)_i-\left(F_{adv,b}^{n+1}\right)_i\right] \\ -\left[\left(F_{con,top}^{n+1}\right)_i-\left(F_{con,b}^{n+1}\right)_i\right]+\left(Q_{source,i}+Q_{phase,i}\right)^{n+1}\Delta x \tag{6.63}$$

Here the advective flux is $F_{adv}=u\rho_g c_{p,g}T$ and the conductive flux is $F_{con}=-k_{eff}\frac{\partial T}{\partial x}$.

The first time (accumulation) is evaluated using the effective properties at node i from the current iteration (updated based on evolving solid densities and porosity). The second term, the advective terms use a first order upwind scheme for stability. For the top face:

- If $u_{top}^{n+1}\geq 0$ (outflow from top), then $F_{adv,top}^{n+1}=u_{top}^{n+1}\rho_{g,w}^{n}T_{i-1}^{n+1}$ (using previous time-step densities to handle the non-linearity)
- If $u_{top}^{n+1}<0$ (inflow), then $F_{adv,top}^{n+1}=u_{top}^{n+1}\rho_{g,w}^{n}T_{i}^{n+1}$ (using previous time-step densities to handle the non-linearity)

Similar logic applies to the bottom face.

For the conductive heat fluxes, a central difference scheme was used where $F_{con,top}^{n+1}=-k_{eff,top}\frac{T_i^{n+1}-T_{i-1}^{n+1}}{\Delta x}$, where $k_{eff,top}$ is the harmonic mean of the nodes i-1 and i (or can also be written as node i-1/2). The source term, $Q_i^{n+1}=\left(Q_{source,i}+Q_{phase,i}\right)^{n+1}$, is evaluated using

the current temperature estimate to compute the reaction rates from the primary pyrolysis of H, C and L, secondary tar reactions and tar phase change.

Boundary conditions

- Left hand boundary (i=1, x=0, Hot plate): A prescribed wall temperature (Dirichlet condition) is applied to represent contact with a hot plate. The plate temperature is ramped linearly from an initial value of 300 K up to a target value, after which it is held constant. At this boundary, the node temperature is directly set to the current plate temperature each timestep. No advective flux occurs through this wall (impermeable boundary).
- Right hand boundary (i=Nx, x=L, Top of bed/Outlet): Combined convective and radiative heat exchange environment is imposed,

$$q_{out} = h_{conv}(T_{Nx}^{n+1} - T_{env}) + \epsilon_{surf}\sigma((T_{Nx}^{n+1})^4 - T_{env}^4) \quad (6.64)$$

This introduces a non-linear term (to the power of 4) and lagged temperature values from the latest outer iteration are used to handle this non-linearity. In the current formulation, the right-hand boundary exchanges heat by convection and radiation with an environment temperature T_{env}. To approximate the rapid radiative heating of the headspace above the chip bed, T_{env} is taken equal to the hot plate boundary temperature. This assumption reflects a closed, isothermal enclosure in which the surrounding gas heats more quickly than the wood. A more detailed treatment could decouple T_{env} from the plate temperature and model the headspace heating separately.

Solution procedure

The discretised equations form a tri-diagonal system of the form:

$$A_T T^{n+1} = b_T \tag{6.65}$$

where,

- Diagonal $A_T(i,i)$: Accumulation coefficient and the central advective and conductive terms
- Off diagonal $A_T(i,i-1), A_T(i,i+1)$: Top/bottom fluxes
- Right-hand side $b_T(i)$: Accumulation using $T_i^n + \text{source} + \text{boundary contributions}$.

The matrix is assembled in the outer iterative loop (coupled with reaction rates and properties updates). Non-linearities are handled by evaluating at the latest iterate, with under-relaxation used to help with convergence. The system is solved using MATLAB's backslash operator. Convergence is checked against a temperature tolerance across iterations, if all node temperatures change less than the tolerance value, then the procedure moves forward in time. This segregated approach nests within the overall time step, ensuring coupling with pressure and species.

The phase change update for tar (section 6.4.4.1.) is performed in the outer iterative loop, after secondary reactions but before solving the gaseous species transport and porosity/permeability updates. This ensures coupling with the current temperature estimate and updates $\rho_{tar,pore}$ for advection in the species equations while incorporating latent heat into Q_i for the energy solver.

6.4 Model Validation

Checking a numerical model against real world data is a crucial step to make sure it's reliable and useful. This section validates the one-dimensional (1D) heat and mass transfer model that was developed. The main way this is done is by comparing the model's predictions for temperature at the centre and char yield over time with experimental results. The data comes from tests on a smoker with a 44 mm thick packed bed of wood. The predictive model was validated against

experimental data obtained from this pilot-scale smoker rig operating at a target peak temperature of 280°C. The selection of 280 °C as the validation baseline was practically driven. Operational guidelines for premium consumer culinary smoke generators such as the Breville – The Smoking gun® recommend operating within the 260 – 280 °C temperature range, as empirical consensus indicates this regime produces the most desirable, balanced smoke aroma profile while minimising acrid high-temperature products. Consequently, the initial bench-scale smoker experiments were specifically designed and conducted within this optimal temperature window. This practical dataset was therefore the most appropriate choice to validate the predictive capabilities of the 1D model under realistic culinary smoking conditions.

The smoker itself is cylindrical, but a 1D Cartesian coordinate system was chosen to model it. This decision is grounded in the physics of the heat and mass transfer occurring within the system.

In the cylindrical smoker, heat is supplied from the outer wall and moves inwards towards the perforated central core. This setup creates a strong radial temperature gradient, making the inward radial direction the dominant path for heat transfer. Similarly, as pyrolysis reactions occur, volatile gases are generated and move towards the centre to exit, establishing a dominant mass transfer path that is also radial. In comparison, temperature and concentration gradients along the length of the smoker and around its circumference are negligible. The model, therefore, focuses on capturing the phenomena along this single, dominant path.

The choice of Cartesian coordinates over cylindrical coordinates to represent this path is a pragmatic simplification. A cylindrical coordinate system would account for the fact that the cross-sectional area for heat and mass flow decreases as you move from the outer wall towards the centre. However, for the relatively thin packed bed in this study (44 mm), the change in radius is small compared to the overall radius. As a result, the effect of this changing area is minimal compared to the driving force of the temperature gradient itself. A Cartesian model assumes a constant cross-

sectional area along the path. For a thin bed, this approximation is reasonable and captures the essential physics without adding unnecessary complexity.

Ultimately, the pyrolysis reactions that determine char yield are strongly dependent on temperature. The model's primary task is to accurately predict the temperature history of the wood bed and the product yields. By correctly modelling the heat transfer along the dominant radial path, the 1D Cartesian model provides an accurate temperature profile, which in turn leads to a valid prediction of the reaction progress and mass loss. Therefore, while geometrically simplified, the model is physically representative of the key transport phenomena.

6.4.1 Temperature Profile

Figure 6-2 below shows how the model's temperature prediction stacks up against the experimental results.

Overall, the model does a good job. It follows the S-shaped curve we'd expect, with a slow start, then a period of fast heating, before levelling off at the end.

However, there's a clear difference at the start of the process, up until the temperature gets to about 100°C. The experimental data shows the temperature stalling around 100°C for a while, but the model doesn't quite capture this. This is because of a key simplification made in the model: the model assumes the wood is completely dry. There's always some moisture in the wood. Evaporation this water off takes energy, which causes the temperature to plateau at 100°C.

The key result is that once you get past this drying stage, the model matches the experimental data well. This gives us confidence that the parts of the model dealing with heat transfer and pyrolysis reactions of wood are working well.

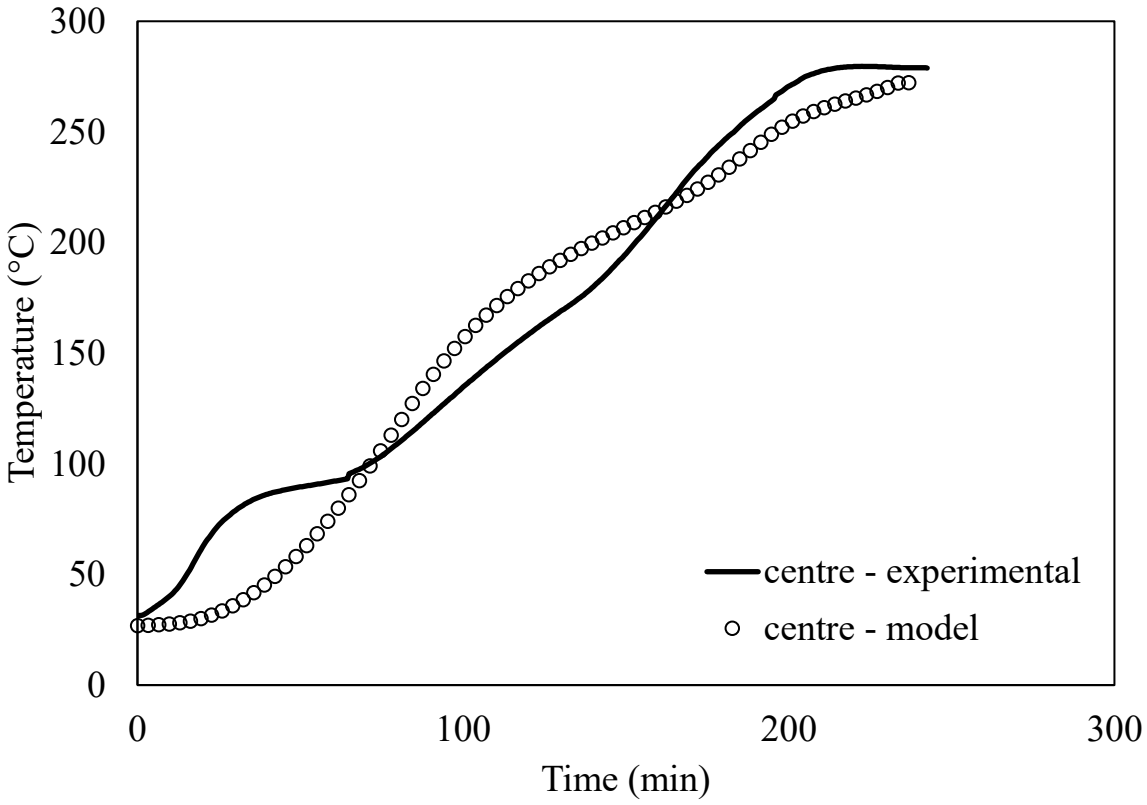

Figure 6-2: Comparison of the centre temperature (22 mm into the 44 mm wood bed) of the model (circles) vs. the experimental results (solid line), heated at 3°C/min up to 280°C

6.4.2 Char yield

The mass loss curves show us how much of the solid material is left as the wood breaks down to form smoke. Looking at Figure 6-2 above, the model's prediction for char yield matches the experimental results closely.

The simulation correctly shows when the wood starts to lose mass and follows the same general trend (Figure 6-3). The model does predict slightly less char at the end than was measured, which suggests the settings for the chemical reactions could be tweaked a bit for a better fit, or that the averaging approached used here is not the best approach for quantifying the mass loss. Still, the fact that it replicates the overall process of decomposition helps to validate the reaction scheme used.

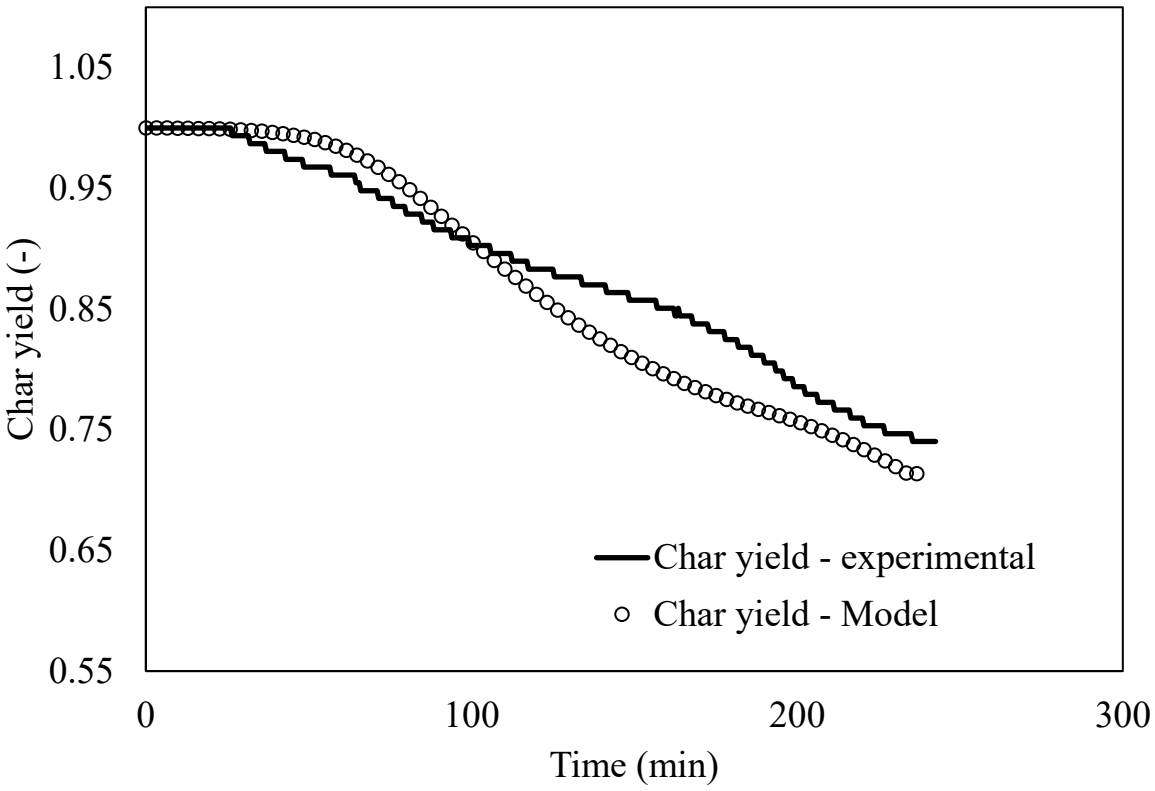

Figure 6-3: Comparison of the char yield, taken as the spatial average (circles) across the packed bed vs. the experimental results (solid line), heated at 3°C/min up to 280°C

6.4.3 Quantitative assessment of Model fit

While visual inspection of the graphs is useful, a statistical analysis provides a more objective measure of the model's performance. The coefficient of determination (R^2) is used to quantify the "goodness of fit" by measuring the proportion of the variance in the experimental data that is predictable from the model.

For the temperature profile, the calculated R^2 value is 0.9292. This is a high value and indicates that the model successfully explains 93.0% of the variation in the experimental temperature data. This strong statistical agreement, despite the visible discrepancy during the initial drying phase, is driven by the model's good performance in the pyrolysis dominant region (above 100°C), confirming the fundamental validity of the heat transfer calculations.

The model's performance is predicting the char yield is even stronger. The analysis yielded an R^2 value of 0.9672, signifying that the model accounts for 96.7% of the variance observed in the experimental mass loss data. Such a high level of agreement provides robust validation for the reaction kinetics scheme implemented in the model, confirming its ability to predict the rate and extent of solid-state conversion. These high R^2 values for both key parameters provide strong quantitative evidence that the model is a reliable representation of the physical process.

6.5 Conclusion

To sum up, even with its simplification the 1D model has proven to be a solid and useful tool for understanding what happens in the smoker. The validation work shows that using a 1D model was a reasonable approach. It predicts the temperature and mass loss well, particularly once the wood is dry and pyrolysis is the main thing happening. This is quantitatively confirmed by high coefficients of determination for both temperature (R^2=0.93) and char yield (R^2=0.967).

The main reason for the difference between the model and the real data is that the model doesn't account for moisture in the wood. Because of this, the model is 'good enough' for validating the main heat transfer and pyrolysis parts of the simulation. It's valid for predicting what happens when dry wood breaks down under these conditions to form smoke.

For future work, the model could be made better by adding water and the energy needed to evaporate it off. This would make the model more accurate over the whole process and allow it to be used for wood with different moisture levels.

This page is intentionally left blank

CHAPTER 7

One-Dimensional Model: Results & Discussion

7.1 Introduction

This chapter uses the one-dimensional hot plate pyrolysis model from Chapter 6 to examine how controllable operating variables shape thermal histories and product distributions in a thermally thick bed of wood chips. The model resolves coupled heat transfer, Darcy transport of volatiles, primary kinetics for hemicellulose, cellulose and lignin and simplified secondary tar pathways. Because aroma is carried predominantly by condensables in practical smoking systems, tar here is allocated by formation temperature as a proxy for the relative contribution of aroma bearing compound classes, using three temperature bands (200-300, 300-400 and ≥400 °C). This proxy is calibrated qualitatively to the GC/MS results summarised in table 4-4 (chapter 4) but it is only an indicative mapping; inferences about aroma are treated as tendencies rather than identifications.

A one-factor-at-a-time sweep was carried out around a common baseline (44 mm bed, kinetics and properties as in Chapter 6). Three levers were investigated: bed depth L = 11, 22, 44 and 66 mm; heating rate, β = 3, 20 and 100 K/min; and final treatment temperature T_f = 260, 350, 450 and 580 °C. For the bed depth study, β = 20 K/min and T_f = 450 °C were held fixed to isolate transport effects for a representative smoking temperature; for the final temperature study, β = 20 K/min and L = 44 mm were fixed to examine how extending thermal severity redistributes tar across bands; for the heating rate study, L = 44mm and T_f = 580 °C were fixed to ensure the core traversed the full temperature range of slow/intermediate pyrolysis and T_f set brackets on the GC/MS window used previously. All simulations use dry wood and neglect moisture evaporation; secondary chemistry is treated in a reduced form sufficient to capture self-heating and tar attrition trends.

These assumptions limit absolute predictions but are adequate for comparing relative shifts in thermal history and the proxy-based allocation of condensables.

Table 7-1: Summary of initial bed properties, thermal constants, and Arrhenius reaction kinetics used to model the pyrolysis of kānuka wood, compiled from literature and experimental data.

Parameter	*Symbol*	*Value*	*Unit*	*Reference*
Initial porosity	ε_0	0.3	-	-
Initial permeability	K_0	1×10^{-17}	m²	(Park *et al.*, 2010)
Initial bulk density of wood	$\rho_{wood,0}$	780	kg/m³	-
Effective thermal conductivity of wood	k_{eff}	0.45	W/(m·K)	(Di Blasi, 2008)
Base thermal conductivity of char	k_{char}	0.15	W/(m·K)	-
Thermal conductivity of gas	k_{gas}	0.03	W/(m·K)	(Di Blasi, 2008)
Effective specific heat capacity of wood	$C_{p,wood}$	1760	J/(kg·K)	(Di Blasi, 1996)
Specific heat capacity of char	$C_{p,char}$	1595	J/(kg·K)	(Dupont *et al.*, 2014)
Specific heat capacity of gas	$C_{p,gas}$	1000	J/(kg·K)	(Di Blasi, 2008)
Gas dynamic viscosity	μ	3×10^{-5}	Pa·s	-
Pre-exponential factor (hemicellulose)	$A_{hemicellulose}$	4.37×10^{9}	s^{-1}	Chapter 3, Table 1
Activation energy (hemicellulose)	$E_{hemicellulose}$	119	kJ/mol	Chapter 3, Table 1
Pre-exponential factor (cellulose)	$A_{cellulose}$	3.2×10^{14}	s^{-1}	Chapter 3, Table 1
Activation energy (cellulose)	$E_{cellulose}$	186.1	kJ/mol	Chapter 3, Table 1
Pre-exponential factor (lignin)	A_{lignin}	13.4	s^{-1}	Chapter 3, Table 1
Activation energy (lignin)	E_{lignin}	38.8	kJ/mol	Chapter 3, Table 1
Pre-exponential factor (tar to secondary gas)	$A_{gas,2°}$	1.48×10^{6}	s^{-1}	(Chan *et al., 1985*)
Activation energy (tar to secondary gas)	$E_{gas,2°}$	144	kJ/mol	(Chan *et al., 1985*)
Pre-exponential factor (tar to secondary char)	$A_{char,2°}$	1×10^{5}	s^{-1}	(Di Blasi, 1993)
Activation energy (tar to secondary char)	$E_{char,2°}$	108	kJ/mol	(Di Blasi, 1993)
Heat of pyrolysis (primary)	$\Delta H_{primary}$	~(500)	kJ/kg	Chapter 5
Heat of secondary tar reaction	$\Delta H_{secondary}$	~(-700)	kJ/kg	Chapter 5

7.2 Results & Discussion

7.2.1 Effect of Bed Depth

At a fixed ramp (20 K/min) and the same final treatment temperature of 450 °C, changing the bed depth alters the allocation of modelled tar across formation bands (table 7-2) and the centre temperature histories (Figure 7-1). If the working assumption holds that the formation temperature of tar is a reasonable proxy for the dominant aroma classes, then increasing bed depth would suggest a gradual tilt from 300-400°C associated compounds towards 200-300 °C associated compounds.

Table 7-2: Final product yields (% of initial wood mass) for varying bed depths.

	Tar (%)		
Bed Depth (mm)	**200-300 °C**	**300-400 °C**	**≥400°C**
11	20.78%	23.35%	1.37%
22	20.45%	23.84%	1.04%
44	23.54%	20.98%	0.20%
66	26.54%	16.94%	0.08%

The shallow beds (11-22 mm) split tar between the 200-300 °C and 300-400 °C bands (~ 21% vs. 23-24%) with a small ≥400 °C share (1.04-1.37%). As depth increases to 44 mm and 66 mm, the 200-300 °C share rises (23.54% → 26.54%), the 300-400 °C share falls (20.98% → 16.94%) and the ≥400 °C fraction becomes negligible (0.2% → 0.08%). Total tar varies only modestly across the sweep (~43-46% of initial wood). Interpreted through the proxy and considering table 4-4 in chapter 4 where carbohydrate leaning classes (furans, aldehydes, ketones) are most represented at 200-300°C and phenolics rise with temperature. Deeper beds would be expected to accentuate notes associated with the lower band and diminish those associated with the higher band due to heat transfer limitations causing most of the wood to spend more time at the lower temperature bands when the wood mass is highest.

The temperature profiles (Figure 7-2) provide a consistent process explanation. Thicker beds heat more slowly and spend more time with the core in the 200-300°C window before approaching the 300-400 °C regime; they also exhibit brief thermal excursions ("self-heating" peaks, due to secondary exothermic reactions); however, these are short lived relative to the prolonged lower-temperature dwell. Longer internal residence and greater solid vapour contact in deeper beds also plausibly increases bed transformations (e.g., cracking/condensation on hot char).

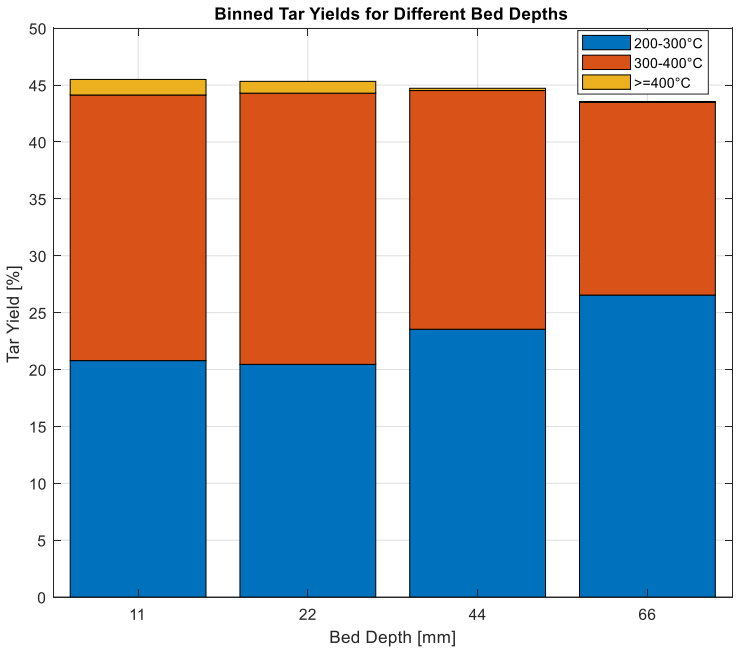

Figure 7-1: Model predicted tar yield (% initial wood) attributed to formation temperature bands as a function of bed depth (11, 22, 44 and 66 mm), at a fixed heating rate of 20 K/min and final treatment temperature of 450 °C. Stacked bars show contributions from 200-300 °C (blue), 300-400 °C (orange) and ≥400 °C (yellow) using tar as a proxy for aroma bearing condensables.

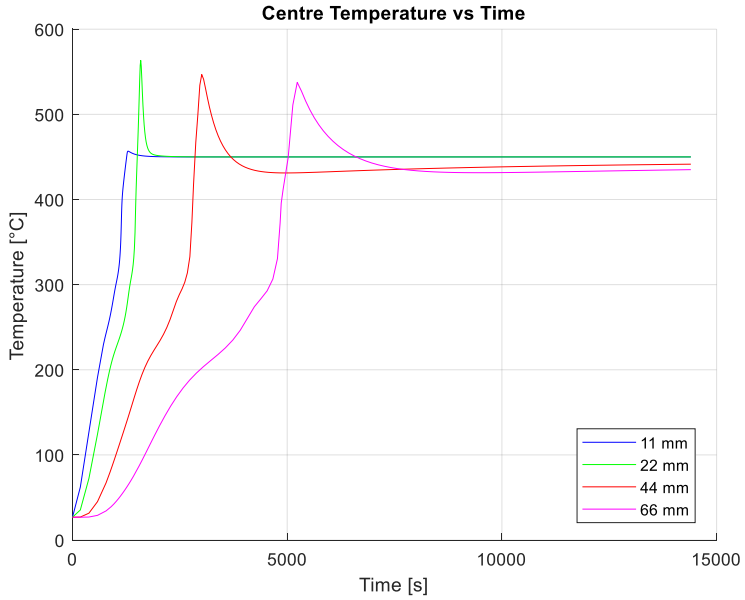

Figure 7-2: Centre temperature as a function of time for varying bed depths (mm) (L = 0.022 mm in blue, L = 0.044 m in red, L = 0.066 m in yellow).

Overall, varying bed depth at constant ramp and final treatment temperature appears to provide a practical handle for nudging the aroma profile. Shallower beds lean towards the profile associated with 300-400 °C, while deeper beds lean towards 200-300 °C with minimal ≥400 °C contribution. Given the proxy nature of the approach and the role of transport effects, these trends should be treated as indicative only.

7.2.2 Effect of Final Treatment Temperature

Simulations varying the final temperature (T_f) from 260 °C to 580 °C with a heating rate of 20 °C/min and bed depth of 44 mm were conducted. At a fixed ramp of 20 K/min, increasing the final treatment temperature redistributes the tar across formation bands (table 7-3). Assuming the tar is a proxy for aroma compound classes then the pattern in table 3 would suggest a gradual shift from compounds commonly associated with the 200-300 °C window toward those typical of 300-400 °C (cf. Table 4-4 from the previous chapter).

Table 7-3: Tar yield as a function of formation temperature (% of initial wood mass) for final treatment temperatures (°C)

	Tar (%)		
Final Treatment Temperature (°C)	**200-300 °C**	**300-400 °C**	**≥400°C**
260	30.46%	0.00%	0.00%
350	35.18%	8.69%	0.00%
450	23.54%	20.98%	0.20%
580	18.28%	24.87%	1.78%

Specifically, when the process is terminated at 260 °C, essentially all condensable are assigned to the 200-300 °C as the temperature was never outside this range. Raising the treatment temperature to 350 °C still favours 200-300 °C (35.18%) but introduces measurable 300-400 °C share (8.69%). By 450 °C, the distribution is more even (23.54% at 200-300 °C; 20.98% at 300-400°C) and at 580 °C the balance tilts towards 300-400 °C (24.87%) with a small ≥400 °C fraction (1.78%). Interpreted through the proxy, this would indicate an aroma profile that moves from carbohydrate leaning notes (furans/aldehydes) toward an increasing contribution from higher temperature classes (e.g., phenolic families) as the treatment temperature rises, in line with the temperature ordering summarised in table 4-4.

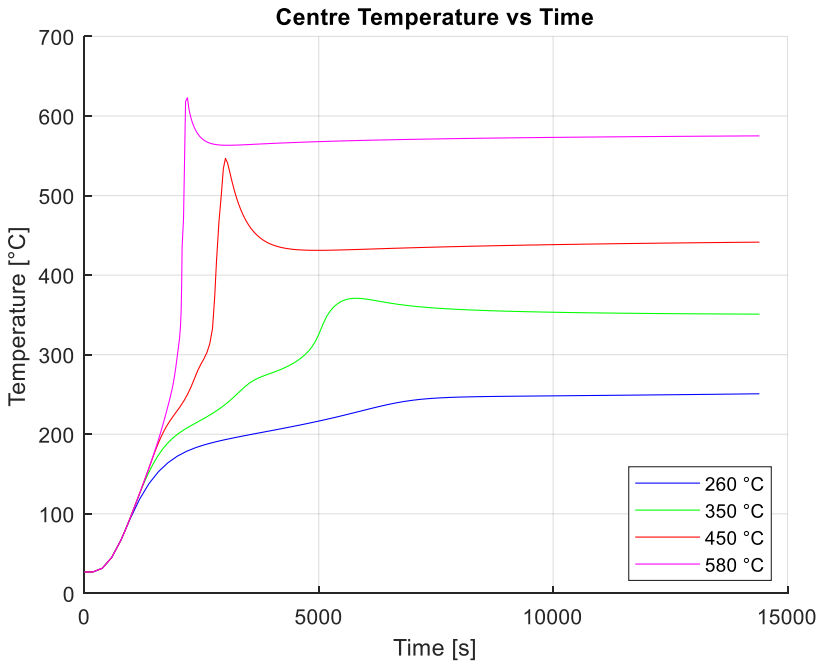

Figure 7-3: Centre temperature (of bed depth L = 44 mm) as a function of time for varying final treatment temperature (°C) (T_f = 260 °C in blue, T_f = 350 °C in green, T_f = 450 °C in red, T_f = 580 °C in pink).

The centre temperature histories for the same runs (Figure 7-3) provide context for these allocations. The 260 °C case does not reach 300 °C at the core (even with secondary reactions). As the final treatment temperature is increased, the bed of wood spends progressively more time at the higher temperatures (even above the final treatment temperature prescribed due to exothermic secondary reactions). It is interesting that even at 580 °C, the portion of tar formed above 400 °C is quite small (1.78%). This is likely due to the heat transfer limitations of wood as modelled here. Due to the thermally thick bed chosen for this study of final treatment temperature (L = 44 mm), the heat traverses rather slowly, during which time, the wood is undergoing thermal breakdown and it is possible that most of the virgin wood has been consumed well before the temperature at that node has reached 400°C and therefore, there is little to no reactant left.

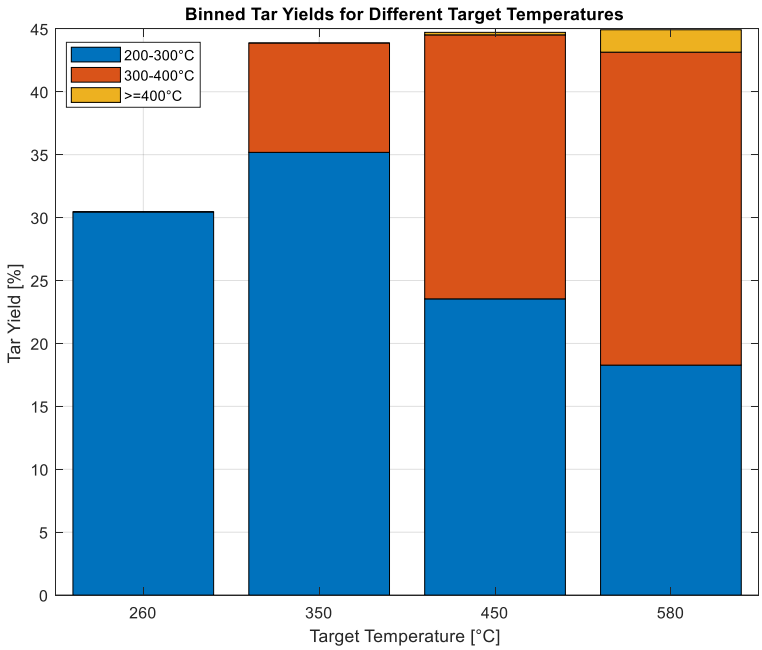

Figure 7-4: Model predicted tar yield (% initial wood) attributed to formation temperature bands as a function of final treatment temperature (260, 350, 450 and 580 °C) at a fixed heating rate of 20 K/min for a slab of thickness 44 mm. Stacked bars show contributions from 200-300 °C (blue), 300-400 °C (orange) and ≥400 °C (yellow) using tar as a proxy for aroma bearing condensables.

7.2.3 Effect of heating rate

The results of varying heating rates (β) from 3 °C/min to 100 °C/min with a final temperature of 580 °C and a bed depth of 44 mm on temperature profiles is shown below in Figure 7-6 and the tar yields with respect to formation temperature in Table 4. Treating tar as a proxy for aroma-bearing condensables and binning it by formation temperature provides a physically grounded bridge between the model and the GC/MS evidence from chapter 4. In table 4-4, carbohydrate-derived classes (furans, aldehydes, ketones) dominate at 200-300 °C (e.g., furan 35%, aldehyde 25%), whereas phenolics rise sharply with temperature (18% at 200-300 °C, 45% at 300-400°C and 62% above 400 °C) consistent with a shift from hemicellulose/cellulose fragments to lignin derived methoxyphenols at higher severity. This temperature ordered chemistry is also summarised in Chapter 4's narrative that VOC yields follow the sequential degradation of hemicellulose (~200-300 °C), cellulose (~ 300-400 °C) and lignin (broadly ≥520 °C).

Table 7-4: Tar yield as a function of formation temperature (% of initial wood mass) for varying heating rates (°C/min)

	Tar (%)		
Heat rate (K/min)	**200-300 °C**	**300-400 °C**	**≥400°C**
3	27.93%	10.97%	0.006%
20	18.28%	24.87%	1.779%
100	15.25%	27.93%	3.636%

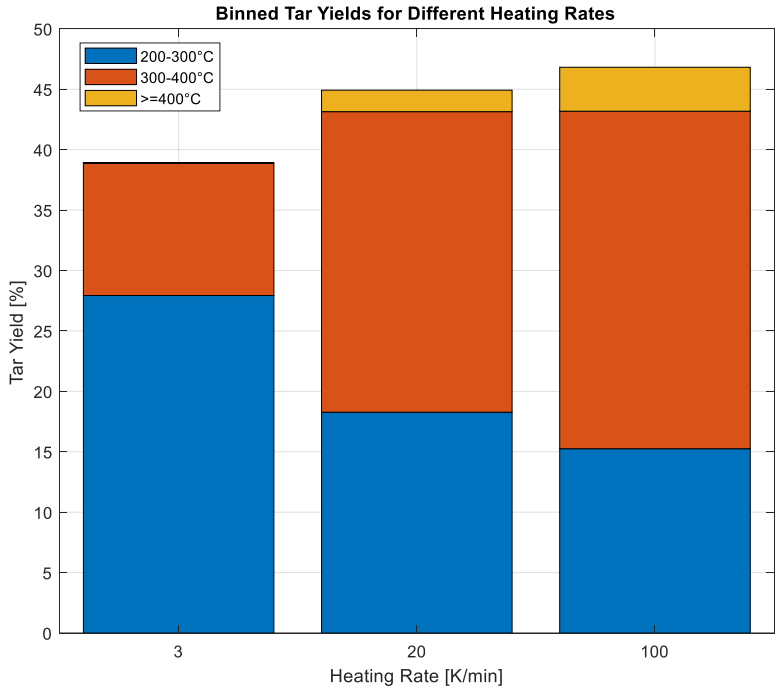

Figure 7-5: Model predicted tar yield (% of initial wood) attributed to formation bands for three heating rates (3, 20 and 100 K/min). Stacked bars show the contribution from 200-300 °C (blue), 300-400 °C (orange) and ≥400 °C (yellow) using tar as a proxy for aroma bearing condensables.

Comparing to those results, the model's banded tar yields show two clear trends (Table 7-4). At 3 K/min most tar forms at 200-300 °C (27.93%) with negligible ≥400 °C material (0.006%), whereas at 20 and 100 K/min the ≥300 °C share predominates (300-400 °C bands of 24.87% and 27.93%, plus ≥400 °C bands of 1.78% and 3.64%, respectively). The total tar increases modestly across these cases (~39% → 45-47% of initial wood), indicating better preservation of condensables at faster ramps.

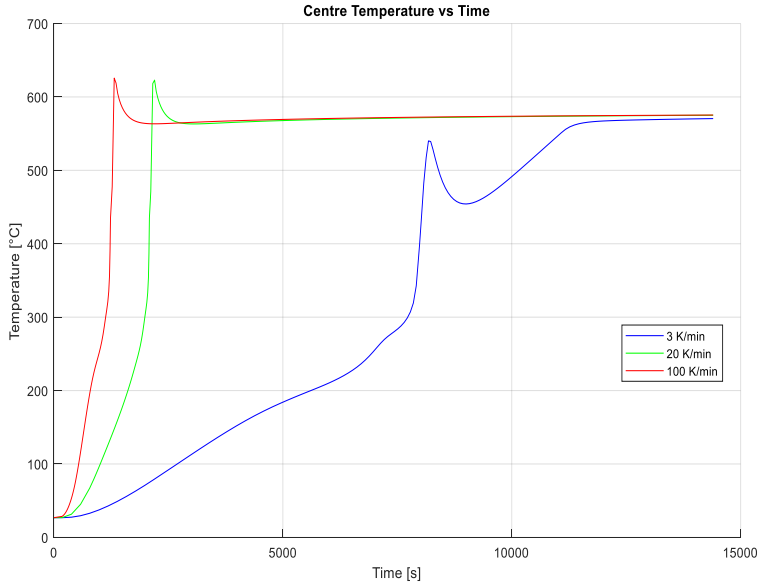

Figure 7-6: Centre temperature as a function of time for varying heating rates,β (°C/min) (β = 3 °C/min in blue, β = 20 °C/min in green, β = 100 °C/min in red).

The centre-temperature traces (Figure 7-6) are consistent mechanistically: faster ramps traverse 200-300 °C range quickly and spend proportionally more of the evolution window in the phenolic forming regime.

7.3 Conclusion

This chapter used the hot plate model to explore how three controllable variables; heating rate, final treatment temperature and bed depth shape thermal profiles and the allocation of tar by formation temperature which was treated (with caution) as a proxy for aroma bearing condensables. Across all sweeps, centre temperature trajectories explained the band allocations: conditions that kept the core longer in the 200-300 °C window produced more tar attributed to that band, whereas conditions that moved the core rapidly into 300-400 °C increased the share assigned there. Transient self-heating peaks were observed near devolatilisation.

With a fixed bed depth and treatment temperature, increasing heating rate shifted the tar distribution from 200-300 °C toward 300-400 °C and modestly raised total tar. With a fixed bed

and heating ramp rate, raising the final treatment temperature introduced a substantial 300-400 °C share although the ≥400 °C band remained small under all conditions. With a fixed heating ramp rate and treatment temperature, increasing bed depth moved the allocation in the opposite direction, towards the 200-300 °C band while suppressing the 300-400 °C and ≥400 °C share. If the proxy assumption holds, these tendencies imply that slower ramp rates, lower treatment temperatures and deeper beds would bias the aroma balance towards compounds typically associated with the 200-300 °C range (e.g., carbohydrate derived classes – table 4-4), whereas faster ramps, higher treatment temperatures and shallower beds would tilt it towards classes more common in the 300-400 °C range. Very severe conditions did not materially enrich the ≥400 °C allocation.

These results are comparative rather than absolute. The proxy aggregates primary and secondary chemistry, moisture was neglected, and the model is one-dimensional with lumped kinetics for tar. The next steps are to (i) validate the predicted shifts with targeted GC/MS across the same factor space, (ii) incorporate moisture evaporation and condensation and more explicit secondary pathways and (iii) examine geometry and residence time effects beyond 1-D. Within these limits, the sweeps provide a practical map for steering the predicted aroma balance through process choices during smoke generation.

This page is intentionally left blank.

CHAPTER 8

Conclusions & Recommendations

8.1 Introduction

Traditional food smoking is central to artisanal food production as well as industrial food production but often yields inconsistent flavour, making outcomes highly dependent on operator skill and experience. This thesis sought to move beyond this operator-dependent art by addressing a central question: can the aroma profile of kānuka wood smoke be deliberately *tuned* and if so, what are the key process levers that govern this control? The investigation was therefore structured to first identify the most significant process parameter influencing the smoke profile. Upon discovery that temperature was the dominant lever, the research then focused on understanding the underlying mechanisms that must be managed to reliably engineer a desired smoke aroma.

8.2 Synthesis of key findings

Initial analysis using Pyrolysis-Gas Chromatography/Mass Spectrometry (Py-GC/MS) identified pyrolysis temperature as the most influential parameter governing the final aroma profile of kānuka wood smoke. This established a foundational principle: any attempt to control smoke aroma must first involve precise control of the thermal environment.

The complexity of this control was revealed through Thermogravimetric Analysis and Differential Scanning Calorimetry (TGA-DSC). These experiments demonstrated that heat flow within the pyrolysing wood bed was significantly influenced by both particle size and sample mass, which served as a proxy for the tar vapour's tortuous path length. As sample mass increased, the net specific enthalpy of reaction became progressively more exothermic, indicating the presence of secondary reactions. This analysis uncovered a non-linear relationship between particle size and exothermicity, identifying an optimal range of 90-600 microns that produced the least exothermic

heat flow, while both smaller (< 90 microns) and larger (>3-5 mm) particles were significantly more exothermic.

The key insight of this research lies in the explanation for this phenomenon, which is rooted in bed permeability. The low inter-particle permeability of the fine (<90 micron) particle bed trapped tar vapours, increasing their residence time and promoting exothermic secondary reactions. Conversely, in large particles (>3-5 mm), low *intra*-particle permeability became the dominant limiting factor, producing a similar outcome. While it was discovered that the exothermicity of the finest particles could be mitigated by employing impractically slow heating rates (e.g., ≤ 1K/min) to limit the rate of tar formation, the more practical and effective solution is to control the physical properties of the bed of wood itself. Therefore, the key practical finding is that selecting an optimal wood particle size, one that maximises inter-particle permeability while ensuring it remains the dominant factor over intra-particle constraints is the most effective method for limiting exothermic secondary reactions and therefore allowing for the precise control of temperature and by extension, the final smoke aroma profile.

8.3 Contribution to Knowledge

The original contributions of this thesis to the fields of Chemical Engineering, Food Science and Thermal Engineering are both specific and conceptual.

Firstly, the research provides a highly detailed, foundational dataset that did not previously exist for kānuka wood. This includes: (i) the specific chemical aroma profiles and their evolution at fine temperature increments (10 °C), (ii) the precise specific enthalpy of reaction values during pyrolysis and (iii) a quantitative analysis of how exothermic secondary reactions are directly influenced by bed permeability. This work also puts forward a preliminary mechanistic model capable of predicting the relative influence of key operational levers on heat flow and by proxy the final aroma

profile. While this model requires further refinement, it serves as a first step towards a predictive tool for smoker design.

Secondly and more significantly, this thesis establishes a new conceptual framework for understanding the inconsistencies inherent in traditional food smoking. It moves beyond the current approach to temperature control of setting a centre or hot plate temperature and leaving it. It demonstrated that the wood bed itself is a dynamic reactor. The core novel mechanism identified is the interdependency of the tar formation rate and the tortuous path length of the vapour through the bed. This research is the first to quantify how this relationship governs local thermal events, leading to inconsistent smoke profiles. By explaining this mechanism and testing it with one-dimensional modelling this work provides a new scientific basis for how food smokers should be designed and operated to achieve consistent and deliberate aroma profiles.

8.4 Limitations of the Study

While the findings of this thesis provide a new and detailed understanding of kanuka smoke generation, it is important to acknowledge the following limitations to contextualise the results.

Firstly, the research was scoped specifically to kānuka wood, the most popular food smoking wood of New Zealand. The quantitative data regarding aroma profiles and reaction heats generated in this research are a function of kānuka's unique composition. Therefore, while the fundamental principles identified may be broadly applicable, e.g., the specific operational parameters such as the optimal particle size, they cannot be directly extrapolated to other wood species without further investigation. Additionally, wood moisture content was not a controlled variable in this study. Although water evaporation largely precedes pyrolysis, potential chemical interactions between residual moisture and tar vapours at high temperatures were not accounted for.

Secondly, the experimental findings and operational parameters are specific to the laboratory-scale equipment used. The method of heat application and vapour extraction in any given smoker will

influence the optimal particle size and processing conditions. While the fundamental temperature-dependence of aroma formation is universal, the precise application of these findings will need to be adapted and validated for different smoker designs at various scales.

Thirdly, there are inherent limitations associated with the specific analytical methods employed to gather the foundational data. The thermogravimetric and calorimetric analyses (TGA-DSC) rely on milligram-scale samples. While utilising such small masses is necessary to isolate chemical kinetics from transport phenomena, extrapolating micro-scale thermal behaviours to bulk macro-scale wood beds introduces inherent scaling uncertainties. Furthermore, as observed during the specific enthalpy experiments, larger TGA sample masses (e.g., 24 mg) approached a physical volume limit of the crucibles, introducing unintended variations in bed density and heat transfer that complicated the isolated of purely kinetic data. Regarding the chemical characterisation, the Py-GC/MS methodology provides relative semi-quantitative data (based on peak areas) rather than absolute concentrations. Additionally, the sensitivity and upper temperature limits of the instrumentation restricted the detection of heavier, high boiling point compounds, most notably Polycyclic Aromatic Hydrocarbons (PAHs), meaning the captured profile, while highly comprehensive for volatile aroma compounds, cannot account for the entirety of the heavier smoke constituents.

Finally, the mechanistic model developed is a simplified one-dimensional representation of a complex process. Its predictive accuracy could be substantially improved by: (i) incorporating a more detailed kinetic scheme based on individual compound formation rather than bulk tar, (ii) evolving the reaction scheme from parallel to competitive to better reflect temperature dependencies and (iii) expanding the model to multiple dimensions to capture complex vapour flow dynamics. The use of Darcy's Law, which assumes laminar flow is another simplification, as turbulent flow regimes within a smoker could significantly alter the thermal and chemical outcomes.

Another important limitation is that this study was limited to the instrumental analysis of the smoke chemical profile. Further research, including sensory panel analysis with a food matrix (e.g., salmon or cheese) would be required to correlate these chemical changes with the final perceived flavour.

8.5 Recommendations

Based on the findings of this thesis, the following recommendations are proposed to provide a scientifically grounded pathway towards greater control and consistency in food smoking.

8.5.1 Recommendations for Industry/Practice

1. **Wood chip suppliers:** A shift form supplying broadly graded wood chips to a more collaborative, customer-centric model is recommended. Suppliers should engage with their clients to identify the optimal particle size distributions that perform best in their specific smokers and for products.
2. **Smoke Equipment Manufacturers:** It is recommended that manufacturers develop more intelligent and adaptive control systems that account for the wood's physical properties. Further smokers could be designed to be more wood agnostic by incorporating control systems where the operator inputs key variables like wood particle size (e.g., small, medium, large) and mass. The system could then use a pre-programmed algorithm, based on the principles identified in this thesis to automatically calculate and implement an optimal heating rate. This would manage the rate of tar formation to match the bed's permeability, actively preventing the pore-blocking and thermal runaway events that cause inconsistency.
3. **Food Producers and Smoking Artisans:** Producers are encouraged to adopt a more systematic approach to wood selection and use. It is recommended that they conduct internal trials to determine the wood chip size and loading parameters. These include for batch, the mass, and for continuous, the char/ash removal rate. The insights gained should then be communicated back to their wood suppliers to establish a supply chain for

consistent, optimised wood chips, ultimately leading to a more reliable and consistent final product.

8.5.2 Recommendations for Future Research

The findings of this thesis open several promising avenues for future research. The following studies are recommended to build upon the foundational knowledge established in this work:

1. **Broadening Pyrolysis Conditions and Feedstocks:** Future studies should extend the methodology of this thesis to other commercially important wood species. A crucial variable to investigate would be the pyrolysis environment; while this work was conducted under inert nitrogen, exploring the use of other gases could reveal significant changes in the resulting aroma profiles.
2. **Enhancing the Kinetic and Predictive Model:** To refine the predictive capabilities of the model, future work should focus on quantifying key aroma compounds as a function of total volatiles. This data, combined with the compound-specific kinetics determined in Chapter 4 would allow for a more precise quantification of the aroma profile. Replacing the current lumped-tar model with a scheme that includes more precise secondary reaction kinetics would be an important step in improving the model's accuracy.
3. **Validation through Scale-Up Studies:** The next step is to validate the principles identified in this research at larger scales. This should be a staged process beginning with a bench-top smoker and progressing to a pilot-scale system. Such studies would be essential for refining the operational parameters and providing new insights into the challenges and dynamics of industrial scale smoke generation.
4. **Correlation of Chemical Data with Sensory Perception:** To complete the link from chemical composition to consumer experience, a dedicated study that matches the

5. instrumental aroma profiles with sensory panel analysis would be useful. Correlating specific chemical signatures with perceived flavour attributes would provide the validation needed for this research and deliver practical value to the food industry.
6. **Correlation of Chemical Data with Sensory Perception:** To complete the link from chemical composition to consumer experience, a dedicated study that matches the instrumental aroma profiles with sensory panel analysis would be useful. Correlating specific chemical signatures with perceived flavour attributes would provide the validation needed for this research and deliver practical value to the food industry.

In conclusion, this research marks a pivotal shift in the understanding of food smoking. It fundamentally demonstrates that the generation of a desired smoke aroma profile need not be an inconsistent art but can instead be a predictable and engineered process. By identifying the critical relationship between wood particle size, bed permeability and localised thermal events, this work provides the scientific framework to move beyond the guesswork of tradition. Ultimately, this thesis provides the knowledge to transform smoke generation from an operator-dependent craft into a precise, tuneable and repeatable technology.

This page is intentionally left blank.

References

Abdel-Shafy, H.I. and Mansour, M.S.M. (2016) 'A review on polycyclic aromatic hydrocarbons: Source, environmental impact, effect on human health and remediation', *Egyptian Journal of Petroleum*, 25(1), pp. 107–123. doi: 10.1016/j.ejpe.2015.03.011.

Aboulkas, A. and El Harfi, K. (2008) 'Study of the kinetics and mechanisms of thermal decomposition of Moroccan Tarfaya oil shale and its kerogen', *Oil Shale*, 25(4), pp. 426–443. doi: 10.3176/oil.2008.4.04.

Ahmad, J.I. (2003) 'Applications of smoking', in Caballero, B., Trugo, L. and Finglas, P.M. (eds.) *Encyclopedia of Food Sciences and Nutrition*. 2nd edn. Oxford: Elsevier, pp. 5309–5316.

Alexander, J. et al. (2008) 'Polycyclic aromatic hydrocarbons in food', *EFSA Journal*, 724, pp. 1–114. doi: 10.2903/j.efsa.2008.724.

Anca-Couce, A. and Zobel, N. (2012) 'Numerical analysis of a biomass pyrolysis particle model: Solution method optimized for the coupling to reactor models', *Fuel*, 97, pp. 80–88. doi: 10.1016/j.fuel.2012.02.033.

Antal, M.J. and Grønli, M. (2003) 'The art, science, and technology of charcoal production', *Industrial & Engineering Chemistry Research*, 42(8), pp. 1619–1640. doi: 10.1021/ie0207919.

Antal, M.J., Várhegyi, G. and Jakab, E. (1998) 'Cellulose pyrolysis kinetics: Revisited', *Industrial & Engineering Chemistry Research*, 37(4), pp. 1267–1275. doi: 10.1021/ie970144v.

Asmadi, M., Kawamoto, H. and Saka, S. (2011a) 'Thermal reactions of guaiacol and syringol as lignin model aromatic nuclei', *Journal of Analytical and Applied Pyrolysis*, 92(1), pp. 88–98. doi: 10.1016/j.jaap.2011.04.006.

Asmadi, M., Kawamoto, H. and Saka, S. (2011b) 'Thermal reactivities of catechols/pyrogallols and cresols/xylenols as lignin pyrolysis intermediates', *Journal of Analytical and Applied Pyrolysis*, 92(1), pp. 76–87. doi: 10.1016/j.jaap.2011.04.004.

ASTM International (2014) *ASTM E1131-08: Standard Test Method for Compositional Analysis by Thermogravimetry*. West Conshohocken, PA: ASTM International.

Babu, B.V. (2008) 'Biomass pyrolysis: a state-of-the-art review', *Biofuels, Bioproducts and Biorefining*, 2(5), pp. 393–414. doi: 10.1002/bbb.92.

Bamford, C.H., Crank, J. and Malan, D.H. (1946) 'The combustion of wood. Part I', *Mathematical Proceedings of the Cambridge Philosophical Society*, 42(2), pp. 166–182. doi: 10.1017/S030500410002288X.

Basile, L., Tognotti, L., Faravelli, T., Ranzi, E. and Mancini, M. (2014) 'Influence of pressure on the heat of biomass pyrolysis', *Fuel*, 137, pp. 277–284. doi: 10.1016/j.fuel.2014.07.071.

Bellais, M. (2007) *Modelling of the pyrolysis of large wood particles*. PhD thesis. Stockholm: KTH Royal Institute of Technology.

Bennadji, H., Leoni, P., Bennadji, A. et al. (2013) 'Low-temperature pyrolysis of woody biomass in the thermally thick regime', *Energy & Fuels*, 27(3), pp. 1453–1459. doi: 10.1021/ef400079a.

Bertsch, W. (1999) 'Two-dimensional gas chromatography. Concepts, instrumentation, and applications – Part 1: Fundamentals, conventional two-dimensional gas chromatography, selected applications', *Journal of High Resolution Chromatography*, 22(12), pp. 647–665. doi: 10.1002/(SICI)1521-4168(19991201)22:12<647::AID-JHRC647>3.0.CO;2-V.

Boroson, M.L., Howard, J.B., Longwell, J.P. and Peters, W.A. (1989) 'Product yields and kinetics from the vapor-phase cracking of wood pyrolysis tars', *AIChE Journal*, 35(1), pp. 120–128. doi: 10.1002/aic.690350112.

Branca, C., Di Blasi, C., & Galgano, A. (2010). 'Pyrolysis of corncobs catalyzed by zinc chloride for furfural production'. *Industrial & Engineering Chemistry Research*, *49*(20), 9743–9752. doi: 10.1021/ie101067v

Branca, C. and Di Blasi, C. (2016) 'A summative model for the pyrolysis reaction heats of beech wood', *Thermochimica Acta*, 638, pp. 10–16. doi: 10.1016/j.tca.2016.06.006.

Bridgwater, A.V. (2006) *Biomass pyrolysis*. IEA Bioenergy Task 34 booklet.

Bridgwater, A.V., Meier, D. and Radlein, D. (1999) 'An overview of fast pyrolysis of biomass', *Organic Geochemistry*, 30(12), pp. 1479–1493. doi: 10.1016/S0146-6380(99)00120-5.

Broido, A. and Nelson, M.A. (1975) 'Char yield on pyrolysis of cellulose', *Combustion and Flame*, 24, pp. 263–268. doi: 10.1016/0010-2180(75)90173-3.

Brown, J.R. and Thornton, J.L. (1957) 'Percivall Pott (1714–1788) and chimney-sweepers' cancer of the scrotum', *British Journal of Industrial Medicine*, 14(1), pp. 68–70. doi: 10.1136/oem.14.1.68.

Brown, A.L., Dayton, D.C. and Daily, J.W. (2000) 'A study of cellulose pyrolysis chemistry and global kinetics at high heating rates', *Energy & Fuels*, 15(1), pp. 124–136. doi: 10.1021/ef000140c.

Brown, T.R., Wright, M.M. and Brown, R.C. (2011) 'Estimating profitability of two biochar production scenarios in Iowa', *Biofuels, Bioproducts and Biorefining*, 5(1), pp. 54–68.

Brownsort, P.A. (2009) *Biomass pyrolysis processes: performance parameters and their influence on biochar system benefits*. MSc Thesis. University of Edinburgh.

Bruchmüller, J., Latham, K., van de Beld, B. et al. (2012) 'Modeling the thermochemical degradation of biomass inside a fast pyrolysis fluidized-bed reactor', *AIChE Journal*, 58(10), pp. 3030–3042. doi: 10.1002/aic.13705.

Burgess, G.H.O. et al. (1965) *Fish handling and processing*. Edinburgh: Her Majesty's Stationery Office.

Cai, J. and Liu, R. (2008) 'New distributed activation energy model: Numerical solution and application to pyrolysis kinetics of some types of biomass', *Bioresource Technology*, 99(8), pp. 2795–2799.

Cavallotti, C., Galano, A., Ruscic, B., Ranzi, E. and Frassoldati, A. (2018) 'Detailed kinetics of pyrolysis and combustion of catechol and guaiacol, as reference components of bio-oil from biomass', *Chemical Engineering Transactions*, 65, pp. 79–84. doi: 10.3303/CET1865014.

Chan, R. and Krieger, B.B. (1983) 'Modeling of physical and chemical processes during pyrolysis of a large biomass pellet with experimental verification', *ACS Division of Fuel Chemistry, Preprints*, 28(5), pp. 330–337.

Chan, W.C.R., Kelbon, M. and Krieger, B.B. (1985) 'Modelling and experimental verification of physical and chemical processes during pyrolysis of a large biomass particle', *Fuel*, 64(11), pp. 1505–1513. doi: 10.1016/0016-2361(85)90364-3.

Chen, B., Liu, X., Cui, S. and Wang, X. (2017) 'Mechanism studies of 5-HMF pyrolysis by quantum chemistry', *Journal of Central South University*, 24, pp. 2565–2571. doi: 10.1007/s11771-017-3664-8.

Chen, D., Zheng, Y. and Zhu, X. (2013) 'In-depth investigation on the pyrolysis kinetics of raw biomass. Part I: Kinetic analysis for the drying and devolatilization stages', *Bioresource Technology*, 131, pp. 40–46. doi: 10.1016/j.biortech.2012.12.136.

Chen, D., Zhou, J. and Zhang, Q. (2014) 'Effects of heating rate on slow pyrolysis behaviour, kinetic parameters and products properties of moso bamboo', *Bioresource Technology*, 169, pp. 313–319. doi: 10.1016/j.biortech.2014.07.009.

Chen, Q., Zhou, J., Liu, B. et al. (2014) 'Investigation of heat of biomass pyrolysis and secondary reactions by simultaneous thermogravimetry and differential scanning calorimetry', *Fuel*, 134, pp. 467–476. doi: 10.1016/j.fuel.2014.06.014.

Chen, W.H., Chen, C.J., Hung, C.I. and Syu, F.S. (2020) 'Independent parallel pyrolysis kinetics of cellulose, hemicelluloses and lignin at various heating rates analysed by evolutionary computation', *Energy Conversion and Management*, 221, 113165. doi: 10.1016/j.enconman.2020.113165.

Chevance, F.F.V. and Farmer, L.J. (1999) 'Identification of major volatile odor compounds in frankfurters', *Journal of Agricultural and Food Chemistry*, 47(12), pp. 5151–5160. doi: 10.1021/jf990515d.

Coats, A.W. and Redfern, J.P. (1964) 'Kinetic parameters from thermogravimetric data', *Nature*, 201, pp. 68–69. doi: 10.1038/201068a0.

Codex Alimentarius (2009) *Code of practice for the reduction of contamination of food with polycyclic aromatic hydrocarbons (PAH)*, CAC/RCP 68-2009. Rome: FAO/WHO Codex Alimentarius Commission.

Commandré, J., Couhert, C., Valette, J. and Salvador, S. (2018) 'Pyrolysis of wood at high temperature: The influence of experimental parameters on gaseous products', HAL Id: hal-01801244. Lyon: EM2C/CNRS-CentraleSupélec.

Commission of the European Communities (2002) *Opinion of the Scientific Committee on Food on the risks to human health of polycyclic aromatic hydrocarbons in food*. Brussels: SCF/CS/CNTM/PAH/29 Final.

Corbetta, M., Frassoldati, A., Bennadji, H. et al. (2014) 'Pyrolysis of centimeter-scale woody biomass particles: Kinetic modeling and experimental validation', *Energy & Fuels*, 28(6), pp. 3884–3898. doi: 10.1021/ef500525v.

Cui, F.M., Zhang, X.Y. and Shang, L.M. (2013) 'Thermogravimetric analysis of biomass pyrolysis under different atmospheres', *Applied Mechanics and Materials*, 448–453, pp. 1616–1619. doi: 10.4028/www.scientific.net/AMM.448-453.1616.

Daouk, E., Le Brech, Y., Grateau, M. et al. (2018) 'Thick wood particle pyrolysis in an oxidative atmosphere: Effects of oxygen concentration and particle size', *Chemical Engineering Science*, 126, pp. 608–615. doi: 10.1016/j.ces.2015.01.017.

Das, A.K., Biswas, D., Chauhan, O.P., Kumar, S., Yadav, M. and Mandal, G.C. (2023) 'Current innovative approaches in reducing polycyclic aromatic hydrocarbons (PAHs) in meat and meat

products: A review', *Chemical and Biological Technologies in Agriculture*, 10, 48. doi: 10.1186/s40538-023-00391-8.

Demirbas, A. (2004) 'Combustion characteristics of different biomass fuels', *Progress in Energy and Combustion Science*, 30(2), pp. 219–230. doi: 10.1016/j.pecs.2003.10.004.

Derba-Maceluch, M., Donev, E., Gorzsás, A. et al. (2023) 'Impact of xylan on field productivity and wood saccharification properties in aspen', *Frontiers in Plant Science*, 14, 1218302. doi: 10.3389/fpls.2023.1218302.

Di Blasi, C. (1993) 'Modeling and simulation of combustion processes of charring and non-charring solid fuels', *Progress in Energy and Combustion Science*, 19(1), pp. 71–104. doi: 10.1016/0360-1285(93)90022-7.

Di Blasi, C. and Russo, G. (1994) 'Modeling of transport phenomena and kinetics of biomass pyrolysis', in Bridgwater, A.V. (ed.) *Advances in Thermochemical Biomass Conversion*. Dordrecht: Springer, pp. 906–921. doi: 10.1007/978-94-011-1336-6_70.

Di Blasi, C. (1996) 'Heat, momentum and mass transport through a shrinking biomass particle exposed to thermal radiation', *Chemical Engineering Science*, 51(7), pp. 1121–1132. doi: 10.1016/S0009-2509(96)80011-X.

Di Blasi, C. (2008) 'Modeling chemical and physical processes of wood and biomass pyrolysis', *Progress in Energy and Combustion Science*, 34(1), pp. 47–90. doi: 10.1016/j.pecs.2006.12.001.

Di Blasi, C., Branca, C. and Galgano, A. (2010) 'Biomass screening for the production of furfural via thermal decomposition', *Industrial & Engineering Chemistry Research*, 49(6), pp. 2658–2671. doi: 10.1021/ie901731u.

Di Blasi, C., Branca, C., Lombardi, V., Ciappa, P., & Di Giacomo, C. (2013). 'Effects of particle size and density on the packed-bed pyrolysis of wood'. *Energy & Fuels*, *27*(11), 6781–6791. doi:10.1021/ef401481j

Ding, Y. et al. (2025) 'Numerical Investigation of Tar Formation Mechanisms in Biomass Pyrolysis', *MDPI*, 12(6), 477. doi: 10.3390/aerospace12060477.

Dou, J., Usino, D.O., Ylitervo, P., Sipponen, M.H. and Richards, T. (2020) 'Identifying the primary reactions and products of fast pyrolysis of alkali lignin', *Journal of Analytical and Applied Pyrolysis*, 151, 104917. doi: 10.1016/j.jaap.2020.104917.

Duan, J. and Ji, J. (2024) 'Mechanism insight into α-D-galactopyranose conversion to 5-hydroxymethylfurfural by combining Py-GC–MS experiments and theoretical calculations', *Chemical Engineering Journal*, 498, 155724. doi: 10.1016/j.cej.2024.155724.

Dufour, A., Ouartassi, B., Bounaceur, R. and Zoulalian, A. (2011) 'Modelling intra-particle phenomena of biomass pyrolysis', *Chemical Engineering Research and Design*, 89(10), pp. 2136–2146. doi: 10.1016/j.cherd.2011.02.013.

Dupont, C., Chiriac, R., Gauthier, G. and Toche, F. (2014) 'Heat capacity measurements of various biomass types and pyrolysis residues', *Fuel*, 115, pp. 644–651. doi: 10.1016/j.fuel.2013.07.086.

Essumang, D.K., Dodoo, D.K. and Adjei, J.K. (2013) 'Effect of smoke generation sources and smoke curing duration on PAH levels in different suites of fish', *Food and Chemical Toxicology*, 58, pp. 86–94. doi: 10.1016/j.fct.2013.04.014.

European Commission (2006) 'Commission Regulation (EC) No 1881/2006 … setting maximum levels for certain contaminants in foodstuffs', *Official Journal of the European Union*, L364, pp. 5–24.

European Union (2003) 'Regulation (EC) No 2065/2003 of the European Parliament and of the Council of 10 November 2003 on smoke flavourings used or intended for use in or on foods', *Official Journal of the European Union*, L309, pp. 1–8.

Faix, O., Fortmann, I., Bremer, J. and Meier, D. (1991) 'Thermal degradation products of wood. Gas chromatographic separation and mass spectrometric characterization of monomeric lignin derived products', *Holz als Roh- und Werkstoff*, 49(5), pp. 213–219. doi: 10.1007/BF02613271.

Fantozzi, F. et al. (2007) 'Rotary kiln slow pyrolysis for syngas and char production from biomass and waste part 2: Introducing product yields in the energy balance', pp. 908–913.

Fengel, D. and Wegener, G. (1989) *Wood: Chemistry, ultrastructure, reactions*. Berlin: Walter de Gruyter. doi: 10.1007/BF02608943.

Fessman, G. (1973) 'Production and utilization of curing smoke', *Fleischerei*, 24(11), p. 14.

Fessman, G. and Fessman, K.D. (1979) 'Steam-generated smoke for hot and cold smoking', *Fleischerei*, 30(12), p. 1006.

Fiddler, W., Doerr, R.C., Wasserman, A.E. and Salay, J.M. (1966) 'Composition of hickory sawdust smoke: Furans and phenols', *Journal of Agricultural and Food Chemistry*, 14(6), pp. 659–662. doi: 10.1021/jf60148a034.

FSANZ (Food Standards Australia New Zealand) (2019) *Survey of polycyclic aromatic hydrocarbons (PAH) in Australian foods: Dietary exposure assessment and risk characterisation*. Canberra: FSANZ.

Gade, P. (2010) *Investigation of volatile products from wood pyrolysis*. Master's Thesis. Western Kentucky University.

Gerdes, C. et al. (2002) 'Design, construction, and operation of a fast pyrolysis plant for biomass', *Chemical Engineering & Technology*, 25(6), pp. 167–174.

Glass, S. V., & Zelinka, S. L. (2010). Moisture relations and physical properties of wood. In R. J. Ross (Ed.), *Wood handbook: Wood as an engineering material* (pp. 4.1–4.19). USDA Forest Service, Forest Products Laboratory.

Goldstein, I.S. (1977) *Wood technology: Chemical aspects*. Washington, DC: American Chemical Society.

González-Vila, F.J., Almendros, G., Del Río, J.C., Martin, F. and Verdejo, T. (2001) 'Pyrolysis-GC–MS analysis of the formation and degradation stages of charred residues from lignocellulosic biomass', *Journal of Agricultural and Food Chemistry*, 49(3), pp. 1128–1131. doi: 10.1021/jf0006325.

Grieco, E. and Baldi, G. (2011) 'Analysis and modelling of wood pyrolysis', *Chemical Engineering Science*, 66(4), pp. 650–660. doi: 10.1016/j.ces.2010.11.018.

Grønli, M.G. (1996) *A theoretical and experimental study of the thermal degradation of biomass*. PhD thesis. Norwegian University of Science and Technology.

Grønli, M.G., Várhegyi, G. and Di Blasi, C. (2002) 'Thermogravimetric analysis and devolatilization kinetics of wood', *Industrial & Engineering Chemistry Research*, 41(17), pp. 4201–4208. doi: 10.1021/ie0201157.

Hagge, M.J. and Bryden, K.M. (2002) 'Modeling the impact of shrinkage on the pyrolysis of dry biomass', *Chemical Engineering Science*, 57(14), pp. 2811–2823. doi: 10.1016/S0009-2509(02)00167-7.

Hanhijärvi, A., Rautkari, L., Maloney, T. and Vuorinen, T. (2003) 'Observation of development of microcracks on wood surface caused by drying stresses', *Holzforschung*, 57(5), pp. 561–565. doi: 10.1515/HF.2003.083.

Holmberg, A.L., Reno, K.H., Nguyen, N.A., Wool, R.P. and Epps, T.H. III (2016) 'Syringyl methacrylate, a hardwood lignin-based monomer for high-Tg polymeric materials', *ACS Macro Letters*, 5(5), pp. 574–578. doi: 10.1021/acsmacrolett.6b00270.

Incropera, F.P., DeWitt, D.P., Bergman, T.L. and Lavine, A.S. (2006) *Fundamentals of heat and mass transfer*. 6th edn. Hoboken, NJ: John Wiley & Sons.

Jayarama Krishna, J.V., Korobeinichev, O.P. and Vinu, R. (2019) 'Isothermal fast pyrolysis kinetics of synthetic polymers using analytical Pyroprobe', *Process Safety and Environmental Protection*, 139, pp. 48–58. doi: 10.1016/j.psep.2019.06.012.

Jones, J.R., Chen, Q. and Ripberger, G.D. (2020) 'Secondary reactions and the heat of pyrolysis of wood', *Energy Technology*, 8(6), 2000130. doi: 10.1002/ente.202000130.

Kasparbauer, R.D. (2009) *The effects of biomass pretreatments on the products of fast pyrolysis*. Graduate Theses and Dissertations, Iowa State University.

Kawamoto, H. (2017) 'Lignin pyrolysis reactions', *Journal of Wood Science*, 63(2), pp. 117–132. doi: 10.1007/s10086-016-1606-z.

Kissinger, H.E. (1956) 'Variation of peak temperature with heating rate in differential thermal analysis', *Journal of Research of the National Bureau of Standards*, 57(4), pp. 217–221. doi: 10.6028/jres.057.026.

Kofman, P.D. (2016) *Wood ash*. COFORD Connects Note No. 43. Dublin: COFORD Department of Agriculture, Food and the Marine.

Koppejan, J. and van Loo, S. (eds.) (2016) *The handbook of biomass combustion and co-firing*. London: Earthscan.

Kosowska, M., Majcher, M., Jeleń, H.H., Fortuna, T., Jaworska, D. and Półtorak, A. (2018) 'Key aroma compounds in smoked cooked loin', *Journal of Agricultural and Food Chemistry*, 66(14), pp. 3683–3690. doi: 10.1021/acs.jafc.7b05996.

Koufopanos, C.A., Lucchesi, A. and Maschio, G. (1989) 'Kinetic modelling of the pyrolysis of biomass and biomass components', *The Canadian Journal of Chemical Engineering*, 67(1), pp. 75–84. doi: 10.1002/cjce.5450670112.

Kpoclou, E.Y., Anihouvi, V.B., Anihouvi, D.G.H. et al. (2014) 'Effect of fuel and kiln type on the PAH levels in smoked shrimp, a Beninese food condiment', *Food Additives & Contaminants: Part A*, 31(7), pp. 1212–1218. doi: 10.1080/19440049.2014.916422.

Lam, K.L., Oyedun, A.O. and Hui, C.W. (2012) 'Experimental and modelling studies of biomass pyrolysis', *Industrial & Engineering Chemistry Research*, 51(36), pp. 11725–11732. doi: 10.1021/ie300369y.

Ledesma, E., Rendueles, M. and Díaz, M. (2016a) 'Contamination of meat products during smoking by PAHs: Processes and prevention', *Food Control*, 60, pp. 64–87. doi: 10.1016/j.foodcont.2015.07.016.

Ledesma, E., Rendueles, M. and Díaz, M. (2016b) 'Smoked food', in *Current Developments in Biotechnology and Bioengineering: Food and Beverages Industry*. Amsterdam: Elsevier, pp. 143–170. doi: 10.1016/B978-0-444-63666-9.00008-X.

Lei, Z., Xu, G., Chen, J., Wang, L. and Zhang, X. (2019) 'Thermal pyrolysis characteristics and kinetics of hemicellulose isolated from Camellia oleifera shell', *Bioresource Technology*, 282, pp. 228–235. doi: 10.1016/j.biortech.2019.02.131.

Li, C. (2015) 'Catalytic transformation of lignin for the production of chemicals and fuels', *Chemical Reviews*, 115, pp. 11559–11624. doi: 10.1021/acs.chemrev.5b00155.

Li, S., Li, S., Li, Y., Dong, J. and He, G. (2025) 'Pyrolysis Kinetic and Radical Mechanisms of Hyperbranched Polyamidoamine, a Macroinitiator for Endothermic Hydrocarbon Fuels', *ACS Omega*, 10(27), pp. 28739–28751. doi: 10.1021/acsomega.4c10279.

Liang, Y., Ries, M.E. and Hine, P.J. (2023) 'Pyrolysis activation energy of cellulosic fibres investigated by a method derived from the first-order global model', *Carbohydrate Polymers*, 305, 120518. doi: 10.1016/j.carbpol.2022.120518.

Lingbeck, J.M., Cordero, P., O'Bryan, C.A., Johnson, M.G., Ricke, S.C. and Crandall, P.G. (2014) 'Functionality of liquid smoke as an all-natural antimicrobial in food preservation', *Meat Science*, 97(2), pp. 197–206. doi: 10.1016/j.meatsci.2014.02.003.

Lu, Y., Lu, Y.C., Hu, H., Xie, F., Wei, X. and Fan, X. (2017) 'Structural characterization of lignin and its degradation products with spectroscopic methods', *Journal of Spectroscopy*, 2017, 8951658. doi: 10.1155/2017/8951658.

Lv, G.J., Wu, S.B. and Lou, R. (2010) 'Kinetic study of the thermal decomposition of hemicellulose isolated from corn stalk', *BioResources*, 5(2), pp. 1281–1291.

Maleknia, S., Bell, T.L. and Adams, M.A. (2009) 'Eucalypt smoke and wildfires: Temperature-dependent emissions of biogenic volatile organic compounds', *International Journal of Mass Spectrometry*, 279, pp. 126–133. doi: 10.1016/j.ijms.2008.10.025.

Mallick, D., Barbhuiya, S.A. and Banik, R. (2019) 'Detailed study of pyrolysis kinetics of biomass using thermogravimetric analysis', *AIP Conference Proceedings*, 2100, 020117. doi: 10.1063/1.5096505.

Mamleev, V., Bourbigot, S. and Yvon, J. (2007) 'Kinetic analysis of the thermal decomposition of cellulose: The main step of mass loss', *Journal of Analytical and Applied Pyrolysis*, 80(1), pp. 151–165. doi: 10.1016/j.jaap.2007.01.013.

Mate, M. and Babler, M. (2016) *Numerical modelling of wood pyrolysis*. MSc thesis. KTH/Chalmers.

Mehrabian, R., Scharler, R. and Obernberger, I. (2012) 'Effects of pyrolysis conditions on the heating rate in biomass particles and applicability of TGA kinetics in particle modelling', *Fuel*, 93, pp. 567–575. doi: 10.1016/j.fuel.2011.09.054.

Meier, D. and Faix, O. (1992) 'Pyrolysis-gas chromatography-mass spectrometry', in Lin, S.Y. and Dence, C.W. (eds.) *Methods in Lignin Chemistry*. Berlin: Springer, pp. 177–199.

Meng, Q., Li, X., Wang, T., Ma, L., Zhang, Q. and Wang, C. (2017) 'The role of water on the selective decarbonylation of 5-hydroxymethylfurfural over Pd/Al2O3 catalyst: Experimental and DFT studies', *Applied Catalysis B: Environmental*, 212, pp. 15–22. doi: 10.1016/j.apcatb.2017.04.024.

Miller, R.S. and Bellan, J. (1997) 'A generalized biomass pyrolysis model based on superimposed cellulose, hemicellulose and lignin kinetics', *Combustion Science and Technology*, 126(1–6), pp. 97–137. doi: 10.1080/00102209708935670.

Mohan, D., Pittman, C.U. and Steele, P.H. (2006) 'Pyrolysis of wood/biomass for bio-oil: A critical review', *Energy & Fuels*, 20(3), pp. 848–889. doi: 10.1021/ef0502397.

Montano, L. et al. (2025) 'Polycyclic aromatic hydrocarbons (PAHs) in the environment: Occupational exposure, health risks and fertility implications', *Toxics*. doi: 10.3390/toxics13030151.

Montazeri, N., Oliveira, A.C.M., Himelbloom, B.H., Leigh, M.B. and Crapo, C.A. (2013) 'Chemical characterization of commercial liquid smoke products', *Food Science & Nutrition*, 1(1), pp. 102–115. doi: 10.1002/fsn3.9.

Morf, P., Hasler, P. and Nussbaumer, T. (2002) 'Mechanisms and kinetics of homogeneous secondary reactions of tar from continuous pyrolysis of wood chips', *Fuel*, 81(7), pp. 843–853. doi: 10.1016/S0016-2361(01)00216-2.

Murugan, P., Mahinpey, N., Johnson, K.E. and Wilson, M. (2008) 'Kinetics of the pyrolysis of lignin using thermogravimetric and differential scanning calorimetry methods', *Energy & Fuels*, 22(4), pp. 2720–2724. doi: 10.1021/ef700730u.

Ndao, A., Ndiaye, F.T., Leveneur, S. et al. (2025) 'Production and valorization of acetic acid from lignocellulosic biomass pyrolysis: Influence of operational conditions and membrane separation processes', *Sustainable Chemistry for the Environment*, 11, 100268. doi: 10.1016/j.scenv.2025.100268.

Nguyen, T.S., He, S., Lefferts, L., Brem, G. and Seshan, K. (2016) 'Study on the catalytic conversion of lignin-derived components in pyrolysis vapour using model component', *Catalysis Today*, 259(2), pp. 381–387. doi: 10.1016/j.cattod.2015.04.043.

Nield, D.A. and Bejan, A. (2013) *Convection in porous media*. 4th edn. New York: Springer.

Oasmaa, A. and Meier, D. (2005) 'Norms and standards for fast pyrolysis liquids: 1. Round robin test', *Journal of Analytical and Applied Pyrolysis*, 73(2), pp. 323–334. doi: 10.1016/j.jaap.2005.03.003.

Obst, J.R. and Landucci, L.L. (1986) 'The syringyl content of softwood lignin', *Journal of Wood Chemistry and Technology*, 6(3), pp. 311–327. doi: 10.1080/02773818608085255.

Oltean, L., Teischinger, A. and Hansmann, C. (2007) 'Influence of temperature on cracking and mechanical properties of wood during drying – A review', *BioResources*, 2(4), pp. 789–811.

Pan, Z., Li, Y., Jiang, W., Ding, S. and Huang, J. (2024) 'Catalytic pyrolysis mechanism of lignin moieties driven by aldehyde, hydroxyl, methoxy, and allyl functionalization: The role of reactive quinone methide and ketene intermediates', *Green Chemistry*, 26(18), pp. 9899–9910. doi: 10.1039/D4GC01743K.

Parikh, J., Channiwala, S.A. and Ghosal, G.K. (2005) 'A correlation for calculating HHV from proximate analysis of solid fuels', *Fuel*, 84(5), pp. 487–494. doi: 10.1016/j.fuel.2004.10.010.

Park, W.C., Atreya, A. and Baum, H.R. (2010) 'Experimental and theoretical investigation of heat and mass transfer processes during wood pyrolysis', *Combustion and Flame*, 157(3), pp. 481–494. doi: 10.1016/j.combustflame.2009.10.006.

Parthasarathy, P. and Narayanan, S. (2019) 'Prediction of pyrolysis and gasification characteristics of different biomass from their physico-chemical properties', *Energy Sources, Part A: Recovery, Utilization and Environmental Effects*, 36(23), pp. 2530–2540. doi: 10.1080/15567036.2014.953713.

Pastorova, I., Botto, R.E., Arisz, P.W. and Boon, J.J. (1994) 'Cellulose char structure: A combined analytical Py-GC/MS, FTIR, and NMR study', *Carbohydrate Research*, 262, pp. 27–47. doi: 10.1016/0008-6215(94)00197-7.

Patankar, S.V. (1980) *Numerical heat transfer and fluid flow*. New York: Hemisphere/McGraw-Hill.

Pavlath, A.E. and Gregorski, K.S. (1988) 'Carbohydrate pyrolysis II: Formation of furfural and furfuryl alcohol during pyrolysis of selected carbohydrates with acidic and basic catalysts', in *Research in Thermochemical Biomass Conversion*. London: Elsevier, pp. 155–163.

Pe III, J.A., Mun, J.S. and Mun, S.P. (2023) 'Thermal characterization of kraft lignin prepared from mixed hardwoods', *BioResources*, 18(1), pp. 926–936. doi: 10.15376/biores.18.1.926-936.

Pettersen, R.C. (1984) 'The chemical composition of wood', in Rowell, R.M. (ed.) *The Chemistry of Solid Wood*. Washington, DC: American Chemical Society, pp. 57–126. doi: 10.1021/ba-1984-0207.ch002.

Pöhlmann, M., Hitzel, A., Schwägele, F. and Speer, K. (2013) 'Influence of different smoke generation methods on the contents of polycyclic aromatic hydrocarbons (PAH) and phenolic substances in Frankfurter-type sausages', *Food Control*, 34(2), pp. 347–355. doi: 10.1016/j.foodcont.2013.05.005.

Radmanović, K., Đukić, I. and Pervan, S. (2014) 'Specific heat capacity of wood', *Drvna Industrija*, 65(2), pp. 151–157. doi: 10.5552/drind.2014.1333.

Ralph, J. and Hatfield, R.D. (1991) 'Pyrolysis-GC-MS characterization of forage materials', *Journal of Agricultural and Food Chemistry*, 39(8), pp. 1426–1437. doi: 10.1021/jf00008a014.

Ratte, J., Dieguez-Alonso, A., De la Cruz-Lovera, C. et al. (2009) 'Mathematical modelling of slow pyrolysis of a particle of treated wood waste', *Journal of Hazardous Materials*, 170(2–3), pp. 1023–1040. doi: 10.1016/j.jhazmat.2009.05.077.

Reina, J., Velo, E. and Puigjaner, L. (1998) 'Kinetic study of the pyrolysis of waste wood', *Industrial & Engineering Chemistry Research*, 37(11), pp. 4290–4295. doi: 10.1021/ie980083g.

Reschmeier, R., Laske, S., Spliethoff, H. and Groß, J. (2014) 'Pyrolysis kinetics of wood pellets in fluidized beds', *Journal of Analytical and Applied Pyrolysis*, 108, pp. 117–129. doi: 10.1016/j.jaap.2014.05.009.

Ringer, M., Putsche, V. and Scahill, J. (2006) *Large-scale pyrolysis oil production: A technology assessment and economic analysis*. NREL/TP-510-37779. Golden, CO: National Renewable Energy Laboratory.

Ripberger, G. D. (2016). *A study of the importance of secondary reactions in char formation and pyrolysis* [Doctoral dissertation, Massey University]. Massey Research Online.

Roberts, A.F. (1971) 'The specific enthalpy of reaction during the pyrolysis of wood', *Combustion and Flame*, 17(1), pp. 79–90. doi: 10.1016/S0010-2180(71)80125-1.

Ross, R.J. (ed.) (2010) *Wood handbook: Wood as an engineering material*. General Technical Report FPL-GTR-190. Madison, WI: USDA Forest Service, Forest Products Laboratory.

Rusz, J. and Kopslova, M. (1974) 'New method for smoking meat and meat products', *Fleisch*, 28(12), p. 236.

Samburova, V., Zielinska, B. and Khlystov, A. (2017) 'Do 16 polycyclic aromatic hydrocarbons represent PAH air toxicity?', *Toxics*, 5(3). doi: 10.3390/toxics5030017.

Sampaio, G.R. et al. (2021) 'Polycyclic aromatic hydrocarbons in foods: Biological effects, legislation, occurrence, analytical methods, and strategies to reduce their formation', *International Journal of Molecular Sciences*, 22(11), 6010. doi: 10.3390/ijms22116010.

Scheller, H.V. and Ulvskov, P. (2010) 'Hemicelluloses', *Annual Review of Plant Biology*, 61, pp. 263–289. doi: 10.1146/annurev-arplant-042809-112315.

Scholze, B. and Meier, D. (2001) 'Characterization of the water-insoluble fraction from pyrolysis oil (pyrolytic lignin). Part I. PY-GC/MS, FTIR, and functional groups', *Journal of Analytical and Applied Pyrolysis*, 60(1), pp. 41–54. doi: 10.1016/S0165-2370(00)00110-8.

Schuldt, P. (1979) 'Application of steam-generated smoke in cold-smoking and controlled environment smoking', *Fleischerei*, 12(30), p. 990.

Scott, D.S., Piskorz, J. and Radlein, D. (1985) 'Liquid products from the continuous flash pyrolysis of biomass', *Industrial & Engineering Chemistry Process Design and Development*, 24(3), pp. 581–588. doi: 10.1021/i200030a011.

Shafizadeh, F. (1984) 'The chemistry of pyrolysis and combustion', in Rowell, R.M. (ed.) *The Chemistry of Solid Wood*. Washington, DC: American Chemical Society, pp. 489–529.

Shafizadeh, F. and Chin, P.P.S. (1977) 'Thermal deterioration of wood', in Goldstein, I.S. (ed.) *Wood Technology: Chemical Aspects*. Washington, DC: American Chemical Society, pp. 57–81.

Shen, D.K. and Gu, S. (2009) 'The mechanism for thermal decomposition of cellulose and its main products', *Bioresource Technology*, 100(24), pp. 6496–6504. doi: 10.1016/j.biortech.2009.06.095.

Shen, Y., Yan, D., Huang, L. et al. (2024) 'Unveiling radical pathways in the pyrolysis of eugenol: Experimental and computational insights', *Journal of Analytical and Applied Pyrolysis*, 177, 105005. doi: 10.1016/j.jaap.2024.105005.

Siau, J.F. (1984) *Transport processes in wood*. Berlin: Springer-Verlag.

Sinha, S. et al. (2000) 'Modelling of pyrolysis in wood: A review', *SESI Journal*, 10, pp. 41–62.

Sjostrom, E. and Alén, R. (1999) *Analytical methods in wood chemistry, pulping and papermaking*. Berlin: Springer.

Slopiecka, K., Bartocci, P. and Fantozzi, F. (2012) 'Thermogravimetric analysis and kinetic study of poplar wood pyrolysis', *Applied Energy*, 97, pp. 491–497. doi: 10.1016/j.apenergy.2011.12.056.

Solanki, S., Baruah, B. and Tiwari, P. (2022) 'Modeling and simulation of wood pyrolysis process using COMSOL Multiphysics', *Bioresource Technology Reports*, 17, 100941. doi: 10.1016/j.biteb.2021.100941.

Soukup-Carne, D., Fan, X. and Esteban, J. (2022) 'An overview and analysis of the thermodynamic and kinetic models used in the production of 5-hydroxymethylfurfural and furfural', *Chemical Engineering Journal*, 442(Part 2), 136313. doi: 10.1016/j.cej.2022.136313.

Stołyhwo, A. and Sikorski, Z.E. (2005) 'Polycyclic aromatic hydrocarbons in smoked fish – A critical review', *Food Chemistry*, 91(2), pp. 303–311. doi: 10.1016/j.foodchem.2004.06.012.

Stumpe-Vīksna, I., Bartkevics, V., Kukāre, A. and Morozovs, A. (2008) 'Polycyclic aromatic hydrocarbons in meat smoked with different types of wood', *Food Chemistry*, 110(3), pp. 794–797. doi: 10.1016/j.foodchem.2008.03.004.

Sun, T., Li, Z., Ding, S. et al. (2023) 'Influences of the reaction temperature and catalysts on the pyrolysis product distribution of lignocellulosic biomass', *Polymers*, 15(9), 2143. doi: 10.3390/polym15092143.

Sung, W. (2013) 'Volatile constituents detected in smoke condensates from the combination of the smoking ingredients sucrose, black tea leaves, and bread flour', *Journal of Food and Drug Analysis*, 21(3), pp. 292–300. doi: 10.1016/j.jfda.2013.07.005.

Surahmanto, F., Saptoadi, H., Sulistyo, H. and Rohmat, T. A. (2017) 'Investigation of the slow pyrolysis kinetics of oil palm solid waste by the distributed activation energy model', *Biofuels*, 11(6), pp. 663–670. doi: 10.1080/17597269.2017.1387750.

Svenson, J., Pettersson, J.B.C. and Davidsson, K.O. (2004) 'Fast pyrolysis of the main components of birch wood', *Combustion Science and Technology*, 176(5–6), pp. 977–990. doi: 10.1080/00102200490428585.

The Culinary Institute of America (2011) *The professional chef*. 9th edn. Hoboken, NJ: John Wiley & Sons.

The Warehouse (2026) *Maxistrike portable fish smoker small*. Available at: The Warehouse.

Thurner, F. and Mann, U. (1981) 'Kinetic investigation of wood pyrolysis', *Industrial & Engineering Chemistry Process Design and Development*, 20(3), pp. 482–488. doi: 10.1021/i200014a015.

Tia, S., Bhattacharya, S.C. and Wibulswas, P. (1991) 'Thermogravimetric analysis of Thai lignite—I. Pyrolysis kinetics', *Energy Conversion and Management*, 31(3), pp. 265–276. doi: 10.1016/0196-8904(91)90005-U.

Tóth, L. and Deutsche Forschungsgemeinschaft (1982) *Chemie der Räucherung*. Weinheim: Verlag Chemie.

Várhegyi, G., Szabó, P., Antal, M.J. et al. (1989) 'Kinetics of the thermal decomposition of cellulose, hemicellulose, and sugar cane bagasse', *Energy & Fuels*, 3(3), pp. 329–335. doi: 10.1021/ef00015a012.

Varlet, V., Prost, C., Serot, T. and Knockaert, C. (2007) 'Organoleptic characterization and PAH content of salmon (Salmo salar) fillets smoked according to four industrial smoking techniques', *Journal of the Science of Food and Agriculture*, 87(5), pp. 847–854. doi: 10.1002/jsfa.2786.

Vassilev, S.V., Baxter, D., Andersen, L.K. and Vassileva, C.G. (2010) 'An overview of the chemical composition of biomass', *Fuel*, 89(5), pp. 913–933. doi: 10.1016/j.fuel.2009.10.022.

Vazquez, T.D. (2022) *Formation of key aroma compounds generated in condensed wood smoke for the flavoring of foods*. PhD thesis. The Ohio State University.

Vazquez, T., Tello, E. and Peterson, D.G. (2025) 'Identification of the key aroma compounds in condensed hardwood smoke', *Molecules*, 30(3), 720. doi: 10.3390/molecules30030720.

Ververis, C., Georghiou, K., Christodoulakis, N., Santas, P. and Santas, R. (2004) 'Fiber dimensions, lignin and cellulose content of various plant materials and their suitability for paper production', *Industrial Crops and Products*, 19(3), pp. 245–254. doi: 10.1016/j.indcrop.2003.10.006.

Vyazovkin, S. (2000) 'Kinetic concepts of thermally stimulated reactions in solids: A view from a historical perspective', *International Reviews in Physical Chemistry*, 19(1), pp. 45–60. doi: 10.1080/014423500229855.

Vyazovkin, S. (2003) 'Reply to "What is meant by the term 'variable activation energy' …"', *Thermochimica Acta*, 397(1–2), pp. 269–271. doi: 10.1016/S0040-6031(02)00391-X.

Wang, Q., Bai, X., Lv, P. et al. (2020) 'Initial pyrolysis mechanism and product formation of cellulose: An experimental and density functional theory (DFT) study', *Scientific Reports*, 10, 7199. doi: 10.1038/s41598-020-60095-2.

Werner, K., Pommer, L. and Broström, M. (2014) 'Thermal decomposition of hemicelluloses', *Journal of Analytical and Applied Pyrolysis*, 110, pp. 130–137. doi: 10.1016/j.jaap.2014.08.013.

WHO, IPCS and FAO/WHO (2009) *Principles and methods for the risk assessment of chemicals in food*. Environmental Health Criteria 240. Geneva: World Health Organization.

Woods, L. (2003) 'Smoked foods: Principles', in Caballero, B., Trugo, L. and Finglas, P.M. (eds.) *Encyclopedia of Food Sciences and Nutrition*. 2nd edn. Oxford: Elsevier, pp. 5173–5180.

Wright, R. (2021) '*Anoxic thermal degradation of kānuka and tobacco between 180°C and 390°C'*. Massey University.

Yang, H., Chen, W.H. et al. (2021) 'Lignin pyrolysis under NH3 atmosphere for 4-vinylphenol product: An experimental and theoretical study', *Fuel*, 297, 120739. doi: 10.1016/j.fuel.2021.120739.

Yang, H., Yan, R., Chen, H., Lee, D.H. and Zheng, C. (2007) 'Characteristics of hemicellulose, cellulose and lignin pyrolysis', *Fuel*, 86(12–13), pp. 1781–1788. doi: 10.1016/j.fuel.2006.12.013.

Ye, L., Chen, H., Liu, Z., Ma, X. and Peng, X. (2021) 'Recent progress in furfural production from hemicellulose and its derivatives: Conversion mechanism, catalytic system, solvent selection', *Molecular Catalysis*, 515, 111910. doi: 10.1016/j.mcat.2021.111910.

Yeo, J.Y., Chin, B.L.F., Tan, J.K. and Loh, Y.S. (2019) 'Comparative studies on the pyrolysis of cellulose, hemicellulose, and lignin based on combined kinetics', *Journal of the Energy Institute*, 92(1), pp. 27–37. doi: 10.1016/j.joei.2017.12.003.

Yerrayya, A., Natarajan, U. and Vinu, R. (2019) 'Fast pyrolysis of guaiacol to simple phenols: Experiments, theory and kinetic model', *Chemical Engineering Science*, 207, pp. 619–630. doi: 10.1016/j.ces.2019.06.042.

Yin, X., Fan, H., Zhang, M. et al. (2021) 'Collaborative analysis on differences in volatile compounds of Harbin red sausages smoked with different types of woodchips based on gas chromatography–mass spectrometry combined with electronic nose', *LWT*, 143, 111144. doi: 10.1016/j.lwt.2021.111144.

Yuan, J.M., Li, C., Sun, Q., Li, S. and Zhang, C. (2022) 'Valorization of lignin into phenolic compounds via fast pyrolysis: Impact of lignin structure', *Fuel*, 319, 123755. doi: 10.1016/j.fuel.2022.123755.

Yuan, Q., Lu, Y., Huang, W. et al. (2021) 'The kinetics studies on hydrolysis of hemicellulose', *Frontiers in Chemistry*, 9, 781291. doi: 10.3389/fchem.2021.781291.

Zugenmaier, P. (2008) *Crystalline cellulose and derivatives: Characterization and structures*. Berlin: Springer-Verlag. doi: 10.1007/978-3-540-73934-0.

Zwaig, K. and Schossig, H. (1979) 'Experience with the type 301 steam-type smoke generator in bratwurst manufacture', *Fleisch*, 33(9), p. 173.

This page is intentionally left blank.

Appendix 1

Table A1-1: Relative intensity of key compounds discussed in chapter 4 with respect to temperature derived from Py-EGA/MS analysis. Intensities are normalized to the maximum value observed for each individual compound, rather than expressed as a proportion of the total ion chromatogram (TIC).

	Relative Intensity (%)															
Temperature (°C)	Total EIC	5-Hydroxymethylfurfural	Vanillin	Creosol	Guaiacol	Furfuryl alcohol	2-methoxy-4-vinylphenol	4-methylsyringol	Eugenol	m-cresol	phenol (2 (6-dimethoxy)	Phenol	Coniferyl Aldehyde	3,5-Dimethoxy-4-hydroxycinnamaldehyde	1,2benzenediol	Furfural
100	0.04	0	0.1	0.1	0.3	0.1	0	0	0	1.4	0	0.1	0.4	0.5	0.4	0
125	0.06	0	0.1	0	0.1	0	0.1	0.1	0.2	0	0	0.1	0.1	0.4	0.1	0.3
150	0.07	0.1	0.2	0.1	0.4	0.1	0.2	0.1	0.1	0.1	0.1	0.3	0.2	0.2	0.1	0.3
175	0.12	0.1	1	0	0.2	0.1	0.1	0.1	0.1	0.1	0.1	0.5	0.1	0.1	0.4	0.8
200	0.32	0.1	2.3	0.3	0.5	0.1	0.2	0.1	0	0.4	0.1	0.2	1	0.5	0.8	1.4
225	0.96	0.2	3	0.8	1.5	0.4	0.5	0.6	0.7	0.8	0.2	1.7	4.2	1.4	1.1	2
250	3.46	1.4	7.3	2.1	4.2	0.7	1.9	2.4	2.2	3.2	0.9	3.4	18.6	8.4	3.2	8
275	13.22	5.9	21	6.1	16.2	2.6	8.3	7.6	11.4	6.4	4.2	9.5	68.7	46	8.5	34.6
300	33.79	10.8	38.7	18.4	35.7	9.2	25.7	19.4	47	20.6	18.2	18.7	98.1	90.6	14.8	64.9
325	45.57	18.6	48.7	29.9	52	17.3	47.4	33.6	75.2	24.1	33.1	27.8	66.9	59.6	21	45.9
350	62.14	37	67.3	54.6	58.4	36.1	86.7	70.1	82.5	42.5	54.4	49.7	46.4	24.7	37.1	48.4
375	92.96	81.4	81.8	83.2	88.5	83.3	77.5	93.3	63.5	80.9	87.9	67	39.5	11.9	86.1	83.9
400	39.53	32.9	49.4	55.7	67.2	25.6	24.4	42	25.8	42.7	57.7	37.2	17.8	4.8	63.7	37.4
425	12.32	4.3	35.1	41.9	73.5	0.6	8.6	18.2	14.4	18.5	32.6	20.2	9.5	1.5	43.8	7.2
450	8.11	1.7	27.4	33.7	77.4	0.4	3.2	3.8	4.4	19.4	9.4	19.3	4.6	2	53.2	4.6
475	4.42	0.4	7.1	13.7	46.6	0.2	2	0.9	2.1	27.3	0.9	24.9	1.4	1.1	31	1.8
500	2.23	0.2	1.8	2.1	12.9	0.1	0.9	0.4	0.1	28.5	0.3	24.7	0.4	1	10.6	0.7
525	1.2	0.2	0.1	0.4	1.9	0.1	0.1	0.3	0	23.4	0.2	29.5	0.3	0.5	1.5	0.4
550	0.68	0	0.5	0.2	0.1	0	0.1	0.2	0.2	11.5	0.2	25.4	0.8	0.1	0.3	0.2
575	0.22	0	0.4	0.2	0.1	0	0.2	0.4	0	0.2	0.3	1	0.7	0.2	0.3	0.2

Table A1-2: Raw Intensity data of compound classes with respect to temperature derived from Py-GC/MS dataset

Temperature (°C)	Phenols	Ketones	Furans	Aldehydes	Alcohol	Acids	Other
200	0	0	0	19691	0	0	0
210	0	0	0	27992	0	0	0
220	0	0	0	17804	0	0	0
230	0	0	0	86107	0	0	0
240	0	0	0	95123	0	0	0
250	25200	0	23051	69161	0	0	0
260	50058	0	32414	133738	11498	33031	15260
270	86392	0	27174	193508	19090	86203	32373
280	125065	0	50502	269770	154394	165841	243635
290	278794	0	60238	412789	61156	181775	118819
300	493108	35062	76929	490323	77461	251386	164300
310	638546	0	104238	413439	77706	278080	175153
320	895751	14391	136246	469729	97360	301871	219829
330	831022	15305	128779	560893	91857	296319	184198
340	1197281	22207	188676	408073	108682	365238	222058
350	1126465	464059	212521	354190	182881	531687	263818
360	1138644	269477	290026	282102	102949	467209	267917
370	1458114	372024	363183	278340	238378	523040	237079
380	2341119	202060	594518	389353	151839	481088	305711
390	2951321	445089	541195	366205	158180	503389	373262
400	2597541	366506	613060	339515	156029	477720	283963
410	3010919	372769	738989	362865	204516	563333	254009
420	3243923	290821	691751	394512	197693	559247	272206
430	3022514	362433	693289	355929	164620	521561	202193
440	3187469	543496	702078	344323	210196	574506	240843
450	3172798	400880	723551	325829	181430	593638	253422
460	2821828	318647	647548	360509	150607	526639	207051
470	3264907	385924	704941	392612	192853	573698	241011
480	3640911	524741	731875	395080	201589	749088	304306
490	3433240	544465	793425	358387	221918	581650	252881
500	3286415	409891	710941	384244	185737	578803	291953
510	3273461	553269	765894	349089	193697	875660	250017
520	3517511	392631	748485	360069	200085	605194	285592

Appendix 2

Determination of Heat Capacity of Kānuka and Char

Experimental materials & procedure

Materials

Manuka wood chips of particle size <600 μm were used. The NETZSCH STA (Simultaneous thermogravimetric analysis) 449 F1 with the Rhodium furnace that can go up to 1650 °C was used. Samples were packed down in aluminium crucibles to maximize the contact between the wood and aluminium, to achieve good contact for heat transfer. For accurate measurements it is recommended to choose a mass of wood of 12-15 mg to match the mass of the sapphire (α-alumina) of ~21.5 mg which has a specific heat capacity of ~0.80 J·kg^{-1}K^{-1} at room temperature (25°C) according to equation (A2-1).

$$\left(m \cdot c_p\right)_{Manuka} = \left(m \cdot c_p\right)_{sapphire} \quad \text{(A2-1)}$$

For the mass estimation, the C_p of the Manuka was approximated based on values of similar woods found in literature. For this study, a value of 1.50 J·kg^{-1}K^{-1} was used (Di Blasi and Russo 1994).

Summary of Test method

The method for the determination of specific heat capacity by TG-DSC consists of heating a sample at a controlled rate and in a controlled atmosphere over a specified temperature range. Heat flow into the sample is measured alongside the heat flow into an empty reference sample. The difference in the heat flows is then recorded over time. The mass loss is simultaneously recorded as well to validate the measurement. Any mass loss of more than 0.3% in the dynamic period (heating phase) deems the measurement invalid.

There are two methods of calculating the specific heat capacity of a material from the DSC analysis, 1) the ratio method and 2) the ASTM/DIN method

The ASTM method was used for this calculation. The following equation (A2-2) describes how the specific heat capacity, C_P of the sample was calculated.

$$C_{P_{sample}} = C_{P_{Standard}} \cdot \frac{D_s \cdot m_{st}}{D_{st} \cdot m_s} \quad \text{(A2-2)}$$

where:

$C_{P_{Sample}}$ = unknown specific heat capacity of the sample, J·g^{-1}K^{-1},
$C_{P_{standard}}$ = known specific heat capacity of the standard used (sapphire), J·g^{-1}K^{-1},
D_s = vertical distance between the sample holder and the sample DSC curve at a given temperature, mW,
D_{st} = vertical distance between the sample holder and the sapphire DSC curve at a given temperature, mW,
m_{st} = mass of sapphire, mg,
m_s = mass of sample, mg.

Procedure

Specific heat capacity determination requires three measurements when using the TG-DSC or even the Modulated-DSC method; (i) empty or baseline: (ii) standard (Sapphire – α-alumina): and (iii) sample (Manuka wood).
The reference crucible on the left hand side is always empty, while the crucible on the right is either left empty for the baseline measurement (a), or filled with a precisely measured sapphire disk (b), or filled with the sample material, Manuka, (c) as shown in Figure 9-1.

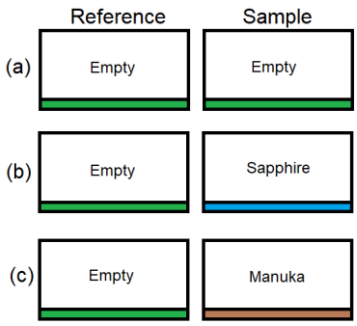

Figure A2-1: Set-up of the measurement series for specific heat capacity determination by DSC.

The three measurements were then carried out under identical conditions, where the furnace was heated to 105 °C at 10 °C min^{-1} and held for 45 minutes. This step was performed to remove moisture. The sample was then cooled down at 5 °C min^{-1} to 30 °C and then held for 50 minutes. The sample underwent another heating phase to 190 °C at 10 °C min^{-1} and held at this temperature for 20 minutes. This temperature range was chosen because pyrolysis reactions do not occur at temperatures <190 °C (Yang et al. 2007) and thus it is considered that the thermochemical and physical properties of the wood do not change significantly at this temperature. This is confirmed later by measuring the mass loss to assure that no more than 0.3% mass loss occurred during the second heating phase. During the entirety of the runs, 50 ml min^{-1} of N_2 gas was flowing through the furnace to purge it with an additional 20 ml min^{-1} to protect the Rhodium furnace and other components in the furnace from oxidative damage. Crucibles were covered with a pierced aluminium lid to minimize the effects of radiation.

DSC Analyses

Figure A2-2 shows the results from the three measurements; baseline, standard and sample. The most important section is the second dynamic step beginning at 118 minutes, which shows the heating of the sample from 30 °C to 190 °C, this section is expanded in Figure A2-2 and is used for the determination of the specific heat capacity. The NETZSCH Proteus® software produces a plot that automatically subtracts the baseline DSC curve from the sample and standard signals and plots the D_s, and D_{st} signals as shown in Figure A2-3.

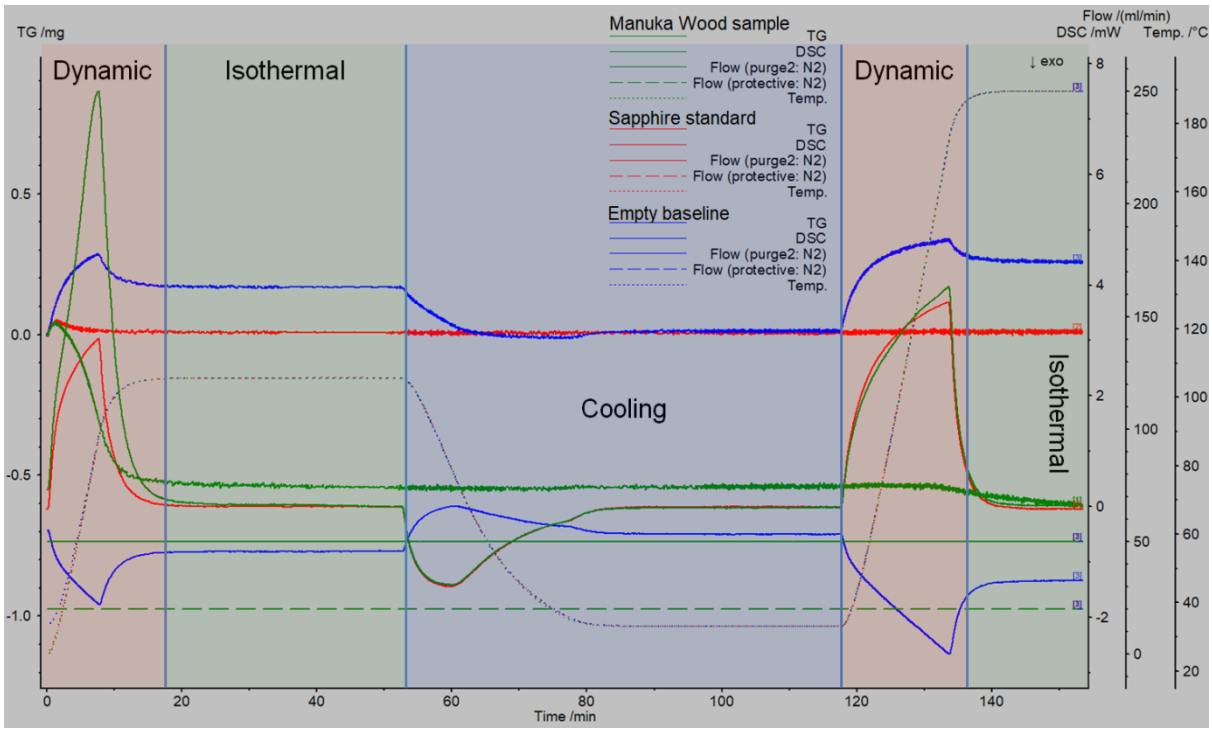

Figure A2-2: Result from all three measurements combined, includes mass loss, DSC signal, and the flowrate of purge and protective gases and the temperature of the furnace.

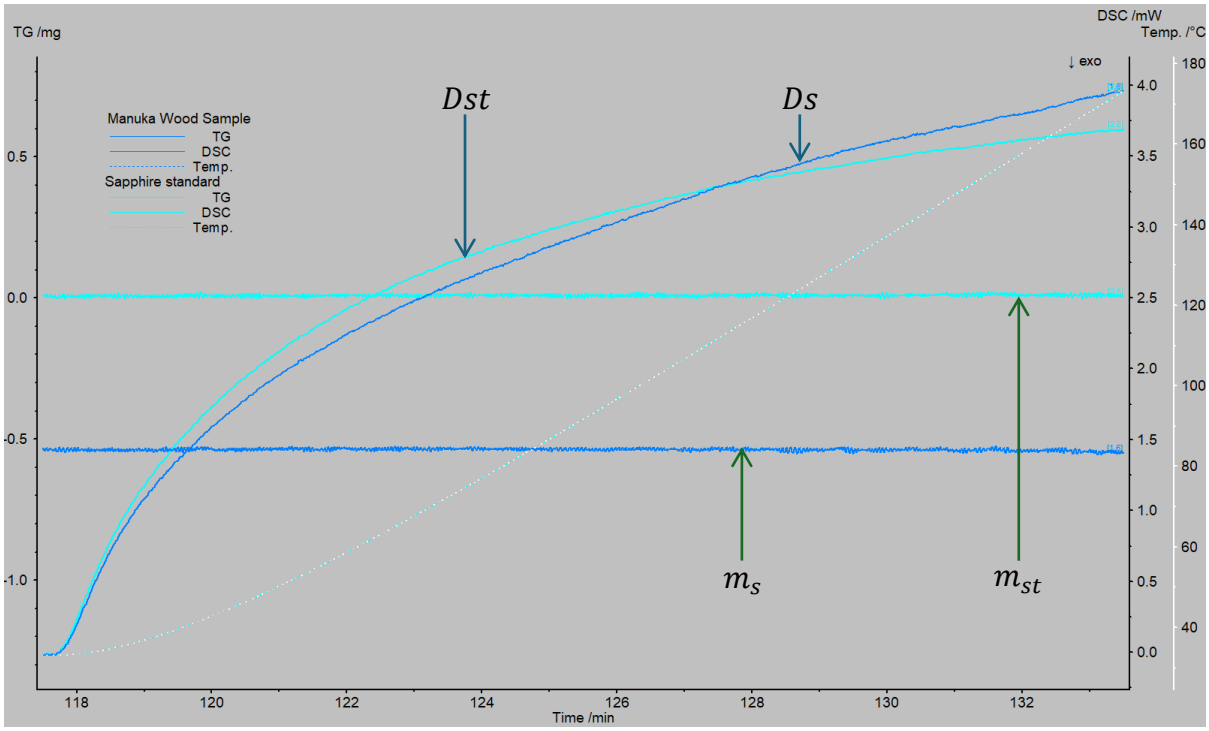

Figure A2-3: Mass loss and DSC signal for the dynamic portion (30 °C – 190 °C) of the plot from Figure 9-2. The flowrate of N_2 purge and protective gas is not shown. D_{st} is the standard minus baseline heat flow. D_s is the sample minus the baseline heat flow.

The specific heat capacity is then able to be calculated for small temperature intervals during heating. The values are shown in Figures A2-4 and A2-5 below. The method was also trialled for the determination of the specific heat capacity of Manuka char, made at 600°C in a muffle furnace for 2 hours. The results for the Manuka char specific heat capacity obtained are shown in Figure 9-6.

4.2 Specific heat capacity of Manuka wood

The experimental result for wood are fitted to a quadratic, given by equation A2-3 above, where, $c_{P,\,Manuka}$ is the specific heat capacity of Manuka wood in kJ $kg^{-1}K^{-1}$ and T is temperature in degrees Celsius (°C). The R^2 value of this relationship was 0.998, which indicates that this is a good fit. The mass loss was 0.15% during the heating up segment from Figure A2-2 from 30°C to 175°C and therefore this result can be considered valid (<0.3% change). A further important point is that wood was dried at 105 °C for 45 minutes before beginning experiments. By conducting them above 100 °C means the confounding effect of water is avoided. Figure A2-5 compare this work to results of other workers who have also measured the specific heat capacity above 100 °C. When experiments are done below 100 °C (Simpson and TenWolde 1999), the presence of adsorbed moisture can begin to dominate because the specific heat capacity of water at 4.18 kJ kg^{-1} K^{-1} is far higher than wood substance.

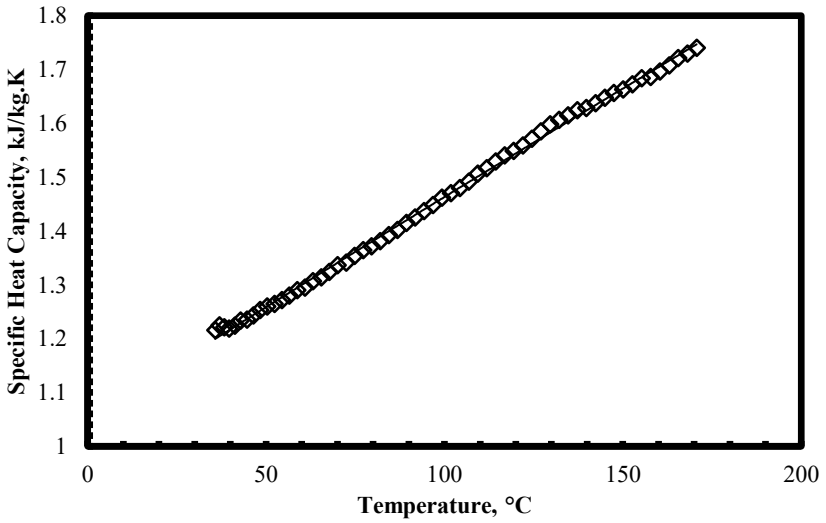

Figure A2-4: Specific heat Capacity of Manuka Wood

$$C_{P,\,Manuka}(dry) = -7 \times 10^{-7}(T^2) + 4.2 \times 10^{-3}(T) + 1.0505 \quad \text{(A2-3)}$$

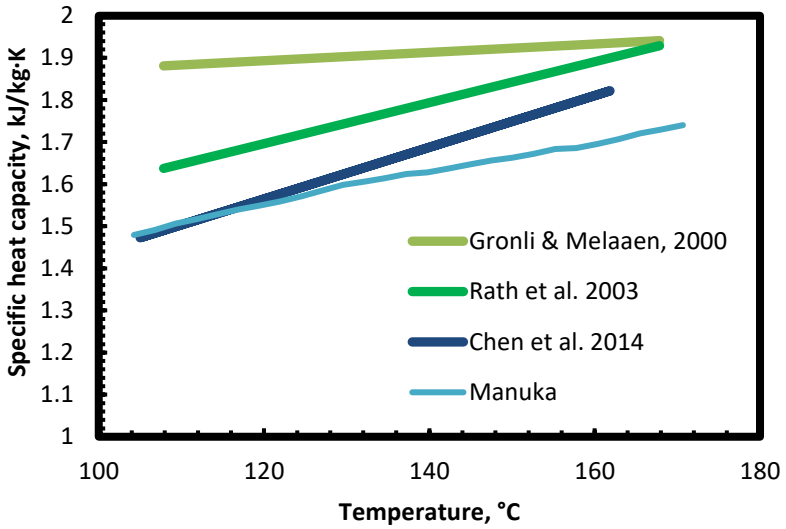

Figure A2-5: Specific heat capacity of the Manuka compared to heat capacity of other woods (References, Gronli, rath and Chen)

4.3 Specific heat capacity of Manuka char

Measurements of the specific heat capacity of char made from Manuka wood at 600 °C were carried out It was found that, when heated above 300 °C, the Manuka char sample lost more than 0.3% mass and therefore the result cannot be used. This highlighted the need to determine how many cycles of heating are required to produce reliable specific heat capacities, given wood is thermally unstable, and the subsequent char may also be partially unstable until all volatiles are driven off. It has been shown by other researchers (Chen et al. 2014) that subjecting the char sample through multiple heating cycles can stabilise the sample and therefore produces more reliable specific heat capacity Figures.

The ASTM E1269-11 method was also applied for the determination of the specific heat capacity of Manuka char produced at 600°C. It was run through the same heating regime as described above, but here the final temperature was 600 °C (for char) instead of 190 °C (for wood). Equation A2-4 was fitted to Figure A2-6 and can be used to predict the specific heat capacity of char in the temperature range of 100-300 °C. The R^2 value of this relationship was 0.9895, which indicates that this is a good fit.

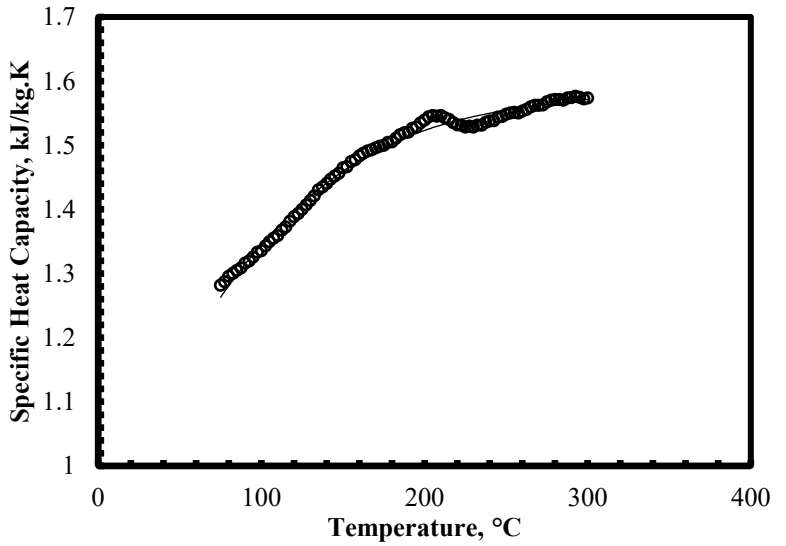

Figure A2-6: Specific heat Capacity of Manuka char made in a muffle furnace at 600°C

$$C_{P,\ ManukaChar}(dry) = 2 \times 10^{-8}(T^3) - 2 \times 10^{-5}(T^2) + 0.0064(T) + 0.8912 \quad \text{(A2-4)}$$

The term $c_{p,ManukaChar}$ is the specific heat capacity of Manuka char in kJ kg^{-1} K^{-1} and T is the temperature in degrees Celsius (°C).

Above 300 °C, a large (>0.3%) mass loss occurs and thus the specific heat capacity past 300 °C cannot be used. It was discovered that some decomposition reactions are occurring at temperatures higher than 300 °C and thus, in order to produce more accurate results, the char samples should be stabilised by running them through multiple heating cycles. This has been shown to produce more reliable specific heat capacity measurements for pyrolysis products (Q. Chen, 2014).

Appendix 3

Table A3-1: Content of extractive, carbohydrate and lignin in wood samples (% wt/wt, o.d.)

Wood	DCM Extractives	Lignin		Neutral Carbohydrates (as anhydrosugars)				
		Acid insoluble (Klason)	Acid soluble	Arabinosyl units	Galactosyl units	Glucoyl units	Xylosyl units	Mannosyl units
Beech	0.27	25.79	4.57	0.39	1.10	51.38	15.26	ND
Pohutukawa	1.33	34.41	2.33	0.42	1.44	43.91	13.59	ND
Kanuka	0.31	34.30	1.74	0.44	1.57	44.75	11.65	ND
Oak	0.45	25.95	3.91	0.43	1.02	47.65	18.33	ND
Tawa	0.34	27.28	2.03	0.72	1.10	50.29	12.95	ND
Rewarewa	0.26	28.55	3.21	0.82	1.19	44.34	14.94	ND
Kanuka bark	3.67	39.26	2.53	1.13	1.34	30.17	10.64	ND

Appendix 4

Table A4-1: Sieve analysis of particles between 90 and 600 microns

	Weight (g)			
Sieves (µm)	Initial	Final	Difference (g)	
600	139.27	139.32	0.05	1%
500	111.43	111.89	0.46	7%
425	123.82	124.27	0.45	7%
355	121.97	122.48	0.51	8%
300	120.07	120.62	0.55	8%
250	105.38	106.06	0.68	10%
90	116.69	119.29	2.6	39%
35	68.29	68.28	0	0%
15	89.32	90.67	1.35	20%

Table A4-2: Sieve analysis of particles < 90 microns

	Weight (g)			
Sieves (µm)	Initial	Final	Difference (g)	
90	296.05	308.62	12.57	69%
75	291	292.26	1.26	7%
63	285.93	287.49	1.56	9%
53	292	293.86	1.86	10%
45	285.75	286.41	0.66	3%
38	288.61	288.77	0.16	1%
15	359.17	359.17	0	0%
10	497.82	497.88	0.06	0%

Appendix 5

Space discretisation: The finite Volume Method (FVM)

The Finite Volume Method (FVM) was selected for the space discretisation of the governing equations. This choice is based on the FVMs inherent capability to enforce the conservation of physical quantities – such as mass, chemical species and energy – at the discrete level. Such conservation is paramount for the accurate simulation of transport phenomena coupled with chemical reactions as is with pyrolysis.

Computational Domain, Control Volumes (CVs), and Node placement

The one-dimensional computational domain, representing the depth of the wood sample, was discretised into N_x neighbouring, non-overlapping control volumes (CVs). A node was situated at

the geometric centre for each CV. Scalar variables, including temperature, pressure, species densities and porosity were evaluated at these cell-centred nodes. Gas phase velocities used to determine convective fluxes across CV faces, were derived from pressure field via Darcy's Law and subsequently used to compute these fluxes at the interfaces between adjacent CVs.

General FVM Approach

The FVM involves integrating the governing PDEs over each individual control volume. For a generic conserved scalar variable ϕ, the integral form of its conservation equation over a control volume $V_P$is expressed as:

$$\frac{\partial}{\partial t}\int_{V_P} \alpha\phi dV + \int_{A_{faces}} \boldsymbol{F}_{total} \cdot d\boldsymbol{A} = \int_{V_P} S_\phi dV \qquad \text{(A5-1)}$$

In this equation, α denotes a property pertinent to the storage of ϕ within the control volume (CV) (e.g., porosity for a gas species or volumetric heat capacity for temperature). The term $\boldsymbol{F}_{total}$ represents the total flux vector (including both advective and diffusive contributions) cross the CV faces (A_{faces}). S_ϕ is the volumetric source or sink term for ϕ. This integration procedure converts the PDE into an algebraic balance equation for ϕ specific for each CV.

Time discretisation: Implicit Euler Scheme

The time derivative term, $\frac{\partial \alpha\phi}{\partial t}$ present in the transient governing equations, was discretised usinga first-order implicit Euler scheme. This scheme approximates the time derivative as:

$$\frac{\partial(\alpha\phi)}{\partial t} \approx \frac{(\alpha\phi)_i^{n+1} - (\alpha\phi)_i^n}{\Delta t} \qquad \text{(A5-2)}$$

Where the superscript n denotes the previous time step and n+1 denotes the current time step, for which the solution is solved. A key characteristic of the implicit scheme is that all spatial derivative terms in the discretised equations are evaluated using the unknown variable value at the new time step n+1. This formulation leads to a system of coupled algebraic equations for the nodal values ϕ_i^{n+1} throughout the domain, necessitating a simultaneous solution. The implicit nature of the scheme confers significant advantages in terms of numerical stability, particularly for stiff systems involving rapid chemical reactions, therefore allowing larger time steps than would be feasible with explicit methods.